Computational studies of the structural and optical properties of organic-inorganic lead halide perovskites.

Thèse N° 9703

Présentée le 20 septembre 2019

à la Faculté des sciences de base
Laboratoire de chimie et biochimie computationnelles
Programme doctoral en chimie et génie chimique

pour l'obtention du grade de Docteur ès Sciences

par

Ariadni BOZIKI

Acceptée sur proposition du jury

Prof. S. Gerber, présidente du jury
Prof. U. Röthlisberger, directrice de thèse
Prof. C. Stoumpos, rapporteur
Prof. G. Tabacchi, rapporteuse
Prof. M. Grätzel, rapporteur

2019

ÉCOLE POLYTECHNIQUE
FÉDÉRALE DE LAUSANNE

"Man cannot sprout wings unless he has first reached the brink of the abyss!"
Nikos Kazantzakis

This dissertation is dedicated
to my beloved parents, Martha and Ioannis.

Contents

Acknowledgements

I would like to express my sincere gratitude to my advisor Prof. Dr. Ursula Röthlisberger, initially for the great opportunity that she gave me in order to conduct research in her group, under her supervision and of course for all the help, support, guidance and encouragement during the course of my PhD studies. However, most importantly, I deeply thank her for her kindness and understanding in very difficult moments of my life, where she truly supported me. The quote of Wayne Teasdale "*kindness is the highest form of intelligence*" always comes to my mind when I am thinking of her. I also want to refer to the great opportunity that she gave me, to daily interact with her two adorable doggies, Ruby and Quanta, which gave me joy in my heart.

Furthermore, I would like to thank Prof. Dr. Michael Grätzel for the fruitful collaboration and for all the comments and suggestions on my research during these years. I would also like to thank him for accepting to be one of the jury members of this dissertation. In addition, I would like to thank the other members of my PhD jury; Prof. Dr. Sandrine Gerber, Prof. Dr. Gloria Tabacchi, and Prof. Dr. Constantinos Stoumpos for revising my dissertation. Of course, special thanks to my mentor Prof. Dr. Vassily Hatzimanikatis for our long discussions and his valuable advice.

In addition, I would like to thank everyone that I collaborated with during these years, starting with Prof. Dr. Stefan Goedecker, Prof. Dr. Majed Chergui and Prof. Dr. Lyndon Emsley. Furthermore, I would especially like to thank the members of LCBC that helped me to accomplish my PhD; Simone, and Negar for especially helping me and teaching me during the first year of my PhD studies; Marko for working together and helping me on different projects as well as for his supportive character; Elisa and Pablo for helping me with the excited-state calculations and Martin for helping me with any problem related to the codes. In addition, I would also like to thank the external collaborators (theoreticians and experimentalists); Dr. M. Ibrahim Dar for the long meetings explaining me the experimental details; Prof. Dr. Chenyi Yi, Dr Dominik Kubicki and Mr Aditya Mishra for the experiments about the mixed cation/mixed halide lead perovskites and Dr José Flores-Livas and Dr Daniele Tomerini for the minimahopping simulations.

Of course, during these years apart from the LCBC members that I worked with and helped me with the projects, there were also other members (and former members) that supported me and their friendship was a real driving force for me. To this end, I would like to start by thanking Karin, the secretary of LCBC for been very supportive. I especially thank her for all these moments that was listening to my problems always trying to give me her advice and help. Of course, I would like to continue by thanking my office mates Polydefkis and Thibaud for the friendly, supportive, honest and trustful environment of our office. Especially since Polydefkis and I share the same nationality, the fact that I was able to speak in my mother tongue (greek) made me feel like home.

I would also like to thank Maria Letizia for her friendship and for always being by my side. In the same spirit I also thank Esra and Farzaneh for their support and kindness. I would further like to thank Murat and his wife Feyza for their support and friendship and Guido for his honest and supportive character. Of course I cannot forget Alicia, Giulia, Elisa, Simran, Marta and Siri that were always there, giving me their positive energy! I would like to continue by thanking François who also revised the french version of my summary and Lucie, Nick, Mathias, Justin, Swarnendu, Daniele, Simon, Pablo and Magnus for the nice interaction during these years. I will always keep in my mind the good memories and moments that I shared with all of you guys, during these years!

However, apart from the LCBC members, there were also other people that made my stay in Lausanne so pleasant and I deeply thank them for this reason and for their friendship. Of course I start with Giuliana for being a great friend and for being by my side when times get hard. Whatever I write here, it would not be enough to express my gratitude. I deeply thank her and I am so glad that I met her. Furthermore, I continue with Kyriaki and Panagiotis, two good friends that are no longer in Lausanne but were the first people that I trusted in this city and of course I miss them a lot. In similar vein, I would like to thank my good friend Olympia for always being by my side, even that she is not staying in Lausanne anymore.

Of course, special thanks to my great friends Anastasia, Myrsini, Maria, Eirini and Argyro that made my stay in Lausanne so pleasant. I am not able to imagine if I would have been able to make it all these years without them. Special thanks to Georgia and Mrs Foteini for their support and to Chrysa, Penny, Anna-Maria, Evaggelia, Kyriaki, Ioanna, Ilianna, Loukia, Vaso, Kalliopi, Sofia, Iro, Apostolis, Theo, Vaggelis, Yannis, Grigoris, Yannis, Yannis, George, Giorgos and Stefanos of course for their friendship and for all the nice memories.

I would like to continue by thanking Father Alexander for always trying to unify the Greek community of Lausanne. I would also like to thank Zira, my first landlord for her great support during the first moments of my arrival in Lausanne as well as Anna the executive director of the non-profit organization, at which I am a volunteer who is an exemplary model of kindness. Finally, I would like to thank my Professor of my Diploma thesis Prof. Dr. Doros Theodorou for transferring me his passion about science and research and for introducing me in the field of molecular simulations as well as Dr George Vogiatzis who helped me during my Diploma thesis and up to today he is always sharing with me his valuable advice.

This is the most emotional part of this acknowledgements section, since I want to continue by thanking my amazing family, starting with my beloved grandmother (*γιαγιά*) Panagiota (*Παναγιώτα*) who since I was a little girl she was always motivating and supporting me to never stop trying to exceed my limits and of course for her endless love and encouragement. Last but of course not least, a huge "thank you for everything" to my beloved parents, my mother (*μαμά*) Martha (*Μάρθα*) and my father (*μπαμπάς*) Ioannis (*Ιωάννης*) for their endless love, support and encouragement. Whatever I write in this paragraph it would not be enough to express my feelings about them. They have always been and they will for ever be the role models of my life. I really thank them for the way they raised me up and for teaching me since I was a little girl that a person does not need to be surrounded by expensive materials or success in order to be happy. It is only true love that can really make us happy. So, to this end, I just want to ask sorry from them, for all these moments that they were really worried because I was not feeling good and to say to them; I love you, Mom and Dad, deeply and abundantly and this feeling is much stronger than anything else.

Finally, I thank all of you that read this dissertation and I am sorry if by mistake I forgot to mention someone in this acknowledgements section.

Résumé

Le développement rapide des pérovskites organiques-inorganiques d'halogénures de plomb a fortement émerveillé la communauté du domaine de l'énergie solaire. Alors que la course à l'efficacité pour cette classe révolutionnaire de matériaux de captation de lumière continue, maintes questions sur les propriétés structurelles, électroniques et optiques concernant les cellules solaires à pérovskite restent encore à être abordées. La chimie computationnelle ainsi que la science et l'ingénierie computationnelle des matériaux sont devenues des domaines scientifiques interdisciplinaires et puissants. Elles consistent en un ensemble de théories et de méthodes développées en mathématiques, physique et chimie servant à s'attaquer aux problèmes qui ne peuvent souvent pas être résolus par des expériences réelles.

Dans cette thèse, un ensemble de méthodes computationnelles disponibles est employé afin de traiter la matière de façon quantique et relier à juste titre son comportement microscopique à ses propriétés macroscopiques. La théorie de la fonctionnelle de la densité (DFT) a été utilisée pour des calculs statiques à température nulle (zéro degré Kelvin) ainsi que pour des simulations de dynamique moléculaire (MD) de premier principe (ab initio), ceci afin d'étudier les caractéristiques structurelles, la stabilité relative ainsi que les propriétés électroniques et optiques d'une variété de pérovskites d'halogénure de plomb. La plupart des études computationnelles présentées ici ont été réalisées en étroite collaboration avec des groupes expérimentaux.

Plus spécifiquement, afin de relever le défi de la stabilité en phase, les origines atomiques de la préférence entre la stabilisation ou la déstabilisation des phases pérovskites à température ambiante sont traitées et ceci dans le cas des pérovskites d'halogénure de plomb à cation mixte/halogénure mixte. Leurs propriétés électroniques sont ensuite étudiées afin d'examiner comment le mélange affecte les propriétés des composés purs. Grâce à ces études, il a été possible de formuler de nouveaux principes de conception pour la synthèse de pérovskites d'halogénure de plomb à cation mixte/halogénure mixte avec des propriétés de stabilité et optiques améliorées.

En outre, certaines questions fondamentales encore non résolues et liées à la nature des états excités des pérovskites d'halogénure de plomb sont traitées en simulant la stabilité transitoire et en étudiant la formation de polarons à température ambiante pour le $CsPbBr_3$. Une bonne compréhension des corrélations entre la nature des états excités et les caractéristiques atomiques de ces matériaux ouvre une voie pour la conception de pérovskites aux halogénures de plomb avec des propriétés optiques améliorées. Finalement, le comportement anormal à basse température de la photoluminescence des spectres de $CsPbBr_3$ est rationalisé par des caractéristiques structurelles de matériaux à basse température. L'exploration de tels phénomènes nous a permis de mieux comprendre les propriétés des pérovskites organiques-inorganiques d'halogénure de plomb en les rendant plus adaptés tant aux applications liées à l'énergie solaire qu'aux applications d'autres domaines.

Mots clés: Pérovskites organiques-inorganiques d'halogénure de plomb, Théorie de la Fonctionnelle de la Densité (DFT), Dynamique Moléculaire (MD) de premier principe (ab initio), Pérovskites d'halogénures de plomb à cation mixte/halogénure mixte, Stabilité de phase, Entropie, Structure de bandes, Caractéristiques structurelles, Spectres d'absorption transitoire.

Summary

The rapid rise of organic-inorganic lead halide perovskites has amazed the photovoltaic community. As the efficiency race continues for this revolutionary class of light-harvesting materials, many questions on the structural, electronic and optical properties of perovskite solar cells have still to be addressed. Computational chemistry as well as computational materials' science and engineering have developed into interdisciplinary and powerful scientific fields. They enclose a portfolio of theories and methods developed in mathematics, physics and chemistry, to help scrutinize and tackle problems that can often not be solved in real experiments.

In this dissertation, a compendium of available computational methods that treat matter in the quantum mechanical sense and appropriately link its microscopic behavior with its macroscopic properties are employed. Density Functional Theory (DFT) both in the form of static calculations at zero temperature and in the form of first-principles Molecular Dynamics (MD) simulations have been performed in order to study the structural characteristics, the relative stability and the electronic and optical properties of a variety of lead halide perovskites. Many of the computational studies presented here have been performed in close collaboration with experimental groups.

More specifically, in order to tackle the challenge of limited phase stability, the atomistic origins of the preferential stabilization or destabilization of the perovskite phase at room temperature is addressed in the case of mixed cations/mixed halide lead perovskites. Their electronic properties, in turn are investigated in order to examine how mixing affects the properties of the pure compounds. Through these studies, it was possible to formulate new design principles for the synthesis of stable mixed cation/mixed halide perovskites with enhanced optical properties.

Furthermore, some fundamental open issues related to the nature of the excited states of lead halide perovskites are addressed by simulating the transient absorption spectra and by studying the possible formation of polarons at room temperature for $CsPbBr_3$. An understanding of the correlations between the nature of the excited states and the atomistic characteristics of these materials is paving the way for the design of lead halide perovskites with enhanced optical properties. Finally, the anomalous low-temperature behavior of the photoluminescence spectra of $CsPbBr_3$ is rationalized in terms of the structural characteristics of the material at low temperatures. The exploration of such phenomena allowed to gain more insights about the properties of organic-inorganic lead halide perovskites that may make them more suitable for applications within and beyond photovoltaics.

Keywords: Organic-inorganic lead halide perovskites, Density Functional Theory (DFT), *first-principles* Molecular Dynamics (MD), mixed cation/mixed halide lead perovskites, phase stability, band gap, structural characteristics, transient absorption spectra.

List of Figures

List of Tables

Chapter 1

Introduction

Energy is one of the main foundations of the economy and economic development. Most of the world's energy demand is met by fossil fuels nowadays.[2] However, technologies for fossil fuel extraction, transportation, processing and combustion have negative consequences on the environment, the public health, and the economy.[3–5] Harmful impacts of fossil fuels and concerns about petroleum supplies have spurred a search for renewable energy sources. Renewable energy sources are primary, clean and inexhaustible energy resources, which include biomass, hydropower, geothermal, solar, wind and marine energies.[6] As far as this kind of energy sources is concerned, solar energy is the most abundant one, being available in both direct and indirect forms. The development of renewable energy sources will make it possible to resolve some of the most crucial tasks, by ensuring sustainable development; contributing to the mitigation of the carbon dioxide-driven global warming; and by meeting rural and small scale energy needs in a reliable, affordable and environmentally-friendly way.[6] For this reason, it is of high importance to conduct research on the development of renewable energy sources, employing all the available methods and techniques, including also computational methods that have become prevalent in virtually any field of research.[7, 8]

In this chapter, solar energy technology is introduced, giving mainly emphasis to the perovskite based solar technology. Perovskites have some exceptional properties that are presented in this chapter, in addition to the description of the different fields of technology in which they are used. Furthermore, the importance and advantage of computational methods in any field of research is presented, along with a description of the foundations of these methods. Finally, the relevant questions that are the objectives of this thesis are posed.

1.1 Solar energy

1.1.1 The development and utilization of solar energy over the years

Solar energy is one of the oldest energy sources ever used. Representative is the hieroglyphic, nowadays kept in the *Museum of Egyptian Antiquities* in Cairo, in which Pharaoh Akhnaton (18^{th} Dynasty) is shown adoring the sun. The first known application was related to drying, for food preservation, with the oldest installation found in South France and dated at 8000 BC. During the medieval period, solar energy was used to fire alembics in order to concentrate dilute alcoholic solutions or herbal extracts for medical applications.[9] The Greek mathematician and philosopher Archimedes used mirrors to concentrate the sun's rays to a common point on the Roman fleet in the bay of Syracuse, a feat that is known as the first large-scale application of solar energy. However, there are doubts on the historical context of the aforementioned application. Nevertheless, Proclus repeated Archimedes' experiment, burning the war fleet of enemies besieging Byzantium in Constantinople.[9] Arab alchemists performed experiments with concave mirrors to concentrate solar radiation onto glass vessels containing salt water in order to produce fresh water.[10] From the 1^{st} to the 4^{th} centuries A.D., Roman bathhouses had large south facing windows to let the sun's warmth in.

The Swiss geologist Horace-Bénédict de Saussure constructed the western world's first solar collector in 1767.[11] In a follow-up work, the French naturalist Buffon made devices called "hot mirrors burning at long distance".[12] Furthermore, the French scientist Alexandre-Edmund Becquerel discovered the photoelectric effect in 1839, laying the foundations for photovoltaic technology.[13] Moreover, the French chemist Lavoisier built a solar furnace and the French engineer Mouchot proposed the idea of solar-powered steam engines, constructing various concentrated collectors in Europe and North Africa between 1866 and 1878.[14] In addition, the American engineer John Ericsson, developed the first steam engine driven directly by solar energy.[15] It was in the same decade and more precisely in 1870, when Wheeler and Evans obtained the first American patent on solar distillation.[16] Almost everything that is known so far about the basic operation of solar stills was described in that patent. Two years after that, in 1872, the Swedish engineer Carlos Wilson built the first large solar distillation plant in Las Salinas (Chile), determined to provide fresh water to the workers of both potassium nitrate and silver mines.[17] In 1876, William Grylls Adams and Richard Evans Day discovered that illuminating a junction between selenium and platinum leads to the photovoltaic effect.[18]

In 1910, Harrington erected the first solar storage device of 19 m^3 capacity. A solar driven pump was used to pump water to a storage tank, which was 6 m higher. Later in 1913, Harrington collaborated with Boys to install the biggest solar power plant ever built up to this point in Meadi (south of Cairo), Egypt. The plant provided irrigation water from the river Nile.[15] 1954 was a very important year for solar energy since photovoltaic technology was born. At Bell Labs, Daryl Chapin, Calvin Fuller, and Gerald Pearson developed the first silicon photovoltaic (PV) cell, being capable to convert enough of the sun's energy into power to run everyday electrical equipment.[19] Vanguard 1 was the first satellite equipped with solar electric power that was successfully launched in 1958.[20] The Sharp corporation succeeded in producing practical silicon photovoltaic modules and in the same year, Japan installed the world's largest array at that time, on a lighthouse. Between the years 1965 and 1970 solar distillation plants were constructed on four Greek islands to provide small communities with fresh water. Their capacity ranged from 2044 to 8640 m^3/day. The installation on the island of Patmos was the largest solar distillation plant ever built.[9] In the beggining of the 80's, Paul MacCready constructed the first solar-powered aircraft (Solar Challenger) and flew it from France to England. The aircraft had over 16,000 solar cells mounted on its wings, which produced 3,000 Watts of power.[21] In 1988, in Berkeley, Brian O'Regan and Michael Grätzel co-invented a low-cost solar cell based on a semiconductor formed between a photo-sensitized anode and an electrolyte, which is a photoelectrochemical system.[22] This cell is known as Grätzel cell named after its inventor Michael Grätzel and paved the way for the development and production of low-cost solar cells.[23]

Humanity of the 21^{st} century is heavily dependent on energy. Without energy the whole society, as we know it today, would crumble. An example is that most of the health care services are relying on electricity and computer systems. However, it is quite promising that, as concern is growing about the significant adverse impact of fossil fuels on the environment resulting in increased health risks and the threat of global climate change, solar energy has already become part of daily life. The solar-powered products available on the market are increasingly sophisticated. Solar powered means of transport from solar buses and cars to the solar aircraft Solar Impulse 2, that made its way around the world, are becoming popular all around the world.[24, 25] Moreover, powering wearable electronics has become a common use nowadays, charging every small device.[26] With so many amazing devices and gadgets related to solar energy in 2019, we tend to forget one of the most important applications, the rooftop photovoltaic power stations. Homeowners that have installed photovoltaic arrays on their rooftops reduce their carbon footprint and save money every year. In addition to the daily use of solar powered devices, the increased allocation of funds to research projects related to the development of solar technology shows that the world has made a major shift toward solar energy. Today, solar energy is made up of discrete ever-evolving technologies. These fields can be classified into; photovoltaic technology; concentrating solar power technology; passive solar heating technology; solar water heating technology; artificial photosynthesis. In this introductory chapter of the thesis, among the different fields of solar energy, we will concentrate on photovoltaic technology.

1.1.2 Photovoltaic technology

Photovoltaic technology or photovoltaics (PV) is the direct conversion of sunlight into electricity. PV are based on the photoelectric effect that Becquerel discovered in 1839, as mentioned above. Later in 1921, Albert Einstein was awarded the Nobel Prize for "his discovery of the law of the photoelectric effect".[27] In short, the photoelectric effect is the ejection of free carriers from the surface (outermost band) of a material (usually a metal) when light shines on it. This process is also often refereed to as photoemission and the free carriers that have been ejected are called photoelectrons. One should mention here that the properties of photoelectrons are not different from the ones of electrons.[13] However, to produce a solar cell that would be able to create electricity and in turn power any device, current has to flow through a conducting wire that connects two semiconducting plates between which electrons accumulate along their boundaries to create a voltage. This principle is known as photovoltaic effect and, even though it is similar to the photoelectric effect, there are some noticeable differences.

Indeed, in both cases, light shines on a material causing excitation of free carriers (most of the time electrons) to higher energy states. The main distinction arises from the way the free carriers are reacting upon irradiation. In the case of the photoelectric effect the electrons are ejected out of the material. On the other hand, according to the photovoltaic effect the excited free carriers are still contained within the material. A built-in potential[1] barrier in the solar cell acts on these free carriers producing a voltage, which is named photovoltage and in turn is used to drive current through a circuit.[29]

There is a series of appealing characteristics that spurred society to use photovoltaic technology. In principle, photovoltaic systems consist of no moving parts (in the classical mechanical sense), unlike electric generators. In addition to this, they do not utilize chemical reactions nor they require a fossil fuel to operate, unlike batteries and fuel cells, hence the environment is not polluted while electricity is produced.[29] However, the growth of photovoltaic technol-

---

[1] The built-in potential in a semiconductor is defined as the potential across the depletion region in thermal equilibrium created by electrons diffusing across the junction.[28]

ogy is highly connected to materials development. Since most of the energy in sunlight and artificial light is in the visible range of the electromagnetic radiation, the solar cell absorber should be efficient in absorbing radiation at those wavelengths. Not all kinds of materials have such properties. The materials that strongly absorb the visible radiation are a category of semiconductors[2] and are used as absorbers in solar cell devices.

To characterize the performance of a solar cell, some parameters have to be taken into account. These are the *peak power*, P_{max}, the *short-circuit current density*, J_{sc}, the *open-circuit voltage*, V_{oc} and the *fill factor*, FF. From these parameters, the *power conversion efficiency* (PCE) can be determined. The short-circuit current density, J_{sc}, is the maximum current delivered by a solar cell and is independent of the solar cell area. It can be described as the current that flows through the cell when the voltage across the solar cell is zero. J_{sc} strongly depends on the generation rate and the diffusion length. The open-circuit voltage, V_{oc}, is the maximum voltage that a solar cell can deliver. It is considered as the voltage at which no current flows through the external circuit. V_{oc} is limited by the amount of recombination in the device and the choice of material. Another defining term in the overall behavior of a solar cell is the fill factor, FF. FF is the ratio between the maximum power P_{max} generated by a solar cell and the product of J_{sc} with V_{oc}, as shown in Equation (5.1).

$$FF = \frac{P_{max}}{J_{sc}V_{oc}} \tag{1.1}$$

The power conversion efficiency (PCE) is roughly the portion of solar energy that can be converted into electricity. It is calculated as the ratio between the maximal generated power and the incident power, as shown in Eq. (5.2).

$$\eta = \frac{P_{max}}{P_{in}} = \frac{J_{sc}V_{oc}FF}{P_{in}} \tag{1.2}$$

---

[2] At least one band of a metal is partially filled in the ground state. For an insulator all bands are either completely free or completely filled in the ground state. In an insulator there is a region of forbidden energies, the *energy gap*, E_g, *(band gap)*, separating the lowest unoccupied bands, called *conduction band minimum* (CBM) and the highest occupied bands, called *valence band maximum* (VBM). A solid with a band gap, at $T = 0$, where T is the temperature, will be non-conducting. However, when $T \neq 0$, there is a non-vanishing probability that electrons can be thermally excited across the band gap. If the thermal excitation leads to conductivity depends on the size of the band gap, with a fraction of electrons excited across the band gap at temperature T roughly of the order of e^{-E_g/k_BT}. With a band gap of 0.25 eV, this factor at room temperature is $e^{-5} \approx 10^{-2}$ and conduction will occur. However, in *conductors* no band gap exists. On the other hand, with a band gap of 4 eV, at room temperature, this factor is $e^{-80} \approx 10^{-35}$ and electrons are not excited across the band gap. Such materials are called *insulators*. Solids that are insulators at $T = 0$ but at temperatures below the melting point can lead to observable conductivity are called *semiconductors*.[30]

Improving PCE is a key goal of research and helps in making PV cost-effective.[31]

Before describing the working principles of solar cells, it is important to introduce some terms. A *PV module* is a larger device in which many solar cells are connected. A *solar panel* consists of several PV modules that are electronically connected and mounted on a supporting structure. Finally, a *PV array* consists of several solar panels. The solar cells can be connected in *series*, where the voltages add up. Hence the total current is equal to the current generated by one single solar cell. On the other hand, when the solar cells are connected in *parallel*, the voltage is the same over all solar cells and the current adds up.[31]

1.1.3 Solar cell technology

The working principle of solar cells and the efficiency limits

Whilst the detailed working principle of one type of solar cells can differ from that of others, the main principles are similar. Photons are absorbed by the absorber of the solar cell device, which is a semiconductor, as mentioned above. Absorption of a photon excites an electron from an initial energy level, E_i, to a higher energy level, E_f. When an electron is excited from the VBM to the CBM, a void is created in the VBM. The void behaves like a particle with positive elementary charge and is called a *hole*. In this way an *electron-hole* pair is created. The energy of the photon is converted to chemical energy of the electron-hole pair. The electron-hole pair usually recombines, *i.e.* the electron falls back to the initial energy level E_i. In such case, the energy is released, either as a photon (radiative recombination) or transferred to other electrons, holes or lattice vibrations (non-radiative recombination)[3].[31]

A solar cell device has to be designed in such a way that the electrons can only flow through one 'membrane' and the holes through another 'membrane' and both electrons and holes reach their respective membranes before

---

[3] Semiconductors can be classified in *direct* or *indirect* semiconductors. In semiconductors, the valence and conduction bands are not flat, but vary depending on the k-vector, *i.e.* the crystal momentum. If the VBM and CBM occur at the same *k-vector*, an electron can be excited from the valence to the conduction band without change in crystal momentum. Such a semiconductor has a *direct* band gap and is called a *direct* semiconductor. In case change of the crystal momentum is required for the electron to be excited from the VBM to the CBM, the semiconductor has an *indirect* band gap and is called *indirect* semiconductor. Therefore, the excitation of an electron induced by photon absorption is more likely to happen in direct semiconductors and in turn their absorption coefficients are significantly higher than the ones of indirect semiconductors. In that way, the reverse process of radiative recombination is also more likely to happen in a direct semiconductor. In indirect semiconductors additional change of momentum is required for electron-hole pair recombination.[31]

they recombine. Hence, the time required for the charge carriers to reach the membranes must be shorter than their lifetimes. In most solar cells, these membranes are made of *n*- and *p*-type semiconductors[4]. When a *p*-type and a *n*-type semiconductor are brought together, the excess concentration of negatively charged free electrons causes a diffusion current of electrons from the *n*-type semiconductor across the *p*-*n* juction[5] into the *p*-type one. Similarly, the excess concentration of positively charged holes causes a diffusion current of holes from the *p*- to the *n*-type material. Due to these diffusion processes, the region close to the *p*-*n* junction becomes almost completely depleted of mobile charge carriers. This phenomenon gives rise to a space charge, which is called *depletion region*, created by the charge of the ionized donor and acceptor atoms that is not compensated by the mobile charges anymore. The depletion region results in the formation of an internal electric field which forces the charge carriers to move in the opposite direction than the initial concentration gradient. The presence of this electric field means that there is an electrostatic potential difference across the depletion region. Finally, the electrons that are attracted by the *p*-type material travel through an external load, causing electric current to flow.[31]

Although nowadays, many different types of solar cells have been created (some of them following the working principle that was just described above and others not), always trying to achieve higher PCEs, there are some efficiency limits that force the PCE of every solar cell to be less than a theoretical efficiency limit. For this reason, it is important to understand why a solar cell cannot convert 100% of incident light into electricity.

The most general efficiency limit is the *thermodynamic* limit[6]. For single-junction solar cells, the theoretical limit that defines the maximum theoretical efficiency is the *Shockley-Queisser* (SQ) limit and is called by Shockley and

---

[4] A semiconductor is called *n*-type or *p*-type, according to whether the dominant carriers are electrons or holes.[30].

[5] Almost all solar cells contain junctions. A junction is a boundary or interface between a *p-type* and a *n-type* material, that coexist inside a single crystal of a semiconductor. Apart from the *p-n homojunction* where the junction is fabricated by the same semiconductor material, there is also the *p-n heterojuntion*, that is formed by two chemically different semiconductors. A MS junction is formed between a metal and a semiconductor. In a *p-i-n junction*, a layer is inserted in between the *p*- and *n*-materials stretching the electric field formed by the *p-n junction* across itself.[31]

[6] The solar cell is treated as a heat engine. A heat engine operates between two heat reservoirs; a hot one and a cold one. There are three energy flows; the heat flow from the hot reservoir to the engine, the work that is performed by the engine and the heat flow from the engine to the cold reservoir. This last flow is a loss. In the solar cell case, the device operates between an absorber that serves as a hot reservoir and the surroundings that are equivalent to the cold reservoir. Assuming that the absorber is open towards the surroundings radiative loss is observed.[31]

Queisser *ultimate efficiency*.[32] According to the SQ limit, the major losses are due to the non-absorbed photons (that are carrying less energy than the semiconductor band gap) and the thermalized energy of photons (that are carrying more energy than the semiconductor band gap), which is released as heat into the semiconductor lattice. We mention here that this formulation of ultimate efficiency is only valid at 0 K. When the temperature is higher than 0 K, the solar cell will absorb thermal radiation and will also emit the same amount of radiation. Hence recombination of electron-hole pairs will be present in the semiconductor, leading to a recombination current different from zero. With increasing recombination current, the open-circuit voltage is reduced, which is an efficiency loss. In such case, one refers to the *detail balance limit of the efficiency*. The maximum efficiency is found to be 33.16% for an energy gap of 1.34 eV.[32, 33] It is worth mentioning, that the SQ limit is not directly applicable to solar cells made of crystalline silicon. Silicon is an indirect band gap semiconductor and a non-radiative recombination mechanish is the dominant one. To this end, the SQ limit only considers radiative recombination and it is mostly valid for direct band gap semiconductors. The SQ limit is an idealised limit from which many losses are neglected. These can be summarized as loss due to total reflection, incomplete absorption due to the finite thickness, shading losses and loss due to the fill factor.[31]

The working principle explained above and the efficiency limits correspond to a specific category of solar cells. Nowadays, solar cells are divided into three generations, with some of them containing devices that are following a different working principle than the one explained above. Below these three generations are presented, as well as improvements of a single-junction system for achieving higher PCEs.

The generations of solar cells

The properties of a solar cell device are intimately related to the materials that are used for its production. For this reason, the National Renewable Energy Laboratory (NREL) works to enhance photovoltaic technology and publishes the *efficiency chart* (Figure 1.1), in which the best certified research-cell efficiencies are presented.[1] All the cells summarized in Figure 1.1 can be categorized into three generations, known as the three generations of solar cells.

First generation of photovoltaic cells: Traditional solar cells are made of silicon and are currently the most efficient solar cells available for residential use. 80% of the solar cells produced at present are crystalline silicon solar cells.[34] There are currently different types of silicon based solar cells. Monocrystalline silicon cells is one of those types with a PCE of 27.6% for laboratory cells,[1]

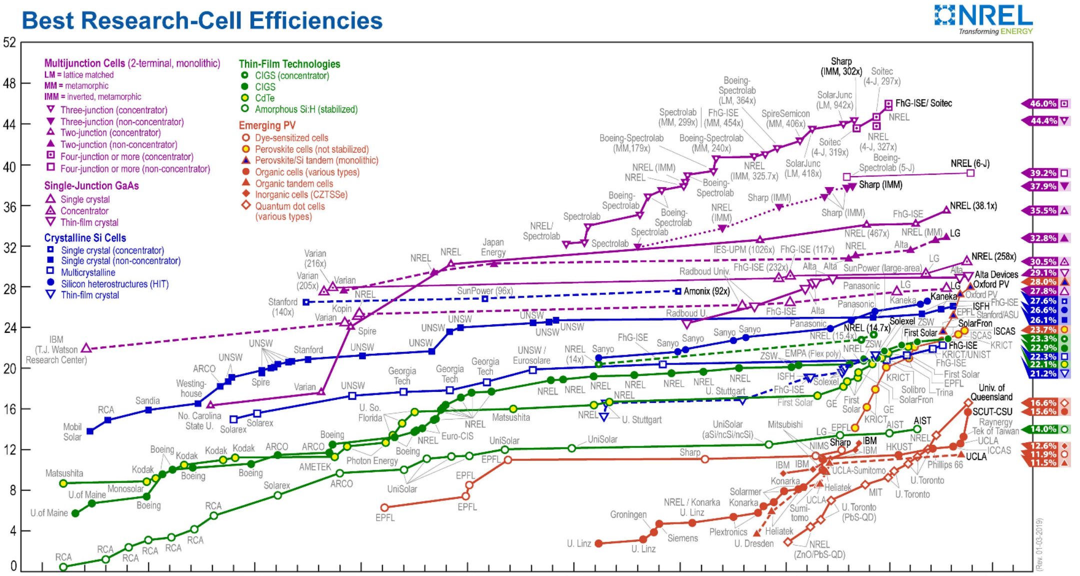

Figure 1.1: Best certified research-cell efficiencies by NREL.[1]

as shown in Figure 1.1 and a PCE of 12 - 16% for commercial modules[34]. The working principle of this kind of cells is the one described above. Such cells have already proven their stability and reliability over several decades. However, there are two main disadvantages associated with this technology; panels made of monocrystalline silicon solar cells may lose their efficiency as temperature increases to more than 25 °C; and the module price is high.[34] On the other hand, the production of polycrystalline silicon solar cells is cheaper. However, they have lower efficiences than the monocrystalline ones.

Second generation of photovoltaic cells: The second generation of solar cells is also known as *thin film solar cells* because, when compared to crystalline silicon based cells, they are made from layers of semiconductors, only a few micrometers thick. Semiconductors with a direct band gap are potential candidates for this generation of solar cells, since they can be thin but still operate efficiently.[34–36] This generation consists of amorphous silicon cells (a-Si, TF-Si),[37, 38] cadmium telluride (CdTe)[39–41] and copper indium gallium selenide (CIGS) cells.[42, 43] The fact that less material can be used for the production of these cells and the lower cost of the manufacturing processes make thin film cells cheaper than the ones made of crystalline silicon.[44] However, they are less efficient than the conventional silicon technology.[1] Applications of thin film solar cells began in the 1980s with small strips that were used for calculators. Nowadays, because of their flexibility, they can be installed on curved surfaces and used in applications of building-integrated photovoltaics.[45]

Third generation of photovoltaic cells: As mentioned above, thermodynamics shows the limit to the conversion of sunlight to electricity as opposed to the detailed balance limit of efficiency of *p-n* junction solar cells. Therefore, if different fundamental concepts are used, someone would be able to design solar cells with PCE that exceeds this theoretical limit, minimizing the different kind of losses. The third generation of photovoltaics, also called "emerging technologies" contains all the cells whose efficiencies can exceed the detailed balance limit of efficiency of single-junction solar cells.[46, 47]

In principle, any new type of solar cells can be included into this category, like copper zinc tin sulfide solar cell (CZTS), (and their derivates CZTSe, CZTSSe),[48–51] dye-sensitized solar cells,[22, 23, 52, 53] organic solar cells,[54–56] quantum dot solar cells[57–59] and perovskite solar cells.[60–67] Perovskite solar cells are going to be discussed in a separate section of this chapter, since they are the main topic of this thesis. The cells that fall into the third generation account for a broad spectrum of concepts, ranging from low-cost low-efficiency to high-cost high-efficiency systems with various applications from building integration to space applications.[68] To improve the PCEs above the SQ efficiency limit different methods have been suggested; multi-junction cells,[69, 70] intermediate-band cells,[71] hot carrier cells,[72] and ultrathin cells[73].[46, 68, 74, 75]

Multi-junction solar cells, which are also known as tandem solar cells are the current efficiency leaders. Such high efficiencies[7] are achieved by dividing the solar spectrum into several wavelength ranges and converting those wavelength ranges with distinct cells of suited band gap, with the highest band gap material being on top of the device. In that way, high energy photons are absorbed by the high band gap junction and lower energy photons are absorbed at the lower band gap material. This allows a large portion of the solar spectrum to be absorbed while avoiding thermalization losses.[68, 74] For this reason, the fundamental *detailed balance limit* of the performance of tandem solar cells is higher than the one of their single-junction counterparts. Especially, the ideal efficiency for an infinite stack of independently operated cells is 68% for unconcentrated sunlight and 86% for concentrated sunlight.[76] The optimum band gaps for such devices, when compared for a series-connected tandem cell under standard reference conditions, were found to be 1.72±0.02 eV for the top cell and 1.14±0.02 eV for the bottom cell.[77]

Dye-sensitized solar cells (DSSCs), also known as "Grätzel cells", (named after their inventor Professor Michael Grätzel from the Ecole Polytechnique

---

[7] According to the NREL, the research cell, with the highest PCE of 46% is currently a four-junction cell.[1]

Fédérale de Lausanne) present a low-cost alternative to p-n junction photovoltaic devices.[22, 23, 52] In contrast to conventional cells, where the semiconductor assumes both tasks of charge carrier transport and of sunlight absorption, in the case of DSSCs these two functions are separated. For this reason, the working principle of DSSCs differs from the one of classical solid-state junction devices, described above.

Indeed, the system is composed of different primary parts. A mesoporous oxide layer (usually TiO_2), in which the nanometer-sized particles are bound together by a process called sintering, allows electronic conduction to take place. On the back of this layer there is a conductive plate made of a glass, on top of which is a transparent anode. The plate is then immersed in a sensitizer, which is the charge transfer dye. By soaking the film in the dye, a thin layer of it is left bound to the TiO_2 surface. A second, separate plate is subsequently made of the electrolyte (usually iodide/triiodide couple; an organic solvent containing a redox system) over a conductive sheet (usually Pt metal). The two plates are then sealed together to prevent the electrolyte from leaking. When incident light is absorbed by the dye, photoexcitation leads to the injection of an electron into the conduction band of the oxide. The injected electrons are transported through the TiO_2 nanoparticles towards the counter electrode via the circuit. The original state of the dye is subsequently restored by electron donation from the electrolyte. The iodide is regenerated in turn by the reduction of triiodide at the counter electrode and the circuit being completed via electron migration through the external load. Since perovskite-based solar cells first appeared as sensitizers for liquid-electrolyte based DSSCs,[60] the latter can be considered as the predecessors of this emerging technology.

1.1.4 Future trends of photovoltaic technology

Photovoltaic technology has recently experienced phenomenal developments, due to both technological improvements resulting in cost reductions of the production processes of solar devices and governmental polices supportive of renewable energy development and utilization. Theoretically, solar energy possesses the potential to adequately fulfill the energy demands of the entire world if technologies for its harvesting and supply are readily available.[78]

In 2015, China surpassed Germany (the first in the global rankings up to that date) as the world's largest producer of photovoltaic power.[78] Nowadays, the 2020 target of 105 GW originally conceived in the 13^{th} five-year plan of China, has already been exceeded by more than 50%. For this reason, China's National Energy Agency is revising the 2020 target to at least 210 GW.[79] On the other hand, according to the Solar Energy Industries Association, the U.S. installed 1.7 GW of solar capacity in 2018, trying to reach 60

GW of total installed capacity. However, this represents a 15% year-over-year decrease. By 2023, over 14 GW of photovoltaic capacity is expected to be installed annually.[80] In 2017, Europe left its several-year long downward trend by adding 9.2 GW, a 30% increase compared to the 7 GW installed the year before. This trend is mainly a result of Turkey's growth, since, among the 28 members of the European Union, there was hardly any growth at all.[81] According to SolarPower Europe's medium development scenario in 2019, demand is expected to surge by 58% to 13.5 GW for the European Union, and if Europe follows the enticing business case of low-cost solar cells, in 2022 the market could reach 39.1 GW.[81] One interesting remark is that according to the Swiss Federal Office of Energy, Switzerland would be able to meet around 20% of the current level of electricity demand through the use of photovoltaic systems by 2050.[82]

Other countries have also made a plan for the exploitation of solar energy. In Morocco, for example, one of the world's largest solar energy projects, that targets the generation of 4500 GWh per year by 2020, has recently been launched.[78] India, on the other hand, is planning to increase its solar power capacity to 100 GW by 2022.[78] Under optimal conditions, SolarPower Europe estimates that, by the end of 2022, the world's solar generation plant capacity could reach a staggering 1,270.5 GW.[81]

From all these installations all around the world, it is clear that solar energy is one of the best options to meet future energy demands. However, in order to reach the point that photovoltaic technology could replace fossil fuels, technologies that use solar energy more efficiently in terms of availability, cost effectiveness, accessibility, capacity and efficiency have to be developed. Perovskite-based solar cells are a new technology that has recently received immense attention due to their impressive photovoltaic performance. The main aspects of this emerging technology are presented in the following section.

1.2 Perovskite materials

Perovskite is the nomenclature of any material that can adopt the same crystal structure as $CaTiO_3$.[83] The structure is named after Russian mineralogist Count Lev Aleksevich von Perovski, but the mineral was first discovered in the Ural Mountains of Russia by Gustav Rose.[84] The general chemical formula for perovskite compounds is ABX_3 where X is an anion and A and B are cations of different sizes with A being larger than B. A and B cations coordinate with 12 and 6 X anions forming cuboctahedral and octahedral geometries, respectively. In case of an ideal perovskite structure, the crystal structure is cubic and is composed of a three-dimensional (3D) framework of corner-sharing

BX_6 octahedra. In other words, A and X form a cubic closest packing where B is contained in the octahedral voids.[84, 85] Structures related to the prototypical cubic (*Pm3m*) perovskite structure through tilting of the BX_6 octahedra are also called perovskites. Especially, halide perovskites, (that recently have attracted significant attention due to the emergence of hybrid perovskite solar absorbers), are compounds that have the same general formula, ABX_3 but A is a monovalent cation, B a divalent cation and X a halide anion. The cubic structure of ABX_3 halide perovskites is shown in Figure 1.2.

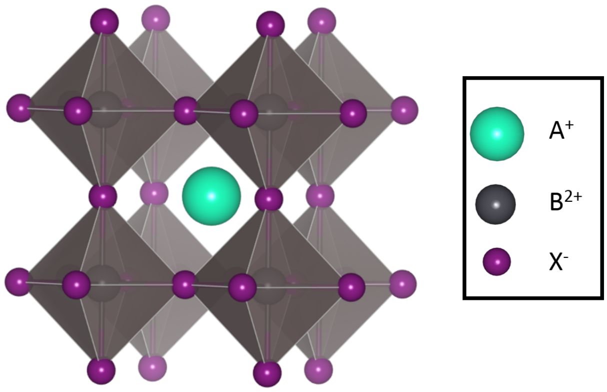

Figure 1.2: Cubic structure of ABX_3 halide perovskites. A is a monovalent cation, B is a divalent cation and X is a halide anion. The structure is composed of a 3D framework of corner-sharing BX_6 octahedra.

Approximate guiding rules about the stability ranges for different compositions can be highly useful in the design of new materials. Goldschmidt was one of the first who not only synthesized a large number of crystal structures of ABX_3 composition, but also introduced the concept of *tolerance factor* for the perovskite arrangement; a way to interpret how far from the ideal packing, the ionic sizes can deviate and still be tolerated by the perovskite crystal structure.[83, 86] The Goldschmidt tolerance factor (t) is a dimensionless number that can be estimated via an empirical formula, which is given by Equation 5.3, where R_A, R_B and R_X are the ionic radii of A, B and X, respectively.

$$t = \frac{R_A + R_X}{\sqrt{2}(R_B + R_X)} \tag{1.3}$$

In general, materials with a tolerance factor of 0.9 - 1.0 form an ideal cubic structure and those that have a tolerance factor of 0.71 - 0.9 are structures with tilted octahedra. In case that $t>1$, this indicates that the components are too large and generally preclude the formation of a perovskite, or if $t<0.71$, the components are too small, again often leading to alternative non-perovskite structures.[86–88] Hence, in principle, the symmetry is lower for materials which have a lower tolerance factor. Goldschmidt's tolerance factor was originally developed for oxide perovskites but it has been widely accepted as a criterion for the formation of the perovskite structure, in general.[87, 89] However, it has been observed that the tolerance factor metric shows limited suitability for predicting the stability of certain organic-inorganic halide perovskites due to their higher degree of covalency that leads to a soft and dynamic crystal lattice.[88, 90] For example, it has been observed that compounds can have tolerance factors in the range of $0.8 \leq t \leq 0.9$ and still not form perovskite structures.[88] These non-perovskites usually adopt hexagonal structures where some proportion of the AX_3 sublattice adopts hexagonal close packing, and some degree of BX_6 edge or face-sharing octahedra is present.[91]

For organic-inorganic halide perovskites, where A is an organic molecular ion, appropriate ionic radii have to be defined in order to apply the Goldschmidt criterion. Kieslich *et al.*[89, 92] used a rigid sphere model for organic cations assuming rotational freedom around the center of mass, leading to a set of effective ionic radii extending in this way Goldschmidt's tolerance factor. The formula that has been proposed is given in Equation 1.4, where $R_{A,eff} = R_{mass} + R_{ion}$, with R_{mass} being the distance between the centre of mass of the molecule and the atom with the largest distance to the centre of mass excluding hydrogen atoms and R_{ion} being the corresponding ionic radius of this atom. Because of the high anisotropy of anions, all molecular anions are treated as rigid cylinders, with effective radius $R_{X,eff}$ and an effective height $h_{X,eff}$.

$$t = \frac{R_{A,eff} + R_{X,eff}}{\sqrt{2}(R_B + 0.5h_{X,eff})} \tag{1.4}$$

The flexibilities of perovskite compositions have enabled versatile applications of this class of materials in energy production and storage devices as well as in electrocatalysis,[93–99] photocatalysis[100–103] and photovoltaics.[60–66, 104, 105] In addition to this, perovskites have long been of interest due to their superconducting,[8][107–112] ferroelectric,[9][114–118] piezoelectric,[10][120–122] ferroelastic,[123] ferromagnetic[124–127] and antiferromagnetic properties,[11][128–130] just to name a few. More recently, they have been used in light-emitting diodes (LEDs)[131–137] and as lasers.[137–140] Even though most of

---

[8] Superconductivity is a phenomenon in which the electrical resistivity of materials called superconductors is exactly zero below a temperature T_c, which is called critical temperature.[106]

[9] Ferroelectricity is a property of certain materials that have a spontaneous electric polarization that can be reversed in direction by the application of an appropriate external electric field.[113]

[10] Piezoelectricity is the ability of certain materials to generate electric charge in response to applied mechanical stress.[119]

[11] Ferromagnetism is a long-range ordering phenomenon by which the unpaired electron spins of certain materials spontaneously line up parallel with each other in regions called domains even in absence of an external field. On the other hand, in antiferromagnetic materials, the spins are aligned antiparallel in magnetic domains below a certain critical temperature.[30]

the known perovskites are metal oxides, metal halide perovskites have recently been taking the field due to their exceptional photovoltaic performance. For this reason, and since this thesis is mainly focused on halide perovskites, an extensive discussion of the properties and the applications of these materials is presented below.

1.2.1 Halide perovskites

As mentioned above, halide perovskites have the general formula ABX_3, where A is a monovalent cation, B a divalent cation and X a halide anion (F, Cl, Br, I) as shown in Figure 1.2. It is expected that halide perovskites will be the focus of research for many applications in the near future.[141] Hence, it is important to understand the properties of such materials.

Kojima *et al.*[60, 142] were the first to report photovoltaic results for halide perovskites. Actually, they were attracted by the self-organization potential of perovskites in the nanoporous TiO_2 layer of DSSCs. They first introduced $CH_3NH_3PbBr_3$ in 2006,[142] and later $CH_3NH_3PbI_3$ in 2009,[60] as sensitizers for liquid-electrolyte based DSSCs achieving mere PCEs of 2.2% and 3.8%, respectively, measured under standard characterization conditions. In 2011, Im *et al.*[61] achieved a PCE of 6.54%, by electrochemical junction with iodide/iodine based redox electrolyte and by changing the method of depositing the perovskite. Although perovskite nanoparticles exhibited better absorption than standard N719 dye sensitizers, $CH_3NH_3PbI_3$ quantum-dots tended to dissolve gradually into the redox electrolyte.[61]

This stimulated the replacement of electrolytes by a solid-state hole conductor or hole-transporting material (HTM).[62, 63] Kim *et al.*[62] introduced as HTM, the 2,2,7,7-tetrakis(N,N-di-p-methoxyphenylamine)-9,9'-spirobifluorene (spiro-MeOTAD), which not only dramatically improved the device stability compared to $CH_3NH_3PbI_3$-sensitized liquid junction cells, but also resulted in a device PCE of 9.7%. At this stage, the working principle of the perovskite solar cell was similar to the solid-state DSSCs. Almost simultaneously, Lee *et al.*[63] also reported success using spiro-MeOTAD, and a mesoporous scaffold made of Al_2O_3 instead of TiO_2 resulting in an improved PCE of 10.9%, although Al_2O_3, due to its large band gap, is unable to assist in electron extraction and transport. This suggested that perovskites have a further potential as electron transporting materials than just being used as sensitizers. Indeed, soon after Etgar *et al.*[64] showed that $CH_3NH_3PbI_3$ nanoparticles can also assume simultaneously the roles of both light harvester and hole conductor obviating the need for employing an additional HTM. Today's best-performing cells have reached a certified PCE of 23.7% confirmed by NREL.[1] It is worth mentioning, that Oxford PV^{TM} (a perovskite company) achieved a PCE of 28%, the highest research-cell efficiency certified by NREL so far, for a 1 cm^2 perovskite-silicon tandem solar cell. This solar cell is not only efficient but also stable due to the exceptional properties of organic-inorganic halide perovskites.[143]

Broad optical absorption is the key to the outstanding performance of these materials. The most widely studied material of this type, $CH_3NH_3PbI_3$, ($MAPbI_3$), for instance, has a direct band gap of 1.5 eV,[62] which is close to the single-junction optimum based on SQ detailed balance considerations.[32] $[HC(NH_2)_2]PbI_3$, ($FAPbI_3$), has a band gap that different experimental measurements show that lies within the range of 1.43 - 1.48 eV,[144–146] which is even closer to the single-junction optimum. In this way, $FAPbI_3$ is a good light absorber over the whole visible solar emission spectrum. However, an active area of research in the field of organic-inorganic halide perovskites is still to obtain a compound with a band gap even closer to the ideal value of 1.34 eV for single-junction solar cells.[32, 33] One should mention here that mixtures of the divalent metal iodides of Sn and Pb with methylammonium iodide, ($CH_3NH_3Sn_{(1-x)}Pb_xI_3$) have a tunable band gap between 1.17 and 1.55 eV and more specifically $CH_3NH_3SnI_3$ has a band gap of 1.30 eV, which is even closer to the optimum for single-junction solar cells.[147] On the other hand, $CsPbI_3$, which is a pure inorganic halide perovskite, *i.e.*, a halide perovskite that has an inorganic monovalent cation, has a band gap of 1.73 eV.[148, 149] This band gap is close to the optimum top cell gap for tandem solar cells, around to 1.7 - 1.8 eV.[77] Since the crystalline phase of a material can crucially affect its optical properties, the relationship between the structural characteristics and the optical properties should be always taken into account.

Meloni *et al.*[150] performed density functional theory calculations aiming at establishing a relationship between the chemical composition, crystal structure and the electronic properties of metal halide perovskites. It turns out that the lattice constants are mainly affected by the chemical nature of halides and divalent cations, whereas the effect of substituting the monovalent cation depends on the crystalline symmetry.[150] Concerning the perovskite crystal structures, the main phases that are formed are, a cubic phase, in which the tilting angles θ_1, θ_2 and θ_3, *i.e.* the angles that represent the relative rotations of the BX_6 octahedra around the main axes, are fixed to zero; the tetragonal phase, in which two out of three tilting angles are different from zero; and the orthorhombic phase, in which all the tilting angles are different from zero.[150] In case the cubic phase is not the ideal cubic $Pm\bar{3}m$ structure, but is a pseudocubic one, the structure is also referred to as α-phase structure.[91] Moreover, two other phases, the β and the γ, have occurred and they are equivalent to orthorhombic phases. Especially, γ-phase structures occur as the temperature decreases close to 100 K for most of the known compounds, leading to structures with low symmetry. Last but not least, non-perovskite phases, mostly known as δ-phases, can be formed. The characteristic of these structures is that no corner-sharing octahedra are present, leading to 1D phases that are unsuitable for photovoltaic applications, due to the high values of their band gaps (usually more than 2.5 eV), which are also indirect.[91, 151] Replacement of the monovalent cation, in the cubic phase, results in a modification of the lattice parameter, while in tetragonal and orthorhombic phases the replacement can alter both the lattice parameter and the tilting angles. In principle in all three phases, the introduction of a larger cation expands the lattice and *vice versa*, while for tetragonal and orthorhombic phases the tilting angles increase if the new cation is smaller and decrease if it is larger.[150]

An interesting feature of all halide perovskites is the global character of the electronic characteristics of their VBM and CBM. Indeed, VBM is formed by an antibonding combination of B ns and X mp orbitals, while CBM is also formed by an antibonding combination, this time by B np and X ms orbitals. Due to this property, some general rules about the relation between the crystal structure and the electronic properties of halide perovskites can be formulated. In fact, when moving from the cubic to tetragonal and finally to the orthorhombic phase, the antibonding overlap between the orbitals of the divalent cation and the anions is reduced leading to an increment of the band gap. The overlap is also affected by the lattice size and the tilting angles. Shrinking of the lattice increases the overlap and in turn reduces the band gap and an increase in the tilting angles decreases the overlap increasing the band gap.[150]

Apart from their ideal band gaps, there are several other features of perovskites that contribute to their outstanding performance. One characteristic feature is the small exciton[12] binding energy.[152–155] Lin *et al.*[153] estimated the exciton binding energy of $CH_3NH_3PbI_3$ perovskite planar devices to be of the order of 2 meV. Nicholas *et al.*[154] demonstrated that the exciton binding energy for $CH_3NH_3PbI_3$ is 16 meV at low temperatures. For the tetragonal phase (the room temperature phase) of $CH_3NH_3PbI_3$ this value falls to only a few meV, which explains the excellent device performance as being due to spontaneous free-carrier generation following incident light absorption.[154] The efficient generation of free charges is crucial for the design of high-performance devices since there can be significant efficiency losses in energy due to exciton migration and dissociation in charge transport and collection.

Moreover, long-range electron-hole diffusion lengths (of at least 100 nm in solution processed $CH_3NH_3PbI_3$ and 1000 nm in mixed halide $CH_3NH_3PbI_{3-x}Cl_x$)[156, 157] are present and result from the long recombination lifetime in halide perovskites.[157, 158] The lifetime of the charge carriers

---

[12] An exciton is a bound state of an electron and a hole.

plays an important role as longer lived carriers will have a higher probability of reaching the electrodes. Some examples of recombination lifetimes have been reported; 100 ns for $MAPbBr_3$ and 446 ns for $MAPbBr_{3-x}Cl_x$.[159] Finally, halide perovskites are defect tolerant,[160, 161] allowing these materials to maintain their excellent electronic properties even in the presence of defects. However, nowadays, it is generally accepted that deep-level defects in perovskite thin films hinder the PCE of such materials to approach the SQ limit.[162] By a series of methods; growth of large size crystals, photo-curing, grain boundary and surface passivation and modification of the substrates,[163] new compositions can be developed that can be more defect-tolerant enhancing in that way the PCE to values closer to the SQ limit.

Given the long lifetimes, which imply low recombination and trapping probabilities, one might expect that the charge-carrier mobilities in metal halide perovskites are exceptionally high.[164] However, this issue is controversial,[158, 164–168] since their charge-carrier mobilities are comparable to those of typical inorganic semiconductors.[164] For lead halide perovskites such as $MAPbI_3$, electron and hole mobility values appear to be limited to at most $\sim$200 $cm^2/(V\ s)$.[166] These values are at least 1 order of magnitude lower in electron mobility and several times lower in hole mobility than those of Si, GaAs and some other inorganic materials.[164] Although the mechanism that limit the charge-carrier mobility in halide perovskites is an issue that still puzzles the scientific community, it has been suggested that Fröhlich interactions between charge carriers and the electric field associated with the longitudinal optical phonon modes of the ionic lattice are the factors that limit the charge-carrier mobilities at room temperature.[166] Apart from that, there still remain fundamental open questions concerning the nature of the excited state of these compounds.[169–172]

Although halide perovskites posses exceptional properties that lead to their outstanding photovoltaic performance, there are still various open issues that have to be addressed for such materials to meet global market needs. Long-term stability is one of those. In a device, instability issues might occur due to perovskite layers, ETMs, HTMs, electrodes and the interfaces between each and every of the aforementioned objects.[173] Especially, the long-term stability of the perovskite layer can be affected by a variety of reasons.[173] Humidity is a major factor, which is usually triggered by moisture or water.[174–177] 2D hybrid organic–inorganic perovskites exhibit high stability and resistance to water in comparison to their 3D counterparts due to high positive adsorption energy.[178–180] In addition, light-induced degradation can occur that is dependent on the structure of halide perovskite and the exposure temperature.[174, 181, 182] It has been observed that light-induced phase segregation occurs in mixed-halide perovskites of $APb(Br_xI_{1-x})_3$ type.[182] For some materials, thermal degradation can also take place when the heating temperature increases.[183] $CH_3NH_3PbI_3$ on the film, for example, decomposes rapidly at 150 °C.[144]

In the case of halide perovskites, various different crystalline phases might exist for the same compound in a narrow temperature range.[91] As mentioned above, apart from the perovskite phases, non-perovskite δ phases can be formed, too. However, if the δ phase is the most stable one at room temperature, the compound cannot be used in photovoltaic applications, due to the high and indirect band gap.[91, 151] That is the case for $FAPbI_3$, for example, that has a band gap that different experimental measurements show that lies within the range of 1.43 - 1.48 eV, in its perovskite phase[144–146] (which is close to single-junction optimum), but this phase is thermodynamically unstable at room temperature since $FAPbI_3$ adopts a δ phase, with a much higher band gap.[91] Nowadays, to overcome the problem of the competing delta phases, a design protocol to mix different halides and cations has been used in order to achieve perovskite cells with enhanced thermal and structural stability.[184–187]

Last but not least, the toxicity of Pb^{2+} which is harmful to human health and the environment is another important concern hindering the wide-scale implementation of lead halide perovskites.[174] Therefore, it seems that identifying lead-free perovskites or other alternative materials is necessary. Sn^{2+} and Ge^{2+} are forming 3D halide perovskites,[188–191] however both elements are susceptible to oxidation forming either Sn^{4+} or Ge^{4+}, respectively, that can act as deep electron traps.[174] The substitution of Pb^{2+} by the non-toxic Ag^+ and Bi^{3+} leads to the formation of double perovskite structures.[174, 192–194] The double perovskite $Cs_2AgBiBr_6$ for example has an indirect band gap of 1.95 eV, suited for tandem solar cells, showing in this way that these materials can be potential candidates for photovoltaic applications.[192]

Within, a decade of intense research and development in perovskite solar cell technology, numerous device architectures and preparation techniques have been proposed.[67, 141, 195, 196] Perovskite film deposition via *solution processing techniques* is very prominent since the production cost is low.[141, 195, 196] In such techniques, the perovskite can be deposited on the substrate in two ways; either by *one-step coating*,[197] or by *two-step coating*.[67] In one-step coating, the perovskite pigment is deposited in a single step onto mesoporous metal oxide films using a mixture of PbX_2 and CH_3NH_3X in a common solvent or solvent mixtures. However, the uncontrolled precipitation of the perovskite results in morphological variations that can significantly affect the PCE of the device. In the two-step coating instead, a sequential deposition method is employed, in which PbX_2 is introduced into the mesoporous metal oxide film and subsequently, by exposure to a solution of CH_3NH_3X, is transformed into perovskite. This technique permits much better control over the perovskite morphology than is possible with one-step coating.[67]

The *vapor deposition technique* is considered as an important process to fabricate halide perovskite films and was introduced by Liu *et al.*[198]. Relatively high PCEs are achieved due to the highly uniform quality of the perovskite films obtained with this method.[198] However, there are also drawbacks of this technique since high vacuum conditions are required, which restricts cost effectiveness and mass production.[199] To overcome this problem, Chen *et al.*[200] demonstrated a low-temperature vapor-assisted solution process which can be used to grow polycrystalline perovskite thin films with small surface roughness, full surface coverage and grain sizes up to the microscale.

Another promising preparation technique of halide perovskites in the bulk is mechanosynthesis.[201, 202] Mechanosynthesis is a solvent-free, solid-state synthesis method[203] that leads to the formation of proper solid solutions of the desired composition by simply grinding and milling the individual components together.[202]

Apart from the preparation method, the device architecture is a crucial factor for the overall performance of perovskite solar cells. So far, six types of device architectures have been reported; the mesoscopic n-i-p configuration, the planar n-i-p configuration, the planar p-i-n configuration, the mesoscopic p-i-n configuration, the electron-transporting layer (ETL)-free configuration, and the hole-transporting layer (HTL)-free configuration.[204]

The mesoscopic n-i-p configuration, also known as *mesoporous scaffold architecture* is the dominant device architecture and the first arrangement of perovskite photovoltaics, when the light-harvesting dye was replaced by lead halide perovskites in a DSSC architecture.[60] In this design, a transparent glass cathode is followed by the ETM. The assembly then continues with a mesoporous metal oxide that contains the perovskite, followed by the HTM, and capped with a metallic anode. The planar n-i-p architecture is an evolution of the mesoscopic structure, in which the perovskite layer is sandwiched between the ETM and HTM. It is possible to achieve a high efficiency even with this simpler structure (that does not contain the mesoporous layer) by carefully controlling the interfaces between the different layers that make up the device. Moreover, the planar device can be fabricated with a low-temperature process unlike the mesoporous structure.[204]

The fact that perovskite nanoparticles can assume simultaneously the roles of both light harvester and hole (and electron) conductor,[64] led Jeng *et al.*[205] to develop the first planar hetero-junction perovskite solar cell device with an inverted structural design. In the case of the p-i-n planar architecture, the HTM layer is deposited first followed by the ETM layer. To construct a mesoscopic p-i-n device, the use of an oxide HTM is necessary. Furthermore, ETM layer-free planar perovskite solar cell architectures have achieved a PCE of 14.14%, without any hole-blocking layer.[206] Regarding the HTL-free mesoscopic perovskite solar cells, a remarkable 12.8% certified efficiency with high stability was obtained by using a double layer of mesoporous TiO_2 and ZrO_2 covered with porous carbon.[204]

These various device architectures might imply some differences in the atomistic mechanism underlying the *working principle of perovskite based solar cells*, however, the basic working principles remain unaffected. Specifically, the perovskite layer absorbs photons and in turn electron-hole pairs are created. Due to the low carrier recombination probabilities of perovskite materials, the diffusion distance and lifetime of the carriers are long and free carriers (free electrons and holes) can be formed, generating in turn a current. Then, electrons are transferred from the perovskite to the ETM and finally collected by the front transparent electrode, which in standard device configuration is FTO-coated glass (cathode). At the same time, the holes are transferred to the HTM, and collected by the back, metal electrode (anode). Finally, both electrodes are connected and photocurrent is generated in the outer circuit.[207] The working principle is shown schematically in Figure 1.3.

Recently, the very first real-world deployment of a perovskite photovoltaic panel has started. The construction company Skanska's Warsaw, Poland, is lighting up its workers' offices with electricity from this panel. The panel made by Warsaw-based Saule Technologies, contains 52 modules and seeks to cover the energy needed to provide light for one employee's workspace for eight hours.[208] However, apart from photovoltaics, many interesting applications of halide perovskites have recently emerged.[141]

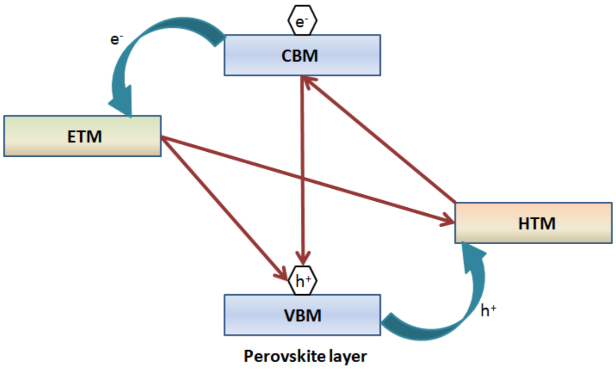

Figure 1.3: Schematic diagram of the working principle of halide perovskite based solar cells.

Indeed, their tunable band gap makes halide perovskites a promising material for use in light-emitting diodes (LEDs).[131–133] Moreover, apart from tunable wavelengths, these materials exhibit good photoluminescence quantum yields. In this context, they are promising candidates as gain media materials in laser devices.[138, 139, 209] Due to the high charge-carrier mobility and the small exciton binding energy, halide perovskites exhibit superior properties compared to traditional semiconducting materials, and thus have potential for applications in resistive-switching memories (ReRAMs).[210–212] Furthermore, halide perovskites are considered to be good X-ray image detectors[12] due to the high atomic numbers of Pb, I and Br.[213–215] Recently, research on lithium storage using halide perovskites has been initiated.[216] Halide perovskite-based electrodes exhibit high stability during electrochemical cycling without any structural rearrangement implying that halide perovskite hosts can accept Li^+ with no distortions in the crystal lattice.[216] Finally, spontaneous polarization, which is attributed to the permanent dipoles in halide perovskites, is a requirement for piezoelectric energy generators.[217, 218] Hence, piezoelectric halide perovskite generators as energy harvesting devices can pave the way to spontaneously producing electrical energy.[141]

Undoubtedly, the low equipment requirement and the simple preparation solution-based processes of organic-inorganic halide perovskite-based solar cells can make these materials suitable for large-scale commercial production.[141, 195, 196] In addition to this, the exceptional properties of halide perovskites enable a broad range of applications, beyond photovoltaics.[141] However, to improve the performance of these materials to such a point that they can be competitive enough to be introduced in industry, it is necessary to further investigate their structure and their various properties and to provide solutions to the aforementioned open issues. One of the most profitable approaches to study the structure and the properties of matter is the close interplay between experimental measurements and theoretical analysis. However, experimental data is often the result of an intricate interplay of different effects that computational methods can help to disentangle. Moreover, thanks to the tremendous increase in computational power over the last decades, nowadays it has become possible to explore a vast range of different systems which would be difficult to be synthesized and characterized experimentally in the same time.

---

[12] In an X-ray detector, the active layer has to be very thick to stop X-ray penetration, as the X-ray photons have high energy and consequently strong penetration capabilities. The X-ray stopping power of a material, which is expressed by the attenuation coefficient, α, is dependent on its atomic number, Z, via the expression $\alpha \propto Z^4/E^3$, where E is the photon energy of the X-ray.[141]

1.3 Computational methods: an efficient approach for material's design and exploration of the fundamental properties of matter

Some of the most interesting problems in all fields of science involve high-dimensional spaces and complex mathematical relations for which no analytical solutions exist. An alternative path is to provide numerical solutions to the problem. Indeed, numerical simulations have become prevalent in virtually any field of research, from physics, chemistry, mathematics, biology, medicine, materials science, engineering up to economics establishing a highly interdisciplinary and new research field often referred to as "Computational sciences".[8, 219–230] In addition to this, the increasing availability of supercomputers and the outstanding development of efficient algorithms enable nowadays numerical simulations to be the connecting tool between experiments and theory, to validate theories but also to make predictions of the system's behavior under different conditions that might not be feasible in real laboratory experiments.[8]

Due to the complexity of structural hierarchies in matter, there is no single computational theory or method which can explain all material properties. On the contrary, according to the length scale (subatomic, atomic, micro, meso, and macro), different algorithms and methods have been developed.[8] The method that is used in a simulation usually depends on the property under investigation. For instance, in heat transfer phenomena, the finite element method is often employed for solving partial differential equations.[226] If the property under investigation is the band gap of a semiconductor (a very important property for the photovoltaic performance of the semiconductor), electronic structure calculations have to be performed, since the system has to be described with atomic detail taking the interactions of electrons and nuclei into account.

From all these branches of computer simulations, computational chemistry includes ab initio approaches based on quantum chemistry, classical physics and empirical approaches in order to study and understand the structures and properties of matter.[221] Nowadays, computational chemistry is a powerful field of science in order to characterize protein-ligand complexes[231] or perform computational drug design.[232] Furthermore, high-throughput computing allows for materials design and discovery, paving the way for the investigation of new exotic properties by simulating compounds under conditions that might not be feasible in real experiments.[233]

One interesting case study carried out on the $Li_3MPO_4CO_3$ (M = transition metal) class of materials, which are unconventional in that they mix two different polyanions (phosphate and carbonate). They were 'invented' by automatic element substitution algorithms applied to all relevant crystal structures, which revealed that a Na-to-Li substitution in natural sidorenkite minerals could yield potential battery cathodes.[234, 235] Na-containing carbonophosphates were prepared hydrothermally, followed by an ion-exchange process, which resulted in the desired Li analogues.[236] This is just one of the thousands of examples, where computational chemistry either predicted the properties of a material or proposed new materials, showing how powerful this field of science is. It is also worth mentioning that in most of the research and development (R&D) departments of big companies all around the world, computational studies are starting to play a major role since they provide quick answers with relatively low cost avoiding the use of expensive equipment and chemical reagents.

1.4 Aim and outline of the thesis

The present thesis aims at developing simulation methodologies and protocols that can address the structure and properties of organic-inorganic lead halide perovskites and also tackle some of the main challenges of these compounds through the design of new materials with further improved properties. Employing atomistic simulations based on quantum mechanics (electronic structure methods) and statistical mechanics, the characterization of the properties and their correlation to atomistic feature can be achieved. Every simulation method should be chosen in such a way as to capture the correct physics at the origin of the phenomena, without significant loss of relevant information, even when there are at least ten orders of magnitude on length scale to be covered, between the atomistic simulation and the macroscopic response.

Answers to some of the main fundamental questions about the nature of the excited state of these materials are addressed together with a mechanistic explanation of various photophysical phenomena. Furthermore, not only new compositions are proposed that could overcome the barrier of limited long term phase stability maintaining the outstanding performance of this emerging technology, but also the reasons of the favorable stabilization of these compounds are explained. Properties such as band gaps are calculated in close interplay with the respective structural arrangements.

In the following chapter, a brief self-contained summary of quantum mechanics, quantum theory of solids and statistical mechanics is provided. In addition to this, the ab initio methods used in this thesis are presented; DFT, Born-Oppenheimer (BO) molecular dynamics, Car-Parrinello (CP) molecular dynamics, the restricted open-shell Kohn-Sham (ROKS) method and time-dependent density functional theory (TDDFT). The overview is limited to the absolute minimum of definitions and methods that were used during this thesis, while trying not to sacrifice rigor and consistency. In Chapters 3, 4 and 5 one of the main challenges of some halide perovskites; the phase instability of the perovskite phase with respect to the δ non-perovskite phase is addressed. Mixtures of different monovalent cations and halides are tested explaining with thermodynamical arguments the fundamental reasons for the favorable stabilization of the perovskite respectively the non-perovskite phase. Moreover, the electronic properties of all new compounds are computed in order to estimate to which extent the new material is suitable for photovoltaic applications. In Chapter 6, photophysical phenomena such as the presence of the asymmetric photoluminescence (PL) spectra of $CsPbB_3$ at low temperatures, and the change in the slope of the band gap as a function of temperature are investigated. Furthermore, in Chapter 7, the excited state dynamics of $CsPbBr_3$ is investigated, by simulating the transient absorption spectra. The possible formation of polarons is also examined. Each Chapter is self-contained in the sense that an introduction is given and the main findings are summarized. In addition, in Chapter 8, the general conclusions and an outlook to future work are presented. In Appendix A, a series of benchmarks to verify which level of theory has to be used in each calculation and the suitable parameters for each type of simulations are examined. The outcome of these tests has been used throughout this dissertation. Appendix B includes supplementary information for Chapter 3, and in Appendix C, a band gap database which is currently used in machine-learning applications is presented. Finally Appendix D includes supplementary information for Chapter 4.

Chapter 2

Theory and Methods

To study the structure and properties of materials, we need to know how their molecules, atoms and in turn subatomic particles like electrons and nuclei move in response to the forces they experience. It was once thought that the motion of atoms and subatomic particles could be expressed using the laws of *classical mechanics* that are very successful at explaining the motion of macroscopic objects. However, the revolutionary change in our understanding of microscopic phenomena that took place during the beginning of the twentieth century is unique in the history of natural sciences. This new "mechanics", called *quantum mechanics*, is richer in scope and in its range of applicability than the theories of classical physics.

In this chapter, some of the basic principles of quantum mechanics are introduced, with emphasis given to the laws of solid state physics. Due to the close interplay of matter and light, principles that can describe the intensities of vibronic transitions or the absorption or emission of a photon are assessed. An introduction to statistical mechanics is also necessary, since its laws allow us to relate the macroscopic properties with the ones of microscopic assemblies. In addition, in this framework concepts such as *entropy* can be described. Finally, all the methods used for each case study of this dissertation and described in the following chapters, are introduced.

2.1 Quantum mechanics

According to classical physics, every object is a discrete entity, which is also called particle, has a well-defined position and momentum and moves in accordance to Newton's laws of motion. On the other hand, an entity that is present in every point of space, and can be defined by electric and magnetic fields is called an electromagnetic wave, and is governed by Maxwell's laws of electromagnetism. This classical world picture began to crumble during the beginning of the twentieth century, when the laws of classical mechanics could not explain a series of experiments that could instead be fully explained by a set of controversial mathematical explanations. These controversial mathematical explanations were the foundations of a new field, called *quantum mechanics*.

In 1900, the German physicist Max Planck studied black-body radiation and found that he could describe the experimental observations by proposing that the energy of each electromagnetic oscillator is limited to discrete values and cannot be varied arbitrarily, introducing in that way the concept of *quantization of energy*.[237] In principle, he was able to account for the observed distribution by supposing that the permitted energies of an electromagnetic oscillator of frequency ν are integer multiples of $h\nu$:

$$E = nh\nu \qquad\qquad \text{for } n = 0, 1, 2, ... \tag{2.1}$$

where h is Planck's constant. The most compelling evidence for the quantization of energy came from observations of spectral measurements, in which radiation was emitted or absorbed at a series of discrete frequencies. In 1905, Albert Einstein invoking Planck's hypothesis, explained why at low temperatures the molar heat capacities of all metals are lower than the classical result of $3R$, (where R is the ideal gas constant), proposed by Dulong and Petit. He actually assumed that each atom oscillates about its equilibrium position with a single frequency ν, and the energy of oscillation is confined to discrete values, $nh\nu$, where n is an integer. In that way he proposed the Einstein formula for the heat capacity:

$$C_{V,m} = 3Rf^2 \qquad\qquad f = \frac{\theta_E}{T}\left(\frac{e^{\theta_E/2T}}{e^{\theta_E/T} - 1}\right) \tag{2.2}$$

where $\theta_E = h\nu/k$ is the Einstein temperature and k is the Boltzmann constant. At high temperatures Equation 2.2 reduces to the classical result, $C_{V,m} = 3R$.[238]

The measurement of the energies of electrons produced in the photoelectric effect strongly suggested that an electron is ejected from a metal when it is involved in a collision with a particle-like projectile that carries enough energy to achieve ejection. On the other hand, the American physicists Clinton Davisson and Lester Germer observed the diffraction (a characteristic property of waves) of electrons by a crystal.[239] Analogous diffraction was also observed when other particles (protons, neutrons, nuclei and small atomic ions) were scattered from crystal planes. These experiments showed clearly that electromagnetic radiation has not only the character classically ascribed to particles, but electrons and in turn all other particles have features classically ascribed to waves, facing for the first time the contradictory up to that point *wave-particle duality.* In the same framework, the French physicist Louis de Broglie in 1924,[240] suggested that any particle with a linear momentum p should have a wavelength given by the de Broglie relation:

$$\lambda = \frac{h}{p} \tag{2.3}$$

As a wave of definite wavelength cannot be localized at a point, scientists during the years of the infancy of quantum mechanics should not have expected an electron in a state of definite linear momentum (and hence a wavelength) to be localized at a single point, since the wave-particle duality of particles was imposing a limit in simultaneous measurements of position and momentum of such particles. Indeed, greater accuracy in position is possible only at the expense of greater uncertainty in momentum and vice versa. This limitation is known as *Heisenberg uncertainty principle*, named after the German physicist Werner Heisenberg, who formulated Equation 2.4, in 1927. The quantitative version of this result is:

$$\Delta p \Delta q \geq \frac{1}{2}\hbar \tag{2.4}$$

where Δp is the uncertainty in the linear momentum parallel to the axis q, Δq is the uncertainty in position along that axis and $\hbar = h/2\pi$.[238]

The wave-particle duality of light and matter asked for a new formalism or a paradigm shift. The first equations based on combining wave and particle properties were introduced in 1926 by the Austrian physicist Erwin Schrödinger. Schrödinger suggested a non-relativistic formulation of quantum mechanics that does not follow deductively from some more fundamental theory but is based on a series of postulates.[241] However, in cases such as high energy physics or accelerator physics, the concepts of special relativity might be important, hence the need of a relativistic quantum mechanical formalism is also needed. Klein-Gordon and Dirac equations are formulations of this kind enabling the description of relativistic effects in quantum mechanics.[242] In this chapter, we will only focus on the non-relativistic Schrödinger equations since these equations are the most commonly used formulations of quantum mechanics in quantum chemistry.

2.1.1 Non-relativistic quantum mechanics - The Schrödinger equation

The whole of quantum mechanics can be expressed in terms of a small set of postulates. Indeed, to describe the state of a system, a function of the particles' coordinates, called wavefunction, Ψ, has been postulated. This function can be considered as the replacement of the classical concept of particle trajectory. Since, in the most general case, the state of the system can also change with time, Ψ is also a function of time t, $\Psi = \Psi(\mathbf{R_1}, \mathbf{R_2}, ..., \mathbf{r_1}, \mathbf{r_2}, ..., t)$, with $\mathbf{R}$ being the set of nuclear coordinates and $\mathbf{r}$ the set of electronic coordinates. The wavefunction contains all the possible dynamical information about the system it describes. However, what information does Ψ directly give to us? The answer to this question is based on an interpretation made by Max Born.[243] By using an analogy to the wave theory of light, Born suggested that if the wavefunction of a particle has the value ψ at some point in space, the probability of finding the particle in an infinitesimal volume $\mathrm{d}\tau$ at that point is proportional to $\mid \psi \mid^2 \mathrm{d}\tau$, with $\mid \psi \mid^2$ called the probability density. Hence, there is no direct significance about the value of the wavefunction that can also be negative or complex; only the square modulus, a positive entity, is directly physically significant. In that sense, both negative and positive regions of a wavefunction may correspond to a high probability of finding a particle in a given region.[238, 244]

In addition to this, to find the future state of a quantum mechanical system from the knowledge of its present state, we need an equation that tells us how Ψ changes with respect to time. Schrödinger came up with an equation, known as the time-dependent Schrödinger equation, by defining the quantum mechanical equivalent of the classical Hamiltonian[13].[246] The time-dependent Schrödinger equation is presented by Equation 2.6. We mention here that we drop all spin dependencies.

$$\hat{\mathcal{H}}\Psi(\mathbf{r}, \mathbf{R}, t) = i\hbar\frac{\partial}{\partial t}\Psi(\mathbf{r}, \mathbf{R}, t) \tag{2.6}$$

where $\Psi(\mathbf{r}, \mathbf{R}, t)$ is the total wavefunction of the electronic and nuclear degrees of freedom and $\hat{\mathcal{H}}$ is the Hamiltonian, which is a differential operator. For a system of nuclei and electrons in vacuum with no external fields, neglecting magnetic interactions, and using atomic units, the Hamiltonian operator is given by Equation 2.7.[247]

---

[13] Hamiltonian mechanics is a mathematical formalism of classical mechanics introduced or formulated by William Rowan Hamilton. A classical physical system is described by a set of canonical coordinates $\mathbf{r} = (\mathbf{q}, \mathbf{p})$ and its time evolution is uniquely defined by Hamilton's equations.

$$\frac{\mathrm{d}\mathbf{p}}{\mathrm{d}t} = -\frac{\partial\mathcal{H}}{\partial\mathbf{q}} \qquad \frac{\mathrm{d}\mathbf{q}}{\mathrm{d}t} = +\frac{\partial\mathcal{H}}{\partial\mathbf{p}} \tag{2.5}$$

where $\mathcal{H} = \mathcal{H}(\mathbf{q}, \mathbf{p}, t)$ is the Hamiltonian, which corresponds to the total energy of the system.[245]

$$
\begin{aligned}
\hat{\mathcal{H}} &= \hat{\mathcal{H}}_{mol} \\
&= -\sum_{I}\frac{\hbar^2}{2M_I}\nabla_I^2 - \sum_{i}\frac{\hbar^2}{2}\nabla_i^2 + \sum_{I<J}\frac{Z_I Z_J}{\mid \mathbf{R}_I - \mathbf{R}_J \mid} \\
&\quad - \sum_{i}\sum_{I}\frac{Z_I}{\mid \mathbf{R}_I - \mathbf{r}_i \mid} + \sum_{i<j}\frac{1}{\mid \mathbf{r}_i - \mathbf{r}_j \mid}
\end{aligned}
\tag{2.7}
$$

We rewrite the molecular Hamiltonian of Equation 2.7 more compactly as:

$$
\hat{\mathcal{H}} = \hat{\mathcal{T}}_N(\mathbf{R}) + \hat{\mathcal{T}}_e(\mathbf{r}) + \hat{\mathcal{V}}_{eN}(\mathbf{r},\mathbf{R}) + \hat{\mathcal{V}}_{NN}(\mathbf{R}) + \hat{\mathcal{V}}_{ee}(\mathbf{r}) \tag{2.8}
$$

where $\hat{\mathcal{T}}_e(\mathbf{r})$ and $\hat{\mathcal{T}}_N(\mathbf{R})$ are the electronic and nuclear kinetic energy operators, respectively. $\hat{\mathcal{V}}_{eN}(\mathbf{r},\mathbf{R})$ is the attractive electron-nucleus Coulomb interaction, $\hat{\mathcal{V}}_{NN}(\mathbf{R})$ is the repulsive nucleus-nucleus Coulomb interaction and $\hat{\mathcal{V}}_{ee}(\mathbf{r})$ is the repulsive electron-electron Coulomb interaction. M_I is the nuclear mass and Z_I is the nuclear charge. I, J and i, j refer to nuclei and electrons, respectively. On the other hand, the time-independent Schrödinger equation is given in Equation 2.9.[246]

$$
\hat{\mathcal{H}}\Psi(\mathbf{r},\mathbf{R}) = E\Psi(\mathbf{r},\mathbf{R}) \tag{2.9}
$$

where E is an allowed energy of the system and $\Psi(\mathbf{r},\mathbf{R})$ is the time-independent wavefunction.

The reference to the Hamilton operator gives us the opportunity to introduce another principal difference between classical and quantum mechanics. While in classical mechanics physical observables are represented by functions, in quantum mechanics they are represented by mathematical operators. Bringing together the concepts of operators and wavefunctions, one can establish the link between experimental observations and calculations. In principle, the mean value of an observable Ω in a series of measurements is equal to the expectation value of the corresponding operator $\hat{\Omega}$ and can be determined for an arbitrary state ψ by Equation 2.10.

$$
\langle\hat{\Omega}\rangle = \frac{\int \psi^*\hat{\Omega}\psi \mathrm{d}\tau}{\int \psi^*\psi \mathrm{d}\tau} \tag{2.10}
$$

If the wavefunction is chosen to be normalized to 1, then the expectation value is simply calculated by Equation 2.11. From now on, unless it is stated differently, we shall assume that the wavefunction is normalized.[238, 244]

$$
\langle\hat{\Omega}\rangle = \int \psi^*\hat{\Omega}\psi \mathrm{d}\tau \tag{2.11}
$$

Another feature that comes out by carefully examining Equations such as 2.9 is that, when an operator operates on a function, the outcome is the same function, multiplied by a constant. Such functions are called *eigenfunctions*. For example, Equation 2.9 is called an *eigenvalue equation*, where Ψ_{tot} is an eigenfunction of operator $\hat{\mathcal{H}}$ and E is an *eigenvalue* of the same operator, which corresponds to an allowed energy of the system. Eigenvalue equations can be written for other observables in quantum mechanics, such as the electric dipole moment or the momentum, with the eigenvalue being the outcome of the observation of these properties.[238, 244]

Whereas the Schrödinger equation can be solved exactly for the hydrogen atom, an exact solution is not possible for any molecule with more than two electrons. Unfortunately, having arrived at the promised land, we are forced to make approximations in order to solve the Schrödinger equation. The Born-Oppenheimer approximation is one of those.[248, 249]

2.1.2 Born-Oppenheimer approximation

The $\hat{\mathcal{V}}_{eN}(\mathbf{r},\mathbf{R})$ term of Equation 2.8 prevents us from writing the molecular time-independent wavefunction as a product of nuclear and electronic terms, $\Psi(\mathbf{r},\mathbf{R}) = \phi(\mathbf{r})\chi(\mathbf{R})$. However, the Born-Oppenheimer approximation allows us to conclude that such separation is approximately correct.[248, 249] The Born-Oppenheimer approximation supposes that the nuclei, being so much heavier than the electrons, move relatively slowly and may be considered as essentially fixed on the time scale of electron motion. The electrons can be regarded as particles that follow the nuclear motion adiabatically, *i.e.* the electrons at the end of the process will be in a state of the new system which corresponds to the state of the old system in which they started since they are somehow dragged along with the nuclei without requiring a finite relaxation time. In that way, one can solve the Schrödinger equation for the electrons, keeping the nuclear configuration fixed at a given $\mathbf{R}$. The computed energy will depend on this position $\mathbf{R}$, and the collection of possible nuclear configurations for all possible values of $\mathbf{R}$, together with the associated energies, $E(\mathbf{R})$, will define a potential energy (hyper)surface, $\mathcal{V}(\mathbf{R})$ for the nuclei.[250]

Initially, for the electronic Hamiltonian, $\hat{\mathcal{T}}_N(\mathbf{R})$ can be neglected, in Equation 2.8, since it is smaller than $\hat{\mathcal{T}}_e(\mathbf{r})$ by a factor of M_A/μ_e, with μ_e being the mass of an electron. The electronic Hamiltonian leads to Equation 2.12.

$$\hat{\mathcal{H}}_e = \hat{\mathcal{T}}_e(\mathbf{r}) + \hat{\mathcal{V}}_{eN}(\mathbf{r};\mathbf{R}) + \hat{\mathcal{V}}_{NN}(\mathbf{R}) + \hat{\mathcal{V}}_{ee}(\mathbf{r}) \tag{2.12}$$

where $;\mathbf{R}$ denotes a parametric dependence on the fixed nuclei.

The Schrödinger equation for the electronic wavefunction in electronic state s is given in Equation 2.13.

$$[\hat{\mathcal{T}}_e(\mathbf{r}) + \hat{\mathcal{V}}_{eN}(\mathbf{r};\mathbf{R}) + \hat{\mathcal{V}}_{ee}(\mathbf{r})]\phi_s(\mathbf{r};\mathbf{R}) = [E_s^{el}(\mathbf{R}) - \hat{\mathcal{V}}_{NN}(\mathbf{R})]\phi_s(\mathbf{r};\mathbf{R}) \tag{2.13}$$

Any many-electron wavefunction can be expanded as a linear combination of the eigenvectors of Equation 2.13, since the solutions form a complete basis in Hilbert space. In that sense, by expanding the molecular wavefunction $\Psi(\mathbf{r},\mathbf{R})$, in terms of the complete set of the electronic wavefunctions $\phi_s(\mathbf{r};\mathbf{R})$, we obtain:

$$\Psi(\mathbf{r},\mathbf{R}) = \sum_k^{\infty} \phi_k(\mathbf{r};\mathbf{R})\chi_k(\mathbf{R}) \tag{2.14}$$

where $\chi_k(\mathbf{R})$ are expansion coefficients, which depend on $\mathbf{R}$. Apart from that, $\Psi(\mathbf{r},\mathbf{R})$ is a solution of Equation 2.9, so that:

$$[\hat{\mathcal{T}}_N(\mathbf{R}) + \hat{\mathcal{T}}_e(\mathbf{r}) + \hat{\mathcal{V}}_{eN}(\mathbf{r},\mathbf{R}) + \hat{\mathcal{V}}_{NN}(\mathbf{R}) + \hat{\mathcal{V}}_{ee}(\mathbf{r})]\Psi(\mathbf{r},\mathbf{R}) = E\Psi(\mathbf{r},\mathbf{R}) \tag{2.15}$$

Substituting Equation 2.14 into Equation 2.15, using Equation 2.13, we obtain:

$$\sum_k^{\infty}[E_k^{el}(\mathbf{R}) + \hat{\mathcal{T}}_N(\mathbf{R})]\phi_k(\mathbf{r};\mathbf{R})\chi_k(\mathbf{R}) = E\sum_k^{\infty} \phi_k(\mathbf{r};\mathbf{R})\chi_k(\mathbf{R}) \tag{2.16}$$

Multiplying on the left by $\phi_l^*(\mathbf{r};\mathbf{R})$ and integrating over all electron positions, using the orthonormality of $\phi_k(\mathbf{r};\mathbf{R})$ functions, we find:[251]

$$\begin{aligned}
&[E_l^{el}(\mathbf{R}) + \hat{\mathcal{T}}_N(\mathbf{R})]\chi_l(\mathbf{R}) \\
&\quad = E\chi_l(\mathbf{R}) \\
&\qquad + \sum_k^{\infty}\sum_I \frac{\hbar^2}{2M_I}\left\{2\left[\int \mathrm{d}r\phi_k^*(\mathbf{r};\mathbf{R})\nabla_I\phi_k(\mathbf{r};\mathbf{R})\right]\nabla_I\chi_k(\mathbf{R})\right. \\
&\qquad \left. + \left[\int \mathrm{d}r\phi_l^*(\mathbf{r};\mathbf{R})\nabla_I^2\phi_k(\mathbf{r};\mathbf{R})\right]\chi_k(\mathbf{R})\right\}
\end{aligned} \tag{2.17}$$

One can rewrite 2.17 more compactly as:

$$[E_l^{el}(\mathbf{R}) + \hat{\mathcal{T}}_N(\mathbf{R})]\chi_l(\mathbf{R}) = E\chi_l(\mathbf{R}) - \sum_k^{\infty} \mathcal{W}_{lk}(\mathbf{R})\chi_k(\mathbf{R}) \tag{2.18}$$

$\mathcal{W}_{lk}(\mathbf{R})\chi_k(\mathbf{R})$ are non-adiabatic coupling terms that are responsible for the mixing of the different electronic states (k,l). Within the Born-Oppenheimer adiabatic approximation, these coupling terms between the nuclear and electronic degrees of freedom are zero. When these terms are neglected, the Born-Oppenheimer nuclear Schrödinger equation for the electronic state l is given in Equation

$$[E_l^{el}(\mathbf{R}) + \hat{\mathcal{T}}_N(\mathbf{R})]\chi_l(\mathbf{R}) = E\chi_l(\mathbf{R}) \tag{2.19}$$

Even within the Born-Oppenheimer approximation, only the hydrogen molecule ion, H_2^+ can be solved exactly. For this reason, other approximations have to be made, too.

2.2 Electronic structure methods

Given a nuclear configuration $\mathbf{R}$, the question is how to compute the required potential $\mathcal{V}(\mathbf{R})$ which acts on the nuclei. For this reason we rewrite the time-independent Schrödinger equation of Equation 2.9, in the following form:

$$\hat{\mathcal{H}}_{el}\Psi_{el}(\mathbf{r};\mathbf{R}) = \mathcal{V}(\mathbf{R})\Psi_{el}(\mathbf{r};\mathbf{R}) \tag{2.20}$$

This question is also known as the electronic structure problem. To tackle this equation we can follow two paths.[251]

Initially, an ansatz for the electronic wavefunction can be proposed, which will produce a combination of single-particle wavefunctions, also called *atomic orbitals* in case of many-electron atoms or *molecular orbitals* in case of molecules. Molecular orbitals are used as approximate solutions to the molecular Schrödinger equation.[244] All the wavefunction-based methods are based on such approximations, where the electronic wavefunction of many-electron systems is written in a form that satisfies the Pauli principle[14], namely using the Slater determinant many-electron wavefunctions:[252]

$$\Psi_{el}(\mathbf{r_1},\mathbf{r_2},...,\mathbf{r_N}) = \sum_{m_1,m_2,...,m_N} C_{m_N} \mid \phi_{m_1}(\mathbf{r_1})\phi_{m_2}(\mathbf{r_2})...\phi_{m_N}(\mathbf{r_N}) \mid \tag{2.21}$$

where $\phi_{m_N}(\mathbf{r_N})$ are one-electron spin-orbitals, and

$$\mid \phi_{m_1}(\mathbf{r_1})\phi_{m_2}(\mathbf{r_2})...\phi_{m_N}(\mathbf{r_N}) \mid = \frac{1}{\sqrt{N!}} \begin{bmatrix} \phi_{m_1}(\mathbf{r_1}) & \phi_{m_2}(\mathbf{r_1}) & ... & \phi_{m_N}(\mathbf{r_1}) \\ \phi_{m_1}(\mathbf{r_2}) & \phi_{m_2}(\mathbf{r_2}) & ... & \phi_{m_N}(\mathbf{r_2}) \\ . & . & . & . \\ . & . & . & . \\ . & . & . & . \\ \phi_{m_1}(\mathbf{r_N}) & \phi_{m_2}(\mathbf{r_N}) & ... & \phi_{m_N}(\mathbf{r_N}) \end{bmatrix} \tag{2.22}$$

---

[14] No two electrons can occupy the same state.

Among the wavefunction-based methods there are methods which are exact within a given basis-set, such as Full Configuration Interaction, and methods such as Hartree-Fock that can only produce an approximate solution, since electron correlation[15] is neglected.[253] However, the higher the accuracy of a method the more expensive the respective calculation is, thus making the treatment of systems with a high number of electrons intractable.

An alternative approach to tackle the electronic structure problem is based on Density Functional Theory (DFT),[254, 255] in which the central quantity is the electron density instead of the molecular wavefunction. The computational cost and complexity are relatively low compared to the wavefunction-based counterparts, allowing for calculations that include many atoms.

Below, Hartree-Fock theory is presented which lies at the basis of all wavefunction based methods used in quantum chemistry. In addition to this, DFT is discussed in this Chapter, since it is the method that was used throughout this thesis. However, we will start our journey into the world of electronic structure methods by introducing the concepts of basis sets and pseudopotentials.

2.2.1 Basis sets

Expanding an unknown function in a set of known functions is not an approximation if the basis is complete, however the use of an infinite number of basis functions is impossible in actual calculations. For this reason, the complex many-electron molecular wavefunctions are usually described in a basis of a finite number of atom centered functions.[250] In order to introduce the formulation of the expansion, it is worth mentioning that Heisenberg formulated a version of quantum mechanics, which is based on matrices and is called matrix mechanics. In that formulation position and linear momentum are represented by matrices $\mathbf{x}$ and $\mathbf{p_x}$, requiring that $\mathbf{x}\mathbf{p_x} - \mathbf{p_x}\mathbf{x} = i\hbar\mathbf{1}$, where $\mathbf{1}$ is the unit matrix. The Schrödinger equation can also be given in a matrix representation. In such a case, solving the Schrödinger equation is equivalent to diagonalizing the Hamiltonian matrix.[244] This approach is adopted by most quantum chemical software packages.

The general procedure consists of the choice of a suitable basis set and the variation of $C's$ and $D's$ in Equations 2.23 and 2.24 respectively,

$$\Psi_{el}(\mathbf{r_1}, s_1, \mathbf{r_2}, s_2..., \mathbf{r_N}, s_N) = \sum_{m_1, m_2, ..., m_N} C_{m_N} \mid \phi_{m_1}(\mathbf{r_1}, s_1)\phi_{m_2}(\mathbf{r_2}, s_2)...\phi_{m_N}(\mathbf{r_N}, s_N) \mid \tag{2.23}$$

---

[15] In the Hartree-Fock method, the instantaneous Coulombic interactions between electrons are not taken into account and the instantaneous electron-electron repulsion is replaced by the repulsion of each electron with an average electron charge cloud.[253]

where

$$\phi_m(\mathbf{r}, s) = \sum_n D_{mn}\chi_n(\mathbf{r}) \otimes s \tag{2.24}$$

trying to find an approximate Ψ_{el} that can solve the Schrödinger equation.[250] Notably, in Equation 2.24 the operation taking place is a dot product in matrix notation and s is the spin.

Slater type orbitals (STO)[256] and Gaussian type orbitals (GTO)[257] are commonly used types of basis functions in electronic structure calculations. However, for periodic systems such as solids, *plane wave* basis sets are a more suitable choice. Plane waves $e^{i\mathbf{Gr}}$ form a complete set of functions in which any function, subject to suitable conditions of regularity, can be expanded.[30] The set of wave vectors for plane waves with the periodicity of the lattice, is just the reciprocal lattice[16], for this reason a function periodic in the direct lattice will have a plane wave expansion of the form:

$$f_i(\mathbf{r}) = \sum_{\mathbf{G}} c_i(\mathbf{G})e^{i\mathbf{Gr}} \tag{2.25}$$

where the sum is over all reciprocal lattice vectors $\mathbf{G}$. In the plane wave basis set framework, matrix operations and forces can be evaluated very efficiently exploiting the Fast Fourier Transform (FFT) algorithm. In addition to this, plane wave basis sets are independent of the nuclear position, simplifying in that way the calculation of forces on the atoms. Furthermore, they are orthonormal and the convergence of the physical properties is only controlled by a single parameter, which is the energy cutoff, given by Equation 2.26.[30]

$$E_{cutoff} = \frac{\mathbf{G}^2_{max}}{2}. \tag{2.26}$$

2.2.2 Pseudopotentials

Core electrons are subject to the very deep Coulomb potential of the nuclei; on account of this, their wavefunctions are very localized. On the other hand, the valence electrons experience a much weaker Coulomb potential from the nuclei, which are partially screened by the core electrons and hence their wavefunctions are more diffuse. Furthermore, valence electrons need to be orthogonal to the core electrons due to the exclusion principle. To satisfy the orthogonality constraint, all-electron wavefunctions of the valence electrons oscillate in the atomic core region.[258] For this reason, it would be a formidable

---

[16] The set of all wave vectors $\mathbf{G}$ that yield plane waves with the periodicity of a given lattice is known as its reciprocal lattice.[30]

task to perform an all-electron calculation employing a sufficiently large plane-wave basis set because of the vast amount of computational time that would be required to calculate the electronic wavefunctions.

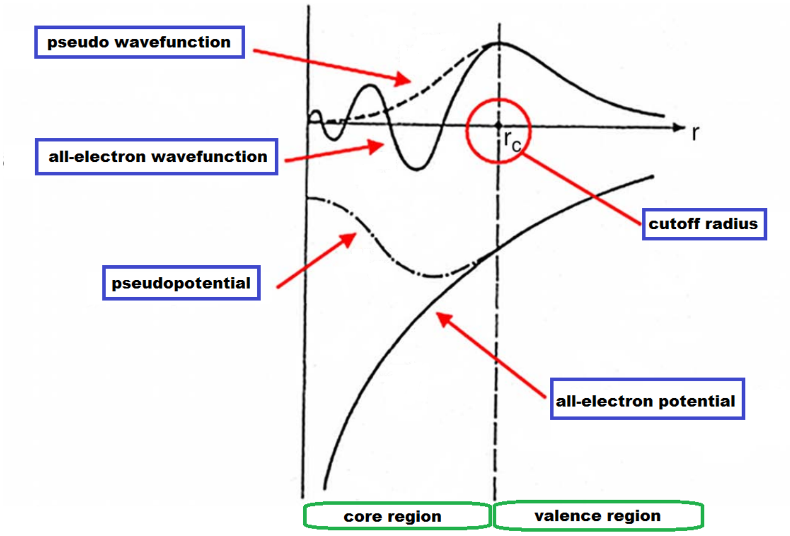

Figure 2.1: Schematic illustration of the all-electron wavefunction (solid line) and the pseudowavefunction (dashed line) together with the corresponding potentials.

The pseudopotential approximation represents an alternative, allowing the efficient application of a plane wave basis set expansion. Actually, the core electrons and the strong ionic potential are replaced by a weaker pseudopotential that acts on a set of pseudo wavefunctions rather than the true valence wavefunctions. The method is based on the assumption that most physical properties of matter are dependent on valence electrons to a much greater extent than on core electrons.[259] Traditionally, pseudopotentials are constructed so as to reproduce faithfully the scattering properties and phase shifts of the ion and the core electrons for the valence wavefunctions, but in a way that the pseudo wavefunction has no nodes in the core region (Figure 2.1). Outside the core region the pseudopotential and the true potential are identical. Since the phase shift produced by the ion core is different for each angular momentum component of the valence wavefunction, the scattering from the pseudopotential must be angular momentum dependent. The most general form of a pseudopotential is given in Equation 2.27.

$$\mathcal{V}_{PS} = \sum_{lm} |lm\rangle \, \mathcal{V}_l \, \langle lm| \tag{2.27}$$

where $|lm\rangle$ are spherical harmonics and $\mathcal{V}_l$ is the pseudopotential for angular momentum channel l.

It is necessary that outside the core regions the integrals of the squared amplitudes of the real and pseudo wavefunctions are identical. This could be done by mere normalization but *norm-conservation* implies that the fraction of charge inside, respectively outside the core region is the same for the pseudo wavefunction and all-electron wavefunction.[260, 261] An important concept is the degree of hardness of a pseudopotential. A pseudopotential is considered hard if it requires a large amount of Fourier components for its accurate representation and soft otherwise. From the early developement stage of accurate norm-conserving pseudopotentials, it has been observed that pseudopotentials for transition metals were extremely hard.[262]

To generate much softer pseudopotentials, David Vanderbilt[263] suggested the relaxation of the norm-conservation requirement. In principle, by removing the charge associated with the tightly bound orbitals that have a substantial fraction of their weight inside the core region, the pseudo wavefunction can be as soft as possible within the core. Ultrasoft pseudopotentials allow calculations to be performed with the lowest possible energy cutoff for plane-wave basis set but lead to computational overhead due to the fact that the loss of norm-conservation has to be compensated with additional terms.[262]

2.2.3 Hartree-Fock theory

Hartree-Fock theory (which is also called self-consistent field (SCF) method) is the basis of molecular orbital theory, according to which each electron or the probability distribution of each electron can be described by an orbital that does not depend explicitly on the position of the other electrons.[264, 265] However, how do we actually calculate such molecular orbitals within the Hartree-Fock theory? Before answering this question, it is important to recall that Hartree-Fock theory was developed to solve the electronic Schrödinger equation that results from the time-independent Schrödinger equation after employing the Born-Oppenheimer approximation. Whereas for the hydrogen atom and other one electron systems, such as He^+, orbitals are exact eigenfunctions of the full electronic Hamiltonian, when we refer to many-electron systems, orbitals are just mathematical constructs that approximate reality. Keeping those principles in mind, we can now develop the basic idea of Hartree-Fock theory.

As a matter of fact, the Hartree-Fock method determines the set of spin-orbitals which minimize the energy. The main assumption that is made is the usage of a single Slater determinant (Equation 2.21) made of one-electron molecular orbitals for the description of the many-electron wavefunction. As discussed above, Slater determinants are used since a many-electron wavefuction must fulfill the *antisymmetry principle* together with the *principle of indistiguishability* of the electrons, as required by the Pauli principle. In addition to this, the *variational theorem*[17] is employed for the minimization of the energy, implying that the Slater determinant with the lowest energy is as close as we can get to the true wavefunction for the assumed functional form of a single determinant.[266]

In practice, a set of approximate one-electron wavefunctions, which in case of a molecular system is typically a linear combination of atomic orbitals (LCAO) is chosen. The Hartree-Fock orbitals are optimized iteratively until the change in total electronic energy falls below a predefined threshold.

To further discuss the mathematical formulation of Hartree-Fock theory, we introduce the electronic Hamiltonian in another notation:

$$\hat{\mathcal{H}}_{el} = \sum_i \hat{h}_i + \sum_{i<j} \hat{v}_{(i,j)} + \mathcal{V}_{NN} \tag{2.29}$$

where $\hat{h}_i$ is a one-electron operator,

$$\hat{h}_i = -\frac{1}{2}\nabla_i^2 - \sum_I \frac{Z_I}{\mid \mathbf{r}_i - \mathbf{R}_I \mid} \tag{2.30}$$

and $\hat{v}_{(i,j)}$ is a two-electron operator.

$$\hat{v}_{(i,j)} = \frac{1}{\mid \mathbf{r}_i - \mathbf{r}_j \mid} \tag{2.31}$$

In this case, $\mathcal{V}_{NN}$ is just a constant that only shifts the eigenvalues.[266]

The Hartree-Fock energy in terms of integrals of one- or two-electron operators is given in Equation 2.32, employing chemists' notation.

$$E_{HF} = \sum_i \langle i|\, \hat{h} \,|i\rangle + \frac{1}{2}\sum_{i,j}[ii|jj] - [ij|ji] \tag{2.32}$$

where $\langle i|\, \hat{h} \,|j\rangle$ is the one electron integral:

$$\langle i|\, \hat{h} \,|j\rangle = \int \mathrm{d}\mathbf{x}_1 \phi_i^*(\mathbf{x}_1)\hat{h}(\mathbf{r}_1)\phi_j(\mathbf{x}_1) \tag{2.33}$$

---

[17] For a time-independent Hamiltonian operator, any trial wavefunction will have an energy expectation value that is greater than or equal to the true ground state wavefunction corresponding to the given Hamiltonian.[266]

$$E = \frac{\langle \Psi|\, \hat{\mathcal{H}} \,|\Psi\rangle}{\langle \Psi|\Psi\rangle} \geq E_0 \tag{2.28}$$

and $[ij|kl]$ is a two-electron integral:

$$[ij|kl] = \int \mathrm{d}\mathbf{x}_1 \mathrm{d}\mathbf{x}_2 \phi_i^*(\mathbf{x}_1)\phi_j(\mathbf{x}_1)\frac{1}{r_{12}}\phi_k^*(\mathbf{x}_2)\phi_l(\mathbf{x}_2) \tag{2.34}$$

In equations 2.33 and 2.34 $\mathbf{x}_i = (\mathbf{r}_i, s_i)$. To minimize the Hartree-Fock energy expression with respect to changes in the spin-orbitals, (ensuring that the variational procedure will leave these orbitals orthonormal), Lagrange's method of undetermined multipliers[18] is employed. This procedure leads to the Hartree-Fock equations (Equation 2.35) defining the orbitals.

$$\hat{h}(\mathbf{x}_1)\phi_i(\mathbf{x}_1) + \sum_{j\neq i}\left[\int \mathrm{d}\mathbf{x}_2 \mid \phi_j(\mathbf{x}_2) \mid^2 r_{12}^{-1}\right]\phi_i(\mathbf{x}_1) \tag{2.35}$$

$$-\sum_{j\neq i}\left[\int \mathrm{d}\mathbf{x}_2 \phi_j^*(\mathbf{x}_2)\phi_i(\mathbf{x}_2) r_{12}^{-1}\right]\phi_j(\mathbf{x}_1) = \epsilon_i \phi_i(\mathbf{x}_1) \tag{2.36}$$

where ϵ_i is the energy eigenvalue associated with orbital ϕ_i. The term 2.37 explains why Hartree-Fock theory is a mean field theory, since it describes the Coulomb interaction of an electron in a spin-orbital ϕ_i with the average charge distribution of the other electrons. This term is called the Coulomb term and the corresponding Coulomb operator is given in Equation 2.38, which represents the average local potential at point $\mathbf{x}_1$ due to the charge distribution from the electron in spin-orbital ϕ_j.

$$\sum_{j\neq i}\left[\int \mathrm{d}\mathbf{x}_2 \mid \phi_j(\mathbf{x}_2) \mid^2 r_{12}^{-1}\right]\phi_i(\mathbf{x}_1) \tag{2.37}$$

$$\mathcal{J}_i(\mathbf{x}_1) = \int \mathrm{d}\mathbf{x}_2 \mid \phi_j(\mathbf{x}_2) \mid^2 r_{12}^{-1} \tag{2.38}$$

The term 2.39 arises from the antisymmetry principle and is responsible for the exchange of spin-orbitals ϕ_i and ϕ_j, this is the reason why it is called the exchange term and in turn an exchange operator that acts on an arbitrary spin-orbital ϕ_i is given in Equation 2.40.[266]

$$\sum_{j\neq i}\left[\int \mathrm{d}\mathbf{x}_2 \phi_j^*(\mathbf{x}_2)\phi_i(\mathbf{x}_2) r_{12}^{-1}\right]\phi_j(\mathbf{x}_1) \tag{2.39}$$

$$\mathcal{K}_j(\mathbf{x}_1)\phi_i(\mathbf{x}_1) = \left[\int \mathrm{d}\mathbf{x}_2 \phi_j^*(\mathbf{x}_2)\phi_i(\mathbf{x}_2) r_{12}^{-1}\right]\phi_j(\mathbf{x}_1) \tag{2.40}$$

---

[18] It is an optimisation method to find the local minima or maxima of a function subject to constraints.

The restrictions $j \neq i$ can be removed since:

$$[\mathcal{J}_i(\mathbf{x}_1) - \mathcal{K}_i(\mathbf{x}_1)]\phi_i(\mathbf{x}_1) = 0 \tag{2.41}$$

and in turn a Fock operator is introduced:

$$\hat{f}(\mathbf{x}_1) = \hat{h}(\mathbf{x}_1) + \sum_j \mathcal{J}_j(\mathbf{x}_1) - \mathcal{K}_j(\mathbf{x}_1) \tag{2.42}$$

Finally, the Hartree-Fock equations are given in Equation 2.43

$$\hat{f}(\mathbf{x}_1)\phi_i(\mathbf{x}_1) = \epsilon_i\phi_i(\mathbf{x}_1). \tag{2.43}$$

As discussed above, Hartree-Fock theory neglects the electron-correlation leading in that way to significant deviations from experimental results. This limitation is nowadays treated by a variety of methods, collectively called post-Hartree-Fock methods.[253] However, an alternative to Hartree-Fock theory is density functional theory, in which the central quantity is the electron density instead of the molecular wavefunction.

2.2.4 Density functional theory

DFT[254, 255] is presently the most successful approach to compute the electronic structure of matter. In its original formulation, it provides all the ground state properties of a many-body system. The central quantity in DFT is the electron density. The total electron density $\rho(\mathbf{r})$ describes the probability density for finding any electron of a many-electron system at position $\mathbf{r}$. It can be calculated by integrating the squared absolute value of the many-electron wavefunction over all but one spatial coordinate (Equation 2.44).

$$\rho(\mathbf{r}) = N \int \mid \Psi(\mathbf{r}, s_1, \mathbf{x}_2, ..., \mathbf{x}_N) \mid^2 \mathrm{d}s_1\mathrm{d}\mathbf{x}_2...\mathrm{d}\mathbf{x}_N \tag{2.44}$$

where $\mathbf{x} = (\mathbf{r}, s)$. By writing out the integration over the corresponding spin variable explicitly, we find:

$$\begin{aligned} \rho(\mathbf{r}) &= N \int \mid \Psi(\mathbf{r}, +\frac{1}{2}, \mathbf{r}_2, s_2, ..., \mathbf{r}_N, s_N) \mid^2 \mathrm{d}\mathbf{r}_2\mathrm{d}s_2...\mathrm{d}\mathbf{r}_N\mathrm{d}s_N && (2.45)\\ &+ N \int \mid \Psi(\mathbf{r}, -\frac{1}{2}, \mathbf{r}_2, s_2, ..., \mathbf{r}_N, s_N) \mid^2 \mathrm{d}\mathbf{r}_2\mathrm{d}s_2...\mathrm{d}\mathbf{r}_N\mathrm{d}s_N && (2.46)\\ &= \rho_\alpha(\mathbf{r}) + \rho_\beta(\mathbf{r}) && (2.47) \end{aligned}$$

where the total electron density is defined as the sum of the electron spin density of electrons with spin up $\rho_\alpha(\mathbf{r})$ and spin down $\rho_\beta(\mathbf{r})$.

In 1964, Hohenberg and Kohn provided two theorems for "the ground state of an interacting electron gas in an external potential $\mathcal{V}_{ext}(\mathbf{r})$".[254] The first theorem demonstrates that the total electron density uniquely determines the Hamilton operator and thus all the properties of the system. More specifically, according to the first theorem, the external potential $\mathcal{V}_{ext}(\mathbf{r})$ that yields the electron density that can be obtained from the ground-state many-electron wavefunction is (to within a constant) a unique functional of $\rho(\mathbf{r})$. Since in turn $\mathcal{V}_{ext}(\mathbf{r})$ completely determines the Hamiltonian of the system, also the many-electron ground state wavefunction is a unique functional of the density.

However, how can one be sure that a certain density is the ground-state density? To answer this question Hohenberg and Kohn provided a second theorem; a variational principle, which is equivalent to the one used for the wavefunction-based methods that states that the ground-state many-electron wavefunction Ψ_0, apart from reproducing the ground-state density, also minimizes the energy, following the requirement:

$$E_{\mathcal{V}}^{\mathrm{GS}}[\rho] = \min_{\Psi \to \rho} \langle \Psi[\rho] | \, \hat{\mathcal{T}} + \hat{\mathcal{V}}_{ee} + \hat{\mathcal{V}}_{eN} \, | \Psi[\rho] \rangle \tag{2.48}$$

where $E_{\mathcal{V}}^{GS}$ is the ground-state energy that corresponds to the ground state density, $\rho_0(\mathbf{r})$. If $\rho(\mathbf{r})$ is an arbitrary density different from the ground state density, then the corresponding wavefunction Ψ will be different from the ground state wavefunction Ψ_0. Hence, according to the variational principle:

$$E_{\mathcal{V}}^{GS}[\rho_0] \leq E_{\mathcal{V}}[\rho] \tag{2.49}$$

where $E_{\mathcal{V}}$ denotes the energy in potential $\mathcal{V}_{ext}(\mathbf{r})$ that corresponds to the density $\rho(\mathbf{r})$. Therefore, an internal energy functional $\mathcal{F}[\rho]$ exists such that the energy $E_{\mathcal{V}}$ of a system subject to the external potential $\mathcal{V}_{ext}(\mathbf{r})$ is given by:[250]

$$\begin{aligned} E_{\mathcal{V}}[\rho] &= \min_{\Psi \to \rho} \langle \Psi[\rho] | \, \hat{\mathcal{T}} + \hat{\mathcal{V}}_{ee} \, | \Psi[\rho] \rangle + \int \mathrm{d}\mathbf{r} \rho(\mathbf{r}) \mathcal{V}_{ext}(\mathbf{r}) \\ &= \mathcal{F}[\rho] + \int \mathrm{d}\mathbf{r} \rho(\mathbf{r}) \mathcal{V}_{ext}(\mathbf{r}) \end{aligned} \tag{2.50}$$

Although the exact density functional $\mathcal{F}[\rho]$ exists, it is not known, and finding approximations is quite a difficult task. If it were known, Equation 2.50 would have been solved exactly, and since it is an universal functional, (it is independent of the potential $\mathcal{V}_{ext}(\mathbf{r})$), it applies equally well to the hydrogen atom as to extended systems, such as proteins. One should mention here that Equations 2.48 and 2.50 constitute the constrained-search proof of the Hohenberg-Kohn theorem, which has been proposed by M. Levy and E. Lieb.[267, 268]

Kohn-Sham density functional theory

In 1965, Kohn and Sham introduced a formalism that in practice simplifies the determination of the density functional.[255] According to them, a fictitious system of non-interacting electrons, $\hat{\mathcal{V}}_{ee} = 0$ can be considered. In that sense, one may separate the classical part of the Coulomb energy $\mathcal{J}[\rho]$ out of $\mathcal{F}[\rho]$ to get:

$$E_{\mathcal{V}}[\rho] = \mathcal{J}[\rho] + \mathcal{G}[\rho] + \int \mathrm{d}\mathbf{r}\rho(\mathbf{r})\mathcal{V}_{ext}(\mathbf{r}) \tag{2.51}$$

where $\mathcal{G}[\rho]$ takes all the non-classical terms into account. $\mathcal{G}[\rho]$ can further be split into:

$$\mathcal{G}[\rho] = \mathcal{T}_s[\rho] + \mathcal{E}_{xc}[\rho] \tag{2.52}$$

where $\mathcal{T}_s$ is the kinetic energy of the non-interacting system, s stands for single particle and $\mathcal{E}_{xc}$ is the *exchange-correlation energy*, which takes care of all the non-classical exchange-correlation effects. It is often decomposed into:

$$\mathcal{E}_{xc}[\rho] = \mathcal{E}_x[\rho] + \mathcal{E}_c[\rho] \tag{2.53}$$

where $\mathcal{E}_c[\rho]$ is due to electron correlation and $\mathcal{E}_x[\rho]$ due to the Pauli exclusion principle (exchange energy).

This system of non-interacting electrons possesses an external potential $\mathcal{V}_{eff}$, which enforces that its electronic density is equal to that of the true, physical system. Kohn and Sham assumed that the electronic wavefunction of the fictitious system can be described by a single Slater determinant of auxiliary single-particle wavefunctions, ψ^{KS} called *Kohn-Sham orbitals*. These wavefunctions have no other physical interpretation, than that they are just an auxiliary tool. Taking into account the known expression for the non-interacting kinetic energy, one can write the energy as:

$$\mathcal{E}_{\mathcal{V}}[\rho] = \sum_i^N \int \psi_i^{KS*}(\mathbf{r})\Big(-\frac{1}{2}\nabla^2\Big)\psi_i^{KS}(\mathbf{r})\mathrm{d}\mathbf{r} + \mathcal{J}[\rho] + \mathcal{E}_{xc}[\rho] + \int \mathrm{d}\mathbf{r}\rho(\mathbf{r})\mathcal{V}_{ext}(\mathbf{r}) \tag{2.54}$$

By applying the variational principle to the energy expression 2.54, Kohn and Sham derived a set of single-particle equations for the Kohn-Sham orbitals that yield the ground-state density:

$$\Big[-\frac{1}{2}\nabla^2 + \mathcal{V}_{eff}\Big]\psi_i^{KS} = \epsilon_i\psi_i^{KS} \tag{2.55}$$

where $\mathcal{V}_{eff}$ is an effective potential given by:

$$\mathcal{V}_{eff} = \mathcal{V}_{ext}(\mathbf{r}) + \int \frac{\rho(\mathbf{r}')}{\mid \mathbf{r} - \mathbf{r}' \mid}\mathrm{d}\mathbf{r} + \mathcal{V}_{xc}(\mathbf{r}) \tag{2.56}$$

where $\mathcal{V}_{xc}$ is the exchange-correlation potential, which is due to non-classical effects.

To conclude, the total effective potential (the sum of all the potentials) can be considered as a new $\mathcal{V}'_{ext}(\mathbf{r})$ potential that fixes the density and thus the ground-state energy. The Hamiltonian corresponding to the effective potential is denoted the effective Hamiltonian $\hat{\mathcal{H}}_{eff}$. Given an expression for the exchange-correlation functional, the problem can be solved self-consistently, as in the case of the Hartree-Fock method, mentioned above. The central assertion used in establishing the Kohn-Sham approach lies in the mapping of a physical problem onto an artificial, but easy-to-solve problem, because the real interacting system and the non-interacting system are sharing the same electron density.

So far no approximations were invoked at all. The Kohn-Sham equations are yielding the exact ground-state density of a system, given that the exact exchange-correlation functional is known. However, this is not the case, since there is no universal analytical expression for it. For this reason, a vast number of approximate exchange-correlation functionals have been developed based either on semiempirical parametrizations or on first principles. The different functional forms can be classified into five families, which are known as *local density approximation* (LDA),[254, 255] *generalized gradient approximation* (GGA),[269] *meta-GGA*,[270] *hybrid*[271] and *double hybrid*[272] exchange-correlation functional families.

2.3 The band theory of solids

The electronic structure of solids can be regarded as an extension of molecular orbital theory to aggregates consisting of an infinite number of atoms. However, there are some characteristics that are unique to solids. One of those is the formation of continuous bands of energy levels. As has been already discussed in the introduction, in a typical solid the band structure consists of bands separated by a band gap, a region of energy to which no orbitals belong. The band gap separates the lowest unoccupied bands (conduction band minimum - CBM) and the highest occupied bands (valence band maximum - VBM).[244]

The electronic problem in solids is in principle a many-electron problem, where the Hamiltonian consists of one-electron potential describing the interactions of electrons with nuclei and pair potentials describing the electron-electron interactions and the kinetic energy. Because ions in a solid are arranged in a regular periodic way, an effective one-electron potential $\mathcal{V}(\mathbf{r})$ that reflects this periodicity can be considered, in this case.

$$\mathcal{V}(\mathbf{r}+\mathbf{R}) = \mathcal{V}(\mathbf{r}) \tag{2.57}$$

According to the *Bloch theorem*, the eigenstates ψ of the one-electron Hamiltonian for a periodic potential:

$$\hat{\mathcal{H}} = -\frac{\hbar^2\nabla^2}{2m} + \mathcal{V}(\mathbf{r}) \tag{2.58}$$

where $\mathcal{V}(\mathbf{r})$ obeys Equation 2.57, can be chosen to have the form of a plane-wave times a function with the periodicity of the Bravais lattice:

$$\psi_{n\mathbf{k}}(\mathbf{r}) = e^{i\mathbf{kr}}u_{n\mathbf{k}}(\mathbf{r}) \tag{2.59}$$

where

$$u_{n\mathbf{k}}(\mathbf{r}+\mathbf{R}) = u_{n\mathbf{k}}(\mathbf{r}). \tag{2.60}$$

and $u_{n\mathbf{k}}(\mathbf{r})$ are the Bloch functions, n is the band index and $\mathbf{k}$ is a vector of real numbers called wave vector. By Equations 2.59 and 2.60, it is implied that:

$$\psi_{n\mathbf{k}}(\mathbf{r}+\mathbf{R}) = e^{i\mathbf{kr}}u_{n\mathbf{k}}(\mathbf{r}) \tag{2.61}$$

and the Bloch theorem can also be stated as:[30]

$$\psi(\mathbf{r}+\mathbf{R}) = e^{i\mathbf{kr}}\psi(\mathbf{r}). \tag{2.62}$$

We refer here to the first Brillouin zone,[273] which is defined as the Wigner–Seitz primitive cell[274] of the reciprocal lattice. In other words, we can define the first Brillouin zone as the set of points that can be reached from the origin without crossing any Bragg planes. In general, Brillouin zones are nothing but allowed energy regions of electrons in reciprocal space. The wave vector **k** can always be confined in the first Brillouin zone, since any **k′** not in the first Brillouin zone can be written as:

$$\mathbf{k}' = \mathbf{k} + \mathbf{G} \tag{2.63}$$

where **G** is a reciprocal lattice vector and **k** lies in the first zone. In fact, wave vectors that differ by a reciprocal lattice vector are equivalent, in the sense that they characterize the same set of Bloch states. By restricting **k** to the first Brillouin zone, every Bloch state has a unique **k**. For this reason, the first Brillouin zone is often used to depict all of the Bloch states.[30]

Given that each electron occupies a state of definite **k**, the infinite number of electrons gives rise to an infinite number of "**k**-points". Only a finite number of energy levels is occupied at each **k**-point. Hence, it is not necessary to consider all of these **k**-points; rather, the wavefunctions can be represented over a region of reciprocal space by considering the wavefunction at a single **k**-point. It is therefore sufficient to consider the electronic states at a finite number of **k**-points in order to determine the ground state density of the solid. In principle, the Bloch theorem replaces the infinite-electron problem with one of considering only the electrons confined in the unit cell, employing a finite number of **k**-points chosen so as to appropriately sample the first Brillouin zone.

2.4 Electronic transitions

When an electromagnetic field (light, laser pulse) is applied to a molecular system, the molecule can absorb more or less efficiently photons leading to a change in its electronic structure. In such way, the molecule is photo-excited, initializing a photophysical and/or photochemical process. Sometimes, the relocation of electrons is so extensive that it results in ionization or dissociation of the molecule. For a transition to take place from one allowed state to another, a series of selection rules exist that describe how probable this transition is.[275] Among such selection rules, the *Franck-Condon principle* describes the almost instantaneous absorption of a photon (that occurs in femtoseconds), involving only the rearrangement of the electrons without changes in the nuclear geometry.[276, 277]

Indeed, the analysis of vibronic transitions[19] is based on the Franck-Condon principle which, like the Born-Oppenheimer approximation, follows from the fact that the nuclear masses are much larger than the electronic mass. More specifically, according to the Frank-Condon principle, because of the differences between the masses of electrons and nuclei, the electronic transition occurs within a stationary nuclear framework. As a result, the electron density is rapidly redistributed with the nuclear positions remaining unchanged during the actual transition and gradually starts readjusting once the electrons have adopted their final distribution. The qualitative implications of this principle are illustrated in Figure 2.2 where two molecular potential curves for the electronic ground state and an electronic excited state of a diatomic molecule are presented. The transition takes place with highest probability when the internuclear distance is equal to the equilibrium bond length R_e of the lower electronic state and termi-

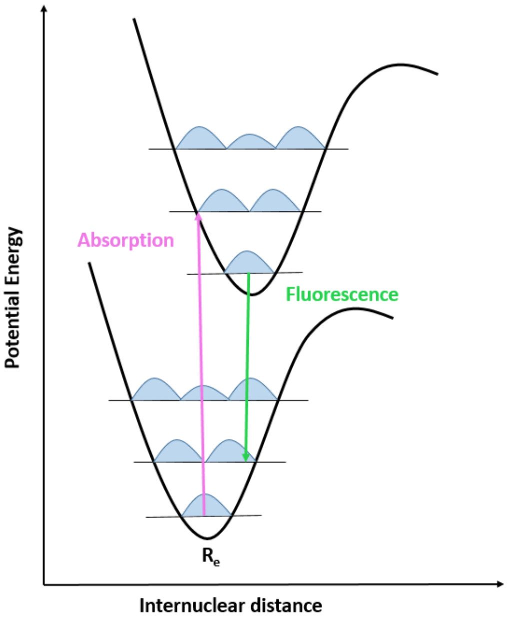

Figure 2.2: Qualitative implications of the Franck-Condon principle illustrated for a diatomic molecule.

---

[19] Simultaneous electronic and vibrational transitions are known as vibronic transitions.

nates, where a vertical line cuts through the upper molecular potential energy curve. Such a transition is called *vertical*.[244]

In the quantum mechanical picture, the transition occurs from the ground vibrational state of the lower electronic state to the vibrational state that it most resembles in the upper electronic state. The wavefunction of such vibrational state corresponds to an energy level that lies in the same position as in the vertical transition of the classical description and undergoes the least change in order to preserve the dynamical state of the nuclei. The quantum mechanical picture is based on the evaluation of the electric dipole transition moment between the ground vibronic state $|\epsilon\nu\rangle$ and the upper vibronic state $|\epsilon'\nu'\rangle$. Within the Born-Oppenheimer approximation, the vibronic state $|\epsilon\nu\rangle$ is described by the wavefunction $\psi_\epsilon(\mathbf{r};\mathbf{R})\psi_\nu(\mathbf{R})$ and the overall electric dipole transition moment can be evaluated by Equation 2.64.

$$\langle\epsilon'\nu'|\,\mu\,|\epsilon\nu\rangle = \mu_{\epsilon'\epsilon}\int\psi^*_{\nu'}(\mathbf{R})\psi_\nu(\mathbf{R})\mathrm{d}\mathbf{R} \tag{2.64}$$

where

$$\int\psi^*_{\nu'}(\mathbf{R})\psi_\nu(\mathbf{R})\mathrm{d}\mathbf{R} \tag{2.65}$$

is the overlap integral between the two vibrational states in their respective electronic states. The electric dipole transition moment is therefore largest between vibrational states that have the greatest overlap. Furthermore, $\mu_{\epsilon'\epsilon}$ is a constant that approximates the electric dipole moment (Equation 2.66), considering that the transition is independent of the locations of the nuclei so long as they are not displaced significantly from equilibrium.

$$\mu_{\epsilon'\epsilon} \approx \int\psi^*_{\epsilon'}(\mathbf{r};\mathbf{R})\hat{\mu}_\epsilon\psi_\epsilon(\mathbf{r};\mathbf{R})\mathrm{d}\mathbf{r} \tag{2.66}$$

In Equation 2.66, $\hat{\mu}_\epsilon$ is the electric dipole moment operator, depending on the positions and charges of the electrons.[244]

Once an excitation has taken place, several pathways can be followed by the photo-excited system, all of them aiming at releasing the excess energy. The molecule can cool down in a given electronic state by radiative decay processes; processes in which a molecule discards its excitation energy in the form of photons. In *fluorescence*, spontaneous emission of radiation occurs within a few nanoseconds after the exciting radiation is removed. In principle, radiation is generated in the course of transitions between states of the same multiplicity. On the other hand, light emission from an electronic state with a spin multiplicity different from the ground state is also possible. Such event is called *phosphorescence* and it continues for at least a short time after the exciting radiation extinguishes.[244, 251]

The molecule can also cool down in a given electronic state by a nonradiative decay process, in which the excess energy is transferred into the vibration, rotation and translation of the surrounding molecules. Apart from that, if the molecule relaxes in regions of potential energy surfaces where two electronic states with the same spin multiplicity come close and are coupled through the motion of the nuclei, the molecule can move to another electronic state. This process is called *internal conversion* and it is a non-adiabatic transition. The Born-Oppenheimer approximation is thus not valid anymore for the description of such events. Another possibility for the molecule would be to hop to an electronic state with a different spin multiplicity, a process which is called *intersystem crossing* and is prohibited in the framework of the non-relativistic description. However, this constraint is relaxed when spin-orbit coupling effects are sizeable.[251]

2.4.1 Time-dependent density functional theory

The goal of a computational approach to the simulation of the photo-induced processes is the complete description of what happens at the molecular level from the promotion to the excited electronic state to the restoration back in the electronic ground state. In 1984, Runge and Gross introduced a formally exact approach to the time-dependent electronic many-body problem for calculating excitation energies, which is called “time-dependent density functional theory” (TDDFT).[278] They formulated with two theorems, the first one stating that (similar to the first Hohenberg-Kohn theorem), there is a one-to-one correspondence between the time-dependent electronic density and the time-dependent external potential.

$$\mathcal{V}_{ext}(\mathbf{r},t) \underset{\Psi_0}{\overset{1:1}{\longleftrightarrow}} \rho(\mathbf{r},t) \tag{2.67}$$

where $\mathcal{V}_{ext}(\mathbf{r},t)$ is the time-dependent external potential and $\rho(\mathbf{r},t)$ the time-dependent electron density. In other words, they proved that if two N-electron systems evolve from the same initial many-body state Ψ_0, but are subject to two different time-dependent potentials ($\mathcal{V}_{ext}(\mathbf{r},t)$ and $\mathcal{V}'_{ext}(\mathbf{r},t) \neq \mathcal{V}_{ext}(\mathbf{r},t) + C(t)$), their respective time-dependent densities will be different ($\rho(\mathbf{r},t)$, $\rho'(\mathbf{r},t)$), allowing, also for the time-dependent case, to write the potential as a functional of the density:

$$\mathcal{V}_{ext}(\mathbf{r},t) = \mathcal{V}[\rho,\Psi_0](\mathbf{r},t) \tag{2.68}$$

The Runge-Gross theorem applies to potentials that can be expanded in a Taylor series about the initial time:

$$\mathcal{V}_{ext}(\mathbf{r},t) = \sum_{k=0}^{\infty} \frac{\mathcal{V}_k(\mathbf{r})}{k!}(t-t_0)^k \tag{2.69}$$

In addition to the first theorem, Runge and Gross also proposed a second theorem (a time-dependent equivalent to the second Hohenberg-Kohn theorem) according to which, in the time-dependent case, the response of the electrons to a time-dependent external potential is derived by searching the extrema of the quantum mechanical action functional. The variational principle applied to the quantum mechanical action, known also as Frenkel's principle, leads to the optimized time-dependent wavefunction.[279]

$$\mathcal{A}[\rho] = \int_{t_0}^{t_1} \langle\Psi(t)|\, i\frac{\partial}{\partial t} - \hat{\mathcal{H}}(t)\, |\Psi(t)\rangle \, \mathrm{d}t \tag{2.70}$$

However, the action functional defined in Equation 2.70 violates the principle of causality. For this reason, van Leeuwen derived a new action functional that fixes the causality problem in TDDFT.[280, 281]

Time-dependent Kohn-Sham equations

In analogy to the Kohn-Sham formalism for the time-independent picture, the exact time-dependent density $\rho(\mathbf{r},t)$ can be calculated from a non-interacting system with N single-particle orbitals. In particular, van Leeuwen's theorem provides a justification for the time-dependent version of the Kohn-Sham equation since it states that for a non-interacting system a unique $\mathcal{V}_s(\mathbf{r},t)$ potential, for the many-electron wavefunction $\Phi_0 = \Phi_0'$ exists, which reproduces $\rho(\mathbf{r},t)$ at all times.[251, 282]

We consider a non-interacting system, in which the time-dependent perturbation is applied. Taking into account that the true time-dependent density is the one that makes the action stationary,

$$\frac{\delta\mathcal{A}[\rho]}{\delta\rho(\mathbf{r},t)} = 0 \tag{2.71}$$

and considering the condition $\rho(\mathbf{r},t) = \sum_{j=1}^{N} \mid \phi_j(\mathbf{r},t) \mid^2$, the time-dependent Kohn-Sham orbitals satisfy time-dependent Kohn-Sham equations (Equation 2.72),

$$i\hbar\frac{\partial}{\partial t}\phi_j(\mathbf{r},t) = \left[-\frac{\nabla^2}{2} + \mathcal{V}_s[\rho,\Phi_0](\mathbf{r},t)\right]\phi_j(\mathbf{r},t) \qquad j = 1,...,N \tag{2.72}$$

where the time-dependent effective potential is given by:

$$\mathcal{V}_s[\rho,\Phi_0](\mathbf{r},t) = \mathcal{V}_{ext}(\mathbf{r},t) + \mathcal{V}_{\mathcal{H}}(\mathbf{r},t) + \mathcal{V}_{xc}[\rho](\mathbf{r},t) \tag{2.73}$$

with $\mathcal{V}_{ext}(\mathbf{r},t)$ being the external potential, $\mathcal{V}_{\mathcal{H}}(\mathbf{r},t)$ the Hartree potential and $\mathcal{V}_{xc}[\rho](\mathbf{r},t)$ the time-dependent exchange-correlation potential.

So far in the derivation of the time-dependent density functional equations, no approximations have been made and the theory is formally exact. However, to apply TDDFT in practice a suitable approximation for the time-dependent exchange correlation potential needs to be found, the time-dependent Kohn-Sham equations need to be solved numerically, as well as the physical observables of interest need to be obtained from the time-dependent density. As far as the exchange-correlation functional is concerned, a suitable approximation would be to neglect its implicit time-dependence and to use the exchange-correlation functionals derived for time-independent DFT. Indeed, it is possible to insert the time-dependent density into the time-independent exchange-correlation functionals. Such approximation is the adiabatic approximation and could be exact for systems with no memory.[251, 282]

2.4.2 Linear-response time-dependent density functional theory

In linear-response time-dependent density functional theory (LR-TDDFT), one studies the density response of a system under the influence of an external time-dependent perturbation. The density-density response function given in Equation 2.74 (which is a basic quantity in LR-TDDFT) relates the first-order response $\delta\rho(\mathbf{r},t)$ to the applied perturbation $\delta\mathcal{V}(\mathbf{r}',t')$ (Equation 2.75).

$$\chi(\mathbf{r},t,\mathbf{r}',t') = \frac{\delta\rho(\mathbf{r},t)}{\delta\mathcal{V}_{ext}(\mathbf{r}',t')} \tag{2.74}$$

$$\delta\rho(\mathbf{r},t) = \int \mathrm{d}\mathbf{r}'\mathrm{d}t'\chi(\mathbf{r},t,\mathbf{r}',t')\delta\mathcal{V}(\mathbf{r}',t') \tag{2.75}$$

Equation 2.75 is usually Fourier transformed into frequency space:

$$\delta\rho(\mathbf{r},\omega) = \int \mathrm{d}\mathbf{r}'\chi(\mathbf{r},\mathbf{r}',\omega)\delta\mathcal{V}(\mathbf{r}',\omega). \tag{2.76}$$

The response function for a physical system of interacting electrons $\chi(\mathbf{r},t,\mathbf{r}',t')$ can be related to the computationally more advantageous Kohn-Sham response, $\chi_s(\mathbf{r},t,\mathbf{r}',t')$ of the non-interacting system. In the Kohn-Sham picture, the effective potential induced by the time-dependent external field generates a density perturbation given in Equation 2.77.

$$\delta\rho_s(\mathbf{r},t) = \chi_s * \delta\mathcal{V}_s \tag{2.77}$$

where the operation that takes place is a convolution. Using the Runge-Gross theorem, this perturbed density of the non-interacting system can be equated with the perturbed density obtained for the real interacting system (Equation 2.75):

$$\delta\rho(\mathbf{r},t) = \delta\rho_s(\mathbf{r},t). \tag{2.78}$$

Furthermore, the relationship between the exact density-density response function and the Kohn-Sham response function is expressed in terms of the inverses of their corresponding Fourier transforms (Equation 2.79).

$$\chi^{-1}(\mathbf{r},\mathbf{r}',\omega) = \chi_s^{-1}(\mathbf{r},\mathbf{r}',\omega) - \frac{1}{\mid \mathbf{r}_1 - \mathbf{r}_2 \mid} - f_{xc}(\mathbf{r}_1,\mathbf{r}_2,\omega) \tag{2.79}$$

where $f_{xc}(\mathbf{r}_1,\mathbf{r}_2,\omega)$ is the TDDFT exchange-correlation kernel,

$$\chi_s(\mathbf{r},\mathbf{r}',\omega) = \sum_{k,j}(f_k - f_j)\frac{\psi_k^*(\mathbf{r})\psi_j(\mathbf{r})\psi_j^*(\mathbf{r}')\psi_k(\mathbf{r}')}{\omega - (\epsilon_j - \epsilon_k) + i\eta} \tag{2.80}$$

and η is a positive infinitesimal.[251]

Moreover, the dynamic dipole polarizability $\alpha(\omega)$ has a particular place in molecular spectroscopy. In principle, the dynamic dipole polarizability is the response function that relates the external potential to the change in dipole.

$$\delta\mu_x(\omega) = \alpha_{xz}(\omega)\mathcal{E}_z(\omega) \tag{2.81}$$

where $\alpha_{xz}(\omega) = -\sum_{ij,kl} x_{ij}\chi_{ij,kl}(\omega)z_{kl}$ and $x_{ij} = \langle\psi_j|\,\hat{x}\,|\psi_j\rangle$.

Equations 2.79, 2.80 and 2.81 allow the determination of the electronic excitation spectrum in the usual dipole approximation:

$$\bar{\alpha}(\omega) = \sum_I \frac{f_I}{\omega_I^2 - \omega^2} \tag{2.82}$$

and taking into consideration that,

$$\omega_I = E_I - E_0 \tag{2.83}$$

and

$$f_I = \frac{2}{3}\omega_I(\mid \langle\Psi_0|\,\hat{x}\,|\Psi_I\rangle \mid^2 + \mid \langle\Psi_0|\,\hat{y}\,|\Psi_I\rangle \mid^2 + \mid \langle\Psi_0|\,\hat{z}\,|\Psi_I\rangle \mid^2) \tag{2.84}$$

the poles of the dynamic polarizability determine the excitation energies, ω_I and the residues f_I the corresponding oscillator strengths. In that way the propagation of the electronic density after an external perturbation allows us to compute the whole excitation spectrum of a system under study, taking also into account that the optical absorption cross-section can be derived by the imaginary part of α_ω. The problem of finding the excitation energies of the interacting system is translated to searching for the poles of the response function.[244, 251]

By expressing the dynamic dipole polarizability in the basis of unperturbed molecular orbitals, Casida was able to show that the TDDFT excitation energies are solutions of Equation 2.85.[283]

$$\begin{bmatrix} A(\omega) & B(\omega) \\ B^*(\omega) & A^*(\omega) \end{bmatrix} \begin{bmatrix} \mathbf{X}_I \\ \mathbf{Y}_I \end{bmatrix} = \omega_I \begin{bmatrix} \mathbf{1} & \mathbf{0} \\ \mathbf{0} & -\mathbf{1} \end{bmatrix} \begin{bmatrix} \mathbf{X}_I \\ \mathbf{Y}_I \end{bmatrix} \tag{2.85}$$

where

$$A_{i\alpha\sigma,jb\tau}(\omega) = \delta_{\sigma\tau}\delta_{ij}\delta_{\alpha b}(\epsilon_{\alpha\sigma} - \epsilon_{i\sigma}) + \langle i\alpha| \, f_H + f_{xc}^{\sigma\tau}(\omega) \, |jb\rangle \tag{2.86}$$

$$B_{i\alpha\sigma,jb\tau}(\omega) = \langle i\alpha| \, f_H + f_{xc}^{\sigma\tau}(\omega) \, |jb\rangle \tag{2.87}$$

and

$$f_{xc}^{\sigma\tau}(\mathbf{r}_1, \mathbf{r}_2; \omega) = \int_{-\infty}^{+\infty} e^{i\omega(t_1 - t_2)} \frac{\delta^2 E_{xc}[\rho\uparrow, \rho\downarrow]}{\delta\rho_\sigma(\mathbf{r}_1, t_1)\delta\rho_\tau(\mathbf{r}_2, t_2)} \mathrm{d}(t_1 - t_2). \tag{2.88}$$

The TDDFT exchange-correlation kernel used in Casida's equations becomes with the adiabatic approximation:

$$f_{xc}^{\sigma\tau}(\mathbf{r}, \mathbf{r}') = \frac{\delta^2 E_{xc}[\rho\uparrow, \rho\downarrow]}{\delta\rho_\sigma(\mathbf{r})\delta\rho_\tau(\mathbf{r}')}. \tag{2.89}$$

Since f_{xc} is time-independent, the number of solutions of the LR-TDDFT equations is equal to the dimensionality of Casida's matrices. This corresponds to the one-electron excitations of the system under study. Finally, the Tamm-Dancoff approximation (TDA) consists in setting $B = 0$ in Equation 2.85, leading to the neglection of all contributions to the excitation energies coming from the de-excitation of the correlated ground state.[284]

LR-TDDFT within the adiabatic approximation has become the most used implementation of TDDFT, since it works well for low-lying excitations of primarily single electron character, which do not involve too much charge density relaxation. However, this method faces several failures mostly arising from the approximations of the exchange-correlation functionals and their functional derivatives. Difficulties such as the description of conical intersections between the ground and the first electronic state and of electronic states with strong double excitation character have been observed.[251]

2.4.3 Simulation of absorption spectra

One method to quantitatively represent the different processes taking place upon excitation is the calculation of absorption respectively, emission spectra. Here we concentrate on the simulation of absorption spectra in order to present the mathematical formulation. However, the main principles for the simulation of spectra stand for the majority of processes described above. The simulation of absorption spectra is based on the construction of a nuclear phase space distribution of the electronic ground state which is followed by a projection onto the electronic excited states.[285]

Given a ground state ensemble $\{\mathbf{R}_k\}$ composed of N_p points, the photoabsorption cross section considering the first order of the time-dependent perturbation theory is given in Equation 2.90.

$$\sigma(\omega) = \frac{4\pi^2\omega}{\hbar c} \sum_{l \neq i} \langle l| \boldsymbol{\epsilon}\hat{\mu} |i\rangle^2 g(\omega_{il} - \omega, \Delta) \tag{2.90}$$

where ω is the angular frequency of the probe radiation, c is the speed of light, $\boldsymbol{\epsilon}$ is the linear polarization direction, $\hat{\mu}$ is the electric dipole operator and $\langle l|$ and $\langle i|$ are the final and initial electronic states, respectively. The g function selects the resonant frequency between the initial and final states and Δ is attributed to it, since it cannot be a Dirac δ function due to a finite excited-state lifetime. It is important to stress here that, for Equation 2.90 to be valid, the molecule should be subject to a harmonic perturbation given by a classical radiation field. Finally the integration over quantum states can be simpler written by a classical average over an ensemble, given in Equation 2.91.

$$\sigma(\omega) = \frac{4\pi^2\omega}{\hbar c} \sum_{l \neq i}^{N_{\text{fs}}} \left[\frac{1}{N_p^l} \sum_{k}^{N_p^l} \mid \boldsymbol{\epsilon}\hat{\mu}_{il}(\mathbf{R}_k) \mid^2 g(\omega - \omega_{il}(\mathbf{R}_k), \Delta) \right] \tag{2.91}$$

where $\hat{\mu}_{il}(\mathbf{R}_k)$ and $\omega_{il}(\mathbf{R}_k)$ are the electronic transition dipole moment and the angular frequency for transitions between initial and final states computed at the fixed nuclear position $\mathbf{R}_k$. The sum with index l runs over electronic states and the one with index k over the different configurations.[285]

To facilitate the estimation of the cross section, in most quantum chemical packages, Equation 2.91 is written in terms of oscillator strengths f_{il} and transition energies ΔE_{il}. In case of an isotropic system Equation 2.91 can be averaged over all orientations, giving:

$$\sigma(E) = \frac{\pi e^2}{2mc\epsilon_0} \sum_{l \neq i}^{N_{\text{fs}}} \left[\frac{1}{N_p^l} \sum_{k}^{N_p^l} f_{il}(\mathbf{R}_k) g(E - \Delta E_{il}(\mathbf{R}_k), \delta) \right] \tag{2.92}$$

where e and m are the electron charge and mass, ϵ_0 is the vacuum permitivity and E is the radiation energy for an angular frequency ω. In general, in order to simulate the absorption spectrum, the transition energy ΔE_{il} and oscillator strength f_{il} for transitions from initial state i to final states l, for each point in the $\{\mathbf{R}_k\}$ ensemble are computed. Then, the intensity is convoluted with a normalized line shape function $g(E - \Delta E_{il}(\mathbf{R}_k), \delta)$ and broadened by a constant $\delta = \hbar\Delta$. The function modeling the line shape depends on the nature of the process and accounts for the broadening of the resonant lines. For instance, thermal broadening (collisions) leads to a Guassian shape:[285]

$$g_{\text{Gauss}}(E - \Delta E_{il}, \delta) = \left(\frac{2}{\pi}\right)^{1/2} \frac{\hbar}{\delta} \text{exp}\left(\frac{-2(E - \Delta E_{il})^2}{\delta^2}\right). \tag{2.93}$$

2.5 Statistical mechanics

The goal of statistical mechanics is the study of the macroscopic properties of matter (especially the thermodynamic ones), taking into account the interactions between the components of their microscopic structure. Indeed, there are several computer simulations methods that are based on the assumption that classical mechanics can be used to describe the motions of atoms and molecules. In contrast to quantum mechanics, the systems that are of interest to statistical mechanics typically contain a large number of particles (*e.g.* systems with $\mathcal{O}(10^{23})$ particles). In what follows, we denote by $\Omega(E, V, N)$ the number of eigenstates with E being the energy of a system of N particles in a volume V. That allows us to express one of the basic postulates of statistical mechanics, according to which a system with fixed E, N and V is equally likely to be found in any of its eigenstates, $\Omega(E)$. Having expressed this basic postulate, we can now define the two laws of thermodynamics, using a formulation of statistical mechanics in quantum mechanical terms.[286]

The first law is concerned with the internal energy E. We can postulate two properties that E obeys. First it is *extensive*, *i.e.*, it depends linearly on the size of the system. For this reason, for two subsystems, we can consider a measure of their degeneracy, which we expect to be additive (Equation 2.94).

$$\ln \Omega(E_1, E - E_1) = \ln \Omega_1(E_1) + \ln \Omega_2(E - E_1) \tag{2.94}$$

where E_1 is the energy of one of the subsystems. The total number of states is the product of the number of states in each individual system. On the other hand, the second postulated property is *energy conservation*, which is the heart of the first law of thermodynamics. This means that, if the energy of a system is changing, that should result in some form of energy flow into or out of the system under study, either by performing mechanical work or as heat.[286, 287] However, what is the most likely distribution of the energy?

As already mentioned, every state of the total system is equally probable. However, the number of eigenstates that correspond to a given distribution of the energy over the subsystems depends on the internal energy of the subsystem from which the energy is transferred. In that way, the most likely distribution of the energy is the one that maximizes $\ln \Omega(E_1, E - E_1)$. From the moment that there is no more energy flow from one subsystem to the other, the two subsystems are in thermal equilibrium and $\ln \Omega$ of the total system is at a maximum.[286, 287]

This brings us to the second law of thermodynamics which states that: "*an extensive function, S, of a state exists, which is called entropy and is a monotonically increasing function of E and if a state A' is adiabatically accessible from state A, then* $S'_A \geqslant S_A$", *i.e.* the entropy of a system is at its maximum when the system is in thermal equilibrium. One should mention here that unlike in quantum mechanics, an adiabatic process here occurs when there is no heat or mass transfer between a system and its surroundings. From our observations about $\ln \Omega$ we can conclude that it is somehow related to entropy as it has been introduced for macroscopic systems. According to a fundamental postulate of statistical mechanics, the entropy of a system is related to its eigenstates via Equation 2.95.

$$S(N, V, E) = k_B \ln \Omega(N, V, E) \tag{2.95}$$

where k_B is Boltzmann's constant.[286, 287]

2.5.1 Motion in phase space

For a system of N atoms, a multidimensional space of $6N$ dimensions which correspond to the positions and momenta is called the *phase space*. Any instantaneous microscopic state of the system can be written as a point $\Gamma = (\{\mathbf{q}_i\}, \{\mathbf{p}_i\})$ of phase space. Given that the Hamiltonian $\mathcal{H}(\{\mathbf{q}_i\}, \{\mathbf{p}_i\}, t)$ is the sum of kinetic and potential energy for a classical system,[20] then the time evolution of the system in phase space is governed by Hamilton's equations of motion.

$$\dot{\mathbf{p}}_i = \frac{\partial \mathbf{p}_i}{\partial t} = -\frac{\partial \mathcal{H}(\{\mathbf{q}_i\}, \{\mathbf{p}_i\}, t)}{\partial \mathbf{q}_i} \tag{2.96}$$

and

$$\dot{\mathbf{q}}_i = \frac{\partial \mathbf{q}_i}{\partial t} = +\frac{\partial \mathcal{H}(\{\mathbf{q}_i\}, \{\mathbf{p}_i\}, t)}{\partial \mathbf{p}_i} \tag{2.97}$$

where $i = 1, 2, 3, ..., N$ and $\frac{\partial}{\partial \mathbf{x}} = \nabla_{\mathbf{x}}$ symbolizes the gradient operator with respect to the vectorial quantity $\mathbf{x}$. As the system evolves in time and its state changes, the system traces out a trajectory in phase space.

---

[20] In such a case the Hamiltonian is not an operator anymore.

2.5.2 Time average, ensemble average and ergodicity

Having defined the phase space, we can now assume that any property $\mathcal{A}$ of a system is a function of the points traversed by the system in phase space. The property at time t is given by $\mathcal{A}(\Gamma(t))$ and the macroscopically meaningful observable property $\mathcal{A}_{obs}$ is the time average of this (Equation 2.98).

$$\mathcal{A}_{obs} = \langle \mathcal{A}(\Gamma(t)) \rangle_t = \lim_{t_{obs} \to \infty} \frac{1}{t_{obs}} \int_0^{t_{obs}} \mathcal{A}(\Gamma(t)) \mathrm{d}t \tag{2.98}$$

In most experiments the time average comes about naturally since a series of measurements are performed during a certain time interval and then the average of these measurements is determined. Indeed, this is the idea that molecular dynamics simulations follow as well, where one can study the average behavior of a many-particle system simply by computing its natural time evolution and averaging the observable under study over a sufficiently long time.[219, 286]

The calculation of time averages in molecular dynamics simulations is not the conventional statistical mechanical approach to estimate thermodynamic properties. Gibbs suggested the replacement of the time average by an *ensemble average*, because of the complexity of the time evolution for systems with a large number of atoms. An *ensemble* is a set of microscopic states distributed in phase space according to a certain probability density. A very important measure of the probability distribution of an equilibrium ensemble is the *partition function*, Q. The partition function, also called the sum over states, can be considered as a normalizing factor. In such a way there is a weight function $w_{ens}(\Gamma)$, which satisfies Equation 2.99.

$$Q_{ens} = \sum_{\Gamma} w_{ens}(\Gamma) \tag{2.99}$$

One conceivable approach to the computation of thermodynamic properties would be the estimation of the partition function for a particular ensemble employing Equation 2.99. However, this calculation over all possible states is not feasible for systems with a large number of particles.[219, 287]

To this end, we can introduce the *ergodic hypothesis*, which states that all accessible microstates with the same energy are equiprobable over a long period of time. Ergodicity allows us to calculate the observables of a system in equilibrium as averages over phase space with respect to the probability density of an equilibrium ensemble, $\rho_{ens}(\Gamma)$ (Equation 2.100).

$$\mathcal{A}_{obs} = \langle A \rangle_{ens} = \int \mathcal{A}(\Gamma) \rho_{ens}(\Gamma) \mathrm{d}\Gamma \tag{2.100}$$

The ergodic hypothesis allows to obtain an average over points in phase space with no need of real time-dependence of the system. That assumes that the system under study as well as the simulation algorithm are ergodic, *i.e.* that no particular region in phase space is excluded. Finally, taking into account that any dynamical trajectory visits all representative regions of phase space, the density distribution of points in phase space (traversed by the trajectory) converges to a stationary distribution.[286]

2.5.3 Statistical ensembles

Central to equilibrium statistical mechanics is the theory of equilibrium ensembles. As mentioned above, an ensemble is a set of microscopic states distributed in phase space according to a certain probability density. The thermodynamic ensembles usually used in molecular simulations are the microcanonical (NVE), the canonical (NVT), the isothermal-isobaric (NPT), the isoenthalpic-isobaric (NPH) and the grand canonical (μVT) ensembles. Below, the mathematical formulation of microcanonical and canonical ensembles are presented, since these two ensembles are used in this thesis.

Microcanonical (NVE) ensemble

The microcanonical ensemble describes the equilibrium phase-space distribution of a system for which the number of particles, N, the total energy, E and the volume V are conserved. Such system is isolated from the environment and lies in a container of fixed volume V. The classical Hamiltonian is given in Equation 2.101 and, since the total energy is conserved, it is equal to a constant E_0.

$$\mathcal{H}(\{\mathbf{q}_i\},\{\mathbf{p}_i\}) = \mathcal{K}(\{\mathbf{q}_i\},\{\mathbf{p}_i\}) + \mathcal{V}(\{\mathbf{q}_i\},\{\mathbf{p}_i\}) = E_0 \tag{2.101}$$

By Equation 2.101, we conclude that only states in phase space with total energy E_0 are accessible, which corresponds to a probability density for the ensemble, given in Equation 2.102.

$$\rho_{NVE}(\{\mathbf{q}_i\},\{\mathbf{p}_i\}) = \frac{1}{Q_{NVE}}\delta[\mathcal{H}(\{\mathbf{q}_i\},\{\mathbf{p}_i\}) - E_0] \tag{2.102}$$

where

$$Q_{NVE} = \sum_{\Gamma} \delta[\mathcal{H}(\Gamma) - E_0] \tag{2.103}$$

is the partition function in the microcanonical ensemble. For classical systems the summation over discrete states in Equation 2.103 is replaced by an integral.

$$Q_{NVE} = \frac{1}{N!}\frac{1}{h^{3N}}\int \mathrm{d}\Gamma\,\delta[\mathcal{H}(\Gamma) - E_0] \tag{2.104}$$

where h^{3N} is the ultimate resolution for counting states allowed by Heisenberg's uncertainty principle. Finally, the proper thermodynamical property for the microcanonical ensemble is entropy.

Canonical (NVT) ensemble

The canonical ensemble provides a statistical microscopic description of a system at constant number of particles, N, volume, V and temperature, T. The probability density in the canonical ensemble is deduced from that of the microcanonical ensemble. In this case, the system has a fixed volume and is in contact with a much larger system, which is called bath. As a result of the interaction with the bath, the energy E of the system fluctuates. The probability density of this ensemble is the Boltzmann (canonical) distribution.

$$\rho_{i,NVT} = \frac{1}{Q(N,V,T)} \exp\left(-\beta E_i\right) \qquad \text{for } i = 0, 1, 2, ... \tag{2.105}$$

where

$$Q(N,V,T) = \sum_i e^{-\beta E_i} \tag{2.106}$$

is the canonical partition function and $\beta = 1/k_B T$.

The classical analogues of Equations 2.105 and 2.106 are:

$$\rho_{NVT}(\{\mathbf{q}_i\},\{\mathbf{p}_i\}) = \frac{1}{Q(N,V,T)} \frac{1}{h^{3N} N!} e^{-\beta \mathcal{H}}(\{\mathbf{q}_i\},\{\mathbf{p}_i\}) \tag{2.107}$$

and

$$Q(N,V,T) = \int_\Gamma \frac{e^{-\beta\mathcal{H}}(\{\mathbf{q}_i\},\{\mathbf{p}_i\})}{h^{3N} N!} \mathrm{d}^{3N}\mathbf{q}_i \mathrm{d}^{3N}\mathbf{p}_i \tag{2.108}$$

Finally, the canonical ensemble is connected with macroscopic thermodynamics via the Helmholtz energy (Equation 2.109).

$$A = -k_B T \ln\left(Q_{NVT}\right) \tag{2.109}$$

However, it is important to mention how the canonical distribution is realized in simulations. There are several methods for temperature control (constraint methods, extended system methods and stochastic methods), all of them introducing a *thermostat* which is an algorithm that allows for simulations at constant temperature. The thermostat can be considered as the equivalence of a bath in a real system, and the behavior of the simulated system should not depend on the details of the bath or the thermostat, respectively. Below we will focus on the Nosé-Hoover thermostat, since it is often used in simulations when the canonical ensemble is employed.[288]

The Nosé-Hoover thermostat is a deterministic algorithm which follows the idea of the extended system method. In the beginning, Nosé introduced a bath with degree of freedom s, with which the system under study exchanges energy. In this way, a Hamiltonian is postulated to describe the extended system (Equation 2.110).

$$\mathcal{H} = \sum_i \frac{\mathbf{p}_i^2}{2m_i s^2} + \Phi(\mathbf{q}) + \frac{p_s^2}{2Q} + gkT \ln s \tag{2.110}$$

where the first term is the kinetic energy and the second term the potential energy of the system under study. The last two terms correspond to the added degree of freedom s, where p_s is a conjugate momentum of s, Q is considered the "mass" for the motion of s and T is the temperature of the bath. The parameter g is equal to the number of degrees of freedom of the physical system.

It is important to define the formalism of the thermal interactions between the system and the bath. The real variables that describe the real motion of a particle i are expressed with a prime, as $\mathbf{p}_i'$, t', v_i', $\mathbf{q}_i'$ and p_s'. The virtual variables that have been introduced for the control of the temperature are expressed without the prime, as $\mathbf{p}_i$, t, v_i, $\mathbf{q}_i$ and p_s. The canonical equations of motion, in that case are given in Equations 2.111, 2.112, 2.113 and 2.114.[288]

$$\frac{\mathrm{d}\mathbf{q}_i'}{\mathrm{d}t'} = \frac{\mathbf{p}_\mathbf{i}'}{m_i} \tag{2.111}$$

$$\frac{\mathrm{d}\mathbf{p}_i'}{\mathrm{d}t'} = -\frac{\partial \Phi}{\partial \mathbf{q}_i'} - \frac{1}{s}\frac{\mathrm{d}s}{\mathrm{d}t'}\mathbf{p}_i' \tag{2.112}$$

$$\frac{\mathrm{d}s'}{\mathrm{d}t'} = s'^2 \frac{p_s'}{Q} \tag{2.113}$$

$$\frac{\mathrm{d}p_s'}{\mathrm{d}t'} = \left(\sum_i \frac{\mathbf{p}_i'^2}{m_i} - gkT\right) \bigg/ s - \frac{1}{s}\frac{\mathrm{d}s}{\mathrm{d}t'} p' s. \tag{2.114}$$

Hoover pointed out that a new variable $\zeta = (1/s)\mathrm{d}s/\mathrm{d}t' = sp_s'/Q$ could be used, which could lead to the simplification of Equations 2.111, 2.112, 2.113 and 2.114. This new formalism is nowadays known as the Nosé-Hoover thermostat (Equations 2.115, 2.116, 2.117 and 2.118).[288]

$$\frac{\mathrm{d}\mathbf{q}_i'}{\mathrm{d}t'} = \frac{\mathbf{p}_\mathbf{i}'}{m_i} \tag{2.115}$$

$$\frac{\mathrm{d}\mathbf{p}_i'}{\mathrm{d}t'} = -\frac{\partial \Phi}{\partial \mathbf{q}_i'} - \zeta \mathbf{p}_i' \tag{2.116}$$

$$\frac{\mathrm{d}\ln s'}{\mathrm{d}t'} = \zeta \tag{2.117}$$

$$\frac{\mathrm{d}\zeta}{\mathrm{d}t'} = \left(\sum_i \frac{\mathbf{p}_i'^2}{m_i} - gkT\right)\Big/ Q. \tag{2.118}$$

2.6 Ab initio molecular dynamics

The molecular dynamics method is a very powerful computational technique to investigate many-body systems. The main question in any molecular dynamics scheme is how to describe the interatomic interactions. In classical molecular dynamics simulations these potentials are determined in advance, and the full interaction is broken up into many-body contributions, (electrostatic, non-electrostatic, short-range, long-range, bonded and non-bonded terms). However, this approach of using predefined interatomic potentials implies serious drawbacks since the parametrization of different interatomic interactions for chemically complex systems is a formidable task.[247]

The advent of *ab initio molecular dynamics* schemes enables simulations of complex systems without relying on any adjustable parameter. The main idea underlying the ab initio molecular dynamics method is based on the on-the-fly computation of forces by accurate electronic structure calculations. In general, the ab initio molecular dynamics concept can be employed in conjunction with any electronic structure method, however, DFT is nowadays the most commonly used electronic structure theory combined with molecular dynamics.[247, 289]

2.6.1 Born-Oppenheimer molecular dynamics

In Born-Oppenheimer molecular dynamics (BOMD), the static electronic structure problem is solved in each molecular dynamics step given the set of fixed classical point-particle nuclear positions at that instant of time.[247] In other words, the time-independent Schrödinger equation is solved for the electrons, concurrently to the propagation of nuclei via classical molecular dynamics.

The resulting BO molecular dynamics method is defined by:

$$M_I \ddot{\mathbf{R}}_I(t) = -\nabla_I \min_{\Psi_0(\mathbf{r};\mathbf{R})} \left\{ \langle \Psi_0(\mathbf{r};\mathbf{R}) | \hat{\mathcal{H}}_{el} | \Psi_0(\mathbf{r};\mathbf{R}) \rangle \right\} \tag{2.119}$$

However, from a first glance, solving Equation 2.119 looks like a formidable task. A standard method for the solution of ordinary differential equations in all molecular dynamics methods is the finite difference approach.

Given the molecular positions and velocities at time t, the positions and velocities at a later time $t + \Delta t$ are obtained, to a sufficient degree of accuracy. The choice of the time interval, Δt, also known as *timestep*, depends on the propagation algorithm, but usually it is determined by the fastest motion of the system. Many algorithms exist that apply the finite difference method. Perhaps the most widely used algorithm to integrate the equations of motion is the *Verlet algorithm*.[219]

Born-Oppenheimer molecular dynamics coupled with time-dependent density functional theory

BOMD can also be applied to dynamics in electronically excited states. In many cases, the response of a system to an external perturbation can be successfully studied within LR-TDDFT. More specifically, derivatives of excited state energies obtained within the LR-TDDFT provide nuclear gradients for molecular dynamics. In other words, the forces are computed as derivatives of the total energy of the excited state with respect to the nuclear positions.[247]

2.6.2 Car-Parrinello molecular dynamics

In 1985, Car and Parrinello introduced an elegant molecular dynamics scheme to cut down the computational expenses, in which the electronic degrees of freedom (described by one-electron wavefunctions) are also treated as fictitious classical variables.[290] The basic idea of the Car-Parrinello method lies in the quantum-mechanical adiabatic time scale separation of fast electronic and slow nuclear motions. The two-component quantum/classical problem is mapped onto a two-component classical problem with two separate energy scales at the expense of losing the physical time information of the quantum subsystem dynamics.[247]

The system basic equation of the Car-Parrinello method is given in terms of an extended Lagrangian, in which the electronic degrees of freedom have been added as classical variables.

$$\mathcal{L} = \sum_{l} \frac{1}{2}\mu \int d^3r \mid \dot{\psi}_l \mid^2 + \frac{1}{2} \sum_{I} M_I \mid \dot{\mathbf{R}}_I \mid^2 - E[\{\psi_l\}, \mathbf{R}_I] \qquad (2.120)$$

where l denotes the level number of the electronic states. The first two terms of Equation 2.120 are the kinetic energies of the electronic degrees of freedom and of the nuclei, respectively. The third term corresponds to the potential energy, which depends both on the electronic potential and the classical interaction between the nuclei. μ is the fictitious mass of the electronic degrees of freedom, which governs the motion of the wavefunctions.[289]

From the Lagrangian (Equation 2.120), the equation of motion for the wavefunctions can be derived (Equation 2.121).

$$\mu\frac{d^2}{dt^2}\psi_l = -\hat{\mathcal{H}}\psi_l + \sum_\nu \Lambda_{lv}\psi_\nu \tag{2.121}$$

where the Λ_{lv} are Langrange multipliers to ensure the orthogonality of the wavefunctions ψ_l.

In analogy to the nuclear degrees of freedom, μ determines the rate at which the electronic variables evolve in time, within an energetic width, which is always slightly above the electronic ground-state (the Born-Oppenheimer surface). More specifically, the ratio of M_I to μ characterizes the relative speed at which the electronic degrees of freedom propagate with respect to the nuclear positions. In particular, for $\mu \ll M_I$, the resulting dynamics is adiabatic, since the electronic degrees of freedom adjust instantaneously to the changes of the nuclear positions. However, in order to ensure the adiabatic energy-scale separation of the electronic and nuclear degrees of freedom, the highest frequency of the nuclear motion ω_I^{max} has to be well separated from the lowest frequency associated with the fictitious motion of the electronic degrees of freedom ω_e^{min}, *i.e.* ω_I^{max} has to be smaller than ω_e^{min}. The latter has been shown to behave like:

$$\omega_e \propto \sqrt{\frac{E_g}{\mu}} \tag{2.122}$$

where E_g is the energy gap. For systems with finite gap, the parameter μ can be tuned in such a way that $\omega_I^{max} \ll \omega_e^{min}$ and no energy transfer can take place between the electronic and nuclear subsystems. However, for metallic systems, special variations of the original Car-Parrinello method have to be adopted.[247, 289]

Nowadays, most of the current implementations of Car-Parrinello molecular dynamics use the original scheme based on DFT as electronic structure method. The system under study is treated within periodic boundary conditions[21] and the Kohn-Sham orbitals are expanded in a plane-wave basis set.

---

[21] Periodic boundary conditions are applied to overcome the problem of surface effects in molecular simulations. The simulation box, (which consists of the unit cell or a replicated unit cell), is replicated throughout space to form an infinite lattice. In the course of the simulation, the periodic image of each molecule moves exactly in the same way as the reference molecule in the simulation box. Hence, if a molecule leaves the simulation box, one image of it will enter through the opposite face.[219]

2.6.3 Restricted open-shell Kohn–Sham coupled with Car-Parrinello molecular dynamics

The restricted open-shell Kohn-Sham, (ROKS) method is an approximate scheme to treat the first non-degenerate excited single state in a Kohn-Sham-like fashion.[291] For the description of the wavefunction of a non-degenerate excited singlet state of a closed-shell system, at least a minimum of two determinants is necessary due to spin symmetry. To construct such a wavefunction, we consider a closed-shell system with $2n$ electrons assigned to n doubly occupied orbitals. The orbitals are taken to be spin-restricted, *i.e.* they have the same spatial part for both spin-up α and spin-down β electrons. Promotion of an electron from the HOMO to the LUMO leads to four different determinants. Two of these states are energetically degenerate triplets t, whereas the two other states are degenerate mixed-spin states m, that are not eigenfunctions of the total spin operator, $\hat{S}^2$. However, by inducing suitable Clebsch-Gordan projections of the mixed states another triplet state and the desired first excited singlet, S_1, states are obtained. Hence, the energy of the first excited singlet state can be calculated using the energies of the mixed and triplet states (Equation 2.123).

$$E_{S_1}^{ROKS}[\{\phi_i\}] = 2E_m^{KS}[\{\phi_i\}] - E_t^{KS}[\{\phi_i\}] \tag{2.123}$$

where

$$E_m^{KS}[\rho] = \mathcal{T}_s[\rho] + \mathcal{J}[\rho] + \int \mathcal{V}_{ext}(\mathbf{r})\rho(\mathbf{r})\mathrm{d}\mathbf{r} + \mathcal{E}_{xc}[\rho_m^\alpha, \rho_m^\beta] \tag{2.124}$$

and

$$E_t^{KS}[\rho] = \mathcal{T}_s[\rho] + \mathcal{J}[\rho] + \int \mathcal{V}_{ext}(\mathbf{r})\rho(\mathbf{r})\mathrm{d}\mathbf{r} + \mathcal{E}_{xc}[\rho_t^\alpha, \rho_t^\beta] \tag{2.125}$$

are expressed in terms of (restricted) Kohn-Sham spin-density functionals. $\mathcal{T}_s[\rho]$ is the kinetic energy, $\mathcal{J}[\rho]$ the Coulomb energy, $\mathcal{V}_{ext}(\mathbf{r})$ the external potential and $\mathcal{E}_{xc}[\rho^\alpha, \rho^\beta]$ the exchange-correlation energy calculated for spin densities ρ^α and ρ^β.[247, 291]

Having defined a density functional for the first excited singlet state, the corresponding Kohn-Sham equations can be obtained by varying the Equation 2.123 subject to the orthonormality constraint. This procedure leads to two sets of equations, one for the doubly occupied orbitals (Equation 2.126),

$$\begin{aligned}\Big\{ -\frac{1}{2}\nabla^2 + \int \frac{\rho(\mathbf{r}')}{\mid \mathbf{r}' - \mathbf{r} \mid}\mathrm{d}\mathbf{r}' + \mathcal{V}_{ext}(\mathbf{r}) + \frac{\delta E_{xc}[\rho_m^\alpha, \rho_m^\beta]}{\delta \rho^\alpha} \\ + \frac{\delta E_{xc}[\rho_m^\alpha, \rho_m^\beta]}{\delta \rho^\beta} - \frac{1}{2}\frac{\delta E_{xc}[\rho_t^\alpha, \rho_t^\beta]}{\delta \rho^\alpha} - \frac{1}{2}\frac{\delta E_{xc}[\rho_t^\alpha, \rho_t^\beta]}{\delta \rho^\beta}\Big\}\psi_i(\mathbf{r}) \\ = \sum_{j=1}^{n+1} \epsilon_{ij}\psi_j(\mathbf{r})\end{aligned} \tag{2.126}$$

and the second one for two singly occupied open-shell orbitals, ψ_α and ψ_β, respectively (Equations 2.127, 2.128).

$$\begin{aligned}\Big\{\frac{1}{2}\Big[-\frac{1}{2}\nabla^2 + \int \frac{\rho(\mathbf{r}')}{\mid \mathbf{r}' - \mathbf{r} \mid}\mathrm{d}\mathbf{r}' + \mathcal{V}_{ext}(\mathbf{r})\Big] \\ + \frac{\delta E_{xc}[\rho_m^\alpha, \rho_m^\beta]}{\delta \rho^\alpha} - \frac{1}{2}\frac{\delta E_{xc}[\rho_t^\alpha, \rho_t^\beta]}{\delta \rho^\alpha}\Big\}\psi_\alpha(\mathbf{r}) \\ = \sum_{j=1}^{n+1} \epsilon_{\alpha j}\psi_j(\mathbf{r})\end{aligned} \tag{2.127}$$

$$\begin{aligned}\Big\{\frac{1}{2}\Big[-\frac{1}{2}\nabla^2 + \int \frac{\rho(\mathbf{r}')}{\mid \mathbf{r}' - \mathbf{r} \mid}\mathrm{d}\mathbf{r}' + \mathcal{V}_{ext}(\mathbf{r})\Big] \\ + \frac{\delta E_{xc}[\rho_m^\alpha, \rho_m^\beta]}{\delta \rho^\beta} - \frac{1}{2}\frac{\delta E_{xc}[\rho_t^\alpha, \rho_t^\beta]}{\delta \rho^\beta}\Big\}\psi_\beta(\mathbf{r}) \\ = \sum_{j=1}^{n+1} \epsilon_{\beta j}\psi_j(\mathbf{r})\end{aligned} \tag{2.128}$$

The set of Equations 2.126, 2.127 and 2.128 could be solved following two different procedures. Either by diagonalization of the corresponding ROKS Hamiltonian or by direct minimization of the associated total energy functional. However, in plane wave codes, the procedure of direct minimization is preferred. Finally, the Car-Parrinello propagation scheme can be used, once an initial set of singly and doubly occupied ROKS orbitals with the proper symmetry has been determined.[247]

Chapter 3

Entropic stabilization of mixed A-cation ABX$_3$ metal halide perovskites for high performance perovskite solar cells

Chapter 3 is a post-print version of an article published as:

Chenyi Yi, Jingshan Luo, Simone Meloni, **Ariadni Boziki**, Negar Ashari-Astani, Carole Grätzel, Shaik M Zakeeruddin, Ursula Rothlisberger, and Michael Grätzel. Entropic stabilization of mixed A-cation ABX$_3$ metal halide perovskites for high performance perovskite solar cells. Energy & Environmental Science, 9(2):656-662, 2016.

My contribution: Performance of DFT calculations for the estimation of the internal energy, the mixing entropy contribution, the free energy and the density of states of the pure and the mixed compounds, respectively.

3.1 Abstract

ABX_3-type organic lead halide perovskites currently attract broad attention as light harvesters for solar cells due to their high PCE. Mixtures of formamidinium with methylammonium as A-cations show currently the best performance. Apart from offering better solar light harvesting in the near IR the addition of methylammonium stabilizes the perovskite phase of $FAPbI_3$ which in pure form at room temperature converts to the yellow photovoltaically inactive δ-phase. We observe a similar phenomenon upon adding Cs^+ cations to $FAPbI_3$. $CsPbI_3$ and $FAPbI_3$ both form the undesirable yellow phase under ambient condition while the mixture forms the desired black perovskite. Solar cells employing the composition $Cs_{0.2}FA_{0.8}PbI_{2.84}Br_{0.16}$ yield high average PCEs of over 17% exhibiting negligible hysteresis and excellent long term stability in ambient air. We elucidate here this remarkable behavior using first principle computations. These show that the remarkable stabilization of the perovskite phase by mixing the A-cations stems from entropic gains and the small internal energy input required for the formation of their solid solution. By contrast, the energy of formation of the delta-phase containing mixed cations is too large to be compensated by this configurational entropy increase. Our calculations reveal for the first time the optoelectronic properties of such mixed A-cation perovskites and the underlying reasons for their excellent performance and high stability.

3.2 Introduction

Organic inorganic hybrid metal halide perovskites have been under intense investigation following their initial use as light harvesting pigments in dye-sensitized solar cells.[60–62, 292] When using optimized fabrication procedures judiciously chosen perovskite formulations exhibit broad absorption spectra with sharp edges in the near infrared making them excellent light harvesters that demonstrate properties as either n- or p-type semiconductors with close to optimal band gaps for solar energy conversion. These favorable characteristics coupled with long carrier diffusion lengths and the feasibility of their fabrication by solution processing, leading to low production costs, make them excellent candidates as opto-electronic materials.[63, 65, 67, 156, 198, 293–300] Methylammonium lead iodide has been the most widely studied ABX_3 (where A is the organic (or inorganic) cation, B is the divalent metal cation and X the halide anion) structured perovskite material up until now. However, it decomposes rapidly at higher temperatures exhibiting discoloration after heating at 150 °C for 30 minutes in the air.[144] Formamidinium lead iodide has emerged as a promising candidate for use in perovskite solar cells (PSCs), primarily due to its absorption spectrum that extends further into the red than that of $MAPbI_3$, potentially leading to higher current densities.[144, 184, 301] Moreover, $FAPbI_3$ is more resistant to heat stress than $MAPbI_3$ although both show degradation in ambient air at relative humidities approaching 100%.[144] However, the black perovskite phase of pure $FAPbI_3$, is thermodynamically stable only above 160 °C,[297] forming a yellow δ phase below the phase transition temperature. To stabilize the perovskite phase of $FAPbI_3$ at room temperature, $MAPbI_3$ has been added to produce mixed cation perovskite solar cells.[184] These mixed $(MAPbX_3)_x(FAPbI_3)_{1-x}$ perovskites were utilized in the fabrication of solar cells and exhibit the highest power conversion efficiencies to date with certified values exceeding 20%.[184, 296, 297] However, the mixed $(MAPbX_3)_x(FAPbI_3)_{1-x}$ perovskite is also prone to decomposition under heat stress, due to the presence of $MAPbX_3$. Hence it is of great importance to develop a perovskite structure that is stable at both low and high temperature ranges.

Purely inorganic perovskites of the general formula, $CsPbX_3$, such as $CsPbI_3$ and $CsPbBr_3$, are drawing attention for use as luminescent materials and in high-energy radiation detectors.[302–306] Perovskite solar cells utilizing $CsPbBr_3$ have exhibited excellent thermal stability with high photovoltages.[307] However, the current is still low due to the wide band gap (2.36 eV) of the light absorber. The perovskite phase of $CsPbI_3$ has a narrower band gap (1.73 eV) than $CsPbBr_3$; however, the perovskite phase of $CsPbI_3$ is only stable at high temperature, converting to the yellow (δ) phase under room temperature conditions.[308] In fact, the first-order reversible phase transition of $CsPbI_3$ from a yellow orthorhombic phase to a dark cubic perovskite phase takes place at 327 °C[148, 305] preventing its use in practical applications such as solar cells. Cesium doped $MAPbI_3$ perovskites, were likewise employed in solar cells, demonstrating higher voltages than pure $MAPbI_3$. However, the best reported PCE of the cesium doped $MAPbI_3$ perovskite is 7.68%.[309]

Here we present a $MAPbX_3$-free mixed cation perovskite, $Cs_xFA_{(1-x)}PbX_3$, as an attractive material for perovskite solar cells exhibiting both high efficiencies and good thermal stability. Although both $FAPbI_3$ and $CsPbI_3$ 3D perovskite phases are unstable at room temperature, room temperature stable $Cs_{0.2}FA_{0.8}PbI_3$ perovskite is formed by adding 20% $CsPbI_3$ into $FAPbI_3$. The film darkens immediately upon the adjunction of the anti-solvent chlorobenzene at room temperature. Moreover, the new perovskite is also stable at higher temperatures. Here we elucidate, for the first time, this remarkable behavior using first principle computations. Our theoretical analysis includes band structure calculations that explain the effect of cation and anion mixing on the opto-electronic properties of the materials. We fabricate mixed cation perovskite solar cells with a high PCE, the average being above 15%, exceeding the efficiency reached with pure $FAPbI_3$ perovskite. The mixed cation perovskite shows good stability with no discernible decrease in efficiency of unsealed solar cells following a time lapse of 1000 h under ambient conditions in the dark. We note that our experimental results agree with those of a very recent study that appeared during the final preparation of our manuscript that investigates similar mixed cation perovskite solar cells.[310] We find that the PCE can be further improved up to 18% by replacing a small fraction of the iodide in the mixed cation perovskite with bromide anions.

3.3 Results and discussion

We produced the perovskite film by spin coating a $Cs_xFA_{1-x}PbX_3$ solution on a mesoporous TiO_2 film. The precursor solution is made by dissolving CsI, formamidinium iodide and formamidinium bromide (for mixed halide devices) with PbI_2 in a mixture of DMF and DMSO. At the last stage of the spin coating, the film is treated with chlorobenzene, as antisolvent, to improve the perovskite crystallization. Following spin coating, the film is annealed at 100 °C for 30 minutes. Perovskite films produced in this manner turn dark immediately after spin coating and subsequent heating, suggesting the formation of the black perovskite (versus δ) phase of the $Cs_{0.2}FA_{0.8}PbI_3$. On the contrary, a spin-coated film of $FAPbI_3$ remains yellow in color even after heating at 100 °C for more than 30 minutes, darkening only at temperatures of 150 °C and above.

The effects of the added Cs and Br on the absorption properties of the $FAPbI_3$ perovskite have been examined by using UV-vis absorption. The absorption spectra (Figure 3.1a) indicate a slight blue shift of 5 nm upon increasing the ratio of Cs in $Cs_xFA_{(1-x)}PbI_3$ from 0 to 0.4, in good agreement with theoretical calculations, suggesting only a minor effect of Cs on the band gap of the perovskite. On the contrary, a significant blue shift from 785 nm to 735 nm is observed when increasing the content of Br added into the perovskite structure, from $Cs_{0.2}FA_{0.8}PbI_3$ to $Cs_{0.2}FA_{0.8}PbI_{2.6}Br_{0.4}$, as shown in Figure 3.1b. This observation indicates that the band gap augments with increasing concentration of Br in the organic-inorganic hybrid lead iodide/bromide perovskites, confirming our theoretical calculations. Although the blue spectral shift decreases the maximum theoretical photocurrent density of the device, it is possible to obtain higher voltages when using the larger band gap absorption materials. Photoluminescence spectra, Figure 3.1c, show a similar trend of blue shift of emission maximum from 806 nm to 772 nm by increasing the Br concentration from $Cs_{0.2}FA_{0.8}PbI_3$ to $Cs_{0.2}FA_{0.8}PbI_{2.6}Br_{0.4}$. By contrast, increasing the Cs concentration from 0 to 0.4 for $Cs_xFA_{(1-x)}PbI_3$ shifts the emission spectra towards the blue by only a few nm. Figure 3.1d shows the intersection point of absorption and emission spectra of $Cs_{0.2}FA_{0.8}PbI_3$ and $Cs_{0.2}FA_{0.8}PbI_{2.84}Br_{0.16}$ are at 792 nm and 782 nm respectively, corresponding to band gaps of 1.56 eV and 1.58 eV.

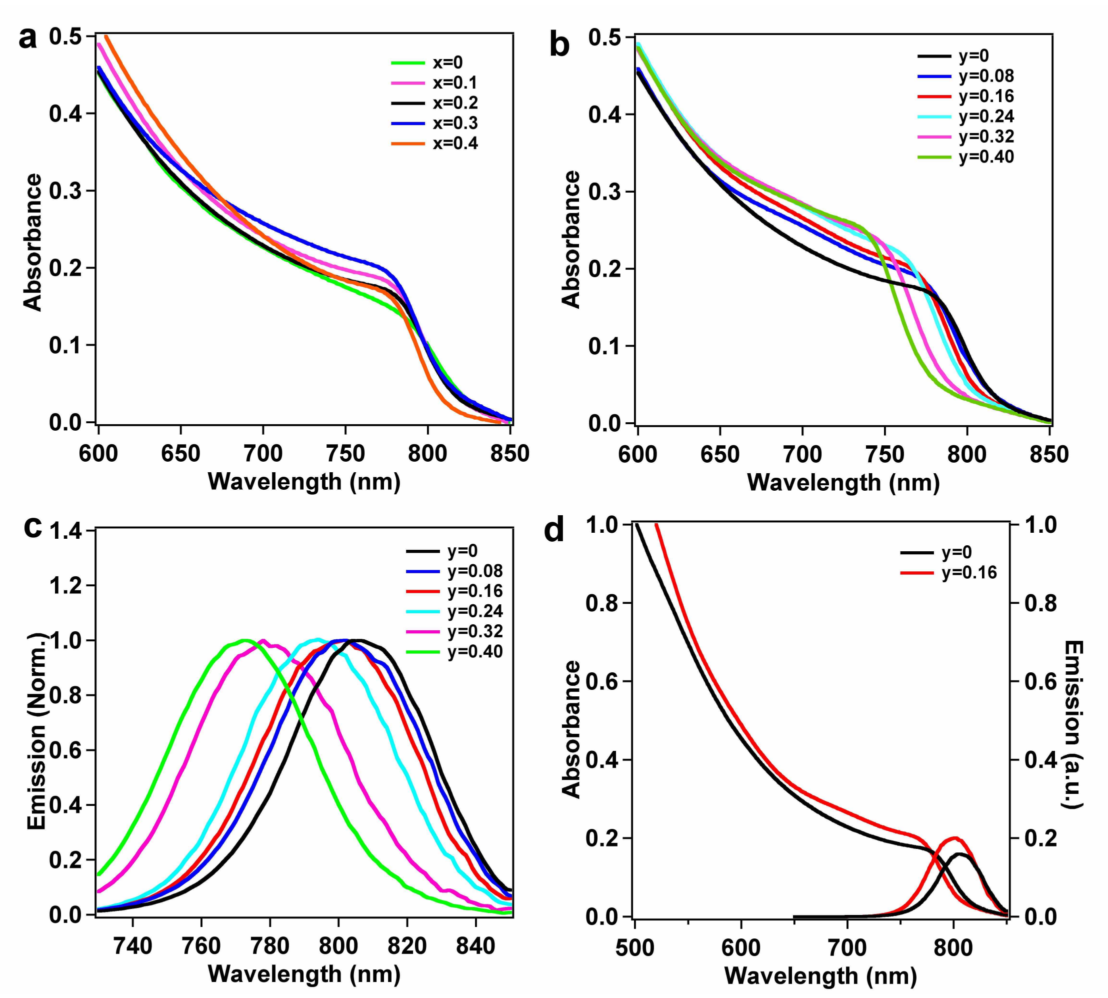

Figure 3.1: Photophysical properties of $Cs_xFA_{(1-x)}PbI_3$ and $Cs_{0.2}FA_{0.8}PbI_{(3-y)}Br_y$. (a) UV-vis spectra of mixed A cation perovskites of different mixing ratios $Cs_xFA_{(1-x)}PbI_3$. (b) Effect of substitution of iodide by bromide on the UV-vis spectra of $Cs_{0.2}FA_{0.8}PbI_{(3-y)}Br_y$. (c) Normalized photoluminescence spectra of $Cs_{0.2}FA_{0.8}PbI_{(3-y)}Br_y$. (d) Absorption and emission spectra of $Cs_{0.2}FA_{0.8}PbI_3$ (black) and $Cs_{0.2}FA_{0.8}PbI_{2.84}Br_{0.16}$ (red).

Differential scanning calorimetry (DSC) was employed to investigate the thermal behavior of the mixed perovskites. Figure B.1 shows the DSC scans of the perovskites from 20 °C to 250 °C under nitrogen gas atmosphere. Neither of the mixed perovskites, $Cs_{0.2}FA_{0.8}PbI_3$ and $Cs_{0.2}FA_{0.8}PbI_{2.84}Br_{0.16}$, shows any peaks, indicating that the perovskite phase of this type of mixed perovskites is stable over the investigated temperature range. On the contrary, the pure $FAPbI_3$ exhibits a peak at 156 °C, indicating a phase transition of $FAPbI_3$ from the yellow δ phase to the perovskite structure at this temperature. This finding is consistent with the color change of the $FAPbI_3$ film from yellow to black at around 150 °C. The thermal stability of the mixed perovskites was investigated by heating the film at 150 °C in ambient air. Whereas $Cs_{0.2}FA_{0.8}PbI_3$ and $Cs_{0.2}FA_{0.8}PbI_{2.84}Br_{0.16}$ are stable, showing no discoloration, the $MAPbI_3$ color changes from dark-brown to yellow after 60 minutes. The $(MAPbBr_3)_{0.15}(FAPbI_3)_{0.85}$ perovskite likewise discolors following 60 minutes heating.

Figure 3.2a shows the XRD spectra of the $Cs_xFA_{(1-x)}PbI_3$ and that of $FAPbI_3$ annealed at 150 °C. Annealing produces the trigonal perovskite phase of $FAPbI_3$. However, the intense peak at 11.7 degrees indicates that the hexagonal non-perovskite δ phase still exists after the heat treatment in agreement with previous work.[297] The peak at 12.7 degrees corresponds to the hexagonal phase of PbI_2. Remarkably, when 10% Cs was added to the $FAPbI_3$, the formation temperature of the perovskite phase decreased sharply allowing the formation of the trigonal perovskite phase to occur already at room temperature. This suggests that the introduction of Cs thermodynamically favors the formation of the perovskite phase, bringing the system into a new equilibrium state. This supposition will be substantiated below by theoretical analysis. Increasing the Cs^+ content beyond 10% does not seem to impact the formation of the perovskite phase. However, when its concentration reaches 40% or above, the peaks at 25.4 and 28.1 degrees become more visible and split into two, due to the larger distortion of the perovskite lattice, in good agreement with the theoretical calculations (Figure B.3). We substituted a small fraction of iodide by bromide in the perovskite lattice to further boost the efficiency.[297] No changes in the phase of the film occurred upon increasing the Br concentration. Even for the formulation with the highest concentration of Br of 13 mol% ($Cs_{0.2}FA_{0.8}PbI_{2.6}Br_{0.4}$) employed here, the film still remained in the trigonal perovskite phase, in agreement with previous studies showing that iodine rich perovskites remain in the trigonal phase, while Br rich ones form the cubic phase.[91, 144]

The Pb 4f core level signals for different samples are shown in Figure B.2. The $Cs_{0.2}FA_{0.8}PbI_3$ sample exhibits two dominant peaks located at 137.1 eV and 141.9 eV, corresponding to the Pb $4f_{7/2}$ and Pb $4f_{5/2}$ level, respectively, indicating a spin-orbit splitting of 4.8 eV. The small satellites at low binding energy are, according to previous reports,[311] due to metallic lead. After Br doping, the Pb^{2+} lines show a 0.3 eV binding energy shift to a higher energy level, which could be attributed to the fact that Pb 6s orbitals have a larger overlap

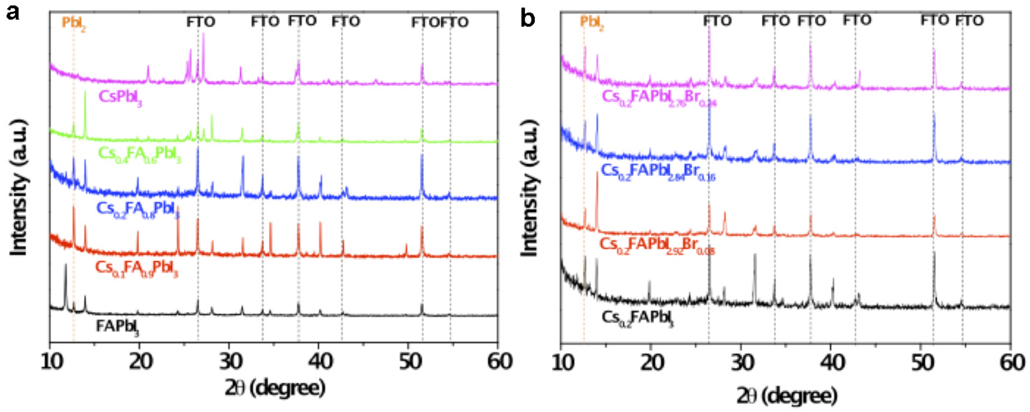

Figure 3.2: (a) XRD spectra of $FAPbI_3$, $CsPbI_3$ and the $Cs_xFA_{(1-x)}PbI_3$. (b) Effect of iodide substitution by bromide on the XRD spectra of $Cs_{0.2}FA_{0.8}PbI_{(3-y)}Br_y$.

with the p-orbitals of iodide than bromide. All samples show strong signals from I 3d and Cs 3d core levels, and their peaks do not show any apparent shift when Br is incorporated into the structure. For the I 3d core level, following Br doping, the intensity of peaks decreased, concomitant with the decrease of I concentration in the sample. Pure $Cs_{0.2}FA_{0.8}PbI_3$ has no signal in the region of the Br core level. After incorporation of Br, the peaks assigned to Br 3d become visible, and the intensity increases as expected as a function of the Br concentration.

The morphology of the film has been investigated by scanning electron microscopy (SEM). Figure 3.3a shows the cross-sectional SEM image of the perovskite solar cell device. From bottom to top, the device consists of successive layers of FTO, compact TiO_2, mesoporous TiO_2/perovskite composite, perovskite capping layer, spiro-OMeTAD hole transporting material (HTM) and gold (Au) as counter electrode. The perovskite capping layer lies in a homogenous layer on top of the mesoporous TiO_2/perovskite composite, separating the HTM from possible contact with TiO_2. This conformal capping layer helps prevent charge recombination between the HTM and the electron transporter, TiO_2. Figure 3.3b shows the top view SEM image of the $Cs_{0.2}FA_{0.8}PbI_3$ perovskite film. It indicates a branchlike structural morphology of the perovskite crystal grains with good surface coverage. As observed in the top view SEM image of $Cs_{0.2}FA_{0.8}PbI_{2.84}Br_{0.16}$, Figure 3.3c, its morphology is similar to that of $Cs_{0.2}FA_{0.8}PbI_3$. Both the pure iodide and bromide containing perovskites' uniform and compact layer formation on the mesoporous TiO_2 are consistent with the cross-sectional SEM results.

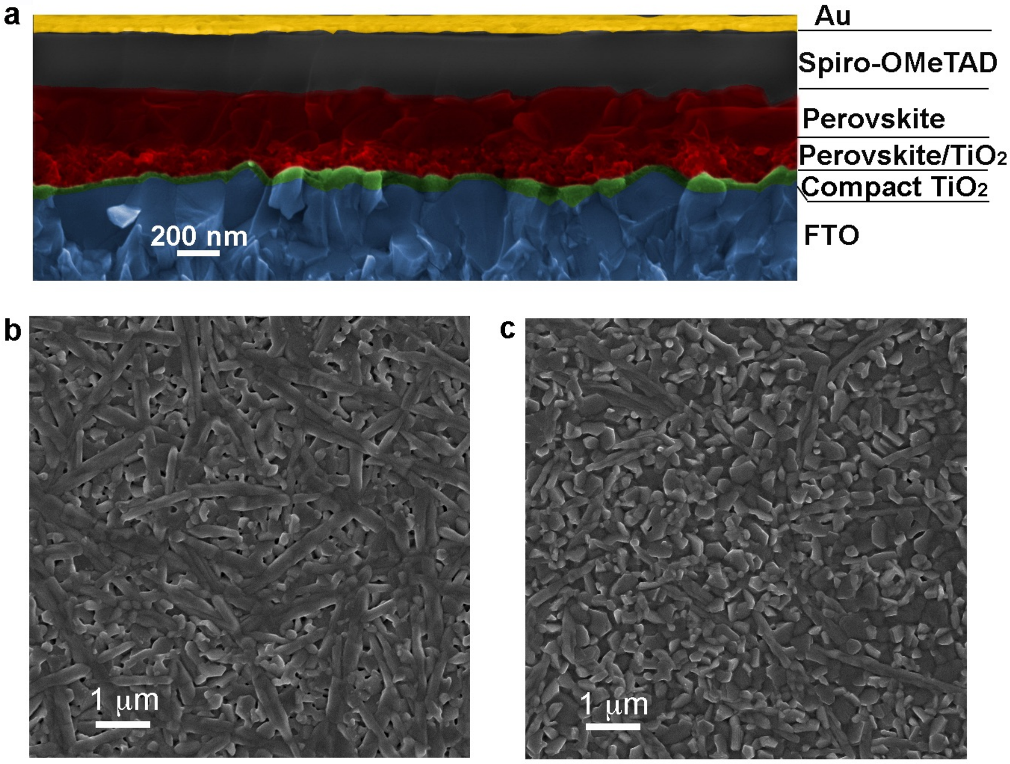

Figure 3.3: (a) Cross-sectional SEM image of a complete photovoltaic device. (b) Top-view SEM image of the $Cs_{0.2}FA_{0.8}PbI_3$ perovskite. (c) Top-view SEM image of the $Cs_{0.2}FA_{0.8}PbI_{2.84}Br_{0.16}$ perovskite.

A high-resolution transmission electron microscopy (TEM) image, Figure B.4, shows periodically aligned parallel lines resulting from the crystalline planes, indicating the high level of crystallinity of the perovskite granular structure. A high-angle annular dark-field scanning transmission electron microscopy (HAADF-STEM) image, Figure 3.4, illustrates the morphology of the perovskite grains, which was analyzed by scanning transmission electron microscopy energy dispersive spectroscopy (STEM-EDS). The STEM-EDS mapping of Cs, Pb, I, Br exhibits a similar pattern compared to the image of HAADF-STEM. These findings signify that the elements Cs, Pb, I, Br are homogeneously distributed within the perovskite crystals, suggesting that the Cs and Br are uniformly incorporated into the $FAPbI_3$ in the perovskite grain rather than existing in separate chemical phases.

We find that the remarkable stabilization of the perovskite over the non-perovskite δ phase upon Cs/FA mixing can be rationalized with simple structural and thermodynamic arguments. The δ phases of $FAPbI_3$ and $CsPbI_3$ differ sig-

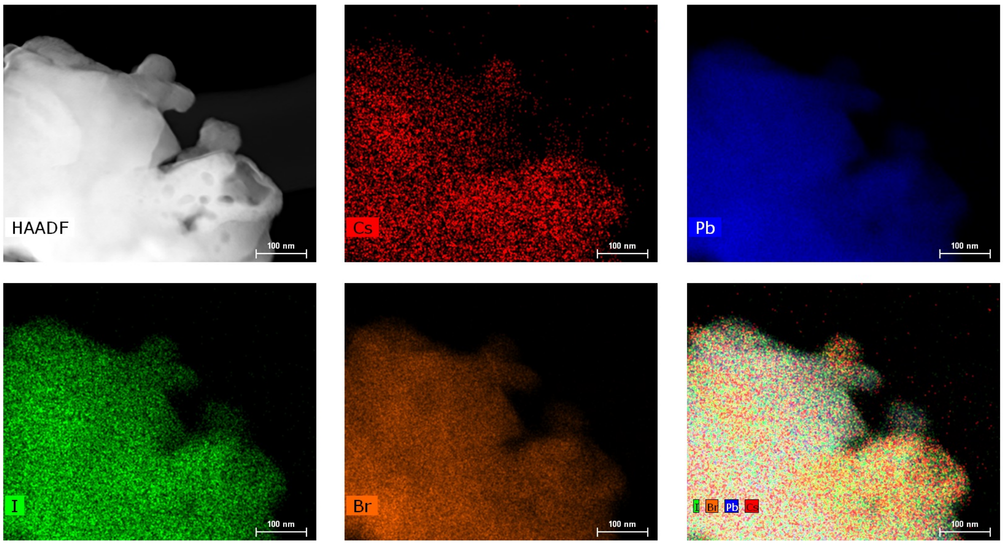

Figure 3.4: HAADF and TEM-EDS image of $Cs_{0.2}FA_{0.8}PbI_{2.84}Br_{0.16}$.

nificantly in their atomistic structure. In the case of the $FAPbI_3$, the δ phase consists of 1D pillars made of face sharing PbI_6 octahedra (Figure 3.5a). These pillars, aligned along the crystallographic c direction, are separated by domains containing only FA. The δ-$CsPbI_3$ crystal is also made of 1D PbI_3 pillars surrounded by the cation, Cs^+ in this case, but these pillars consist of stacked and shifted edge sharing PbI_6 octahedra (Figure 3.5b). Another significant difference is the volume per stoichiometric unit of the two systems: ($V_{\delta-FAPbI_3} \sim 256$ Å^3 vs $V_{\delta-CsPbI_3} \sim 222$ Å^3).[91] On the contrary, the α and β perovskite $FAPbI_3$ phases (Figures 3.5c and 3.5d) are very similar to the perovskite phase of $CsPbI_3$ (Figure 3.5e), and the volume per stoichiometric unit of the three crystals is also very close ($V_{\alpha-FAPbI_3} \sim 256$ Å^3 and $V_{\beta-FAPbI_3} \sim 249$ Å^3 vs $V_{\alpha-CsPbI_3} \sim 250$ Å^3).[91, 308] This suggests that cation mixing in the δ phase is energetically highly unfavorable, while it is more favorable for the perovskite α and β phases. According to this hypothesis, in the δ phase the unfavorable energetic contribution due to mixing is too large to be compensated by the mixing entropy. On the contrary, in the α and β perovskite phases the sum of the energy and mixing entropy contribution leads to a reduction of the free energy, resulting in a stabilization of the mixed 3D perovskite over the δ phase. Since Cs and FA are mixed in solution, thanks to the stability enhancement the perovskite phase forms directly, before the separated δ-phases can prevent mixing. This hypothesis is confirmed by the results shown in Figure 3.5f where the energy and mixing entropy contributions to the free energy, together with their sum, are plotted as a function of the Cs content, in the compounds comprising $Cs_xFA_{(1-x)}PbI_3$ in their α, β, and δ phases.

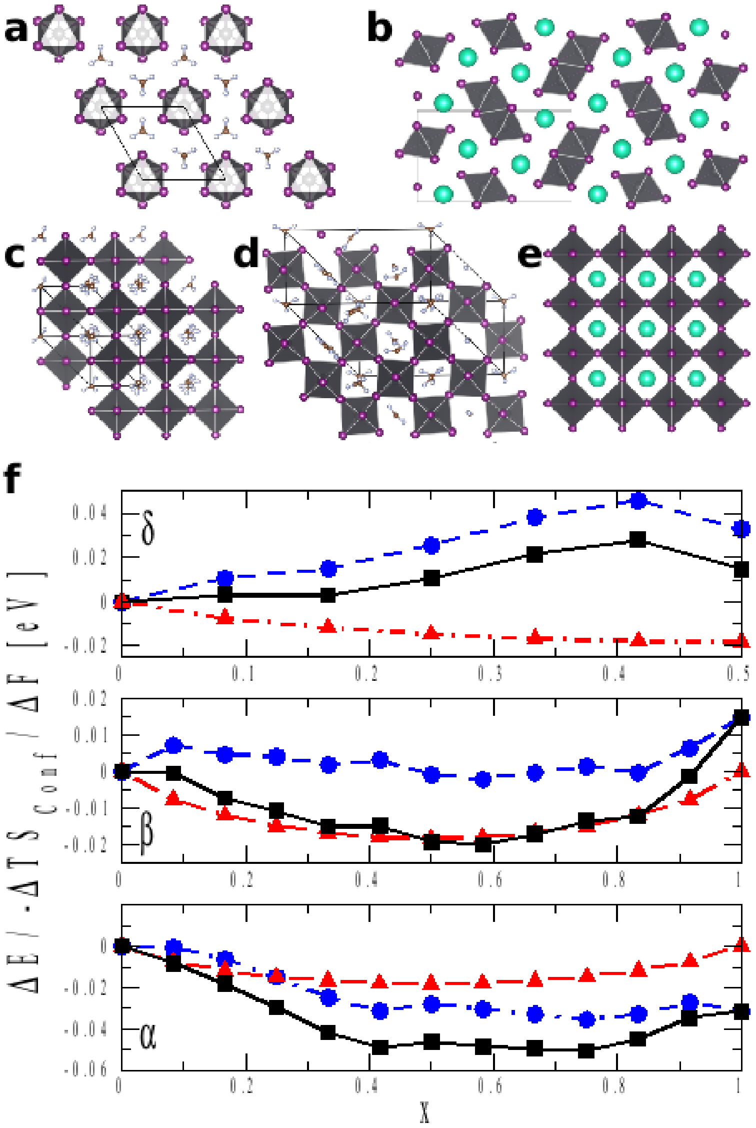

Figure 3.5: Various phases of $FAPbI_3$ and $CsPbI_3$ and variation of internal energy of mixed $Cs_xFA_{(1-x)}PbI_3$ in different phases. (a and b) Represent the δ phase in the FA and Cs perovskites, respectively; (c and d) show the α and β $FAPbI_3$, respectively. (e) Shows the cubic phase of the $CsPbI_3$ structure. (f) Variation of internal energy, ΔE (dashed blue line), mixing entropy contribution, $-T\Delta S$ (dot-red dashed line), and free energy, $\Delta F = \Delta E - T\Delta S$ (black continuous line) as a function of Cs content.

Analysis of the energetics in the δ phase shows that replacement of the organic cation FA^+ by the inorganic cation Cs^+ leads to a significant destabilization (energy increase) with respect to the two pure FA and/or $CsPbI_3$ δ phases, $\Delta E_{\delta-Cs_xFA_{(1-x)}PbI_3} = E_{\delta-Cs_xFA_{(1-x)}PbI_3} - (xE_{\delta-CsPbI_3} + (1-x)E_{\delta-FAPbI_3})$. The mixing entropy contribution to the free energy, $T\Delta S_{\delta-Cs_xFA_{(1-x)}PbI_3} = k_BT[x\ln x + (1-x)\ln(1-x)]$, does not compensate this energetic penalty and, as hypothesized above, cation mixing cannot take place in the δ phase. On the contrary, for the perovskite phases, either the α and β types, the sum of the energetic and mixing entropy contributions to the free energy is favorable, resulting in a stabilization of the mixed phases (see Appendix B for more details). This stabilization is of the order of 0.05 eV ($\sim 2\ k_BT$ at room temperature) and 0.02 eV ($\sim 0.8\ k_BT$) per stoichiometric unit for the α and β phase, respectively. Within this simple model, the $\delta \rightarrow \alpha$ or β transition temperature is reduced by ~200-300 K when going from the pure $FAPbI_3$ to the mixed $Cs_xFA_{(1-x)}PbI_3$ system, which explains why the perovskite phase is stable at room temperature for the mixed compound. The increase of compound stability upon mixing may also account for the observed resistance towards decomposition at higher temperatures of mixed cation perovskites.

Figure 3.5f shows that the maximum stabilization is achieved at 40-60% Cs content. However, this might not be the best composition to maximize the efficiency of the solar cell. Thus, in the following we investigate how A-cation mixing affects the electronic properties of perovskites. Cation mixing alters the electronic structure of the perovskite in two ways. First, it leads to a slight widening of the band gap (Figure B.6), which is blue-shifted by ~ 15 nm in the case of β-$Cs_{0.25}FA_{0.75}PbI_3$, in good agreement with the experimental results. This shift arises from the distortion of the PbI_3 lattice upon mixing, with the average Pb-I-Pb angle passing from 167° in the pure β FA-perovskite to 164.5° at ~25% Cs mixing (more details are given in the Appendix B). The distortion of the lattice reduces the p-I/s-Pb antibonding overlap of the VBM, (Figure B.7), resulting in a reduction of its energy and an increase of the band gap. A second effect of cation mixing is an increase of the density of states (DOS) in the region up to 0.5 eV below the VBM, which is consistent with the observed increase of the incident-photon-to-current conversion efficiency (IPCE). Summarizing, concerning the electronic and optical properties, the optimal Cs content is the result of a trade-off between the opposing effects of the Cs concentration on the band structure, *i.e.*, the widening of the band gap and the increase of the DOS in the sub-VBM region.

Replacement of iodide with a limited amount of bromide in mixed Cs/FA perovskites, is thermodynamically favored for both the α and β phases (Figure B.8). The band structure of β-$Cs_{0.25}FA_{0.75}PbI_{(3-y)}Br_y$ is shown in Figure B.9.

The main effect of substituting iodide by bromide on the perovskite lattice is a widening of the band gap consistent with the observed blue shift of the absorption edge (*vide infra*). This increase of the band gap is due to a decrease of the antibonding overlap between the X-np (X=Br or I) and Pb-6s orbitals with respect to the pure iodide perovskite. There are two reasons for this effect. On the one hand, the different size of I and Br ions further distorts the $\mathrm{PbI}_{(3-y)}\mathrm{Br}_y$ framework, resulting in a reduction of the Pb-6s/I-5p overlap (Figure B.11). Moreover, the more compact Br-4p orbital has a limited antibonding overlap with the Pb-6s in the inorganic framework that, at the compositions investigated, has a size that is still close to that of the corresponding iodide perovskite.

The photovoltaic properties of the perovskites were ascertained by measuring the current-voltage ($J-V$) curves and by evaluating the devices' corresponding IPCE spectra. The representative $J-V$ curves and their corresponding photovoltaic parameters are illustrated in Figure 3.6 and tabulated in Table 3.1, respectively. The device fabricated by pure $\mathrm{FAPbI_3}$ perovskite films gives a PCE of 10.4% with V_{oc} of 809 mV, J_{sc} of 21.4 mA cm^{-2} and a FF of 59.2%. Following incorporation of Cs, the mixed cation perovskite $\mathrm{Cs_{0.2}FA_{0.8}PbI_3}$ device yields an enhanced PCE (compared to pure $\mathrm{FAPbI_3}$) of 15.69%, with photovoltaic parameters of V_{oc} = 1017 mV, J_{sc} = 21.5 mA cm^{-2} and FF = 70.1%. Substituting 5% of the iodide in the mixed cation perovskite by bromide yielding the $\mathrm{Cs_{0.2}FA_{0.8}PbI_{2.84}Br_{0.16}}$, improves the PCE further to a value of 17.35%, with V_{oc} = 1073 mV, J_{sc} = 21.9 mA cm^{-2} and a FF of 74.2%. The champion cell shows an overall PCE of 18.02%, with a V_{oc} of 1072 mV, a J_{sc} of 23.3 mA cm^{-2} and a FF of 72.3%. Moreover, preliminary stability tests show that the device based on $\mathrm{Cs_{0.2}FA_{0.8}PbI_3}$ is much more stable than $\mathrm{FAPbI_3}$ under ambient conditions when kept unsealed in the dark. The device based on $\mathrm{Cs_{0.2}FA_{0.8}PbI_3}$ (Figure B.10) shows no performance decrease within 1000 h. The bromide doped perovskite's performance Figure 3.6c matches that of the pure iodide mixed cation perovskite. On the contrary, perovskite solar cell based on pure $\mathrm{FAPbI_3}$ degrades within 48 h under the same conditions. As shown in Figure 3.6b, the onset of the IPCE spectra for the $\mathrm{Cs_{0.2}FA_{0.8}PbI_3}$ device is at 860 nm and that for the $\mathrm{Cs_{0.2}FA_{0.8}PbI_{2.84}Br_{0.16}}$ device is at 830 nm, agreeing well with the UV-vis spectra. On the other hand a somewhat higher overall IPCE value is observed for the $\mathrm{Cs_{0.2}FA_{0.8}PbI_{2.84}Br_{0.16}}$ device compared to the pure iodide device, probably due to its higher absorbance and longer carrier diffusion length.[295] The integrated current densities calculated from the IPCE spectra agree well with the corresponding measured photocurrent densities, indicating that the emission of our solar simulator matches well the spectrum of standard air mass 1.5 solar light.

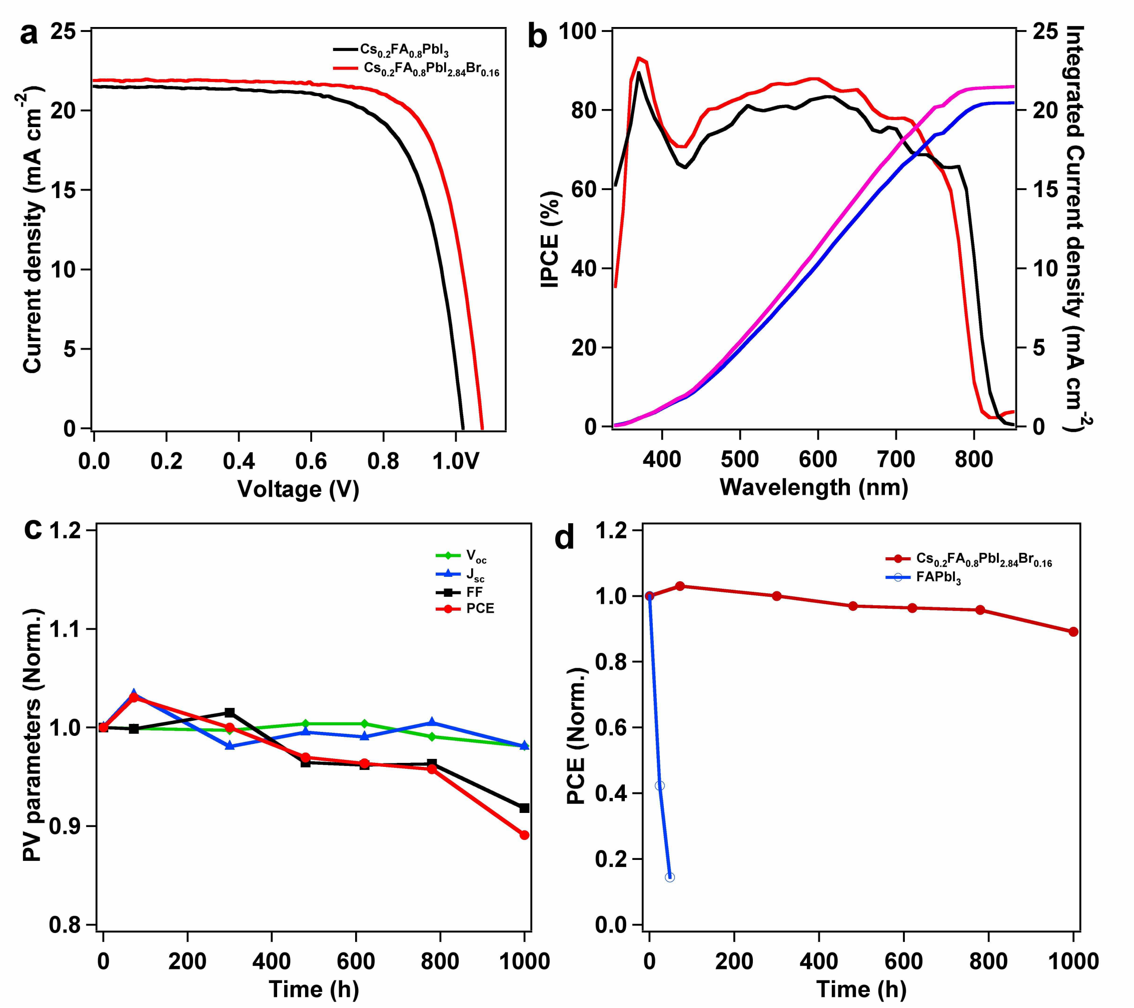

Figure 3.6: Photovoltaic properties of $Cs_{0.2}FA_{0.8}PbI_3$ and $Cs_{0.2}FA_{0.8}PbI_{2.84}Br_{0.16}$ perovskite solar cells. (a) $J-V$ curves of the $Cs_{0.2}FA_{0.8}PbI_3$ and $Cs_{0.2}FA_{0.8}PbI_{2.84}Br_{0.16}$ perovskite solar cells. (b) IPCE spectra of the $Cs_{0.2}FA_{0.8}PbI_3$ (black) and $Cs_{0.2}FA_{0.8}PbI_{2.84}Br_{0.16}$ (red) perovskite solar cells and their integrated currents $Cs_{0.2}FA_{0.8}PbI_3$ (blue) and $Cs_{0.2}FA_{0.8}PbI_{2.84}Br_{0.16}$ (purple). (c) Evolution of the photovoltaic parameters with time for the $Cs_{0.2}FA_{0.8}PbI_{2.84}Br_{0.16}$ perovskite solar cells. The unsealed solar cells were kept under ambient conditions in the dark and the performances were re-evaluated at periodic intervals. (d) Comparison of the stability of $Cs_{0.2}FA_{0.8}PbI_{2.84}Br_{0.16}$ and $FAPbI_3$ perovskite solar cells, conditions as in (c).

Table 3.1: Photovoltaic parameters of the pure FA and the doped Cs and Br perovskite solar cells.

Composition	J_{sc} **(mAcm^{-2})**	V_{oc} **(mV)**	**FF** (%)	**PCE** (%)
$FAPbI_3$	21.4	809	59.2	10.4
$Cs_{0.2}FA_{0.8}PbI_3$	21.5	1017	70.1	15.69
$Cs_{0.2}FA_{0.8}PbI_{2.84}Br_{0.16}$	21.9	1073	74.2	17.35

3.4 Conclusions

We have demonstrated that a mixed A cation inorganic-organic perovskite prepared by incorporating Cs into $FAPbI_3$ can be used to produce high performance solar cells. These perovskite films are homogeneous and can be conformally coated onto the TiO_2 photoanode, showing no separation into different chemical phases. They can be produced at temperatures lower than the 150 °C required for the pure $FAPbI_3$ films, remaining stable with no (reversible) phase transitions to the inactive, yellow colored, δ phase, over a large temperature range down to room temperature. This stabilization can be rationalized in terms of the miscibility of $CsPbI_3$ and $FAPbI_3$ in the perovskite phase, while the same compounds are not miscible in the δ phase due to the fact that $CsPbI_3$ and $FAPbI_3$ are very similar in the atomistic structure and volume in the former but not in the latter. This results in a large energy penalty for mixing in the δ phases, while the mixing of the perovskite phases is energetically favorable. The high performance of the mixed $Cs_xFA_{(1-x)}PbI_3$ perovskite exemplifies the great potential of this newly developed material not only in the production of high efficiency solar cells, but also as materials for optoelectronic devices such as photoconductors and organic LEDs.

Chapter 4

Atomistic origins of the limited phase stability of Cs^+-rich $FA_xCs_{(1-x)}PbI_3$ mixtures

Chapter 4 is a pre-print version of an article in preparation as:

Ariadni Boziki, Dominik J. Kubicki, Aditya Mishra, Simone Meloni, Lyndon Emsley, Michael Grätzel, and Ursula Rothlisberger. Atomistic origins of the limited phase stability of Cs^+-rich $FA_xCs_{(1-x)}PbI_3$ mixtures. *In preparation.*

My contribution: Performance of all the calculations and simulations, interpretation of the results as well as preparation of the manuscript.

4.1 Abstract

Mixed cation perovskites, $Cs_x[HC(NH_2)_2]_{(1-x)}PbI_3$, ($Cs_xFA_{(1-x)}PbI_3$) with $x = 0.2$ achieve high solar cell PCEs while exhibiting long-term stability under ambient conditions. In this work, we perform DFT calculations, first-principles MD simulations, solid-state nuclear magnetic resonance (NMR) and X-ray powder diffraction (XRD) measurements aimed at investigating the possible phase stability of Cs^+-rich $FA_xCs_{(1-x)}PbI_3$ mixed-cation materials as potential candidates for tandem solar cell applications. Estimations of the free energy of the mixtures with respect to the pure compounds together with calculations of the relative phase stability at 0 K and at finite temperature show that although the mixtures can form, the delta phase remains the thermodynamically most stable phase at room temperature. This is fully corroborated by solid-state NMR and XRD measurements. This is in contrast to FA^+-rich Cs/FA mixtures where small additions of Cs^+ are sufficient to stabilize the perovskite phase at ambient conditions. The atomistic origin for this contrasting behavior is an energetic destabilization for the perovskite phase caused by the volume difference between the γ-$CsPbI_3$ and the α-$FAPbI_3$.

4.2 Introduction

Over the last years, organic-inorganic hybrid lead halide perovskites have attracted great attention due to their impressive photovoltaic performance.[60–65, 312] However, the long-term stability of perovskite solar cells remains a major challenge in order to approach commercialization. Indeed, the most widely studied material of this type, $MAPbI_3$ has a band gap of 1.5 eV,[313] which is close to the single-junction optimum of 1.34 eV, based on Shockley and Queissers detailed balance considerations, with a theoretical efficiency limit of 33.16%.[33, 314] In fact $MAPbI_3$ cells fabricated by regulated nucleation and Ostwald recrystallization, reach an impressive PCE of 20.3%.[315] Unfortunately, $MAPbI_3$ on the film decomposes rapidly at 423 K due to the presence of solvents and water.[312] In a similar vein, the perovskite phase of $FAPbI_3$ has a band gap that different experimental measurements show that lies within the range of 1.43-1.48 eV,[145, 312, 316] even closer to the single-junction optimum, but the thermodynamically most stable phase at room temperature is a non-perovskite hexagonal δ-phase (yellow phase) and the transition to the perovskite phase only occurs at high temperatures ($T = 333$ K).[91]

Purely inorganic cesium lead trihalide perovskites could present an alternative since for instance $CsPbBr_3$ forms a perovskite structure at room temperature.[307] However, $CsPbBr_3$ has a rather wide bandgap of 2.25 - 2.36

eV, according to measurements performed at different groups.[303, 308]. $CsPbI_3$, on the other hand has an experimental band gap of 1.73 eV,[148, 149] which is close to the optimum top cell band gap for tandem solar cells of 1.7 - 1.8 eV,[77] which offers a promising way for increasing the efficiency with a minimal cost increase.[317–320] Unfortunately, $CsPbI_3$ crystallizes in a non-perovskite hexagonal, insulating phase, the yellow δ phase at room temperature.[91] While the δ phase of $FAPbI_3$ consists of face-sharing octahedra that are surrounded by the monovalent cations, the δ phase of $CsPbI_3$ consists of edge-sharing octahedra. Only, at 600 K, $CsPbI_3$ undergoes a first order phase transition from the non-perovskite to a black perovskite phase.[308]

This black perovskite phase has been assumed to be cubic,[308] however recent synchroton powder diffraction measurements of Stoumpos *et al.*[321] showed that on cooling down from temperatures above 633 K, the perovskite structure remains kinetically stable converting to two black perovskite phases with distorted octahedra at 533 and 448 K, respectively. In addition to this, Lai *et al.*[322] also observed an orthorhombic perovskite phase for $CsPbI_3$ nanowires from X-ray diffraction (XRD) patterns measured at 300 K. It has also been reported that $CsPbI_3$ can adopt a black phase at room temperature by adding HI during the preparation process without any noticeable changes to the optical properties of the material.[323] Despite this apparent success, the mechanism of stabilization of the black phase of $CsPbI_3$ by HI, remained unclear. It was only recently that Ke *et al.*[324] showed that the black phase does not correspond to pure $CsPbI_3$ but that a new compound, $(CH_3)_2NH_2^+PbI_3$ ($DMAPbI_3$) is formed, where dimethylammonium (DMA) is the HI catalyzed decomposition product of the acidic hydrolysis of the solvent dimethylformamide (DMF). In the same study, the stabilization of the black perovskite phase of $CsPbI_3$ through mixing with DMA was demonstrated. In particular, the mixed cation compound $Cs_{0.7}DMA_{0.3}PbI_3$ achieved a maximum PCE of 12.62% and has a band gap of around 1.7 eV. Finally, Sutton *et al.*[325] demonstrated that at room temperature the most stable among the black perovskite polymorphs of $CsPbI_3$ is an orthorhombic structure, that all the while remains less stable than the yellow non-perovskite form.

Consequently, the most studied pure compounds although they possess band gaps either close to the single-junction optimum or to the optimum top cell band gap for tandem solar cells, are thermodynamically not stable in the perovskite phase over a sufficient temperature range. To overcome this problem, a design protocol has been introduced that mixes different monovalent cations and halides in order to achieve perovskite cells with enhanced thermal and structural stability.[184, 186, 187]

Indeed, Pellet *et al.*[184] produced cells with an enhanced short-circuit current by using a mixture of FA^+ and MA^+ as monovalent cations. However, like for $MAPbI_3$ itself also the mixed compounds are prone to decomposition at high temperatures. To circumvent problems related to thermal decomposition of the MA^+, Cs cations have attracted attention for use in mixed organic-inorganic lead halide perovskites. Choi *et al.*[309] presented cesium-doped $MAPbI_3$ cells, achieving an efficiency of 7.68% upon addition of 10% cesium. Moreover, Lee *et al.*[310] presented mixtures of cesium and formamidinium with enhanced thermal and humidity stability, achieving a power conversion efficiency of 16.5%. We have shown previously that the addition of Cs^+ into $FAPbI_3$ leads to a reduction of the phase transition temperature by $\sim$ 200 - 300 K, explaining why the perovskite phase becomes stable at room temperature for $Cs_xFA_{(1-x)}PbI_3$ compounds.[185] Furthermore, Saliba *et al.* proposed a triple cation perovskite compound, which consists of Cs^+, FA^+ and MA^+, achieving a PCE of 18 %.[186] In a follow up work, Saliba *et al.* added Rb^+ into this triple cation perovskite, achieving a PCE of 20.2 %.[187] Hence, it appears that Cs^+ is highly efficient in suppressing yellow phase impurities. Li *et al.*[87] suggested that tuning the Goldschmidt tolerance factor[86, 326] and its extension to organic cations proposed by Kieslich *et al.*[89, 92], through solid-state alloying could be a way to stabilize the black perovskite structure. Specifically, the authors report that by mixing $FAPbI_3$ with $CsPbI_3$, the effective tolerance factor can be tuned and mixtures of low Cs^+ concentration, which are stable in the perovskite phase, can be formed.

In contrast to the FA^+-rich case of FA/Cs mixtures, Cs^+-rich compounds have been less investigated so far although they might be promising candidates for tandem solar cells. In this study, we study Cs^+-rich, $FA_xCs_{(1-x)}PbI_3$ mixtures, for Cs^+ concentrations up to 50%, through an interplay of density functional theory, molecular dynamics simulations and experiments. The goal of our investigation is to examine if stable Cs^+-rich mixtures can be formed and if they lead to the desired stabilization of the perovskite phase. Our approach consists of an estimation of the free energy for the mixtures with respect to the pure phases, in order to establish if mixing is possible and if it leads to any preferential stabilization of the perovskite phase with respect to the delta phase. In addition, the energy difference between the δ and the perovskite phase at 0 K, provides a first indication about the relative stability of the two phases and MD simulations are used to gain information about the relative phase stability at finite temperature. The results from these different studies show that although stable mixtures can be formed they do not lead to significant extension of the stability range of the perovskite phase. This is also corroborated by solid-state NMR and XRD measurements that show the Cs^+-rich mixtures albeit stable adopt the delta phase at room temperature. A study of structural characteristics of the mixed compounds suggest a rationale for this contrasting behavior between FA^+-rich versus Cs^+-rich FA/Cs perovskites. Calculations of the optical properties of the metastable Cs^+-rich perovskite materials show that they would be potential candidates for solar cells applications if were stable, motivating a search of alternative ways of preparation.

4.3 Results and Discussion

4.3.1 Properties of the pure $CsPbI_3$

As mentioned above, it is now well-known that apart from the two thermodynamically stable phases of $CsPbI_3$; a non-perovskite δ-phase from 0 up to 600 K and a cubic perovskite phase above 600 K (Figure 4.1),[308] two more kinetically stabilized black perovskite phases with distorted octahedra have been observed. These phases are known as β and γ phases, respectively, with the orthorhombic γ-$CsPbI_3$ being the most stable one among the perovskite polymorphs at room temperature, but still remaining less stable than the yellow non-perovskite phase.[321, 325] For this reason, in our study we have taken the three phases, δ, γ and cubic into account.

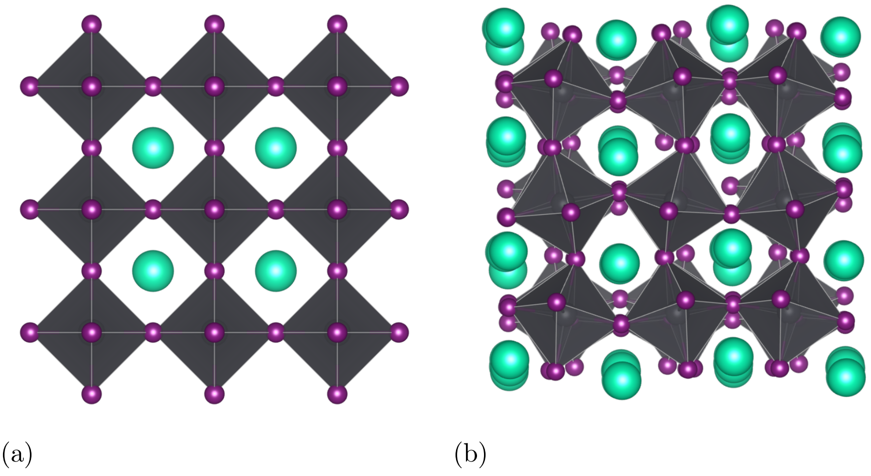

(a) (b)

Figure 4.1: DFT optimized structures of the perovskite phases. (a) Cubic perovskite phase. (b) Orthorhombic perovskite structure.

The calculated single-particle Kohn-Sham band gap of the cubic perovskite phase at 0 K, as predicted by DFT calculations, employing the PBE functional,[327] is 1.44 eV in good agreement with other theoretical studies,[328] but somewhat in contrast to the experimentally measured band gap of 1.73 eV.

To make a meaningful comparison with the experimental data, which has been measured at finite temperature, thermal effects should also be taken into account. For this reason, we performed Car-Parrinello molecular dynamics simulations of 5.4 ps in the *NVT* ensemble at a temperature of 300 K, for a cubic $CsPbI_3$ real-space cell of 320 atoms at the gamma point. The band gap of this real-space equivalent of the fully **k**-point converged sample is 1.39 eV. In Figure 4.2, the histogram of the band gaps for different finite temperature configurations is shown, allowing to calculate the contribution of temperature effects on the 0 K band gap. It turns out that this contribution is as large as 0.49 eV. This is unusually large, since in previous studies, contributions of thermal effects to the band gap, for similar types of materials, is of the order of 0.15 eV.[329] However, it is worth mentioning that Wiktor *et al.*[328] also estimated a 0.47 eV contribution of thermal effects to the 0 K gap of cubic $CsPbI_3$, employing the rVV10 functional.[330, 331] In this way, the calculated finite temperature band gap converges to 1.83 eV for the real space cell.[148, 323]

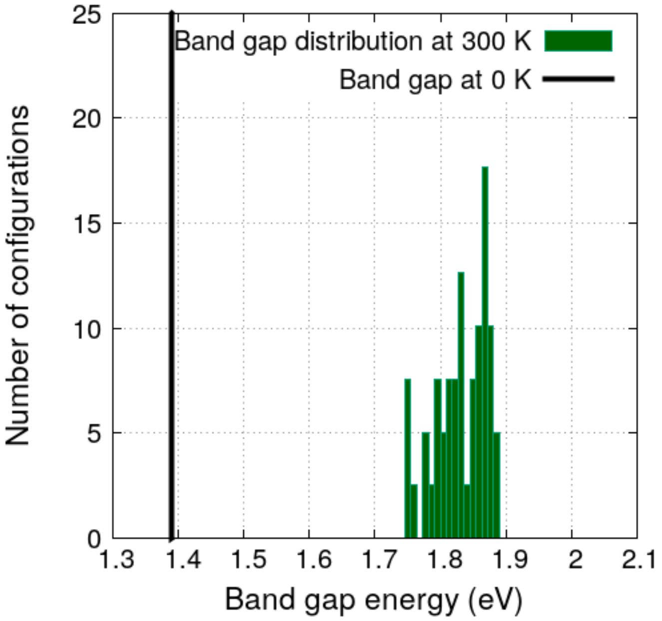

Figure 4.2: Histogram of the thermal distribution of the band gap compared to the value at 0 K for the cubic phase of $CsPbI_3$.

Alternatively, since the metastable γ-$CsPbI_3$ phase is the most stable among the different perovskite polymorphs at room temperature, we also examined an orthorhombic structure with a cell containing 240 atoms. The fully DFT optimized structure at 0 K has average Pb-I-Pb angles of (DFT 155° versus 154°

in experiments) in very good agreement with the experimental orthorhombic structure of γ-$CsPbI_3$.[325] The fully converged, **k**-point sampled 0 K band gap is 1.77 eV. As shown in Figure D.1 (Appendix D), thermal effects at 300 K are much smaller than in case of cubic-$CsPbI_3$ and amount only to 0.1 eV. The difference between the thermal effects of the cubic and the orthorhombic cell arises from the nature of the VBM which is formed by an antibonding combination of B ns and X mp orbitals. For this reason when moving form cubic to orthorhombic phase, the antibonding overlap between the orbitals of divalent cation and anions is reduced leading to an increment of the band gap. For reasons of completeness, we considered both the orthorhombic as well as the cubic phases in the subsequent investigation of the mixed cation phases of $FA_xCs_{(1-x)}PbI_3$.

4.3.2 Mixed $FA_xCs_{(1-x)}PbI_3$ compounds

In order to study if mixed compounds in the three phases δ, γ, cubic are stable and if any preferential phase stabilization takes place upon mixing, we performed structural relaxations (atomic positions and cell parameters) of the mixed $FA_xCs_{(1-x)}PbI_3$ compounds at 0 K and compared them with the energies of the corresponding pure compounds.

$$\begin{aligned}\Delta E_{phase}(FA_xCs_{(1-x)}PbI_3) = {} & E_{phase}(FA_xCs_{(1-x)}PbI_3) \\ & - [xE_{phase}(FAPbI_3) + (1-x)E_{phase}(CsPbI_3)]\end{aligned} \tag{4.1}$$

$$T\Delta S_{phase}(FA_xCs_{(1-x)}PbI_3) = -k_BT[xlnx + (1-x)ln(1-x)] \tag{4.2}$$

Analysis of the enthalpic contribution to the mixing free energy, which is expressed by equation (4.1) shows that in case of the δ phase replacement of Cs^+ by FA^+ leads to a destabilization (energy increase) with respect to the two pure FA and/or $CsPbI_3$ δ phases, (magenta line in Figure 4.3 upper panel). The mixing entropy contribution to the free energy expressed by equation (4.2) and calculated at room temperature, only partially compensate this penalty. Similarly, in the γ phase, where the enthalpic contribution is calculated with respect to β-$FAPbI_3$,[91], mixing induces almost no or slightly positive enthalpic contributions (magenta line in Figure 4.3 lowest panel) and the estimated free energy of mixing is close to zero (black line in Figure 4.3 lowest panel). Indeed, for both cases (δ and γ phases, excluding only the δ-$FA_{0.33}Cs_{0.67}PbI_3$, where mixing leads to destabilization with respect to the pure phases) the estimated free energy of mixing is of the order of 0.006 eV per stoichiometric unit that is smaller than the typical variations among different substitution pattern. Since these values lie within the intrinsic error of the calculations, we cannot conclude if mixing in the orthorhombic γ and δ phase leads to marginally stable, respectively slightly unstable compounds with respect to decomposition into the pure phases.

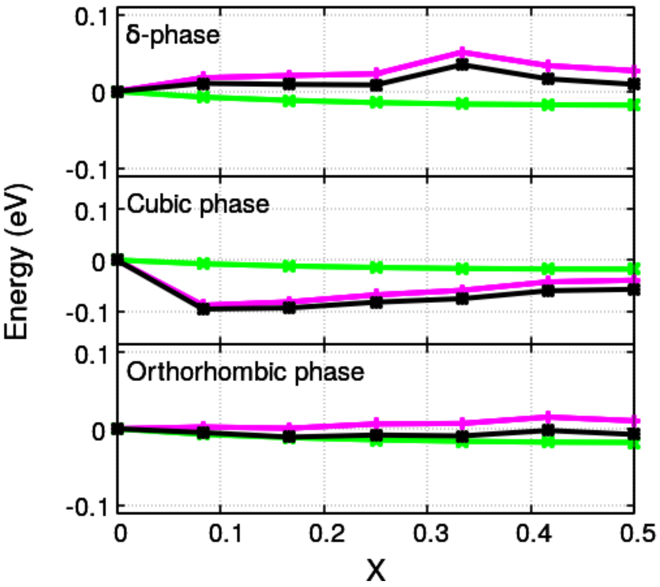

Figure 4.3: Variation of the free energy, of $FA_xCs_{1-x}PbI_3$ expressed as $\Delta F = \Delta E - T\Delta S$ (black line), the internal energy, ΔE (magenta line), and the mixing entropy contribution, $-T\Delta S$ (light-green line), as a function of FA^+ ratio. In the top graph the variations of free energy, enthalpy and mixing entropy contribution are estimated with respect to the pure δ phases. In the middle and bottom graphs each contribution to the free energy is estimated with respect to cubic-$CsPbI_3$ and orthorhombic-$CsPbI_3$, respectively.

In contrast, in case that cubic-$CsPbI_3$ is employed as reference, the enthalpic contribution is already favoring mixing (Figure 4.3 central panel). As expected, the mixing entropy contribution favors the stabilization of the perovskite phase even more, leading to a stability maximum around $FA_{0.08}Cs_{0.92}PbI_3$ with respect to the pure compounds. One should mention here that the calculation of any possible stabilization of the mixtures with respect to the cubic-$CsPbI_3$ does not imply that the mixtures themselves adopt the cubic phase. In fact, fully optimized structures of all mixtures in the perovskite phase are always adopting an orthorhombic phase.

An issue that demands further investigation is if the inclusion of zero point energy and vibrational entropy contributions influence the relative free energies. Calculations of the vibrational entropy term are not trivial in case of perovskites. Indeed, both harmonic and quasi-harmonic phonon calculations lead to imaginary modes.[332] In our case, since we are considering relative stabilities within the same phase, these relative differences in contributions might to a first approximation considered to be small. However, substitution of Cs^+ with FA^+ that has more degrees of freedom, certainly adds an entropic stabilization.

The energy difference at 0 K, can serve as a first indicator of the relative stability of the perovskite with respect to the δ phases. As shown in Table 4.1, the δ phase is lower in energy for the pure ($CsPbI_3$) compound at 0 K, which is consistent with the experimental data that predict the δ phase to be the most stable low temperature phase.[91] In case that cubic-$CsPbI_3$ is used as reference, FA^+ substitution leads to a relative stabilization of the perovskite phase by reducing the energy difference to roughly half, independent of the concentration of FA^+. Contrary, when orthorhombic-$CsPbI_3$ is used as reference, the energy difference is only reduced by about 12 - 17% up to 25% of FA^+ and 17 - 35% for higher concentrations up to 50% FA^+. We should mention again here that only the pure cubic-$CsPbI_3$ is cubic. As soon as the mixtures are generated, the structures become orthorhombic explaining why the energy differences for cubic and orthorhombic are identical for all mixed compounds. For comparison, in the case of FA^+-rich mixed compounds (generated by substitution of Cs^+ ions into the $FAPbI_3$ lattice), where addition of Cs^+ result in a stabilization of the perovskite phase at room temperature, the energy difference between the δ and the β $FAPbI_3$ phase at 0 K is of the order of 0.12 eV. This energy difference is reduced to 0.11 eV for 8% of Cs^+ doping and to 0.10 eV for concentrations up to 25% Cs^+. For higher concentrations up to 50% Cs^+, the energy is reduced to 0.08 - 0.09 eV. The energy difference at 0 K can only provide a first rough indication about the relative stability trends at finite temperature.

To shed more light on the finite temperature phase stability, we performed MD simulations at 300 K employing the NVT ensemble at the gamma point for δ and orthorhombic $FA_{0.33}Cs_{0.67}PbI_3$ compounds, using simulation cells of 176 atoms. From the average potential energy of an equilibrated trajectory of 2.2 ps, as shown in Figure 4.4, we observe that the δ phase is more stable at room temperature. In addition, within the time scale of these simulations no phase segregation towards the pure phases was observed.

We verified the theoretical predictions by synthesizing $FA_{0.08}Cs_{0.92}PbI_3$ and $FA_{0.16}Cs_{0.84}PbI_3$ using solid-state mechanosynthesis[201, 333, 334] and characterizing them using solid-state magic angle spinning (MAS) NMR (Figure 4.5). Our and other groups have previously shown that solid-state NMR,[335–343] and in particular ^{133}Cs,[340, 344–347] can be used to probe the atomic-level microstructure of halide perovskites. Cesium environments corresponding to Cs^+

Table 4.1: Relative energetic stability, expressed by $\Delta E_{a\delta} = E_a - E_\delta$ per stoichiometric unit of the cubic/orthorhombic perovskite phase with respect to the δ phase upon doping of $CsPbI_3$ with FA^+.

	Difference in energy (per stoichiometric unit) between perovsite and δ phases at 0 K (eV)	
Fraction of FA^+ doped into $CsPbI_3$ structure	Estimation of the energy difference with respect to cubic-$CsPbI_3$	Estimation of the energy difference with respect to orthorhombic-$CsPbI_3$
0	0.23	0.14
8%	0.12	0.12
17%	0.11	0.11
25%	0.12	0.12
33%	0.09	0.09
42%	0.11	0.11
50%	0.11	0.11

incorporated into the 3D perovskite lattice of α-$FAPbI_3$ (Figure 4.5a, 13 ppm, fwhm (1169 ± 20) Hz), Cs^+ inside the black orthorhombic γ-$CsPbI_3$ 3D perovskite (Figure 4.5b, 154 ppm, fwhm (440 ± 4) Hz) and yellow non-perovskite δ-$CsPbI_3$, (Figure 4.5c, 242 ppm, fwhm (353 ± 4) Hz) are characterized by distinct and unambiguous shifts in ^{133}Cs MAS NMR spectra. The as-prepared powders of $FA_{0.08}Cs_{0.92}PbI_3$ and $FA_{0.16}Cs_{0.84}PbI_3$ are yellow and their color is not affected by annealing at 170 °C. Their spectra (Figure 4.5d, e) feature a peak which is identical to that of δ-$CsPbI_3$, confirming the non-perovskite nature of these Cs-rich $FA_xCs_{(1-x)}PbI_3$ phases.

That said, in both spectra there is an overlapping broad component ($FA_{0.16}Cs_{0.84}PbI_3$: fitted shift of 236 ppm and fwhm (1885 ± 30) Hz) which corresponds to a distribution of structurally disordered cesium environments due to the incorporation of FA^+ into the non-perovskite δ-$CsPbI_3$ structure. We corroborate this hypothesis by measuring ^{1}H and ^{13}C CP MAS NMR spectra of the mixed-cation $FA_{0.16}Cs_{0.84}PbI_3$ material (Figure 4.5h, 4.5k) and comparing them to those of α-$FAPbI_3$ (Figure 4.5f, 4.5i) and δ-$FAPbI_3$ (Figure 4.5g, 4.5j). For both nuclei, the FA resonances of $FA_{0.16}Cs_{0.84}PbI_3$ are significantly shifted with respect to those of the reference phases, confirming that FA^+ is present in a new microscopically different chemical environment and that there is no phase segregation into pure α-$FAPbI_3$ or δ-$FAPbI_3$, in contrast to pre-

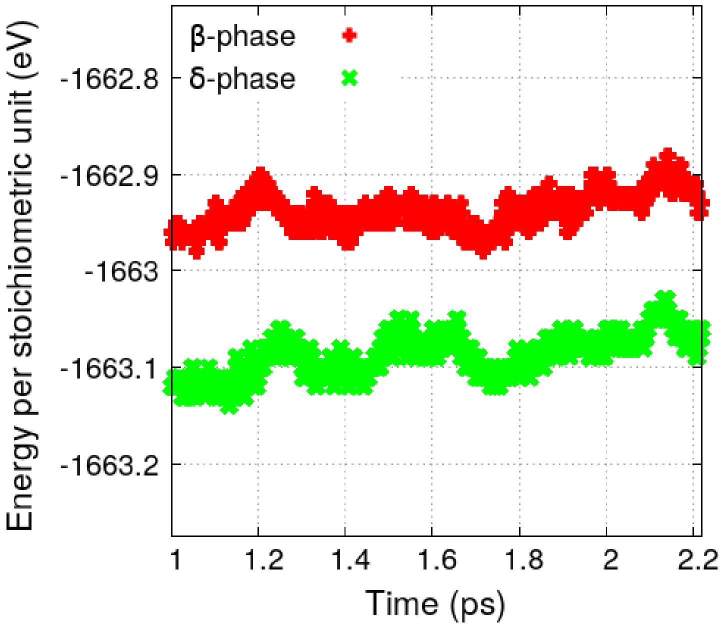

Figure 4.4: Energy per stoichiometric unit for each frame of both δ and perovskite $FA_{0.33}Cs_{0.67}PbI_3$ mixtures across a 3 ps trajectory, derived by MD simulations.

vious experimental results, suggesting that for high Cs^+ concentrations, phase separation to the pure δ phases is observed.[87] However, our solid-state NMR results are also consistent with the XRD patterns of the materials (Figure D.2 in Appendix D), whereby the mixed phases feature reflections corresponding to δ-$CsPbI_3$ which are broadened due to the presence of static chemical disorder. In addition, the longitudinal relaxation time, T_1, of FA^+ in $FA_{0.16}Cs_{0.84}PbI_3$ is significantly longer (17 s) compared to that of α-FAPbI3 (2.5 s) and δ-FAPbI3 (1 s). Since the main source of T_1 relaxation in protonated solids is the ^{1}H-^{1}H dipolar interaction,[348] which scales approximately as r_{HH}^{-6} with the distance, r, between protons, the increase in T_1 by an order of magnitude in the case of $FA_{0.16}Cs_{0.84}PbI_3$ suggests longer average FA^+-FA^+ distances in this phase. This result is consistent with FA^+ being sparsely dispersed within the δ-$CsPbI_3$ phase.

The interplay between theoretical analysis and experiments confirm that in contrast to the FA^+-rich case, Cs^+-rich mixed perovskite phases are not ther-

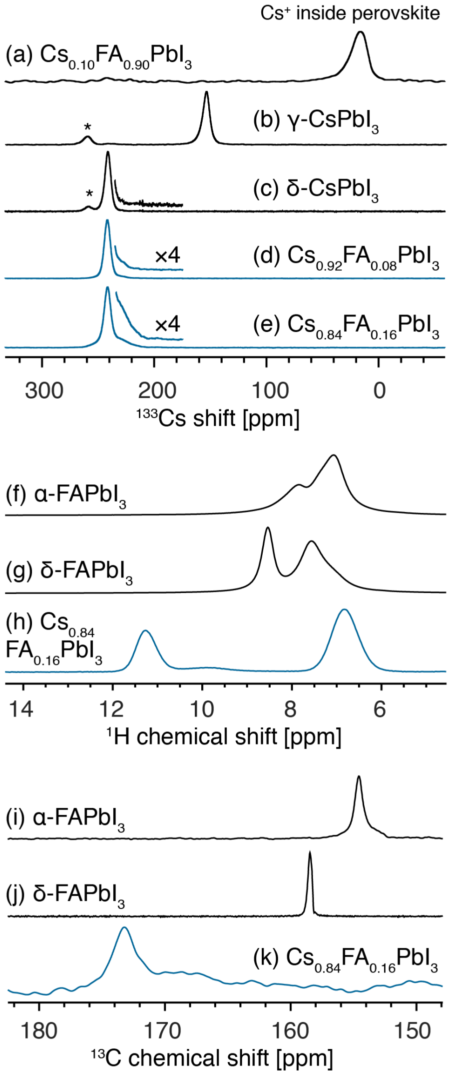

Figure 4.5: Solid-state MAS NMR characterization of the materials. ^{133}Cs spectra at 11.7 T, 298 K and 22 kHz MAS of (a) $FA_{0.9}Cs_{0.1}PbI_3$, (b) γ-$CsPbI_3$, (c) δ-$CsPbI_3$, (d) $FA_{0.08}Cs_{0.92}PbI_3$, (e) $FA_{0.16}Cs_{0.84}PbI_3$. ^{1}H and ^{13}C spectra at 21.1 T, 100 K and 12 kHz MAS of (f, i) α-$FAPbI_3$, (g, j) δ-$FAPbI_3$, (h, k) $FA_{0.16}Cs_{0.84}PbI_3$. Asterisks (*) indicate an impurity phase (Cs_4PbI_6).

modynamically stable at room temperature. However, it is still important to study the reasons why in contrast to the FA^+-rich case, mixing in the γ phase is enthalpically significantly disfavored. An analysis of the structural characteristics of the mixed compounds provides a possible atomistic rationale for the destabilization of the Cs^+-rich mixtures in the γ phase. The volume per stoichiometric unit of γ-$CsPbI_3$ (252.73) is 7.3 % smaller than the one of α-$FAPbI_3$ (272.58). Upon FA^+ substitution into the γ-$CsPbI_3$ lattice, the available volume for the monovalent cation is thus smaller.

In addition, following the evolution of the volume upon FA^+ doping into $CsPbI_3$ (Figure 4.6a), even in the case of cubic $CsPbI_3$ abrupt decrease is observed, when moving from the pure compound to the lowest concentration (8 %), consistent with a transition from cubic to orthorhombic phase, due to the lowering of symmetry and some induced structural distortions upon cation substitution. This is also manifested in the Pb-I-Pb angle distribution (Figure 4.6b), that moves from an average of 180° (characteristic Pb-I-Pb angle distribution of the cubic phase) to 155° upon low concentration doping, indicating the adoption of an orthorhombic phase. This can again be explained by the difference between the ionic radii of the two cations (Cs^+ and FA^+). In this case the smaller Cs^+ is substituted by the larger FA^+, imposing distortions in the lattice. Upon increasing FA^+ concentration, the volume of the cell is increasing in proportion to the concentration, leading at 50 % of doping to a volume which is even larger than the one of the initial cubic perovskite phase. The inclusion of more and more FA^+ imposes less distortions in the lattice, something that also explains the gradual increase of the Pb-I-Pb angles distribution at high FA^+ concentrations. On the other hand, the volume of the orthorhombic $CsPbI_3$ structure is significantly smaller than the one of the corresponding cubic phase, and comparable to the volumes of the mixtures. Having characterized the structural properties of the mixed compounds, we now turn to an analysis of their electronic properties. It has been shown from several studies that PBE-GGA, without the inclusion of SOC effects provides fortuitous good predictions of the band gap of lead halide perovskites.[349, 350] Using this protocol for our calculations, Table 4.2 shows the evolution of the calculated band gaps. It is obvious that upon mixing the band gap remains remarkably unaffected, with values close to the optimum for tandem solar cell applications. We observe that the highest band gap values correspond to the most distorted orthorhombic structures, consistent with the well-known electronic characteristics of the VBM of organic-inorganic lead halide perovskites, in which when moving from cubic to orthorhombic phase the overlap between I p orbitals and Pb s orbitals is reduced.[150]

4.4 Conclusions

The static DFT/PBE calculations, MD simulations and experiments show that in contrast to the FA^+-rich case, the perovskite phase of Cs^+-rich $FA_xCs_{(1-x)}PbI_3$ mixtures ($0 \leq x \leq 0.5$) is thermodynamically unstable at room

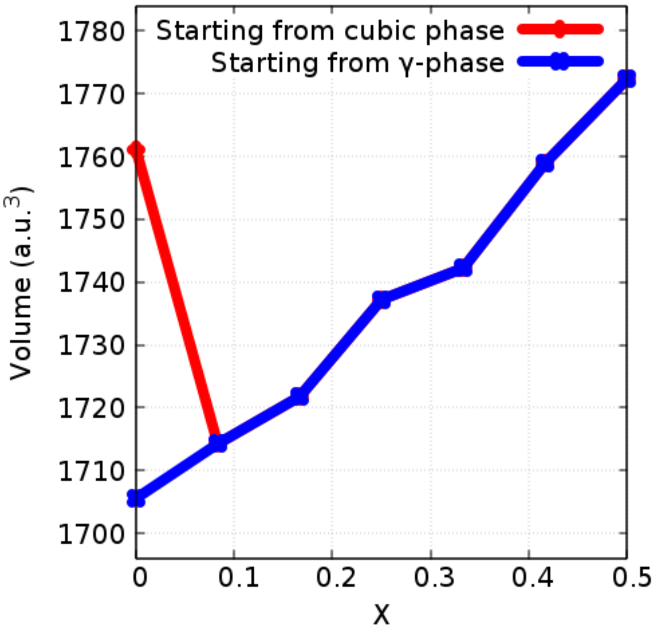

(a)

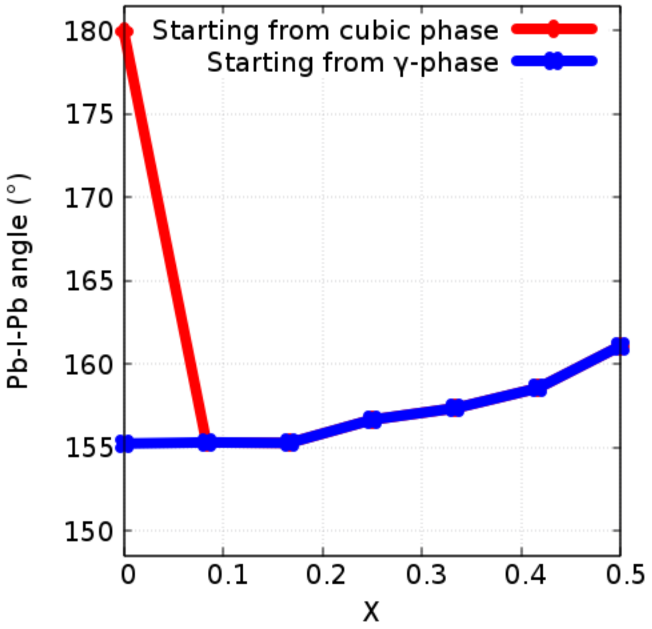

(b)

Figure 4.6: Volume (a) and average Pb-I-Pb angles (b) evolution upon FA^+ doping into $CsPbI_3$.With red and blue lines are represented the trends if as 0 % doped structure we consider, the cubic perovskite structure and the orthorhombic perovskite structure, respectively.

Table 4.2: Average DFT/PBE band gaps of cubic/orthorhombic $CsPbI_3$ and of Cs^+-rich $FA_xCs_{1-x}PbI_3$ mixtures as a function of different FA^+ concentrations. The standard deviation indicates variations due to different substitution pattern.

Fraction of FA^+ doped into $CsPbI_3$ structure	Band gap (eV)
0	1.44 (cubic-$CsPbI_3$)
0	1.77 (orthorhombic-$CsPbI_3$)
8%	1.81
17%	1.81 ± 0.03
25%	1.80 ± 0.02
33%	1.79 ± 0.02
42%	1.79 ± 0.01
50%	1.74 ± 0.03

temperature. DFT calculations show that among the perovskite phases, the orthorhombic γ phase is the energetically most stable form for the pure compound and the only stable perovskite phase for all the considered mixtures. Estimates of the free energy of mixing with respect to the pure phases show that mixing in both δ and γ phases might lead to only marginally stable structures. The energy difference between the δ and γ phases at 0 K, shows that the δ phase is more stable for the pure and the mixed compounds. Furthermore, MD simulations at room temperature predict that the mixtures are stable at least within the time scale of the simulations in the δ phase and no phase segregation is observed. This observation is also supported by solid state NMR and XRD measurements suggesting that stable mixtures are formed and adopt the δ phase.

The contrasting behavior of FA^+-rich versus $Cs\text{-}^+$rich $FA_xCs_{(1-x)}PbI_3$ mixtures arises from an enthalpic destabilization of the latter that is due to the volume difference between the α-$FAPbI_3$ and the γ-$CsPbI_3$ phase. While substituting Cs^+ into the $FAPbI_3$ lattice is possible, the contrary does not hold since the large FA^+ ion cannot fit in. This observation suggests a new design principle for the preparation of mixed cation/mixed halide lead perovskites, in which the mixing is getting unfavorable upon incorporation of a large cation into a relatively small lattice. Finally, the calculation of the band gaps of the mixed compounds, allows us to conclude that if the perovskite phase could be kinetically trapped it would be a potential candidate for tandem solar cell applications.

4.5 Computational details

DFT[254, 255] calculations have been performed using the Quantum Espresso suites of codes.[351, 352] The GGA to DFT in the PBE formulation has been used.[327] The interactions between valence electrons and core electrons and nuclei are described by ultrasoft pseudopotentials.[353] The Kohn-Sham orbitals are expanded in a plane wave basis set with a kinetic energy cutoff of 40 Ry and a density cutoff of 240 Ry. The Brillouin zone is sampled with a 4x4x4 Monkhorst-Pack k-points shifted grid.[354] These values have been chosen after having performed convergence tests for the total energy, the band gap, the pressure, the stresses and the atomic forces. SOC effects are not explicitly included in the calculations due to the well-known fortuitous error cancellation of SOC and many-body effects in the case of lead halide perovskites.[349]

Comparing, the absolute energy of Kohn-Sham orbitals in solid state systems is not trivial since for an infinitely periodic system there is no reference value for the energy origin. A technique to cope with this problem is to use localized deep impurity states or states that are expected to be unaffected by the chemical and structural nature of the system such as semicore or core states. As a reference, an approach analogous to the one used by Alkauskas *et al.*[355] for band alignment in solids has been employed here, where the energy of the Pb_{5d} semicore state is used as reference.[150] This is the only band which is rigidly shifted, something that supports the idea that the vacuum level of these atomic orbitals are independent of the system.[150]

For the mixed compounds, the structures have been prepared starting from the experimental cubic phase of $CsPbI_3$, replacing Cs^+ by FA^+ in different ratios. All the structures consist of superlattices that contain 12 stoichiometric units. For each stoichiometry, when allowed, we considered 10 different possible replacements, starting from the energetically lowest configuration at the next lower FA^+ content. The structures were fully relaxed (atomic positions and cell parameters). The maximum standard deviation of the difference in energy per stoichoiometric unit among the different configurations is of the order of 0.006 eV.

Car-Parrinello molecular dynamics simulations in the NVT ensemble were performed using the CPMD code.[356] The wavefunction cutoff was set to 90 Ry and Goedecker normconserving pseudopotentials were used.[357–359] A time step of 5 a.u. was used with a fictitious mass parameter of 800 a.u.. The temperature in the simulations was set to 300 K and was controlled by a Nosé-Hoover thermostat with a coupling frequency of 1000 cm^{-1}.[360–362]

4.6 Experimental details

Perovskite mechanosynthesis: Starting materials were stored inside a glove box under argon. Perovskite powders were synthesized by grinding the reactants in an electric ball mill (Retsch Ball Mill MM-200 using a grinding jar (10 ml) and a ball (10 mm) for 30 min at 25 Hz. The resulting powders were annealed for 5 minutes at temperatures specified below. The amounts of reagents taken into the synthesis were as follows:

- δ-$FAPbI_3$: 0.172 g formamidinium hydroiodide (1.00 mmol) and 0.461 g PbI_2 (1.00 mmol). No annealing.
- α-$FAPbI_3$: δ-$FAPbI_3$ was annealed at 170 °C to induce the phase transition.
- δ-$CsPbI_3$: 0.260 g CsI (1.00 mmol) and 0.461 g PbI_2 (1.00 mmol). No annealing.
- γ-$CsPbI_3$: δ-$CsPbI_3$ was annealed at 350 °C to induce the phase transition to the α phase. After cooling to room temperature the black γ phase is obtained and the material transforms back to the δ phase with a half-life of about 1 hour.
- $FA_{0.9}Cs_{0.1}PbI_3$: 0.154 g of FAI (0.90 mmol), 0.026 g of CsI (0.10 mmol) and 0.461 g of PbI_2 (1.00 mmol).
- $FA_{0.08}Cs_{0.92}PbI_3$: 0.014 g of FAI (0.08 mmol), 0.234 g of CsI (0.90 mmol) and 0.461 g of PbI_2 (1.00 mmol). The material was annealed at 170 °C.
- $FA_{0.16}Cs_{0.84}PbI_3$: 0.028 g of FAI (0.16 mmol), 0.218 g of CsI (0.84 mmol) and 0.461 g of PbI_2 (1.00 mmol). The material was annealed at 170 °C.

Solid-state NMR measurements: Room temperature ^{133}Cs (65.6 MHz) NMR spectra were recorded on a Bruker Avance III 11.7 T spectrometer equipped with a 3.2 mm CPMAS probe. Low-temperature ^{1}H (900 MHz) and ^{13}C (225 MHz) NMR spectra were recorded on a Bruker Avance Neo 21.1 T spectrometer equipped with a 3.2 mm low-temperature CPMAS probe. ^{133}Cs shifts were referenced to 1 M aqueous solution of CsCl, using solid CsI (=271.05 ppm) as a secondary reference. ^{1}H and ^{13}C chemical shifts were referenced to solid adamantane (δ_H=1.91 ppm and C=29.45 (CH) and 38.48 (CH_2) ppm). Low-temperature ^{1}H-^{31}P cross-polarization (CP) experiments used 1 ms optimized contact pulses, 63 kHz SPINAL-64 1H decoupling and the following recycle delays: 1.7 s (δ-FAPbI$_3$), 3 s (α-FAPbI$_3$), 22 s (FA$_{0.16}$Cs$_{0.84}$PbI$_3$), Quantitative echo-detected ^{133}Cs spectra used a recycle delay of 400 s. ^{1}H spectra were acquired with recycle delays between 2 and 20 s. Peak widths were fitted in Topspin 3.2 and the uncertainties are given at one standard deviation.

Chapter 5

Why choosing the right partner is important: stabilization of ternary $Cs_yGUA_xFA_{(1-y-x)}PbI_3$ mixtures via incorporation of Cs^+

Chapter 5 is a pre-print version of an article in preparation as:

Ariadni Boziki, Marko Mladenović, Michael Grätzel, Ursula Rothlisberger. Why choosing the right partner is important: stabilization of ternary $Cs_yGUA_xFA_{(1-y-x)}PbI_3$ mixtures via incorporation of Cs^+. *In preparation.*

My contribution: Performance of all the calculations and simulations apart from the ones related to the energy and band gaps of the $GUA_xFA_{(1-x)}PbI_3$ mixtures in α-phase, interpretation of the results as well as preparation of the manuscript.

5.1 Abstract

Lead halide perovskites with mixtures of monovalent cations have attracted wide attention due to the possibility of preferentially stabilizing the perovskite phase with respect to photovoltaically less suitable competing phases. Here, we present a theoretical analysis and interpretation of the phase stability of binary $(CH_6N_3)_x[HC(NH_2)_2)]_{(1-x)}PbI_3$, $(GUA_xFA_{(1-x)}PbI_3)$ and ternary $Cs_yGUA_xFA_{(1-y-x)}PbI_3$ mixtures. We first try to estimate if such mixtures are stable and if they lead to a stabilization of the perovskite phase based on static DFT calculations. In order to investigate the finite temperature stability of the phases, we also employ first-principles molecular dynamics simulations. It turns out that in contrast to the FA^+-rich case of FA/Cs mixtures, although mixing of FA/GUA is possible, it is not sufficient to stabilize the perovskite phase at room temperature. In contrast, stable ternary mixtures that contain 17% of Cs^+ and GUA^+ up to 33%, can be formed, leading to a preferential stabilization of the perovskite phase. In such a way, picking monovalent cations in a suitable Goldschmidt tolerance range can lead to the formation of ternary stable perovskite mixtures.

5.2 Introduction

Solar cells based on organic-inorganic lead halide perovskites[60–65, 312] are achieving nowadays PCEs exceeding 24%.[1] The unique properties of this kind of materials, including high absorption coefficient,[363] small exciton binding energy,[156] large charge-carrier diffusion length,[157] low-trap density[295] and the low production cost when they are produced by low-temperature solution processes,[66] make them commercially attractive materials for photovoltaic technologies. Nevertheless, in spite of their exceptional performance, perovskite solar cells still face some unresolved issues, one of them being their limited long-term stability.

Indeed, $MAPbI_3$, $CsPbI_3$ and $FAPbI_3$, the three most widely studied perovskite materials exhibit limited stability for different reasons. More specifically, $MAPbI_3$ with a band gap of 1.5 eV,[62] which is close to the single-junction optimum, (1.34 eV according to Shockley and Queisser's detailed balance considerations, for AM 1.5 G illumination and T = 298.15 K),[33, 314] when is on the film in presence of solvents and water decomposes rapidly at 423 K.[312] The perovskite phase of $FAPbI_3$, has a band gap that according to different experimental measurements lies within the range of 1.43-1.48 eV,[145, 312, 316] and is even closer to the single-junction optimum. However at room temperature it adopts a non-perovksite hexagonal δ-phase (yellow phase) that is unsuitable for photovoltaic applications due to the large band gap.[91] This δ phase only undergoes a phase transition to a black perovskite α-phase at 433 K,[297] but a metastable β-$FAPbI_3$ phase ($P3$ trigonal space group) that $FAPbI_3$ adopts at 150 K has also been reported.[91] The purely inorganic $CsPbI_3$, on the other hand, has a band gap of 1.73 eV,[148, 323] which is close to the optimum top cell band gap for tandem solar cells of 1.7 - 1.8 eV.[77] However, as in case of $FAPbI_3$, it crystallizes in a non-perovskite insulating hexagonal δ-phase (yellow phase) at room temperature.[91]

Consequently, to overcome the problems of limited thermal, structural and phase stabilities, different strategies have been proposed. Indeed, it has been shown that mixing two different monovalent cations results in a preferential stabilization of the perovskite phase at room temperature.[184, 185, 310] Many of the devices that have achieved high PCEs are including mixtures of monovalent cations.[184, 185, 187] Pellet *el al.*[184] successfully added $MAPbI_3$ in order to stabilize the perovskite phase of $FAPbI_3$ at room temperature, however at higher temperatures the compound is prone to decomposition due to the presence of MA^+. Additionally, Lee *et al.*[310] prepared mixtures of cesium and formamidinium with enhanced thermal and humidity stability achieving a PCE of 16.5% and in one of our previous works, we have shown that $Cs_{0.2}FA_{0.8}PbI_{2.84}Br_{0.16}$ solar cells yield a PCE of over 17% exhibiting excellent long term stability in ambient air.[185] This design protocol of mixed cations has been further extended. Saliba *et al.*[186] proposed that the incorporation of Cs^+ into the mixtures of $MAPbI_3$ and $FAPbI_3$ results in an improved thermal stability achieving a PCE of 18%. In a follow up work, Saliba *et al.*[187] mixed the triple cation perovskite mentioned above with Rb^+ achieving a PCE of 20.2%.

As a rule of thumb, ions that are within the range of the Goldschmidt tolerance factor,[86] $(R_A + R_X)=t\sqrt{2}(R_B + R_X)$, where R_A, R_X and R_B are the ionic radii, of the monovalent cation (A), anion (X) and divalent cation (B), respectively are potential candidates for forming a stable perovskite structure. This allows for a selection of monovalent cations with tolerance factors that are in the range of 0.8 to 1.0.[326] This rule has been extended by Kieslich *et al.*[89, 92] to organic (molecular) cations assuming a rigid sphere model and full freedom for rotation around the center of mass leading to a set of effective ionic radii for mixtures of monovalent cations.[187, 344] $CH_6N_3^+$ (guanidinium - GUA^+) for example is an organic cation with a zero dipole moment and a Goldschmidt tolerance factor which is slightly above the upper limit.[89, 364] Indeed, no perovskite phase formation has been reported, so far for pure $GUAPbI_3$; a tetraiodide GUA_2PbI_4 is formed instead for which a continuous phase transition at 307 K takes place and a low-dimensional (1D) triiodide $GUAPbI_3$ that undergoes two phase transitions at 255 and 432 K, has also been reported.[365, 366]

Following the design protocol of mixing two different monovalent cations in order to form a stable perovskite phase at room temperature, GUA^+ has been mixed with $MAPbI_3$.[367, 368] The devices based on this mixed $GUA_xMA_{(1-x)}PbI_3$ solar cells resulted in an average PCE of 19.2% and enhanced stability, breaking in that way new ground in the exploration of cations with radii beyond the tolerance factor limit.[368] Originally, it has been proposed that upon mixing, GUA^+ is not directly incorporated into the perovskite structure but acts as a passivating agent,[367] however, a later study, demonstrated an increased micro-strain and distortions of the lattice upon GUA^+ doping of $MAPbI_3$, providing evidence for direct incorporation.[368] This was further confirmed by recent solid-state NMR measurements that supplied atomic-level evidence that GUA^+ is directly incorporated into the $MAPbI_3$ lattice.[336]

Nevertheless, in spite of the formation of a stable perovskite phase at room temperature in the case of MA/FA, FA/Cs (FA^+-rich case) and GUA/MA mixtures, GUA/FA mixtures follow another trend. Giorgi *et al.*[364] proposed through a theoretical analysis at 0 K that the mixed $FA_{(1-x)}GUA_xPbI_3$ becomes energetically favored in the perovskite phase; yet Kubicki *et al.*[336] through solid-state NMR studies revealed that although black $GUA_xFA_{(1-x)}PbI_3$ is formed, it is thermodynamically unstable, turning yellow within hours after annealing. Furthermore, mixtures of guanidinium with cesium, in different stoichiometries, are adopting layered crystal structures ($CsGUAPbI_4$, $CsGUAPbBr_4$ and $Cs_2GUAPb_2Br_7$) that are thermally stable and do not decompose up to 573 K.[369] In addition to this, a 2D perovskite structure of a mixture of formamidinium and guanidinium ($FAGUAPbI_4$), is thermally stable up to 528 K, exhibiting photoluminescence at room temperature and pronounced photoconductivity.[370] In an attempt to stabilize GUA/FA mixtures in the perovskite phase, compositions of triple cation mixtures have been proposed.[371, 372] For instance $(FA_{0.33}GUA_{0.19}Cs_{0.47}Pb(I_{0.66}Br_{0.34})_3$ and $(FA_{0.58}GUA_{0.10}Cs_{0.32}Pb(I_{0.73}Br_{0.27})_3$ have been proposed as possible candidates for tandem multijunction devices, since they have band gaps of 1.84 eV and 1.75 eV, respectively.[371] In addition to this, the incorporation of 2% of GUA^+ into $FA_{0.83}Cs_{0.17}PbI_3$ has been demonstrated to tailor the crystal structure resulting in an increment of the device efficiency from 14% to 17% under one sun illumination.[372] On the other hand, samples with less than 10% of GUA^+ doping exhibited a band gap around 1.54 eV, suitable for single-junction solar cells. Beyond that ratio the absorption of the films reduces as a consequence of the formation of δ-$FAPbI_3$-like and δ-$CsPbI_3$-like phases.[372] During thermal stability tests at 403 K for 5 h, in spite of no visible color change, XRD results indicate that all tested films were partially decomposed. However, an enhanced stability for 5% to 10% GUA^+ doping has been observed compared to lower doping concentrations. XRD, UV-VIS and SEM measurements showed that higher concentrations than 20% of GUA^+ doping leads to the formation of secondary δ-like phases.[372]

In this work, through a theoretical analysis, we investigate the relative stability of binary $GUA_xFA_{(1-x)}PbI_3$ mixtures with GUA^+ up to 50% and ternary $Cs_yGUA_xFA_{(1-y-x)}PbI_3$ mixtures with Cs^+ up to 17%. The relative stability of the mixtures with respect to the pure $FAPbI_3$, $GUAPbI_3$ and $CsPbI_3$ phases is calculated by estimating the free energy of mixing. In order to investigate any preferential stabilization of the perovskite phase over the non-perovskite one, not only the thermodynamical stable δ and α phases are considered, but also the kinetically stable β phase. In addition to this, we estimate the phase stability of the mixtures by calculating the relative energetics between the different phases. Our approach differs from the one followed by Giorgi et al.[364], where the absolute stability is calculated through the relative substitution energies, and only the α-$FAPbI_3$ perovskite phase was considered. For all mixed compounds the structural characteristics as well as the electronic properties, via band gap calculations, are determined.

5.3 Results and discussion

5.3.1 Stability

We employ DFT[254, 255] within the generalized gradient approximation employing the PBEsol[373] functional to estimate the relative stability at 0 K of the perovskite over the non-perovskite phase for $GUA_xFA_{(1-x)}PbI_3$ mixtures up to 50% of GUA^+ doping and $Cs_yGUA_xFA_{(1-y-x)}PbI_3$ up to 17% of Cs^+ and 50% of GUA^+ doping into the $FAPbI_3$ structure. Since $GUAPbI_3$ crystallizes into two non-perovskite phases,[365, 366, 374] as mentioned before, to compare the mixed perovskite compounds with the corresponding pure ones, we consider different 3D perovskite $GUAPbI_3$ phases that we constructed by substituting FA^+ by GUA^+ in the α and the β $FAPbI_3$ phases. We conclude that the structures with the lowest energy and thus the most stable ones at 0 K are arising from α-$FAPbI_3$ with GUA^+ molecules adopting identical orientations.

For the mixed cation systems, FA^+ has been successively replaced by GUA^+. In particular, for each stoichiometry in both the β and the δ phases, when allowed by the composition, we consider ten different possible positions and orientations for the substituted cations, starting from the previous lower GUA^+ content, in order to find the structure with the lowest energy. This scheme is only applied to the β perovskite phase and not to the α one, since the unit cell of the β phase consists of 144 atoms and allows for a larger configurational space. The structure as well as the cell of each composition is in turn fully relaxed using DFT calculations at 0 K. Once the lowest-energy β-$\mathrm{GUA}_x\mathrm{FA}_{(1-x)}\mathrm{PbI}_3$ and δ-$\mathrm{GUA}_x\mathrm{FA}_{(1-x)}\mathrm{PbI}_3$ structures are found, FA^+ is replaced by Cs^+, up to a concentration of 17% for the construction of ternary $\mathrm{Cs}_y\mathrm{GUA}_x\mathrm{FA}_{(1-y-x)}\mathrm{PbI}_3$ mixtures. The maximum standard deviation of the difference in energy per stoichiometric unit for different substitution pattern for each composition is of the order of 0.005 eV for the β and 0.006 eV for the δ phase, respectively.

This small energy difference among various substitution pattern can justify the use of the analytical formula for ideal alloys for the estimation of the mixing entropy contribution to the free energy, as given by Equation (5.1).[375]

$$T\Delta S_{mix} = -k_B T \sum_{i=1}^{N} c_i \ln c_i \tag{5.1}$$

where k_B is the Boltzmann constant, T is the temperature, N is the number of components and c_i is the atomic fraction of component i. Equation (5.1) reduces to Equation (5.2) for the triple $\mathrm{Cs}_y\mathrm{GUA}_x\mathrm{FA}_{(1-y-x)}\mathrm{PbI}_3$ cation mixture.

$$\begin{aligned} &T\Delta S_{phase}(Cs_yGUA_xFA_{1-y-x}PbI_3) = \\ &-k_BT[y\ln y + x\ln x + (1-y-x)\ln(1-x-y)] \end{aligned} \tag{5.2}$$

where y is the concentration of Cs^+, and x is the concentration of GUA^+ doped into the FAPbI_3 structure. On the other hand, the relative enthalpic contribution of the mixtures with respect to the pure FAPbI_3, GUAPbI_3 and CsPbI_3 compounds is computed by Equation (5.3). In both Equations 5.2 and 5.3 the subscript *phase* corresponds to one of the three, α, β or δ phases.

$$\begin{aligned} &\Delta E_{phase}(Cs_yGUA_xFA_{1-y-x}PbI_3) = \\ &E_{phase}(Cs_yGUA_xFA_{1-y-x}PbI_3) \\ &-[yE_{phase}(CsPbI_3) + xE_{phase}(GUAPbI_3) + \\ &(1-y-x)E_{phase}(FAPbI_3)] \end{aligned} \tag{5.3}$$

As one can see in Figure 5.1, where the enthalpic and mixing entropy contributions to the free energy are plotted as a function of x for the three phases, the replacement of the cations leads to a destabilization (energy increase) in the α phase for all $\mathrm{GUA}_x\mathrm{FA}_{(1-x)}\mathrm{PbI}_3$ compositions. However the permutational entropy contribution compensates this energetic penalty, thus cation mixing can take place in the α phase. On the other hand, in the δ phase, the mixture is only energetically destabilized for concentrations lower than 42%. However, the mixing entropy contribution is able to compensate this penalty for concentrations

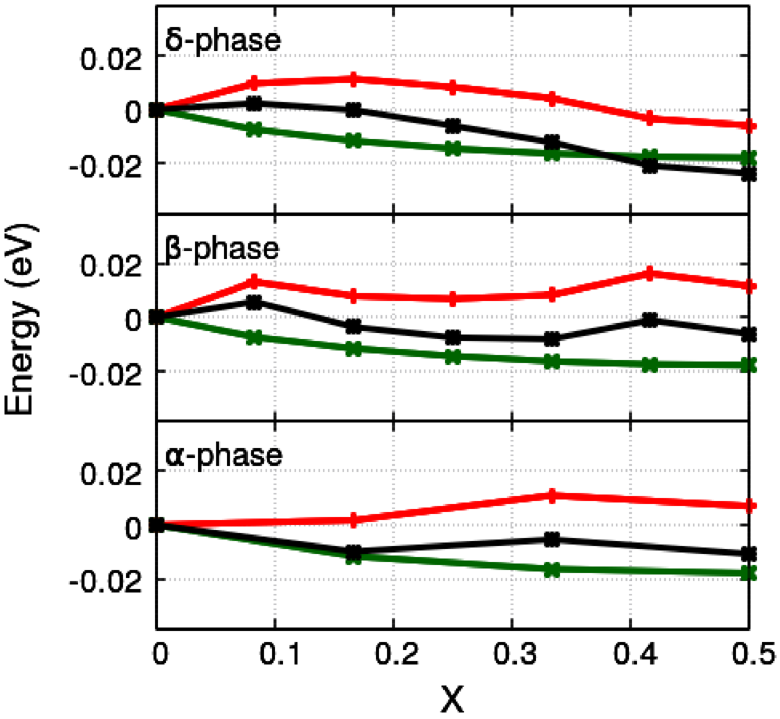

Figure 5.1: Variation of the free energy, which is expressed as ΔF = ΔE - TΔS (black line), the internal energy, ΔE (red line), and the mixing entropy contribution, -TΔS (green line), as a function of x GUA^+ ratio in $GUA_xFA_{1-x}PbI_3$ mixtures, for the α, β and δ phases, respectively.

higher than 16% and for lower concentrations the overall mixing free energies are essentially zero (certainly when considering the accuracy of the calculations and the variations due to different substitution pattern that are of the order of 0.006 eV). Finally, the β phase exhibits almost the same qualitative trend as the δ phase, apart from the fact that the replacement of cations leads to a destabilization for all $GUA_xFA_{(1-x)}PbI_3$ compositions. The mixing entropy contribution is again able to counterbalance this penalty for concentrations higher than 16%. These observations are in contrast to FA^+-rich FA/Cs mixtures where mixing leads to a preferential stabilization of the perovskite phase.[185]

To estimate the relative stability, the relative energetics at 0 K per stoichiometric unit between the δ and the β phases are shown for the binary $GUA_xFA_{(1-x)}PbI_3$ mixtures (Table 5.1). Mixing is not affecting significantly the relative stability of the two phases, with the δ phase always being the phase with the lowest energy at 0 K.

Table 5.1: Relative energetic stability expressed by $\Delta E_{a\delta} = E_a - E_\delta$ per stoichiometric unit of the β phase with respect to the δ phase upon doping of $FAPbI_3$ with GUA^+.

Fraction of GUA^+ doping into $FAPbI_3$ structure	Energy difference at 0 K with respect to δ phase (eV)
0%	0.10
8%	0.11
17%	0.10
25%	0.10
33%	0.12
42%	0.12
50%	0.13

An issue that demands further investigation is how the relative phase stability is evolving at finite temperature. Indeed, the vibrational entropy contribution can dramatically affect the phase stability but in the case of lead halide perovskites such corrections are not easy to be included since calculations of harmonic and quasi-harmonic phonons lead to imaginary modes.[332]

Therefore, to assess the relative phase stability at finite temperature, we performed ≈6 ps MD simulations at 300 K for both β and δ $GUA_{0.17}FA_{0.83}PbI_3$ phases. As shown in Figure 5.2 where equilibrated trajectories of 4.3 ps are used, we observe that at 300 K the mixture is more stable in the δ phase. This is consistent with the observation from solid state NMR measurements, where although black mixed-cation $GUA_xFA_{(1-x)}PbI_3$ phases do form, they are thermodynamically unstable and become yellow within hours from annealing.[336]

In contrast to the FA^+-rich FA/Cs mixtures, where mixing leads to a stabilization of the perovskite phase at room temperature,[185] the addition of GUA^+ into $FAPbI_3$ does not lead to a sufficient stabilization of the perovskite phase and the δ phase remains the thermodynamically most stable form. We also explored if this trend can be reversed through the addition of an additional cation. In particular, we tested the hypothesis if the energetic penalties induced by substitution of a large cation such as GUA^+ could possibly be balanced through addition of a small cation such as Cs^+. For this reason, we probed the possible stabilization in ternary $Cs_yGUA_xFA_{(1-y-x)}PbI_3$ mixtures, where we expect the permutational entropy to induce a further stabilization due to the addition of a third cation.

Figure 5.3(a), shows that in the δ phase, addition of 8% Cs^+ to $GUA_xFA_{(1-x)}PbI_3$ mixture with different GUA^+ content leads to an energetic destabilization, which is however compensated by the larger mixing entropy con-

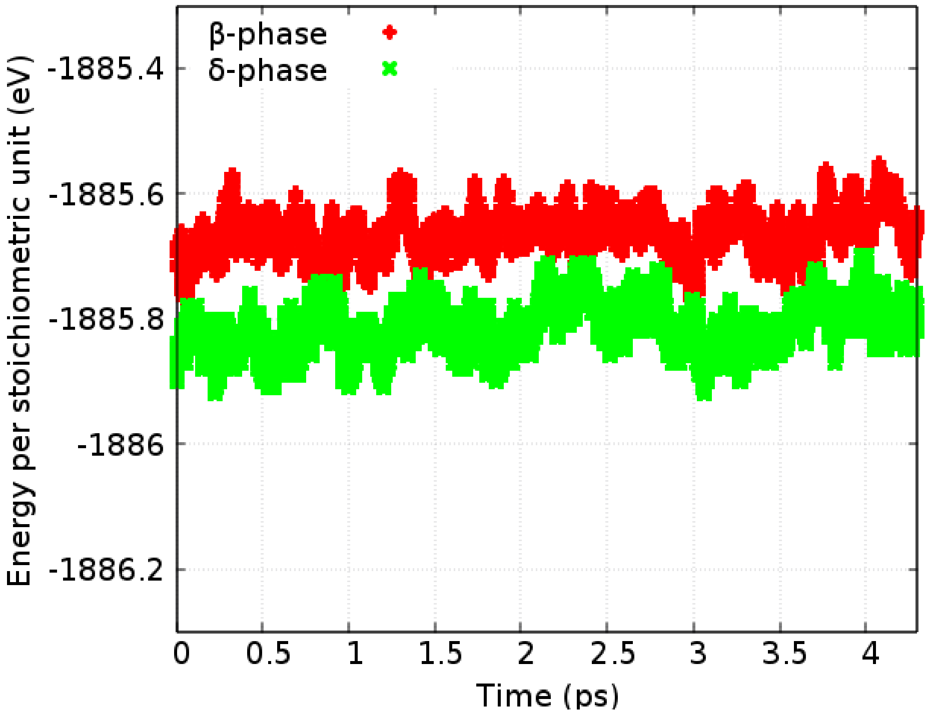

Figure 5.2: Potential energy per stoichiometric unit for both β and δ phases from first-principles based molecular dynamics simulations, in the NVT ensemble at 300 K.

tribution. For the β phase, on the other hand, mixing is energetically favorable or only slight disfavored (in the case of $x = 0.33$) and the permutational entropy induces a further stabilization. In contrast to the binary GUA/FA mixtures the stabilization is significantly larger in the perovskite phase than in the δ phase counterparts. This trend is further enhanced by adding 17% Cs^+ (Figure 5.3(b)). For the δ phase, mixing leads to an energetic destabilization that the mixing entropy contribution can no longer compensate. In contrast in the β-phase, mixing leads even to a slight stabilization especially for the lower GUA^+ concentration range and adding the mixing entropy contribution leads to a free energy that has negative values for all β-$Cs_yGUA_xFA_{(1-y-x)}PbI_3$ mixtures. It is worth mentioning that the pronounced stability of the ternary $Cs_yGUA_xFA_{(1-y-x)}PbI_3$ mixtures in the perovskite phase is consistent with the recent measurements for GUA^+ doping into $FA_{0.83}Cs_{0.17}PbI_3$. According to these measurements, a remarkable enhanced thermal stability of the perovskite phase is observed for 5% and 10% GUA^+ doping content.

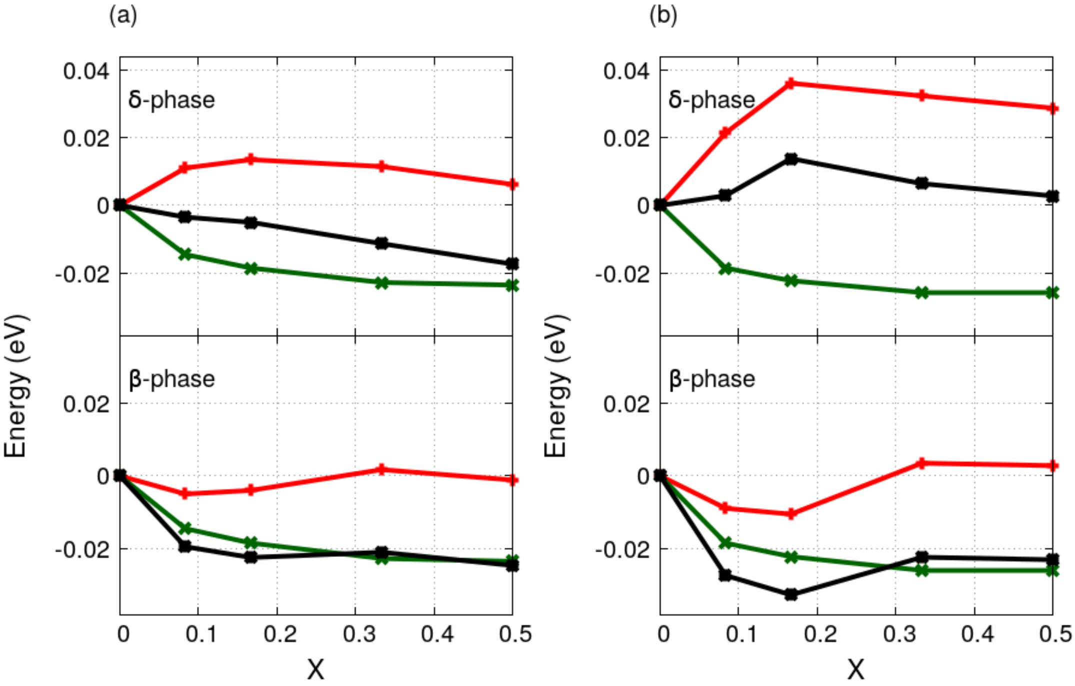

Figure 5.3: Variation of the free energy expressed as ΔF = ΔE - TΔS (black line), the internal energy, ΔE (red line), and the mixing entropy contribution, -TΔS (green line), as a function of x GUA^{+} ratio in $Cs_yGUA_xFA_{1-y-x}PbI_3$ mixtures, for the β and δ phases, respectively. (a) The concentration of Cs^{+} is 8% (y=0.08). (b) The concentration of Cs^{+} is 17% (y=0.17).

5.3.2 Structural characteristics

In FA^{+}-rich FA/Cs mixtures,[185] the preferred stabilization of the perovskite phase upon mixing has been rationalized in terms of the structural similarity or dissimilarity of the perovskite and the δ phases of the pure compounds, respectively. Here, we employ a similar analysis and trace the evolution of the volume per stoichiometric unit and average Pb-I-Pb angles upon mixing for different binary and ternary GUA/FA mixtures plotted in Figures 5.4, 5.6 and 5.7, 5.8, respectively.

As a function of x, the volume is increasing significantly for the δ and slightly for the β phase, while it remains almost the same for the α phase. The overall volume increase is consistent with the incorporation of a larger cation than FA^{+} into the lattice. Especially, in the case of the non-perovskite phase, the crystal structure consists of edge-sharing octahedra that are surrounded by monovalent cations. When GUA^{+} is incorporated into the lattice, it expands due to the presence of the larger cation that needs to be fitted in between the

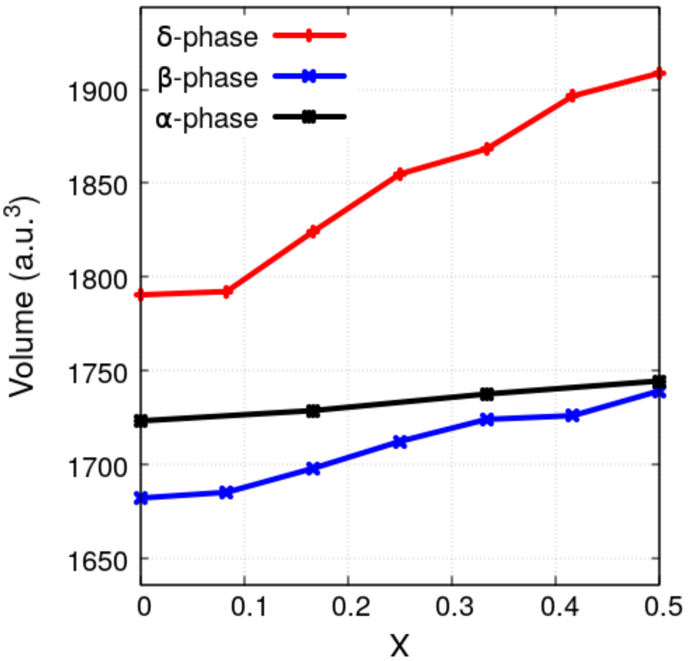

Figure 5.4: Volume evolution of $GUA_xFA_{1-x}PbI_3$ mixtures, upon GUA^+ doping into the $FAPbI_3$ lattice.

edge sharing octahedra. Similarly, in the case of the perovskite phases, the lattice expands isotropically, with this phenomenon being more pronounced in the beta phase. In Figure 5.5, the DFT optimized structures of pure $FAPbI_3$ and mixed $GUA_{0.5}FA_{0.5}PbI_3$ in the β phase are shown. Upon mixing, the beta phase, which is an orthorhombic phase, tends towards a more cubic like behavior and especially at 50% mixing concentration, the volumes of both α and β phases are almost the same (Figure 5.4). This is consistent with the trend of the volume evolution in the orthorhombic and the cubic like phases, where the incorporation of a larger cation in the former leads to an expansion of the lattice and an increased population at $\sim 0°$ tilting angle, while in the latter the incorporation of a larger cation is favored due to the larger cavities between the octahedra leading only to a further expansion of the lattice.[150]

This observation is also supported by the evolution of the average Pb-I-Pb angles. Figure 5.6 shows that for the β phase, the average angles tend to a more cubic like behavior with increasing GUA^+ content, in contrast to the results for the α phase where the angles remain almost unaffected since the structure is already cubic.

For the ternary $Cs_yGUA_xFA_{(1-y-x)}PbI_3$ mixtures, the volume evolution upon Cs^+ and GUA^+ doping into the $FAPbI_3$ lattice, for both Cs^+ concentra-

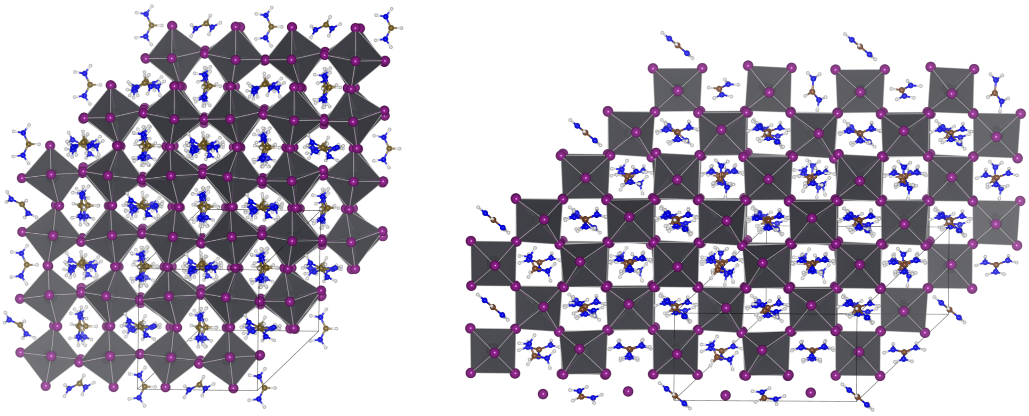

Figure 5.5: DFT optimized (a) β-FAPbI$_3$ and (b) β-GUA$_{0.5}$FA$_{0.5}$PbI$_3$ structures, illustrating that the structure becomes more cubic upon mixing.

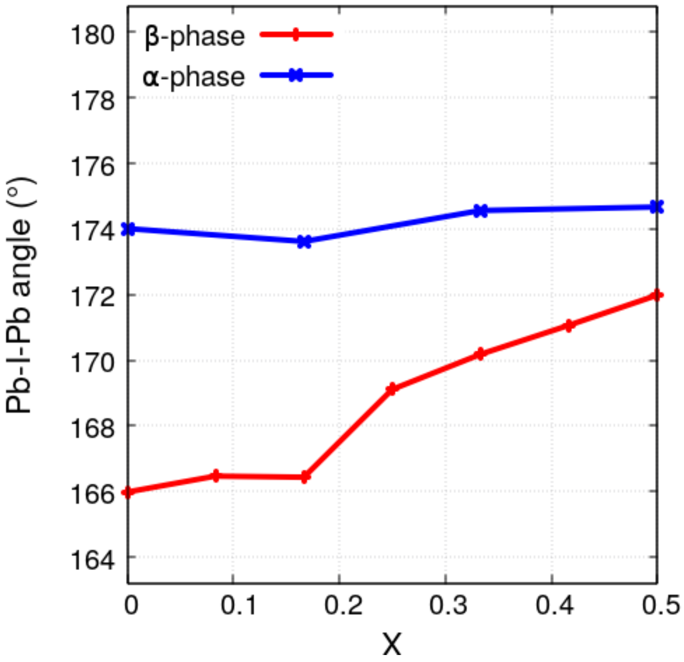

Figure 5.6: Average of Pb-I-Pb angle evolution of GUA$_x$FA$_{1-x}$PbI$_3$ mixtures, upon GUA$^+$ doping into FAPbI$_3$.

tions leads to an increase of the lattice volume, as shown in Figures 5.7(a) and 5.7(b), similar to the binary mixtures. This is consistent with the incorporation of a larger cation, however, it is important to take into consideration that

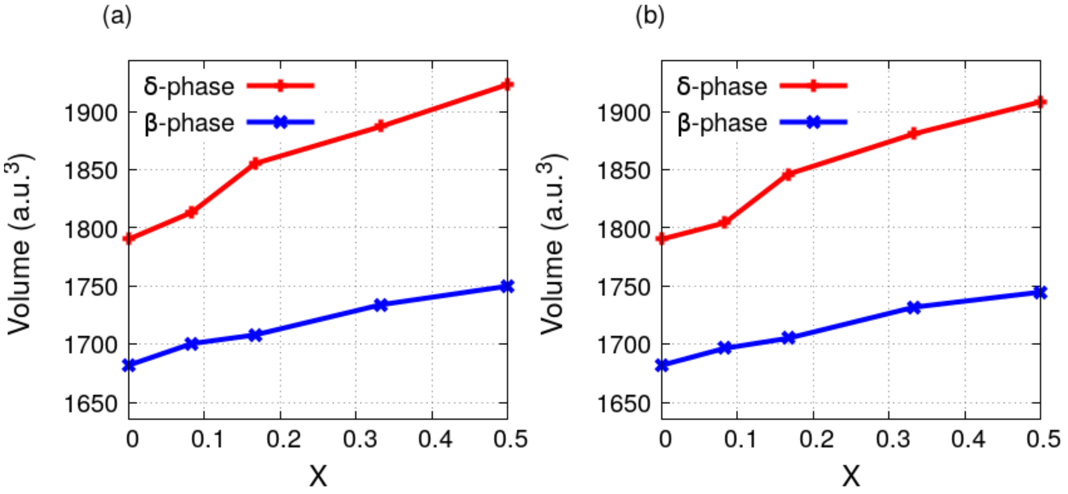

Figure 5.7: Volume evolution of $Cs_yGUA_xFA_{1-y-x}PbI_3$ mixtures. (a) The concentration of Cs^+ is 8% (y=0.08). (b) The concentration of Cs^+ is 17% (y=0.17).

the incorporation of both Cs^+ and GUA^+ cations counterbalances the overall volume increase to some degree, since the space required for the larger GUA^+ is compensated by the smaller space required by Cs^+. This observation seems to hold only for a concentration range which is similar for both cations. For GUA^+ concentrations that are higher than the Cs^+ counterparts, the main effect that influences the evolution of the volume of the lattice is related to the incorporation of the much larger GUA^+.

The volume increase is accompanied by a widening of the average Pb-I-Pb angles, as shown in Figure 5.8 proposing that the substitution of FA^+ by Cs^+ and GUA^+ leads to a more cubic-like structure.

5.3.3 Optical properties

Although the perovskite phase of some of the mixtures might only be metastable, it is important to understand how mixing affects the optical properties. To this end, calculations have been performed using different protocols. For the calculations of the energetics, the proposed modification designed specifically for solids, PBEsol[373], has been employed. In previous work,[151] we showed that PBEsol provides volumes in excellent agreement with the experimental results and a negligible deviation of the individual lattice constants.[151] In addition, it has been shown that PBE without including spin-orbit coupling (SOC) effects accurately predicts the band gap of organic-inorganic halide perovskites.[349, 350] This happens due to error cancellations between spin orbit coupling and many-body effects described *e.g.* by means of GW-self energy

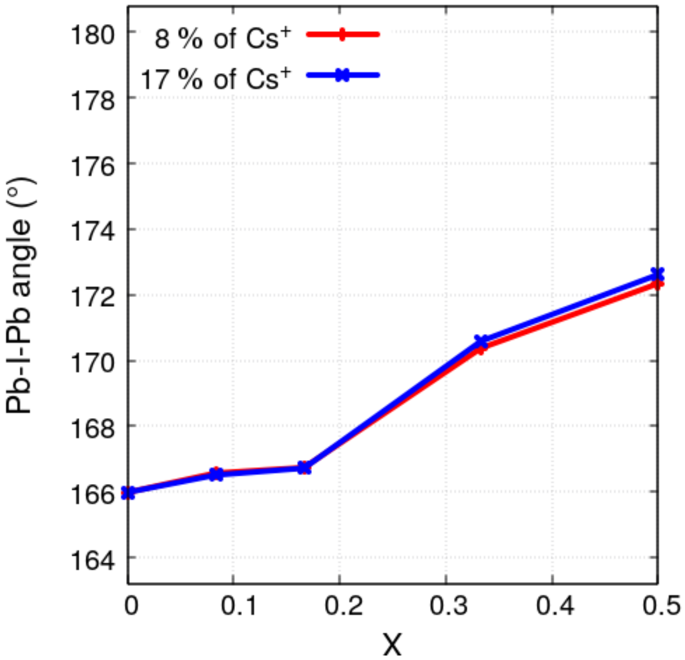

Figure 5.8: Average of Pb-I-Pb angles evolution as a function of x for $Cs_yGUA_xFA_{1-y-x}PbI_3$ mixtures, upon Cs^+ and GUA^+ doping into $FAPbI_3$.

correction.[376]

However, for a more accurate description of the band gaps, we employ the hybrid functional PBE0 and take spin orbit effects explicitly into account.[377] The results are summarized in Table 5.2.

Table 5.2: Band gaps of $GUA_xFA_{1-x}PbI_3$ mixtures upon mixing including spin-orbit coupling effects.

Fraction (x) of GUA^+ doping into $FAPbI_3$ structure	β-$GUA_xFA_{1-x}PbI_3$ Band gap (eV) PBE0 + SOC	α-$GUA_xFA_{1-x}PbI_3$ Band gap (eV) PBE0 + SOC
0%	1.47	1.41
8%	1.46	
17%	1.48	1.60
25%	1.43	
33%	1.44	1.63
42%	1.44	
50%	1.45	1.65

The calculated band gap for pure α-$FAPbI_3$ is in good agreement with the experimental results.[145, 312, 316] In case of α-$GUA_xFA_{(1-x)}PbI_3$ a slight red shift is observed upon mixing, as shown in Table 5.2. This is consistent with previous studies, where a volume increase in the cubic phase leads to a widening of the band gap.[150] Nevertheless, in case of β-$GUA_xFA_{(1-x)}PbI_3$, the band gap remains almost unaffected upon mixing and is very close to the single-junction optimum. However, as shown above, mixtures in the β phase are thermodynamically unstable.

For this reason, we also computed the band gaps of the triple cation $Cs_yGUA_xFA_{(1-y-x)}PbI_3$ mixtures. As can be seen in Table 5.3, the band gaps of both β-$Cs_{0.08}GUA_xFA_{(0.92-x)}PbI_3$ and β-$Cs_{0.17}GUA_xFA_{(0.83-x)}PbI_3$ compounds are comparable, with a maximum standard deviation of 0.05 eV. Apart from that, the estimated band gaps are close to the single-junction optimum. Given that for β-$Cs_{0.17}GUA_xFA_{(0.83-x)}PbI_3$ systems, mixing in the perovskite phase seems favorable for low GUA^+ concentrations, such compounds could be potential candidates for efficient solar cell applications. However, it has been observed experimentally that for concentrations of GUA^+ higher than 10%, the absorption of the film reduces considerably due to the formation of secondary δ phases and leads to an additional absorption peak at $\approx$ 600 nm for GUA^+ concentrations higher than 20%.[372] If under certain preparation condition $Cs_yGUA_xFA_{(1-y-x)}PbI_3$ mixtures can be stabilized, their optical properties are very interesting and these materials should be further investigated as candidates for solar cell applications.

Table 5.3: Band gaps of β-$Cs_{0.08}GUA_xFA_{0.92-x}PbI_3$ and β-$Cs_{0.17}GUA_xFA_{0.83-x}PbI_3$ mixtures upon mixing including spin-orbit coupling effects.

Fraction (x) of GUA^+ doping into $FAPbI_3$ structure	β-$Cs_{0.08}GUA_xFA_{0.92-x}PbI_3$ Band gap (eV) PBE0 + SOC	β-$Cs_{0.17}GUA_xFA_{0.83-x}PbI_3$ Band gap (eV) PBE0 + SOC
0%	1.47	1.41
8%	1.48	1.47
17%	1.48	1.47
33%	1.44	1.43
50%	1.46	1.44

5.4 Conclusions

We have demonstrated that in contrast to FA^+-rich FA/Cs mixtures,[185] in binary $GUA_xFA_{(1-x)}PbI_3$ mixtures, the addition of GUA^+ alone into $FAPbI_3$

does not sufficiently stabilize the perovskite phase. In contrast, a slight stabilization of the δ phase for GUA^+ concentrations higher than 33% is observed. Consistently, molecular dynamics simulations performed at room temperature reveal that the binary mixtures are more stable in the δ phase. This observation is in agreement with recently published experimental results.[336] Since mixing with one additional monovalent cation is not sufficient for stabilising the perovskite phase, at difference to MA/FA, FA^+-rich FA/Cs, and GUA/MA mixtures, we also examined the phase stability of triple $Cs_yGUA_xFA_{(1-y-x)}PbI_3$ cation mixtures for both 8% and 17% of Cs^+ concentration. It turns out that for 8% of Cs^+, mixing is favorable in both β and δ phases with the stabilization in the β phase being more pronounced. However, for 17% of Cs^+, mixing only favors the perovskite phase, suggesting that the inclusion of a third cation into an unstable or metastable binary mixture could pave the way for materials that are thermodynamically stable in the perovskite phase at room temperature. Estimating the resulting structural characteristics upon mixing, we propose that the inclusion of a larger cation leads to a volume increase and structures with cubic-like characteristics. Band gap calculations show a slight widening for the α phase of the binary mixtures. On the other hand, for the ternary mixtures, the band gap remains unaffected upon mixing and close to the single-junction optimum. Taking into account the pronounced stabilization of the perovskite phase for mixtures with 17% of Cs^+, cells based on these materials could constitute possible candidates for single-junction solar cells as also demonstrated in recent experiments.[372]

5.5 Computational details

DFT calculations[254, 255] have been performed using the Quantum Espresso suite of codes.[351, 352] DFT in the proposed modification of PBE designed specifically for solids, PBEsol[373] formulation has been used for geometry and cell relaxations. The band gaps of the binary and ternary perovskite mixtures were calculated using the hybrid functional PBE0,[377] with taking spin orbit effects (PBE0+SOC) into account. The Kohn-Sham orbitals are expanded in a plane wave basis set with a kinetic energy cutoff of 40 Ry and a density cutoff of 240 Ry. The Brillouin zone is sampled with a Monkhorst Pack **k**-points grid[354] that varies from 2x2x2 for cell and geometry relaxation calculations up to 6x6x6 for band structure calculations. All values have been chosen after performing convergence tests for the total energy, the band gap, the pressure, the stresses and the atomic forces. Ultrasoft pseudopotentials are used for the interactions between valence electrons, core electrons and nuclei.[353] On the other hand, fully relativistic norm-conserving pseudopotentials[353] are used in PBE0+SOC calculations and Kohn-Sham orbitals are expanded in a plane wave basis set with a kinetic energy cutoff of 80 Ry and a density cutoff of 320 Ry. To compare the absolute energy of Kohn-Sham orbitals, we followed the protocol suggested by Meloni *et al.* in which the energies were aligned with respect to the energy of the Pb_{5d} semicore state.[150]

Car-Parrinello molecular dynamics simulations in the NVT ensemble at 300 K were performed using the CPMD code[356] for systems of 150 atoms. The wavefunction cutoff was set to 90 Ry and Goedecker normconserving pseudopotentials were used.[357–359] A time step of 3 a.u. was used with a fictitious mass parameter of 550 a.u.. The temperature was controlled by five different Nosé-Hoover thermostats, one for each species, with a coupling frequency of 1500 cm^{-1}.[360–362]

To estimate the relative energetics of the different phases at 0 K, the alignment procedure demands the same number of stoichiometric units. For this reason, the δ and the β phases' superlattices contain 12 stoichiometric units since the crystal structure of β-phase consists of 12 stoichiometric units (144 atoms). It was not possible to employ δ-$GUAPbI_3$ since there is no way to create supercells that could have the same number of stoichiometric units with the β phase. For this reason, we prepared δ-$GUAPbI_3$ structures starting from the known δ-$FAPbI_3$ and δ-$CsPbI_3$ structures by substituting FA^+ or Cs^+ by GUA^+. We conclude that the pure δ-$GUAPbI_3$ structure, constructed from the δ-$CsPbI_3$ by substituiting Cs^+ with GUA^+ is the lowest in energy and in turn the structure that was used in our calculations. One should also mention here that both experimental δ-$GUAPbI_3$ and δ-$CsPbI_3$ structures consist of edge-sharing octahedra that are surrounded by the cations. For the preparation of the mixtures, for each stoichiometry, when allowed by the composition, we considered 10 different possible replacements starting from the best configuration at the previous next lower GUA^+ content. We also performed calculations with different GUA^+ and FA^+ orientations, where the maximum standard deviation of the difference in energy per stoichiometric unit is of the order of 0.007 eV. In the α phase the structure consists of 6 stoichiometric units instead. Finally, the ternary $Cs_yGUA_xFA_{(1-y-x)}PbI_3$ mixtures were prepared by substituting FA^+ with Cs^+ in the lowest-energy structure of both δ-$GUA_xFA_{(1-x)}PbI_3$ and β-$GUA_xFA_{(1-x)}PbI_3$. The protocol discussed above was also employed for structure and cell relaxation and band gap calculations.

Chapter 6

Molecular origin of the asymmetric photoluminescence spectra of $CsPbBr_3$ at low temperature

Chapter 6 is a pre-print version of an article in preparation as:

Ariadni Boziki, M. Ibrahim Dar, Michael Grätzel, and Ursula Rothlisberger. Molecular origin of the asymmetric photoluminescence spectra of $CsPbBr_3$ at low temperature. *In preparation.*

My contribution: Performance of all the calculations and simulations, interpretation of the results as well as preparation of the manuscript.

6.1 Abstract

$CsPbBr_3$ has received wide attention due to its superior emission yield and better thermal stability compared to other organic-inorganic lead halide perovskites. In this study, through an interplay of theory and experiments we investigate the molecular origin of the asymmetric low temperature photoluminescence (PL) spectra of $CsPbBr_3$. We conclude that this phenomenon is due to the preferential localization of Cs^+ in either of the two off-centre positions of the interstitial space between the surrounding PbI_6 octahedra. With increasing temperature, the Cs^+ are gradually occupying positions more and more near the centre of the cavities. Finally, the gradual loss of ordering in the Cs^+ position with increasing temperature is the driving force for the formation of tetragonal-like arrangements within the orthorhombic lattice.

6.2 Introduction

Hybrid organic-inorganic lead halide perovskites have received much attention due to their broad spectrum of applications as promising materials for solar cells,[60–63, 65] LEDs,[131–133] lasers,[138, 139] resistive-switching memories,[210, 212] X-ray image detectors[213, 214] and piezoelectric energy generators.[217] Among the different halide perovskite compounds, $CsPbBr_3$ has recently attracted wide interest due to its superior emission yield and better thermal stability compared to other organic-inorganic lead halide perovskites.[209, 303, 378–380] Till now, a variety of LED devices and lasers based on $CsPbBr_3$ have been realized.[381–384] However, despite the rapid progress in material synthesis and device fabrication, the understanding of the fundamental properties of $CsPbBr_3$ is still evolving.[303, 385–388] For the identification of its potential for several technological applications, it is important to gain further insight into the interplay of the photophysical processes and the structural characteristics of $CsPbBr_3$.

Indeed, many of the properties of $CsPbBr_3$ have been known for over 60 years.[148] It is well-known that $CsPbBr_3$ undergoes two phase transitions, one at 361 K from an orthorhombic to a tetragonal phase and a second one at 403 K from the tetragonal to a cubic phase, respectively.[389] In addition to this, absorption spectroscopy suggests that the compound is a direct semiconductor with a band gap that lies within the range of 2.25 eV - 2.36 eV, as measured by different groups.[303, 308] The exploration of the emission characteristics across a wide temperature range, can provide important information regarding the performance of solar cells and LED devices under realistic conditions. Previous studies have reported that temperature-dependent PL measurements for MAPbI$_3$ and MAPbBr$_3$ exhibit a double emission peak at low temperatures.[329, 390–392] The two PL peaks are associated to MA-ordered and MA-disordered tetragonal domains with different emission characteristics due to the presence/absence of a Stark effect induced by the dipolar field of the organic cations.[329] However, for CsPbBr$_3$, there seem to exist a disagreement between experimental results concerning the presence, respectively absence of a double emission peak.[303, 393–397] Stoumpos *et al.*[303] reported that in PL measurements at 46 K, two emission peaks are observed at 2.29 and 2.31 eV, respectively. Similarly, Lee *et al.*,[396] observed an asymmetry of the PL spectra of CsPbBr$_3$ quantum dots for temperatures lower than 250 K, which was attributed to a side-peak emission that is located at a lower energy than the band-edge peak. The authors rationalized this anomalous splitting of the emission peak at temperatures $\leq$ 250 K with a phase transition of the crystal structure. On the other hand, Han *et al.*[394] performed temperature-dependent PL measurements for CsPbBr$_3$ nanocrystals in the temperature range of 80 to 270 K, and observed a spectral band which is approximately symmetric with no obvious double emission peak.

Here, we approach this problem from a combined theoretical and experimental perspective. With the help of first-principles molecular dynamics simulations and temperature-dependent PL experiments, we investigate the asymmetric PL spectra of CsPbBr$_3$ at low temperatures. Our first-principles molecular dynamics simulations show that at low temperature the Cs$^+$ cation occupy asymmetric positions that are gradually shifted to the centre of the cavities with increasing temperature. Our investigation thus provides new insights into the interplay between the photophysical processes and the structural characteristics of CsPbBr$_3$ at temperatures below the first phase transition ($\leq$ 361K).[389]

6.3 Results and Discussion

We performed ab initio molecular dynamics simulations within the Car-Parrinello molecular dynamics scheme,[290] employing the NVT ensemble for a range of different temperatures (50, 100, 120, 150, 200 and 300 K, respectively) using a real-space super cell of 240 atoms. The band gap of this real-space cell at 0 K is 2.07 eV compared to the fully **k**-point converged value of 2.14 eV. Equilibrated trajectories of approximately 4 ps for temperatures at 50, 100, 120, 150 and 200 K as well as an equilibrated trajectory of 12 ps at 300 K were produced. The analysis of these trajectories allows us to determine the finite-temperature band gap of CsPbBr$_3$ by calculating the maximum of the peak and the standard deviation of the thermal distribution at each temperature.

As shown in Figure 6.1 the band gap increases as a function of temper-

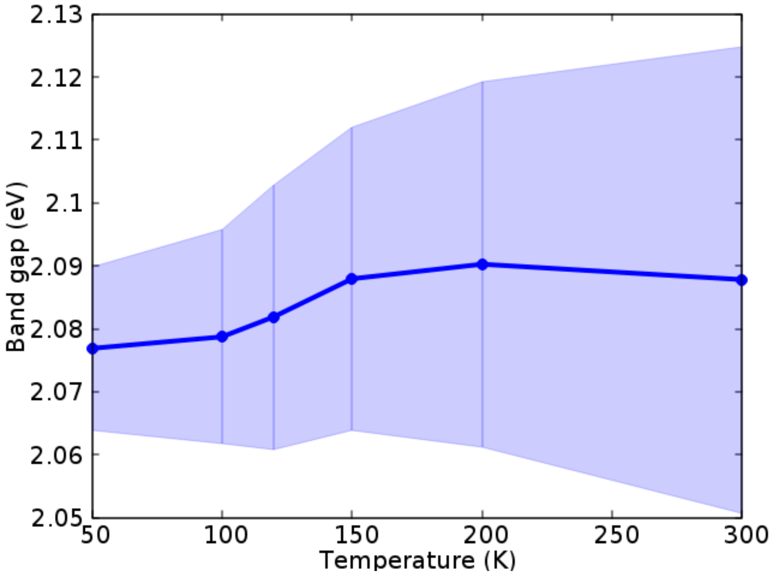

Figure 6.1: Thermal evolution of the average Kohn-Sham band gap of $CsPbBr_3$ from ab initio molecular dynamics simulations.

ature. This behavior of lead-halide perovskites is well-known[329] due to the decrease in orbital antibonding overlap of the divalent cations and anions due to thermal fluctuations, but at variance to the behavior of classical Varshni semiconductors. In addition, the band gap does not increase as a linear function of temperature as shown in Figure 6.1. In fact, the variation of the band gap as a function of temperature can roughly be divided into two regimes with a change of slope, which takes place around a temperature range of 100 to 150 K. This change in slope is similar to the case of $MAPbI_3$ and could thus be associated with two different microscopic environments. To confirm such hypothesis, we also performed temperature-dependent time-integrated and time-resolved PL measurements in film samples. The temperature-dependent emission shown in Figure 6.2a shows an asymmetric peak at low temperatures (< 180 K), which vanishes with increasing temperature. To compare the finite-temperature band gap that we calculated by performing molecular dynamics simulations with experimental values, we plotted the shift of the maximum of the PL bands in Figure 6.2a as a function of temperature (Figure 6.2b). Indeed, as predicted by the calculations, a change of slope around 120 K is also observed.

Dual emission behavior has been observed for organic-inorganic halide perovskites where it is attributed as mentioned above to MA^+ disordered tetragonal domains with different emission characteristics due to the presence/absence of a Stark effect induced by the dipolar field of the organic cations.[329] However,

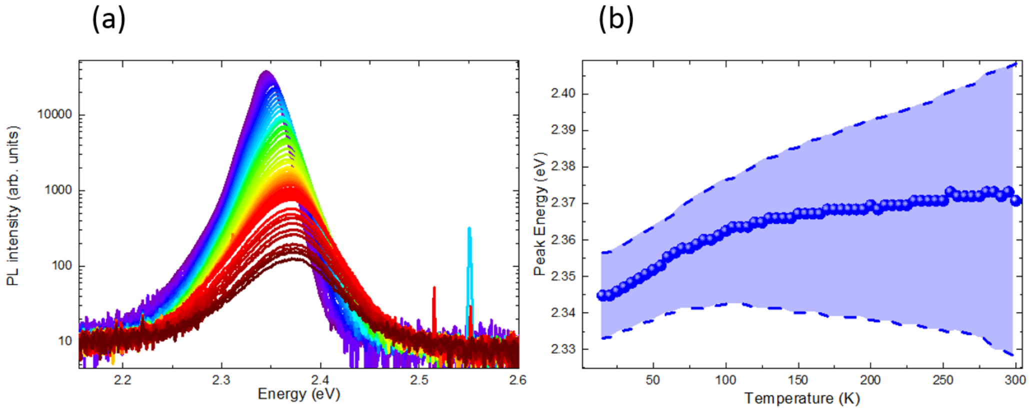

Figure 6.2: Temperature-dependent emission characteristics of CsPbBr$_3$. (a) Temperature-dependent PL spectra of CsPbBr$_3$. The transition from purple to brown color corresponds to an increase of temperature from 15 K to 300 K. (b) The shift of the maximum of the PL bands as a function of temperature.

in the case of purely inorganic CsPbBr$_3$, it is not obvious what the molecular origin could be. For this reason, we analyzed the data from the first-principles MD simulations to identify the structural characteristics of CsPbBr$_3$ at different temperatures.

In Figure 6.3 two local structures extracted from the trajectories at 50 K and 300 K, respectively are shown. We observe that at 50 K (Figure 6.3(a)), the Cs$^+$ ions show a particular pattern when occupying the empty space between the octahedra. This pattern can be described by two different alternating layers, each of them consisting of a series of horizontally aligned Cs$^+$ occupying either of the two off-centre positions as shown in the right-hand side of Figure 6.3(a). This effect is obvious only when looking along one direction of the lattice. By observing the lattice from the other two directions, Cs$^+$ are forming only one layer, their position being near to the centre of the empty space between the octahedra. At higher temperatures this ordered behavior vanishes and at 300 K, Cs$^+$ are occupying positions near the centre of the cavities with respect to all three lattice directions.

Given that CsPbBr$_3$ adopts an orthorhombic structure at temperatures lower than 361 K, we expect the Pb-Br-Pb angle distribution to be represented by angles that deviate from 180°. This is indeed the case for temperatures ≤ 150 K, where the angle distributions have symmetric Gaussian forms, as shown in Figure 6.4. However, for temperatures higher than 200 K the angle distributions are getting asymmetric. Especially at 300 K the percentage of Pb-Br-Pb angles around 180° is starting to get significant, consistent with the formation of pseu-

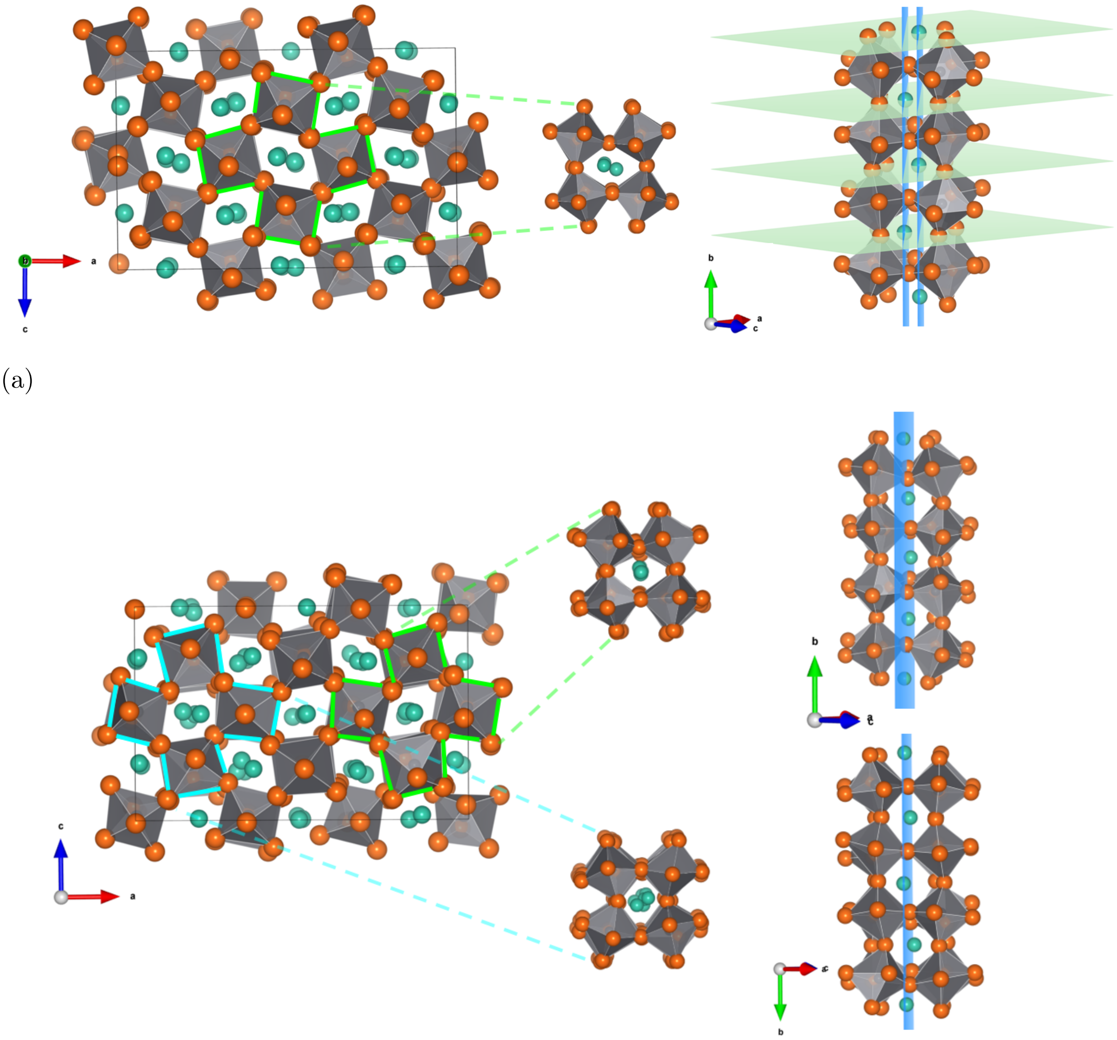

(a)

(b)

Figure 6.3: Local structures. At left-hand side, snapshots of the simulation box are shown, where specific areas are selected and projected, by orienting the a, b and c axis differently, (shown on the right hand side). (a) Local structure of the 50 K trajectory. The position of Cs^+ in the empty space between the octahedra has a characteristic pattern, where each Cs^+ that belongs to a specific layer (light green layers shown at the right-hand side of the figure), is shifted towards the opposite direction of the Cs^+ that belongs to the next neighboring (light green) layer, creating two distinct layers (light blue) of Cs^+. (b) Local structure of the 300 K trajectory. Cs^+ are occupying positions which are more and more near to the centre of the cavities.

dotetragonal domains within the orthorhombic crystal structure of $CsPbBr_3$.

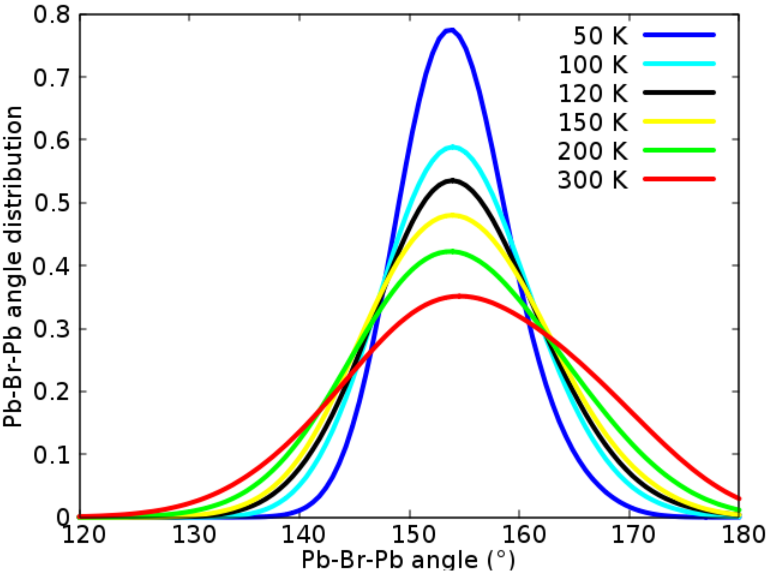

Figure 6.4: Thermal evolution of the Pb-Br-Pb angle distributions. The data have been fitted by employing Gaussian functions.

In order to quantify the amount of pseudotetragonal domains formed in the lattice as a function of temperature, we consider the fraction of Pb-Br-Pb angles that lie in the range of [160°, 180°]. In Figure 6.5, we plot the fraction of pseudotetragonal domains defined in this way as a function of temperature. As expected, the fraction of tetragonal-like arrangements increases with temperature from 0.1 to 0.34 in between 50 and 300 K. The adoption of tetragonal-like arrangements with increasing temperature does not correspond to a phase transition to the tetragonal structure since on average the phase that $CsPbBr_3$ adopts is still orthorhombic. This phenomenon can be explained by the existence of a double well potential in which the Cs^+ moves. On the top of the barrier of this double well potential, the Cs^+ occupies the central position between the octahedra leading to local structures with tetragonal-like arrangements that start to be populated at higher temperatures. At lower temperatures ($k_BT \ll$ as the barrier), the Cs^+ occupies either of two off-centre sites that corresponds to the minima of the double well.

To support these arguments, we also analyzed the Cs-Pb distance distribution shown in Figure 6.6. At low temperatures, the distribution of the nearest-neighbor Cs-Pb distance is characterized by two distinct peaks. However, with increasing temperature the second peak starts to vanish leading finally at 300 K to a (slightly asymmetric) unimodal Cs-Pb distance distribution con-

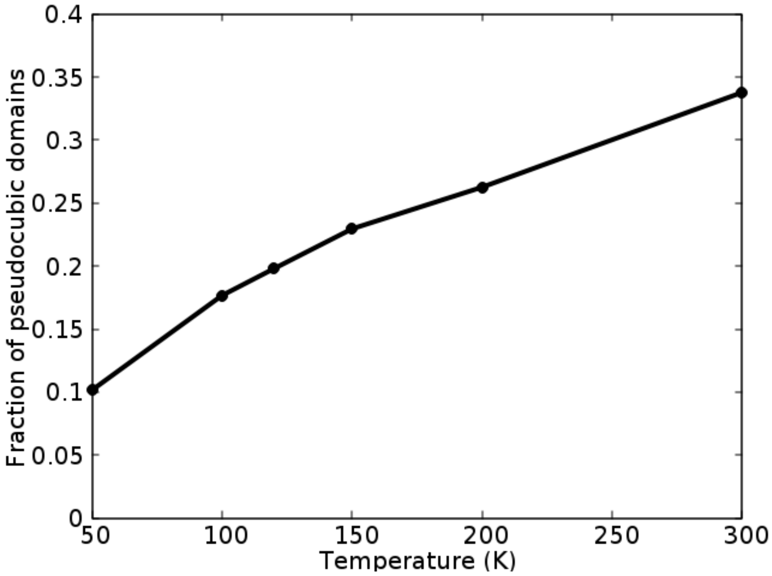

Figure 6.5: Fraction of pseudotetragonal domains in the orthorhombic structure of $CsPbBr_3$ as a function of temperature.

sistent with configurations in which the Cs^+ occupies a position near the centre of the interoctahedral cavities. This temperature dependent change in the localisation of the Cs^+ ions could be the rationale for the gradual transition of the experimental PL spectra from an asymmetric band at low temperature to a symmetric form at higher temperature accompanied by a change in the slope of the finite-temperature band gap.

6.4 Conclusions

PL spectra of $CsPbBr_3$ have been recorded over a temperature range of 15 to 300 K. The low temperature ($<$ 180 K) bands show a pronounced asymmetry that is lost with increasing temperature. Similarly, the measured band gap exhibits a change of slope around 15-150 K. Using first-principles MD simulations we have been able to identify the molecular origin of these effects. We conclude that their origins lie in a local dipole moment (*i.e.* Stark effect) that the isotropic Cs^+ produces when displaced away from the center of the cavity, due to a preferential localization of it in either of two off-centre sites in the empty space between the octahedra that appears at low temperatures. At higher temperatures this effect vanishes and the Cs^+ assumes positions more and more near the centre of the cavities leading to an increment of tetragonal-like arrangements within the orthorhombic phase of $CsPbBr_3$. Finally, the popula-

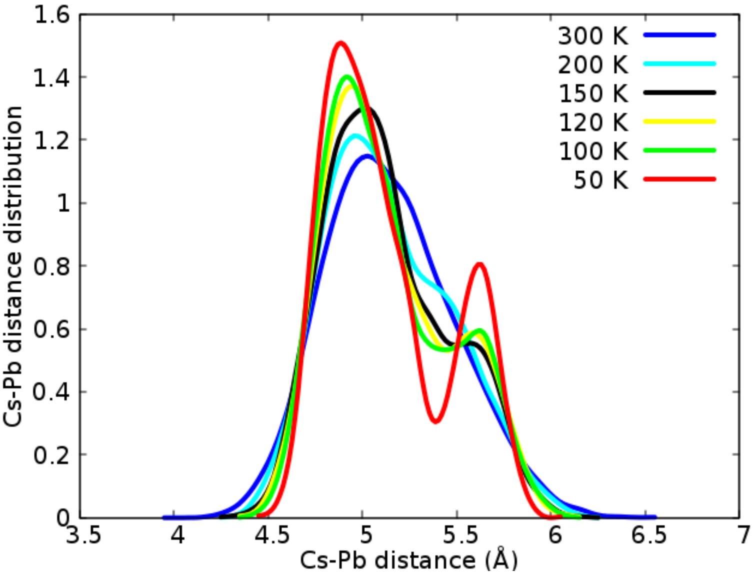

Figure 6.6: Thermal evolution of the nearest Cs-Pb distance distribution. The data have been fitted by employing Gaussian functions.

tion of pseudotetragonal domains is not correlated with a phase transition from the orthorhombic to tetragonal phase since the average structure of all the local structures that contain these pseudotetragonal arrangements still maintains the orthorhombic phase of $CsPbBr_3$.

6.5 Computational details

Car-Parrinello molecular dynamics simulations[290] in the NVT ensemble at 50, 100, 120, 150, 200 and 300 K, respectively, were performed using the CPMD code.[356] The wavefunction cutoff was set to 90 Ry and Goedecker normconserving pseudopotentials were used.[357–359] A time step of 5 a.u. was used with a fictitious mass parameter of 800 a.u.. The temperature in the simulations was controlled by a Nosé-Hoover thermostat with a coupling frequency of 1000 cm^{-1}.[360–362] The values of the plane wave cutoff and the mass parameter selected, after performing convergence tests. The coupling frequency of the thermostat was selected after performing tests about the equilibration of the trajectories.

Using the Quantum Espresso suites of codes,[351, 352] a band gap calculation at DFT/PBE level,[254, 255] at 0 K was performed, employing a 4x4x4 Monkhorst-Pack **k**-points grid to sample the Brillouin zone.[354] Molecular dynamics simulations were performed at the Gamma point only with a real-space cell containing 240 atoms. This size was the bigger cell that could be used in MD simulations and was able to reproduce sufficiently enough the band gap of the fully converged **k**-sampled band structure calculation (2.07 eV vs 2.14 eV). The generalized gradient approximation to density functional theory in PBE formulation has been used.[327] In case where the Quantum Espresso suites of codes were used, the interactions between valence electrons, core electrons and nuclei are described by ultrasoft pseudopotentials.[353] The Kohn-Sham orbitals are expanded in a plane wave basis set with a kinetic energy cutoff of 40 Ry and a density cutoff of 240 Ry. The above values have been chosen after having performed convergence tests for the total energy, the band gap, the pressure, the stresses and the atomic forces.

6.6 Experimental details

Materials : $PbBr_2$ (TCI), CsBr (Alpha Aesar), and N,N-dimethylformamide (Acros Organics). All chemicals were used as received unless stated otherwise.

Preparation of Al_2O_3 substrates : Al_2O_3 films were deposited on a non-conducting glass substrate by spin coating diluted Al_2O_3 paste (1:3.5 wt. ratio in ethanol) composed of 30 nm Al_2O_3 nanoparticles at 5000 rpm with an acceleration of 2000 rpm for 30 s). 250 nm-thick mesoporous Al_2O_3 films were obtained by sintering the substrates at 450 °C for 30 min in dry air.

Deposition of $CsPbBr_3$ films : Solution-based sequential method was used to deposit the $CsPbBr_3$ films onto 250 nm-thick mesoporous Al_2O_3 substrates under controlled atmospheric conditions with humidity $<1\%$. Typically, 50 μL of 1 M $PbBr_2$ dissolved in N,N-dimethylformamide was spin coated onto mesoporous substrates at 5000 rpm (acceleration 2000 rpm) for 30 s. After heating at 70 °C for 30 minutes, the $PbBr_2$ films were obtained, which were dipped subsequently into CsBr (Alpha Aesar) solution (17 mg/mL in methanol) at 60 °C for 10 minutes. Finally, after annealing at 250 °C for 10 minutes, the $CsPbBr_3$ samples were obtained.

Spectroscopic characterization : Temperature-dependent time-integrated and time-resolved PL spectroscopy was used to analyze the $CsPbBr_3$ perovskite film sample supported onto mesoporous Al_2O_3 substrate. The samples were excited with the second harmonic ($\sim$ 425 nm) of a picosecond mode-locked Ti/sapphire laser (80.5 MHz), and the excitation beam was focused on the sample by means of a 90-mm focal. The collected emission spectra were spectrally and temporally analyzed, respectively, using a 32-cm focal length monochromator equipped with a charge-coupled device (CCD), which has a spectral resolution of $>$1 meV and a streak camera with a temporal resolution of $\sim$ 20 ps.

Chapter 7

Simulations of the ultrafast transient absorption dynamics and of the possible formation of polarons in $CsPbBr_3$

Chapter 7 is a summary of preliminary results on
the simulations of transient absorption spectra
and on the possible formation of polarons in $CsPbBr_3$.

7.1 Abstract

Simulations of the transient absorption spectra of $CsPbBr_3$ can give answers to some open issues concerning the nature and the dynamics of the photoexcited state of lead halide perovskites. Our results reveal that properties such as the finite temperature band gap, and the Stokes shift and therefore also the transient absorption spectra of $CsPbBr_3$ are strongly size-dependent. Finally, the difference in density between the electronic excited and ground states shows temporary charge localization (of both electrons and holes) at room temperature due to thermal fluctuations.

7.2 Introduction

Characterization of the nature of the excited states of organic-inorganic halide perovskites is an important ingredient for further optimization, as excited state processes can crucially affect the optoelectronic performance of these solar-cell devices. Among the different hybrid organic-inorganic halide perovskites,[60–63, 65] $CsPbBr_3$ is especially suited for investigations of the excited state dynamics via transient absorption spectroscopy experiments due to its higher stability under ambient conditions compared to other organic-inorganic lead halide perovskites.[209, 303, 378–380, 385, 398–400]. The large band gap of $CsPbBr_3$ that lies within the range of 2.25 eV - 2.36 eV, according to measurements performed by different groups, prevents direct application in solar cells but,[303, 308] $CsPbBr_3$ is instead a promising material for LEDs and lasers.[381–384] Despite the rapid progress in device fabrication, a thorough understanding of the fundamental nature of the excited states of $CsPbBr_3$, and of the organic-inorganic lead halide perovskites in general is still missing.[399, 401–408]

Photoluminescence measurements of $CsPbBr_3$ nanocrystals and of bulk material reveal size-dependent absorption spectra and Stokes shifts.[399, 409, 410] Specifically, Brennan *et. al.*,[411] performed first-principles calculations, suggesting that the Stokes shift in $CsPbBr_3$ is due to the existence of an intrinsic confined hole state 260 to 70 meV above the valence band edge. In addition, ultrafast transient-absorption studies of $CsPbBr_3$ nanocrystals as a function of size show that for the smallest nanocrystals of $\sim$ 4 nm edge length, strong quantum confinement effects are manifested in the excited state dynamics different from the one for bulk $CsPbBr_3$.[409]

Although several studies of femtosecond transient absorption spectroscopy measurements have been conducted for $MAPbI_3$ and $CsPbBr_3$,[385, 398, 405, 406, 408, 412] the interpretation of their mechanistic origin is still under debate. The time-dependent transient absorption measurements of $CsPbBr_3$ performed by Yarita *et al.*[408] reveal the early (0.4 ps) evolution of a positive transient absorption signal at 509 nm and a negative one at 528 nm. The latter disappears giving rise to a unique positive feature at later delay times ($\geq$7.5 ps). Ultrafast transient absorption spectroscopy was also used in order to investigate the origin of the exceptionally high photoluminescence quantum yield of $CsPbBr_3$ quantum dots.[385] At early delay times (0.2-0.5 ps), the spectra show an exciton bleach feature at $\sim$480 nm and an exciton absorption feature at $\sim$495 nm, which the authors assign to state-filling-induced bleach and hot-exciton-induced red-shift, respectively. After the hot-exciton relaxation ($\geq$2 ps), the exciton-induced shift disappears and the transient absorption spectra are only dominated by the exciton bleaching feature.[385] According to the authors the high photoluminescence quantum yield of $CsPbBr_3$ quantum dots is a result of the negligible electron- and hole-trapping pathways.

On the other hand, Wei *et al.*[398] observed three features in the time-dependent transient absorption spectra of $CsPbBr_3$ quantum dots. A band of photoinduced bleach at 510 nm and two bands of photoinduced absorptions; the first one being very well-resolved and centered at 521 nm, while the second is subtle, with a small amplitude and very wide spectrum throughout the visible region.[398] At later time delays, after 2-5 ps, although there are still some contributions from the two bands of photoinduced absorptions, the transient absorption spectra are dominated by the band of photoinduced bleach. The authors attribute the 0.1 ps transient absorption spectrum mostly to a carrier-induced Stark effect.[398] They also correlate the red-shift of the energies with two-body recombination possibly due to a strong coupling between excitons.[398]

In order to explain further the nature of the excited state of organic-inorganic lead halide perovskites and phenomena such as the reduction of the exciton binding energy at room temperature, the possibility of polaron formation has been considered.[401, 402, 404] Ambrosio *et al.*[402] performed molecular dynamics simulations for $MAPbI_3$ with an additional electron or hole, in order to analyze the origin of the slow electron-hole recombination in metal halide perovskites. Their simulations reveal charge localization of the electron and the hole in specific regions of the inorganic part of the lattice, which they mainly attribute to thermal distortions. Furthermore, Miyata *et al.*[401], with a combined experimental and theoretical study suggest that electrons and holes are localized in spatially distinct regions at finite temperature. They also observe that the structural reorganization is larger when a hole is introduced than the one caused by an added electron, proposing in that way that the electrons experience less localization than the holes. In addition, the authors suggest the formation of a large polaron based on an analysis of the Pb-Br distance distribution (along the longest cell dimension) upon the addition of a hole.[401]

The debate between the various interpretations regarding the features of the transient absorption spectra of $CsPbBr_3$, calls for further studies to shed light on the mechanistic origin, and on fundamental issues related to the excited state of organic-inorganic halide perovskites in general. In this work, we simulate the transient absorption spectra of $CsPbBr_3$ at early delay times using ROKS and LR-TDDFT excited state simulations. To the best of our knowledge, this is the first attempt of simulating the transient absorption spectra of $CsPbBr_3$. In addition, we study the possible polaron formation by calculating the time-resolved density difference between the electronic ground and first excited state, thus going beyond the conventional approach, in which either an electron or a hole is added in ground-state molecular dynamics simulations.[401]

7.3 Results and Discussion

7.3.1 Simulations of the ultrafast transient absorption dynamics of $CsPbBr_3$

Before simulating the transient-absorption spectra of $CsPbBr_3$, we first determined the material's band gap at 0 K and at finite temperature. We employ the orthorhombic $CsPbBr_3$ phase in our calculations since it is the most stable phase at room temperature.[389] DFT within the GGA employing the PBE functional is used to calculate the Kohn-Sham band gap at 0 K, for which the Brillouin zone was sampled with a 7x7x7 Monkhorst-Pack **k**-points grid.[354] The band gap calculated in this way is 2.13 eV.

For the simulation of the finite temperature band gap, molecular dynamics simulations of the ground state at 300 K using a real-space cell of 160 atoms were performed. The 0 K band gap calculated for this real space cell is of the order of 2.08 eV. For the estimation of the finite temperature band gap, 166 configurations were sampled from the equilibrated trajectory of 9.5 ps and the probability distribution of the Kohn-Sham band gaps, *i.e.*, the lowest singlet excitations, is shown in Figure 7.1.

Since spin-orbit coupling is known to be strong in lead halide perovskites, we also determined the analogous spectrum of the triplet excitations.[349] The triplet excitations are estimated by performing single point calculations for the same configurations that have been used in the calculation of the singlet excitations but using different multiplicity (multiplicity 3) this time. As shown in Figure 7.1, the probability distributions of singlet and triplet excitations overlap with each other suggesting that both singlet and triplet states can contribute to the absorption spectrum of $CsPbBr_3$ in similar ways. Furthermore, the maximum of the peak for both singlet and triplet transitions is 2.11-2.12 eV showing that the band gap experiences a slight (0.04 eV) blue-shift at finite temperatures. This observation is consistent with previous work, where typical blue-shifts of the order of 0.01-0.03 eV have been observed.[329] This can be rationalized in terms of the decrease in antibonding orbital overlap of the divalent cation and anion due to thermal fluctuations at variance to the behavior of classical semiconductor.

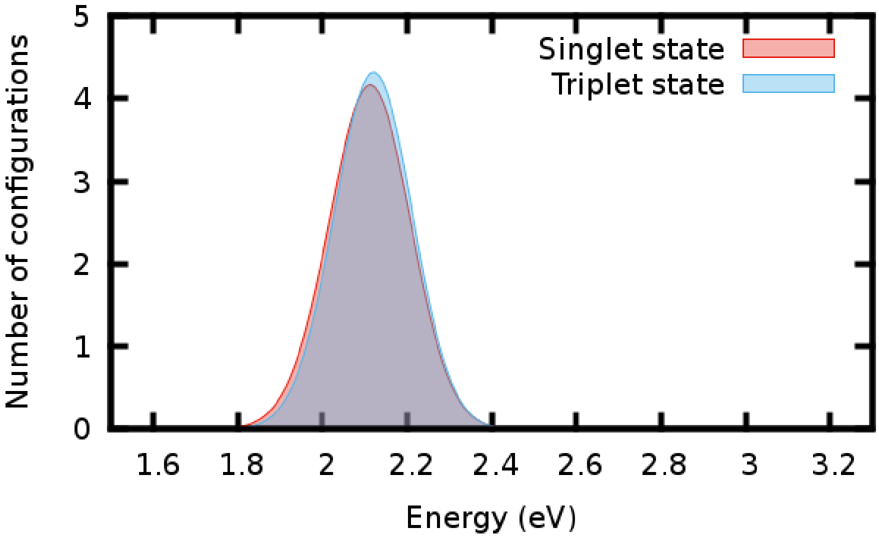

Figure 7.1: Probability distribution of the Kohn-Sham single particle and triplet excitations of $CsPbBr_3$, for a simulation box containing 160 atoms. The maximum of the peak for singlet and triplet states is 2.11 eV and 2.12 eV, respectively. The data have been fitted to a Gaussian function.

Since it is too costly to perform explicit excited-state dynamics of a system with 160 atom at the LR-TDDFT level, we make use of an alternative more expedient approach. ROKS is a DFT-based method that can describe the first non-degenerate excited singlet state as described in Chapter 2.[291] To verify that ROKS is an appropriate method for the calculation of the transient-absorption spectra we first tested the method in calculating the absorption and emission energy and the Stokes shift at 0 K.

In Figure 7.2, the energy differences between the ground state and the first excited state for the ground state optimized structure and the first excited state optimized counterpart are shown. The difference between these energies results in the Stokes shift. ROKS predicts a Stokes shift of 0.02 eV consistent with experimental results for bulk $CsPbBr_3$ of roughly 0.02 eV.[411] On the other hand, surprisingly, LR-TDDFT calculations result in no Stokes shift, indicating

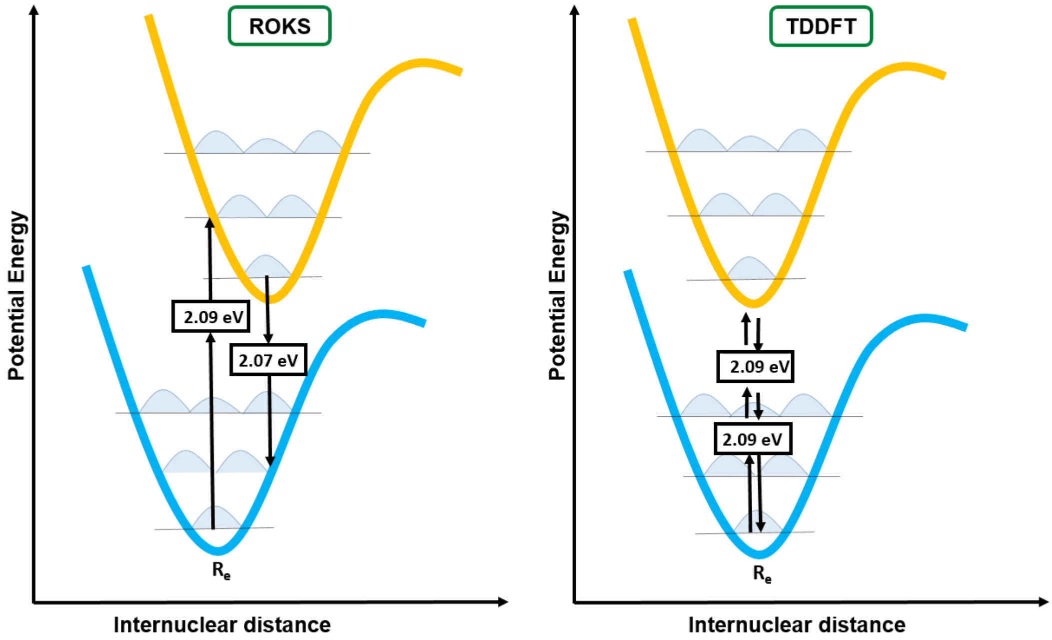

Figure 7.2: Energy differences between the ground and the first excited state at the minimum of the ground respectively excited state structure for a simulation box of 160 atoms, calculated with ROKS and LR-TDDFT.

some potential problems possibly related to the adiabatic approximation or the use of a (semilocal) GGA exchange-correlation functional and kernel.

In order to have a first indication about possible size effects on the steady-state absorption spectrum and the Stokes shift,[399, 409–411] we also performed simulations for a minimal size system containing a single unit cell of the orthorhombic structure with 20 atoms. Following the approach described above to simulate the finite temperature band gap (Figure 7.3) and Stokes shift (Figure 7.4), we find that for this smaller size system temperature effects lead to a more pronounced blue-shift of the steady-state spectrum. In fact, the maximum of the band for the lowest singlet and triplet Kohn-Sham single-particle excitations (Figure 7.3) lies at 2.75 and 2.68 eV, respectively. This is consistent with the blue-shifted absorption spectra that have been reported in experiments of $CsPbBr_3$ perovskite quantum dots and nanocrystals upon decrease of the size of the quantum dots and the nanocrystals.[399, 409]

In addition, as shown in Figure 7.4, the Stokes shift is larger than in the case of the simulation box with 160 atoms. More specifically, the Stokes shift is of the order of 0.24 eV and 1.14 eV when calculated with ROKS and LR-TDDFT, respectively. Such an increase in the Stokes shift from $\sim$ 30 meV to 100 meV with decreasing crystal size (from 11.7 nm to 4.1 nm), has been reported

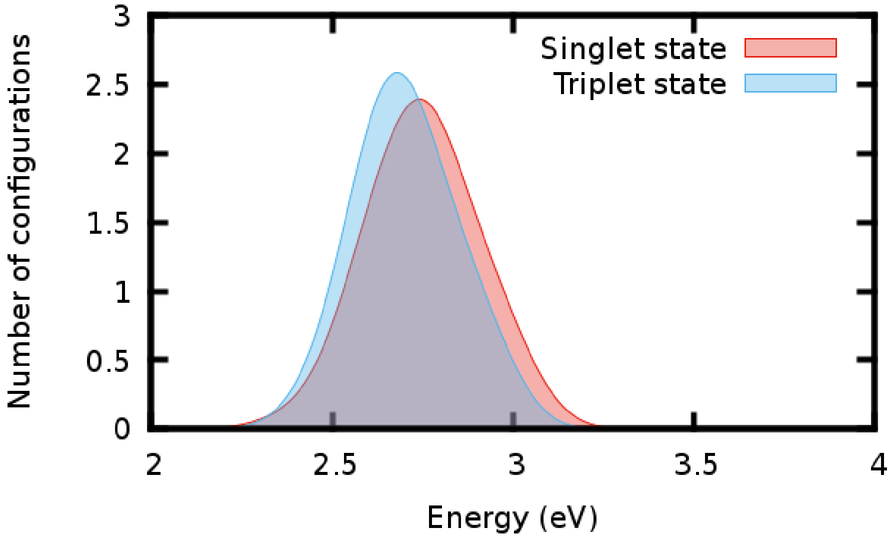

Figure 7.3: Probability distribution of the Kohn-Sham single particle and triplet excitations for CsPbBr$_3$, when a simulation box of 20 atoms is employed. The maximum of the peak for singlet and triplet states is 2.75 eV and 2.68 eV, respectively. The data have been fitted to a Gaussian function.

in experiments of CsPbBr$_3$ perovskite nanocrystals.[411] However, although the absorption energies are in good agreement between the two approaches (ROKS and LR-TDDFT), the LR-TDDFT calculations clearly lead to a spurious overestimation of the Stokes shift showing again that there might be some intrinsic problems for applying LR-TDDFT within the adiabatic local density approximation (ALDA)/GGA.

After having tested ROKS in case of the steady-state absorption and emission properties, we proceeded with the calculations of the transient absorption spectra. Transient absorption spectroscopy is a time-resolved technique that allows monitoring the absorption of a sample after photoexcitation through a pump laser pulse at different delay times. In detail, when a sample is photoexcited, its absorption spectrum is modified due to the different distribution of the photoinduced charge carriers.[413] The transient absorption signal ΔA at a certain delay time τ is defined as the difference between the pumped $A(E,\tau)$ and unpumped $A(E)$ signals, as described by Equation 7.1.[413]

$$\Delta A(E,\tau) = A(E,\tau) - A(E) \tag{7.1}$$

Following a similar approach in our simulations, we calculate the transient absorption spectrum as the difference between the excited state dynamics and its ground state counterpart, at different delay times. More specifically, we

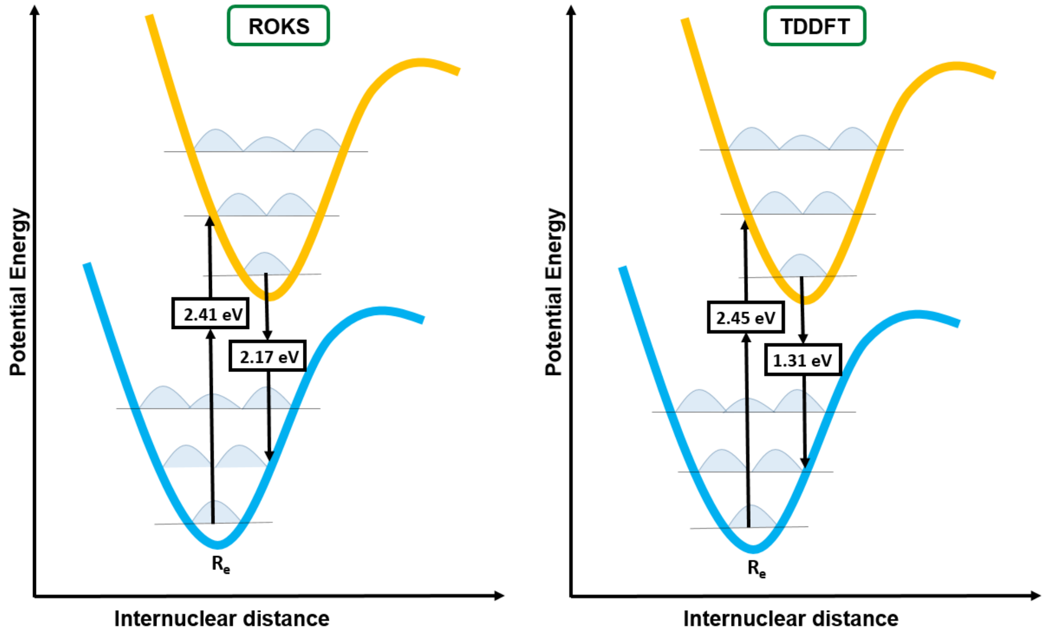

Figure 7.4: Energy differences between the ground and the first excited state at the minimum of the ground respectively excited state structure for a simulation box of 20 atoms, calculated with ROKS and LR-TDDFT.

perform molecular dynamics simulations for the non-degenerate excited singlet state by coupling the Car-Parrinello molecular dynamics scheme with ROKS or by coupling BO molecular dynamics with LR-TDDFT. In Figures 7.5 and 7.6 the transient-absorption spectra simulated either performing 100 ROKS excited dynamics simulations or LR-TDDFT excited dynamics of the system containing only one unit cell are shown for different delay times.

In both cases, the qualitative features of the transient-absorption spectra are similar. More specifically, after 120 fs the spectra experiences a red-shift indicated by the appearance of a positive peak, which can be attributed to the excited state relaxation and a negative feature due to ground state bleaching. These two features have also been reported in transient-absorption experiments of $CsPbBr_3$ nanocrystals and quantum dots for short delay times,[385, 398, 408] as well as in the transient-absorption measurements of $CsPbCl_{1.05}Br_{1.95}$ nanocrystals performed in the group of Prof. Dr. Majed Chergui Figure (7.9). These measured spectra compare nicely with our simulations apart from the blue-shifted feature appearing at 400 fs. For an easier analysis of the spectra, we are also plotting them for different delay time ranges, (Figures 7.7 and 7.8).

The main differences between the two sets of computed spectra arise from the fast decay of the red-shifted positive feature in LR-TDDFT compared to the slower decay of the same feature in the spectra calculated by ROKS. In addition, a big difference is also the magnitude of the shift that seems completely unrealistic in LR-TDDFT. Part of these differences can be explained by the possible intrinsic problems when applying LR-TDDFT within ALDA/GGA and by the fact that for the LR-TDDFT simulations the 5 lowest lying excited states were included while in ROKS only dynamics in the lowest excited states is described. In the case of TDDFT calculations more accurate kernels such as the bootstrap approximation for the exchange-correlation kernel might have been more efficient in producing the optical absorption, however their choice would not be viable in this case due to the higher computational cost.[414]

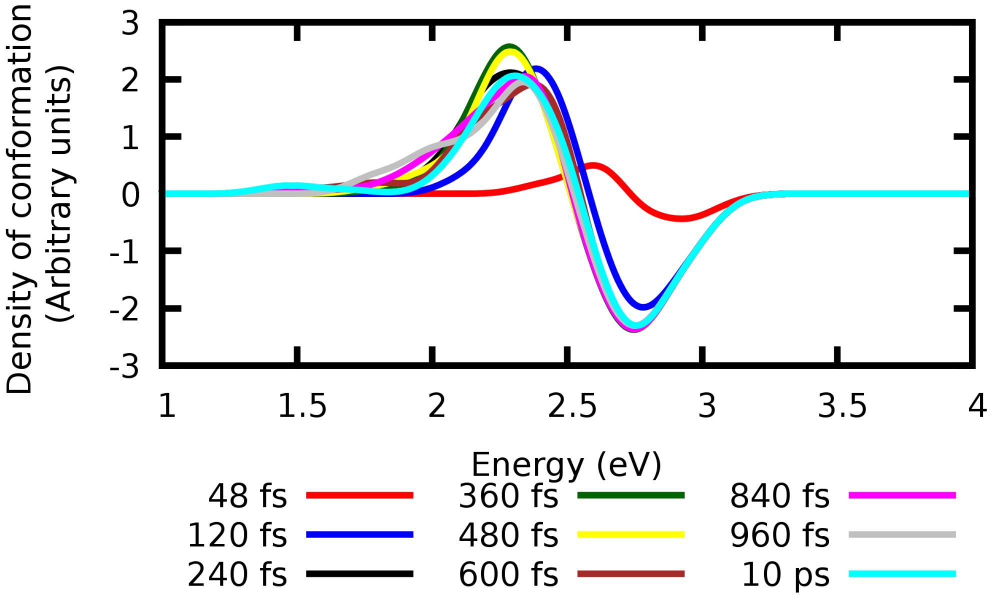

Figure 7.5: Transient absorption spectra for a simulation box of 20 atoms of $CsPbBr_3$ at 300 K, simulated with ROKS. The data have been fitted to Gaussian functions.

To test possible size-effects, we also performed 10 ROKS based simulations for the estimation of the transient absorption spectra for the larger supercell containing 160 atoms. The resulting spectra are shown in Figures 7.10 and 7.11. The main qualitative features are different from those of the spectra obtained for a single unit cell. However, it seems to be attributed to numerical noise instead of systematic trends or shifts. In this case, the absorption spectrum in the ground state and the excited samples are basically identical and the contributions to the transient absorption spectra due to geometric changes become negligible. To this end it is important to mention that our approach

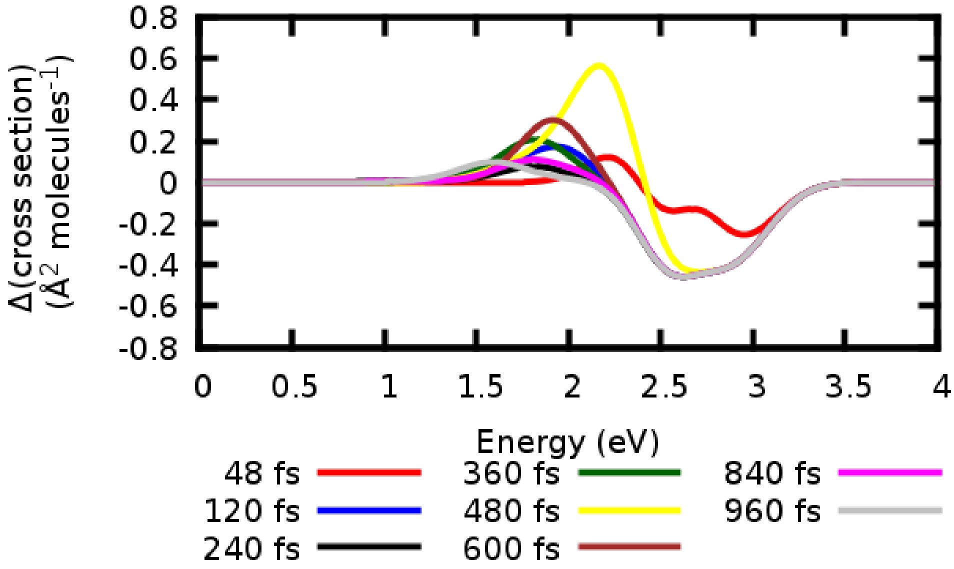

Figure 7.6: Transient-absorption spectra for a simulation box of 20 atoms of $CsPbBr_3$ at 300 K simulated with LR-TDDFT. The data have been fitted to Gaussian functions.

includes the differences between the excited and ground state geometries as factors that could contribute to the transient absorption measurements. However, other effects such as band gap renormalization, many-body effects and excitonic effects cannot be captured with this approach.

7.3.2 Possible formation of polarons in $CsPbBr_3$

The standard computational approach to investigate the formation of polarons is to compare the electron/hole distribution of a system with an added respectively removed electron and with the one of the neutral system. Here, we follow another strategy by performing explicit excited state dynamics for the neutral system in the simultaneous presence of excited electron and hole. [401, 402] In our approach the possible formation of charge localized regions can be determined by the density difference between the electronic ground and excited state. For this reason, molecular dynamics simulations of the ground state and the excited state with the ROKS method at 30 K and 300 K are performed for the cell of 20 atoms. As shown in Figure 7.12, no charge localized regions are formed at low temperatures. At room temperature, the thermal fluctuations induce temporary localizations of the electron (purple color in Figure 7.12) and hole (cyan color in Figure 7.12) distributions.

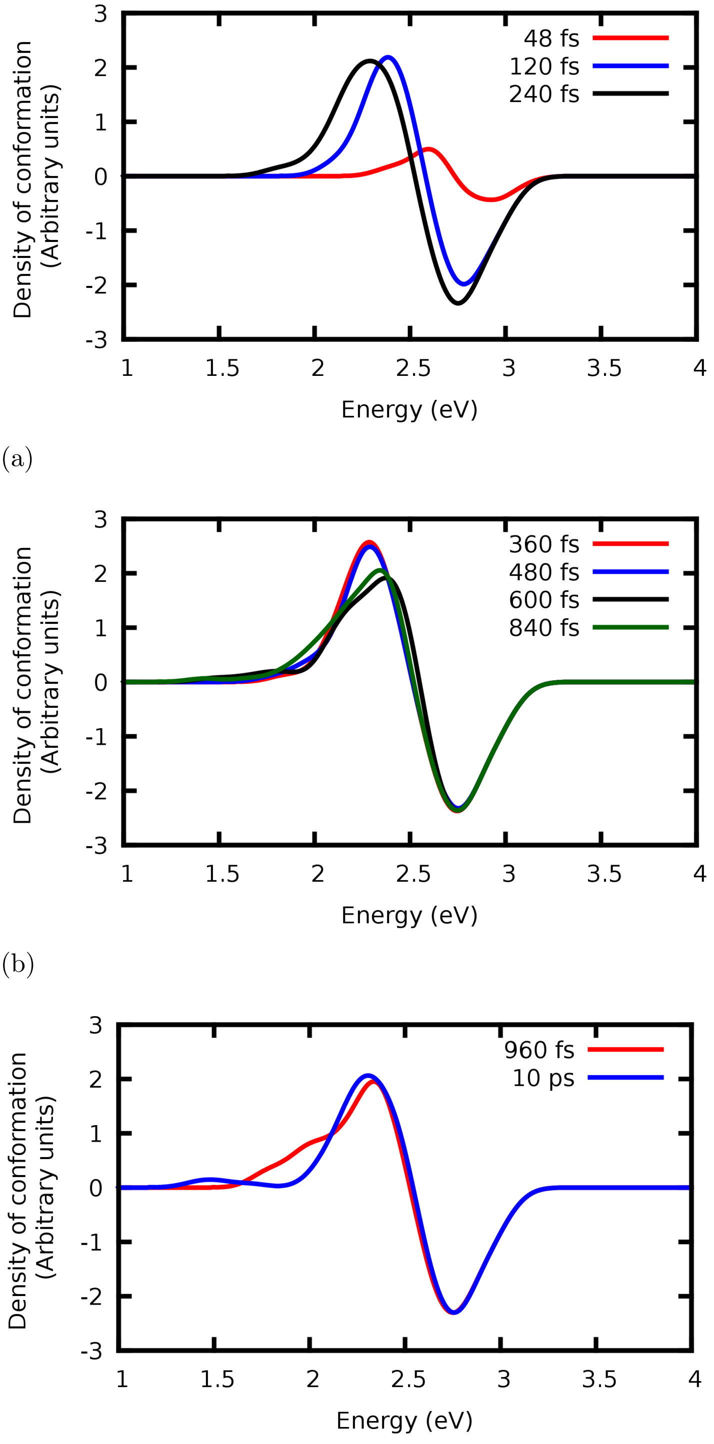

(a)

(b)

(c)

Figure 7.7: Transient absorption spectra for a simulation box of 20 atoms of CsPbBr$_3$ at 300 K, simulated with ROKS plotted for different delay time ranges. The data have been fitted to Gaussian functions.

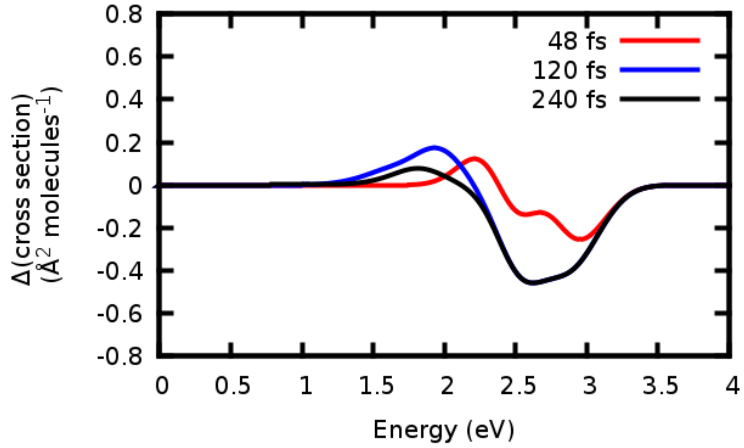

(a)

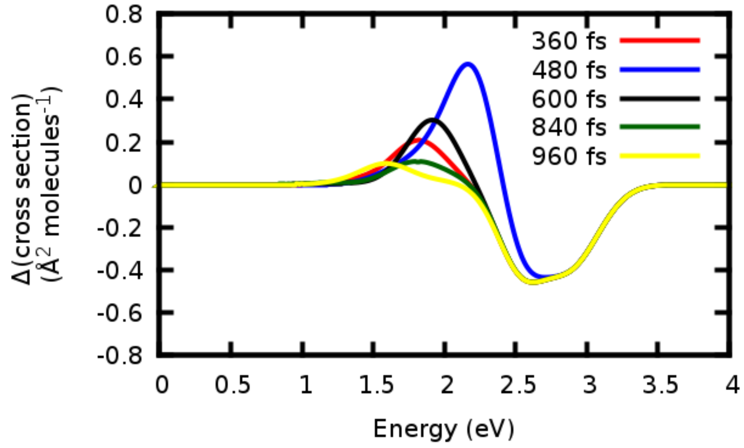

(b)

Figure 7.8: Transient absorption spectra for a simulation box of 20 atoms of $CsPbBr_3$ at 300 K, simulated with LR-TDDFT plotted for different delay time ranges. The data have been fitted to Gaussian functions.

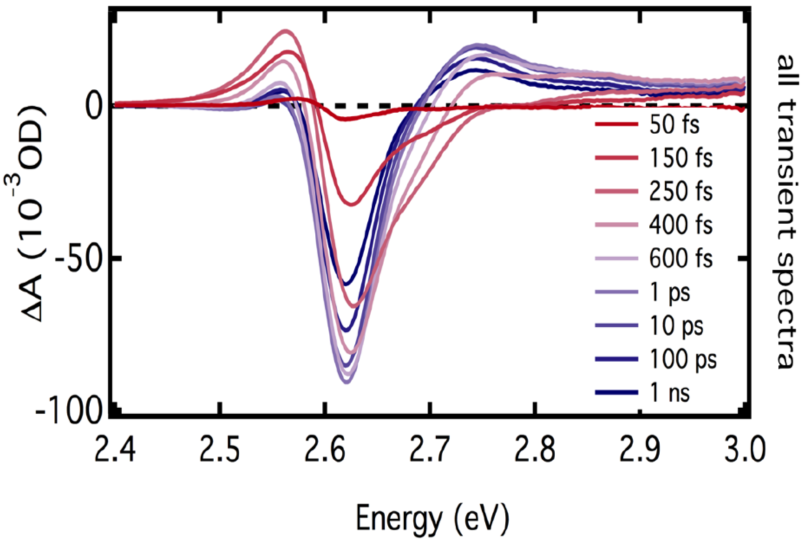

Figure 7.9: Transient absorption spectra measured in the group of Prof. Dr. Majed Chergui for $CsPbCl_{1.05}Br_{1.95}$ nanocrystals. The experiments were performed by Ms Tania Palmieri.

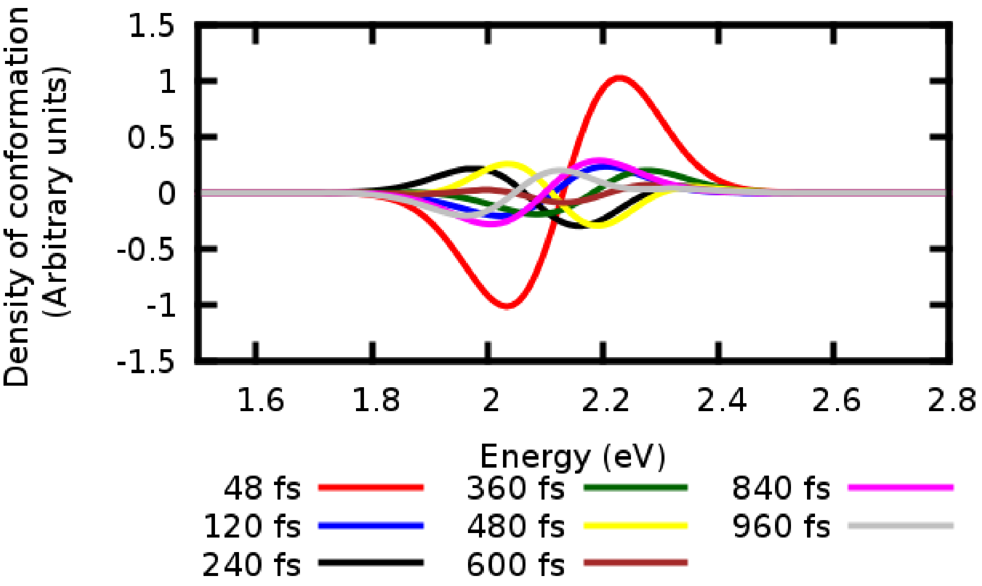

Figure 7.10: Transient absorption spectra for a simulation box of 160 atoms of $CsPbBr_3$ at 300 K, simulated with ROKS. The data have been fitted to Gaussian functions.

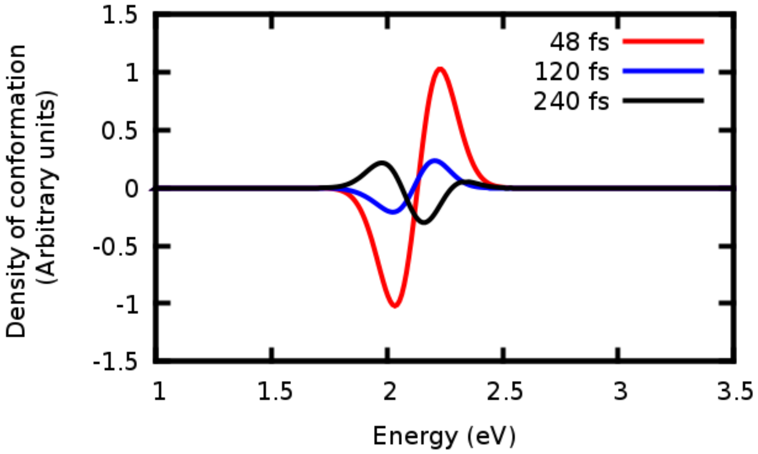

(a)

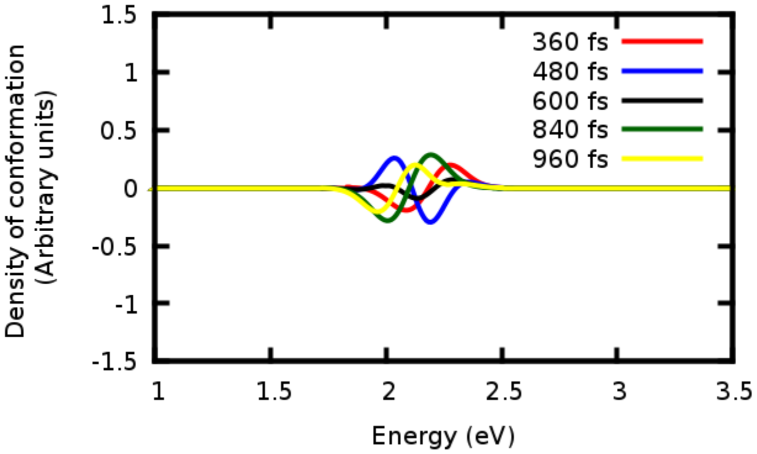

(b)

Figure 7.11: Transient absorption spectra for a simulation box of 160 atoms of $CsPbBr_3$ at 300 K, simulated with ROKS, plotted for different delay time ranges. The data have been fitted to Gaussian functions.

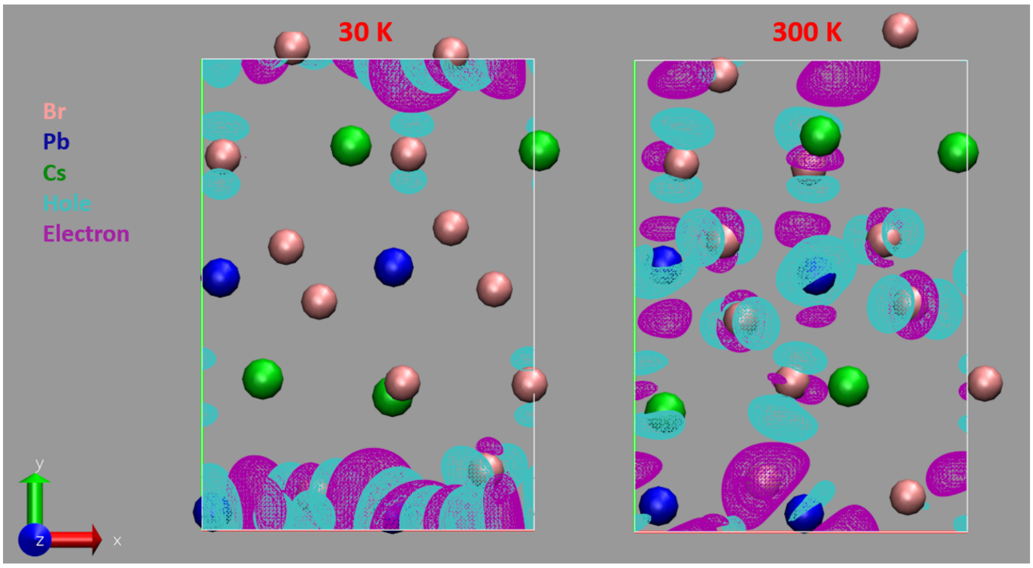

Figure 7.12: Snapshots at 30 K and 300 K, respectively, visualizing the density difference. The localization of electron is represented with purple and of hole with cyan.

To analyze if charge localization is accompanied by simultaneous geometric distortions, we compare the Pb-Br distances of a structure from the ground-state trajectory at 300 K with one from the excited-state trajectory. As shown in Table 7.1, the structure from the ground-state trajectory at 300 K has only one set of similar Pb-Br distances. On the other hand, for the structure extracted from the excited-state dynamics trajectory, the Pb-Br distances can be classified into two different sets suggesting a tetragonal distortion of the lattice at higher temperatures.

Table 7.1: Average Pb-Br distance for a structure from the ground state trajectory at 300 K and a structure from the excited state dynamics trajectory.

Pb-Br distance (Å) (structure from the ground state trajectory at 300 K)	**Pb-Br distance (Å) (structure from the excited-state dynamics trajectory)**
3.046	3.232 2.986

7.4 Conclusions

The finite temperature band gap and the transient absorption spectra of $CsPbBr_3$ have been simulated. We observe that properties such as the finite temperature band gap and the Stokes shift are size-dependent. In analogy to these size-dependent properties the transient absorption spectra varies with the size of the super cell. The simulations of the transient absorption spectra for the smallest sample agree well with the experimental results on nanocrystals. Finally, the calculation of the density difference between the electronic ground and excited states at room temperature and low temperatures allows us to propose temporary charge localizations of electrons and holes due to thermal fluctuations.

7.5 Computational details

DFT[254, 255] calculations have been performed using the Quantum Espresso suites of codes,[351, 352] and the CPMD code.[356] The GGA to DFT in the PBE formulation has been used.[327] SOC effects are not included in the calculations, due to error cancellations between spin orbit coupling and many-body effects described *e.g.* by means of GW-self energy correction.[376]

Quantum Espresso was chosen for the band gap calculations at 0 K, with a sampling of the Brillouin zone with a Monkhorst-Pack **k**-points grid.[354] To calculate the corresponding gap of the real-space sample, the CPMD code was used instead. In Quantum Espresso calculations, the interactions between valence electrons, core electrons and nuclei are described by ultrasoft pseudopotentials.[353] The Kohn-Sham orbitals are expanded in a plane wave basis set with a kinetic energy cutoff of 40 Ry and a density cutoff of 240 Ry. The Brillouin zone is sampled with a 7x7x7 Monkhorst-Pack shifted **k**-points grid.[354] The above values have been chosen after having performed convergence tests for the total energy, the band gap, the pressure, the stresses and the atomic forces. For the calculations with CPMD, the wavefunction cutoff was set to 90 Ry and Goedecker normconserving pseudopotentials were employed.[357–359]

Car-Parrinello molecular dynamics simulations for the ground state in the NVT ensemble were performed using the CPMD code.[356] A time step of 5 a.u. was used with a fictitious mass parameter of 800 a.u.. The temperature in the simulations was set to 30 K and 300 K and was controlled by three Nosé-Hoover thermostats, (one for each species) with a coupling frequency of 1500 cm^{-1}.[360–362] For the excited state dynamics, the LR-TDDFT and ROKS methods were coupled with BO molecular dynamics and Car-Parrinello molecular dynamics, respectively. In both LR-TDDFT/BO molecular dynamics and ROKS/Car-Parrinello molecular dynamics, a time step of 5 a.u. was employed. For ROKS/Car-Parrinello molecular dynamics, a fictitious mass parameter of 800 a.u. was used. Especially, for the estimation of the transient absorption spectra with ROKS, 100 simulations were performed for the system that contains only the unit cell. For the respective cell of 160 atoms, 10 simulations were performed, instead. Finally, the convolution of the spectra was done by applying Gaussian functions, employing the comp_chem_py package.[415]

Chapter 8

Conclusions and Future Prospects

Ab initio methods have been proven to be a powerful computational tool for the investigation of many open questions related to the emerging technology of photovoltaic devices based on organic-inorganic lead halide perovskites. In particular, it has been possible to identify the microscopic origin of several phenomena that take place either during the fabrication process or during the use of the device. In addition, new design principles for the synthesis of materials with enhanced properties could be proposed.

More particularly, our studies related to the limited phase stability of these materials, which is considered one of the major issues preventing commercialization, resulted in the proposition of a series of design principles for the fabrication of stable mixed cation/mixed halide perovskite solar cell materials. From our calculations of FA^+-rich $Cs_xFA_{(1-x)}PbI_3$, ($0 \leq x \leq 0.5$), we concluded that if the structural characteristics of the non-perovskite δ phases of the pure compounds differ significantly, mixing is enthalpically favoring the perovskite over the non-perovskite phase and there is a high chance that stable perovskite structures can be formed as the thermodynamically most stable form at ambient conditions. However, in Cs^+-rich $FA_xCs_{(1-x)}PbI_3$, ($0 \leq x \leq 0.5$), stable perovskite phases cannot be formed at room temperature although the δ phases of the pure compounds differ significantly. This surprising finding gave rise to a second design principle that apart from the structural differences of the δ phases one has also to consider the differences between the volumes of the structures of the pure compounds. If the volume differences are significant, the incorporation of large cations such as FA^+ into a small volume lattice such as γ-$CsPbI_3$ is energetically not favorable.

In a similar spirit, the stabilization of binary $GUA_xFA_{(1-x)}PbI_3$ mixtures through introduction of a smaller cation such as Cs^+ allowed us to put forward a third design principle, according to which the simultaneous incorporation of small portions of a large (GUA^+) and a small (Cs^+) cation in a material that adopts the non-perovskite phase at room temperature can result in a mixture which adopts the perovskite phase, instead. This is an effective way to extend the Goldschmidt tolerance factor to ions that on their own would lie outside the stability range.

The proposition of design principles via computational studies could accelerate the exploration of potential stable compounds in the perovskite phase at room temperature, avoiding the performance of expensive and time-consuming experiments for unsuitable candidates. Indeed, in the near future the proposed design principles could serve not only in the investigation of potential stable mixtures of mixed cation/mixed halide lead perovskites, but also in mixtures of 3D perovskites with the emerging class of 2D perovskites that have recently shown superior long-term stability over their pure 3D counterparts.

Moreover, it is important, instead of only focusing all efforts on the design of very efficient and stable perovskite solar cells, to also investigate the fundamental laws and mechanisms that govern their exceptional properties. The decoding of all these mechanisms could lead to the production of devices that concentrate all the desirable properties that the case-study compounds combine avoiding unwanted features. In such a way, the rational design (based on these mechanisms and structure-function relationships) could help in materials' discovery. For instance, this approach could be important considering the toxicity of lead and the search for lead-free materials with similar properties. A thorough understanding of the underlying mechanisms can be exploited in the search for lead-free perovskites that could combine all exceptional properties avoiding environmentally-precarious lead compounds.

For this reason, throughout this dissertation, we also invested efforts in investigating the fundamental properties of excited states since their nature determines the electronic properties of a material and in turn, to a large degree, the PCE of the device. Our calculations provide some interesting insights of the size-dependent Stokes shifts, steady-state absorption spectrum and transient-absorption spectra of $CsPbBr_3$. This observation suggests a possible engineering of the optical properties of this kind of materials by tuning their size, which can be easily done by producing nanocrystals or quantum dots with defined size distributions. However, still much remains to be studied; for instance, how the excited state properties are influenced by different monovalent cations and halides.

Apart from the general perovskite solar cell fever, halide perovskites have a broad spectrum of applications. Hence, we also investigated the atomistic origin of the anomalous behavior of the photoluminescence spectra of $CsPbBr_3$ at low temperatures, a material unsuitable for photovoltaic applications due to its wide band gap, but popular in LED and laser applications. Our calculations reveal that this phenomenon is due to a local dipole moment (*i.e.* Stark effect) that the isotropic Cs^+ produces when displaced away from the center of the cavity, due to a preferential localization of it in either of two off-centre sites in the empty space between the octahedra. On the other hand, around 300 K, below the phase transition to a tetragonal structure, the Cs ions occupy symmetric positions close to the centre of the interoctahedral cavities (and the centre of the double-well potential).

Finally, through the studies of the phase stability of halide perovskites, we also came across a variety of non-photoconductive δ phases. So far no systematic study of the properties of these structures has been conducted. Thus, it would be interesting in the future to thoroughly characterize these non-perovskite phases and maybe discover that these structures can be useful for specific applications. Who knows? It could be that one day the non-attractive δ phases may be the pioneering materials of a specific technological field, similar to the revolutionary role that lead halide perovskites had for applications in the field of photovoltaic technology that started just one decade before the defense of this dissertation.

Appendix A

Benchmarks

In order to assess the relative performance of different methods and ensure the convergence of a calculation, a series of benchmarks has been performed. The benchmarking procedure that was followed is associated with several iterative rounds for each parameter under study, in order to arrive at a converged and useful result. All parameters, as well as density functionals used for the calculations mentioned throughout this dissertation are chosen based on the benchmarks presented below.

More specifically, in this appendix the benchmarks performed in order to estimate a suitable density functional for DFT calculations of organic-inorganic halide perovskites are presented. In addition to this, convergence tests were performed in order to estimate the suitable parameters that are associated with this kind of simulations, such as the kinetic energy cutoff for the wavefunction, the kinetic energy cutoff for the charge density and the Monkhorst-Pack **k**-points grid. Finally, the benchmarks of the fictitious mass associated with the electronic degrees of freedom (in the Car-Parrinello molecular dynamics) and of the coupling frequency of the thermostat that was used in order to produce equilibrated molecular dynamics trajectories are presented. For the sake of simplicity, we only report one case study for each parameter. However, in order to ensure the suitability of the parameters associated with each method, the protocol presented below was followed for each organic-inorganic halide perovskite under study.

A.1 Choice of functional

In the case of organic-inorganic lead halide perovskites, GGA based DFT calculations are in general in good agreement with experimental results. This agreement is fortuitous and stems from efficient error cancellations between the

GW corrections and the SOC effects.[349] A full treatment, including many-body effects and SOC is far beyond available computational resources for large systems as organic-inorganic lead halide perovskites. To this end, the suitability of different functionals is estimated by comparing the calculated lattice parameters, relative energetics and band gaps, with the experimental counterparts.

A.1.1 Lattice parameters

As a case-study, we consider the low temperature orthorhombic phase of $MAPbI_3$.[416]

Table A.1: Effect of different exchange-correlation functionals on the lattice parameters and the volume of the low temperature orthorhombic phase of $MAPbI_3$.

Functional	**α** (Å)	**b** (Å)	**c** (Å)	**Volume** (Å^3)
Experimental[416]	8.8116	12.5871	8.5597	949.38
PBE	9.2215	12.8395	8.6236	1021.03
PBEsol	8.8722	12.5670	8.4344	940.41
SCAN	8.8740	12.6582	8.6000	966.03

Lattice parameters as well as volumes estimated with the PBEsol functional are in good agreement with the experimental results.

A.1.2 Relative energetics

In order to define which exchange-correlation functional could produce correct relative energetics between the different halide perovskite phases, we compare the relative energetics of the δ-$CsPbI_3$ versus the orthorhombic $CsPbI_3$. Experimental data on the relative stability of δ-$CsPbI_3$ versus the orthorhombic $CsPbI_3$ reveal that the δ phase is the most stable one at low and room temperatures and the compound undergoes a first order phase transition at 600 K to the perovskite $CsPbI_3$ phase.[308]

As shown in Table A.2, the correct energetic ordering is produced by employing the PBE exchange-correlation functional.

A.1.3 Band gap

As a case study, we consider the α-$FAPbI_3$. The experimental band gap of α-$FAPbI_3$ as measured by different groups lies within the range of 1.43-1.48 eV.[145, 312, 316]

Table A.2: Effect of different exchange-correlation functionals on the relative energetics of the δ-$CsPbI_3$ versus the perovskite $CsPbI_3$ phases.

Functional	**Relative energetics (perovskite $CsPbI_3$ *vs* δ-$CsPbI_3$) eV**
PBE	0.18
PBEsol	-0.003

Table A.3: Effect of different exchange-correlation functionals on the band gap of $FAPbI_3$.

Functional	**Band gap eV**
PBE	1.71
PBEsol	1.46
PBE0	2.60
PBE0+SOC	1.47

Both PBEsol and PBE0+SOC reproduce correctly the band gap of $FAPbI_3$. However, it should be mentioned that PBEsol can only be used for band gap calculations of lead halide perovskites. For other halide perovskites, PBEsol cannot produce the correct band gap.[417]

A.2 Kinetic energy cutoff for the wavefunction

The use of ultrasoft pseudopotentials allows for lower kinetic energy cutoffs for the wavefunction than in case where norm-conserving pseudopotentials are used. Here as a case study, we consider the cubic $CsPbI_3$. In Figures A.1 and A.2 the energy as a function of the kinetic energy cutoff for the wavefunction for $CsPbI_3$ is presented, when ultrasoft and norm-conserving pseudopotentials are used, respectively.

Indeed, ultrasoft pseudopotentials allow for low kinetic energy cutoffs for the wavefunction of the order of 40 Ry. On the other hand, norm-conserving pseudopotentials demand higher cutoffs of the order of 70 Ry.

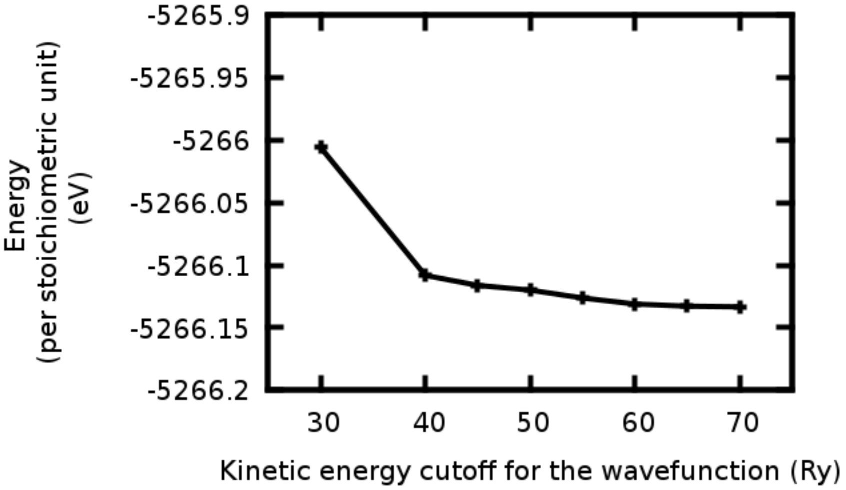

Figure A.1: Benchmarks for the kinetic energy cutoff for the wavefunction for the perovskite $CsPbI_3$, when ultrasoft pseudopotentials are used.

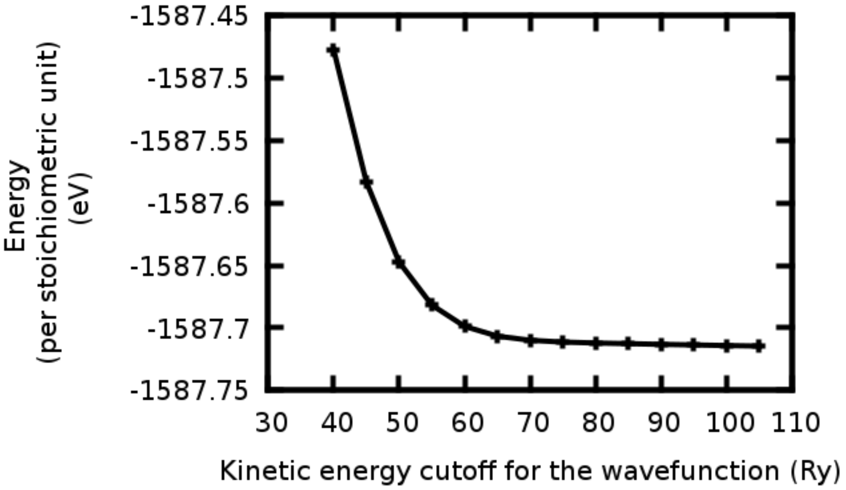

Figure A.2: Benchmarks for the kinetic energy cutoff for the wavefunction for the perovskite $CsPbI_3$, when norm-conserving pseudopotentials are used.

A.3 Kinetic energy cutoff for the charge density

The density can vary twice as rapidly as the wavefunction. Hence, within a plane-wave basis set for the translational symmetry to be maintained, the density should contain eight times more plane-waves than the corresponding wavefunction expansion, (Equation A.1)

$$\frac{1}{2} \mid \mathbf{G}_{max} \mid^2 \leq 4E_{cutoff} \tag{A.1}$$

This applies for norm-conserving pseudopotentials. However, if ultrasoft pseudopotentials are used, a larger value than the default one is often desirable. In Figure A.3, the energy as a function of the kinetic energy cutoff for the charge density is shown for the cubic CsPbI$_3$ when ultrasoft pseudopotentials are used.

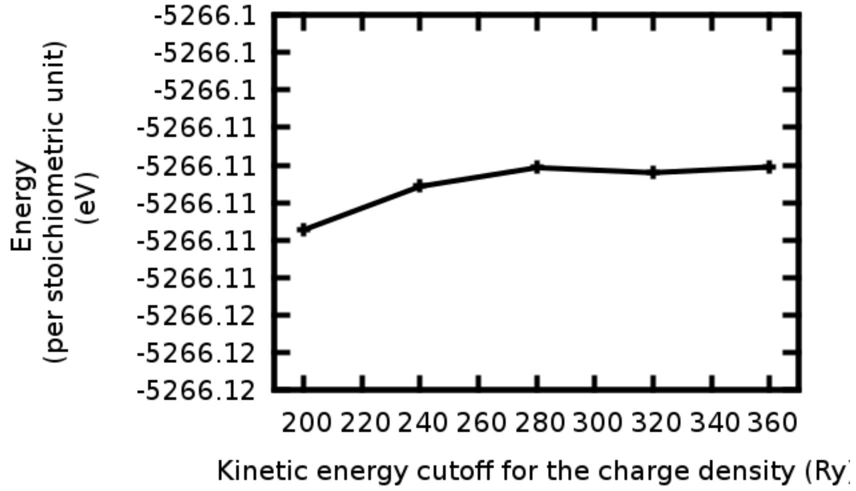

Figure A.3: Benchmarks for the kinetic energy cutoff for the charge density for the perovskite CsPbI$_3$, when ultrasoft pseudopotentials are used.

A.4 Monkhorst-Pack k-points grid

The selection of the right Monkhorst-Pack **k**-points grid depends on the space group of the structure. In Figure A.4 the evolution of energy as a function of the number of **k**-points used is shown, for FAPbI$_3$. It seems that a Monkhorst-Pack **k**-points grid of 27 **k**-points (3x3x3) is sufficient for a converged description of the reciprocal lattice.

A.5 Fictitious mass associated with the electronic degrees of freedom

The fictitious mass associated with the electronic degrees of freedom is the parameter to control adiabaticity in Car-Parrinello molecular dynamics. How-

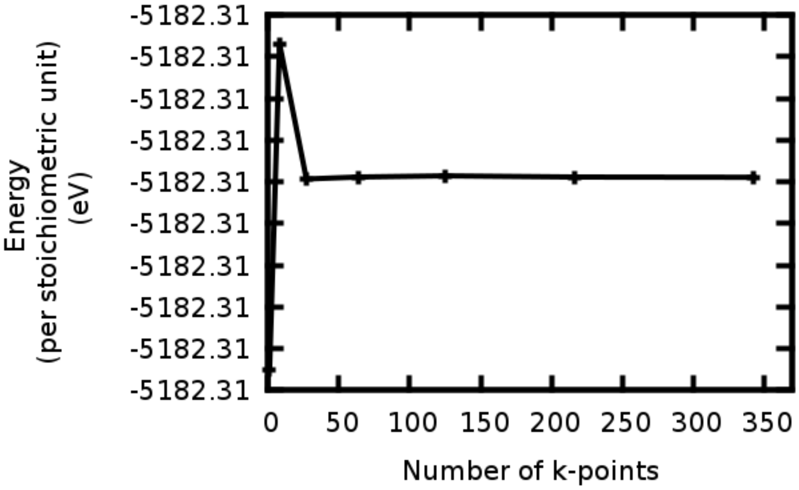

Figure A.4: Benchmarks for the Monkhorst-Pack **k**-points grid for the perovskite $FAPbI_3$.

ever, there is an interplay between the decrease of μ and the maximum time step Δt_{max} that can be used (Equation A.2).

$$\Delta t_{max} \propto \sqrt{\frac{\mu}{E_{cut}}} \tag{A.2}$$

In Figure A.5 the evolution of the potential energy from the Kohn-Sham equations (EKS), the classical first principles energy (ECLASSIC) and the conserved energetic quantity of the Car-Parrinello Hamiltonian (EHAM) are illustrated for a case where adiabaticity is maintained. The trajectory under study represents the dynamic evolution of the perovskite $CsPbI_3$ where μ = 800 a.u. and Δt = 5 a.u.. In Figure A.6 the evolution of the kinetic energy of the electronic sub-system (EKINC) for the same trajectory is presented.

For each molecular dynamics simulation performed, we have tested that the correlation between EKS, ECLASSIC and EHAM is represented by plots similar to Figure A.5 and that EKINC oscillates around a constant value as shown in Figure A.6.

A.6 Coupling frequency of the thermostat

In order to produce an equilibrated trajectory, in the NVT ensemble, a suitable coupling frequency for the thermostat should be used. In order to ensure that our trajectory is equilibrated, we do not only consider that the

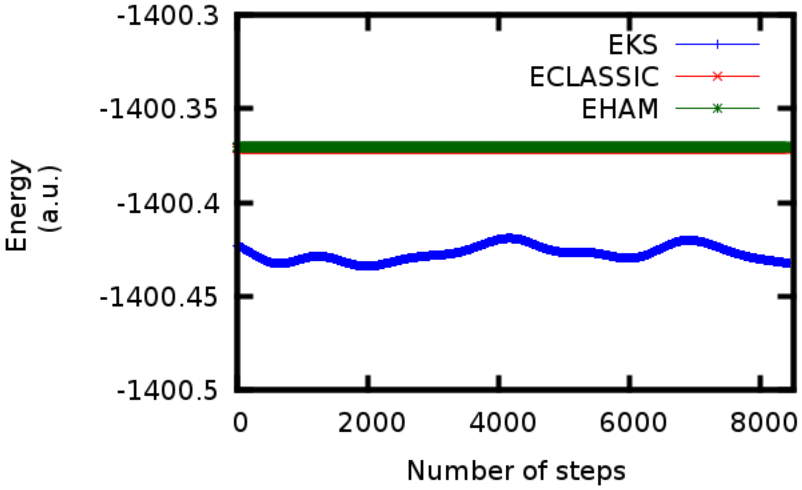

Figure A.5: Evolution of the potential energy from the Kohn-Sham equations (EKS), the classical energy (ECLASSIC) and the conserved energetic quantity of the Car-Parrinello Hamiltonian (EHAM) of a perovskite $CsPbI_3$ trajectory. Adiabaticity is maintained.

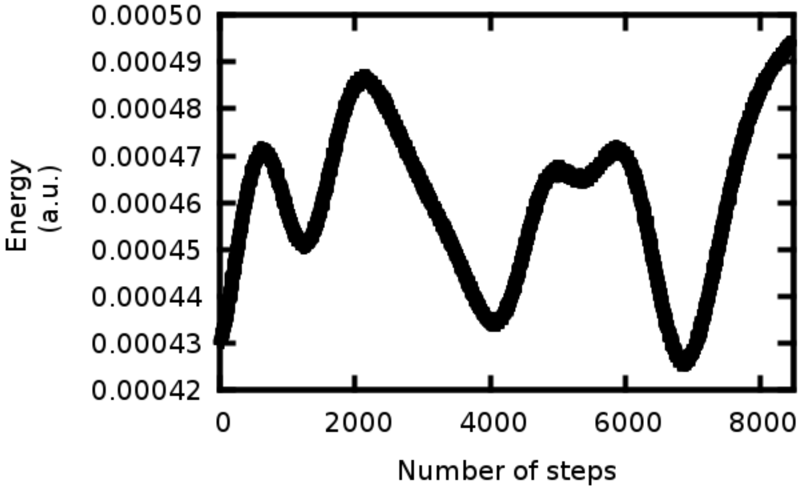

Figure A.6: Evolution of the kinetic energy of the electronic sub-system (EKINC) of a perovskite $CsPbI_3$ trajectory.

average temperature is close to the set target temperature but also that the temperatures of the individual atomic species are the same. This protocol has been employed in every molecular dynamics simulation that has been performed. In Figure A.7, the evolution of the total temperature and of the temperature of every species as a function of the number of sampled configurations for $CsPbBr_3$ is shown.

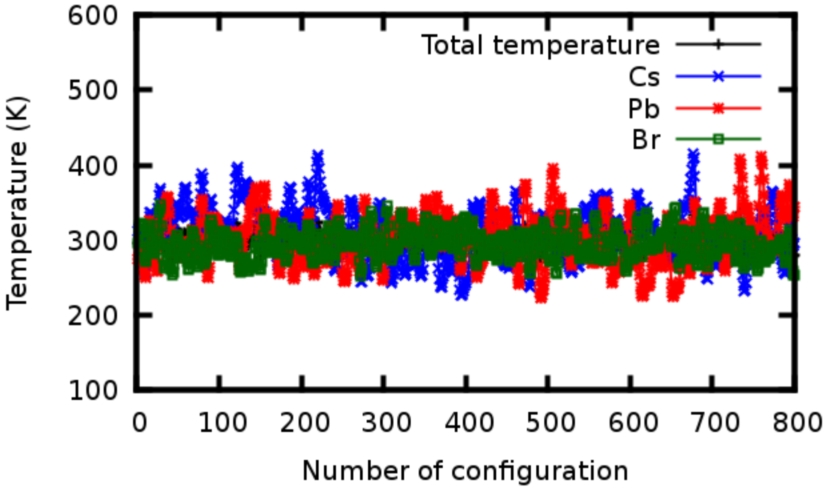

Figure A.7: Evolution of the total temperature and the temperature of every species as a function of the number of sampled configurations for $CsPbBr_3$.

A.7 High-Performance Computing (HPC) resources

Most of the calculations have been performed using the Piz Daint cluster of the Swiss national supercomputing centre (CSCS) and Fidis cluster of Scientific IT and application support of EPFL (SCITAS). Piz Daint is a hybrid Cray XC40/XC50 system and Fidis is an Intel Broadwell based cluster. Such supercomputers allowed us to produce first principles molecular dynamics trajectories up to 10 ps for systems containing up to 240 atoms in one month.

Appendix B

Supporting Information - Entropic stabilization of mixed A-cation ABX_3 metal halide perovskites for high performance perovskite solar cells

B.1 Materials

FAI was synthesized according to a reported procedure.[301] All the other materials were purchased from commercial sources and used as received.

B.2 Device Fabrication

FTO-coated glass substrates were patterned by laser scribing and cleaned by ultra-sonication in aqueous washing solution, then rinsed with deionized water, acetone and ethanol. A TiO_2 compact layer was then deposited on the substrates by aerosol spray pyrolysis at 450 °C using a titanium diisopropoxide bis(acetylacetonate) solution (75% in 2-propanol, Sigma-Aldrich) in ethanol (1:19, volume ratio) as precursor and oxygen as carrier gas. The mesoporous TiO_2 layer composed of 30-nm-sized particles was deposited by spin coating at 5,000 r.p.m. for 20 s using a TiO_2 paste diluted in ethanol (1:6, weight ratio). After drying at 125 °C, the TiO_2 films were gradually heated to 500 °C, annealed at this temperature for 15 min and cooled to room temperature. The films were sintered at 500 °C for 20 min before use. The 1.0 M perovskite precursor solutions were prepared by dissolving corresponding amounts of CsI, FAI, FABr and

PbI_2 in DMSO/DMF (1:9 v/v) mixed solvent. The perovskite precursor solution was coated onto the mp-TiO_2/bl-TiO_2/FTO substrate by a consecutive two-step spin-coating process at 1,000 and 6,000 r.p.m for 10 and 15 s, respectively. At the last stage of spin-coating, 0.1 mL of chlorobenzene was dripped into the film to assist the crystallization and the formation of a smooth capping layer. Following spin-coating, the films were annealed on a hotplate at 100 °C for 10 minutes (the $FAPbI_3$ films were annealed at 150 °C). After cooling to room temperature, the HTM was deposited by spin coating at 4,000 r.p.m. for 30 s. The HTM solution consists of 72.3 mg (2,29,7,79-tetrakis(N,N-di-p-methoxyphenylamine)-9,9-*spiro*bifluorene)- (*spiro*-OMeTAD), 28.8 μl 4-tert-butylpyridine and 17.5 μl of 520 mg ml^{-1} lithium bis(trifluoromethylsulphonyl)imide acetonitrile solution dissolved in 1 ml chlorobenzene. Finally, 80-nm of gold was thermally evaporated on top of the device to form the back contact.

B.3 Device characterization

Current-voltage characteristics of the devices were measured with a solar simulator employing a light source and a digital source meter (Keithley Model 2400) using a scan rate of 50 mVS^{-1}. The light source was a 450 W xenon lamp (Oriel) equipped with a Schott K113 Tempax sunlight filter (Praezisions Glas & Optik GmbH) to match the emission spectrum of the lamp with the AM1.5G standard. Before each measurement, the light intensity was calibrated by a Si reference diode equipped with an infrared cut-off filter (KG-3, Schott). IPCE spectra were recorded as a function of wavelength under a constant white light bias of approximately 5 mWcm^{-2} supplied by an array of white light emitting diodes. The excitation beam coming from a 300-W xenon lamp (ILC Technology) was focused through a Gemini-180 double monochromator (Jobin Yvon Ltd) and chopped at approximately 2 Hz. The signal was recorded using a Model SR830 DSP Lock-In Amplifier (Stanford Research Systems). All measurements were conducted using a non-reflective metal aperture of 0.16 cm^2 to define the active area of the device and avoid light piping through the sides and the cover glass. For the stability tests, the devices were kept in the dark and new device performances were measured at periodic intervals.

B.4 Materials Characterization

The perovskite films used for UV-vis spectra, XRD, XPS, SEM and TEM were prepared by spin-coating on mesoporous TiO_2 films following the above-mentioned procedure. The powders for the DSC measurement were prepared by scratching the spin-coated film from the glass support (all the films were annealed at 100 °C for 5 minutes to remove the solvents). The UV-vis spectra were measured with a PerkinElmer Lambda 950 spectrophotometer. DSC is measured with a DSC 8000 from Perkin Elmer under N_2 atmosphere. The XRD patterns were acquired with a Bruker D8 Discover diffractometer in Bragg–Brentano mode, using Cu K α radiation (1.540598) and a Ni β-filter. Spectra were acquired with a linear silicon strip 'Lynx Eye' detector from 2θ = 10°-60° at a scan rate of 2° $\min^{-1}$, step width of 0.02° and a source slit width of 1 mm. The morphology of the films was characterized using a high-resolution scanning electron microscope (ZEISS Merlin). The perovskite structures and compositions were examined by a high-resolution transmission electron microscope (Technai Osiris, FEI), equipped with an Oxford energy-dispersive X-ray (EDS) detector.

B.5 First principles calculations

DFT based first principles calculations were performed starting from the experimental α, β and δ phases of $FAPbI_3$ and $CsPbI_3$.[91] The simulation cells of α and δ phases were obtained replicating the corresponding unit cells so as to obtain the same number of stoichiometric units as in the unit cell of β phase, i.e. 12 units. Mixed cation and halide systems were obtained replacing FA with Cs and I with Br, respectively. For each stoichiometry, when allowed by the composition, we considered 10 different possible replacements, starting from the best configuration at the previous, lower Cs or Br content, stoichiometry. The geometry and cell were then fully relaxed. The difference in energy among the 10 configurations per stoichiometry is typically very low, with a maximum deviation of $\sim$ 0.0003 eV per stoichiometric unit, i.e. $\sim$1/100 of the thermal energy, k_BT, at room temperature. This justifies an estimate of the mixing entropy contribution to the free energy by the analytical formula for ideal alloys: $T\Delta S = k_BT[xlnx + (1-x)ln(1-x)]$.

Geometry and cell optimization of the various systems was performed using the GGA-DFT in the PBE formulation.[269] The interaction among valence and, in the case of Pb, semi-valence electrons and core electrons and nuclei is described in terms of Rappe-Rabe-Kaxiras-Joannopoulos pseudopotentials.[418] Kohn-Sham orbitals have been expanded in a plane-wave basis set with an energy cutoff of 40 Ry. The cutoff for the density is set to 280 Ry. The Brillouin zone is sampled with a 4x4x4 shifted Monkhorst-Pack mesh of **k**-points.[354]

The accurate determination of the mixing energy requires an energy alignment among the various systems. In fact, in electronic structure calculations in periodic system, there is no unique reference energy. In this article, we use an approach analogous to the one used by Alkauskas *et al.* for band alignment in solids.[355] The band structure of selected systems was computed including SOC effects. It has been previously shown that while this approach results in a too small band gap, it produces correct band dispersion.[350] Since cation and halide mixing can induce structural distortions, we computed the band structure along the high symmetry directions of the triclinic analogue of the simulation boxes, according to the paths reported in literature.[419]

Calculation of the variation of the free energy as a function of stoichiometric composition consisted of several idealized steps. We start from the δ phase. A reference system is considered to consist of a fraction, x, of δ-FAPbI$_3$ and a complementary fraction, $(1-x)$, of δ-CsPbI3. From a thermodynamic point of view, a mixed, single phase, system can be formed if its free energy is lower than that of the weighted sum of the free energy of the two compounds (neglecting interface and surface free energy terms). Here, the variation of the free energy is estimated by the sum of the enthalpic and the mixing entropy contribution (see the discussion above about the mixing entropy contribution). For the results discussed in this article, T in the mixing energy formula was set to 300 K. Figure 3.5 shows that in the case of the δ phase, cation mixing increases the free energy. Thus, for the system, it is energetically more convenient to segregate the δ phase into two separated pure (in terms of cationic composition) domains.

A similar analysis, still taking as a reference the pure δ-FAPbI$_3$ and δ-CsPbI$_3$ phases, is performed for the perovskite α and β phases. For convenience of presentation, we further apply a shifting to the variation of free energy such that this is set equal to zero for the pure α and β FAPbI$_3$. Thus, a negative value of the variation of free energy at a given value of Cs content denotes an improved stability of the mixed cation perovskite system, α and β Cs$_x$FA$_{(1-x)}$PbI$_3$. Figure 3.5f shows that the relative stability of the mixed cation perovskite phases over the yellow δ phase improves up to a given amount of Cs content, and then, for further Cs mixing, it worsens. It is because of this improved stability that no phase transition from the δ to α/β phases, and *vice versa* is observed in DSC measurements at the operative temperature.

It is worth remarking that the reduction of free energy with Cs content is achieved in different ways between the α and β phase. In the β phase the enthalpic and entropic contributions to the free energy are of opposite sign, with an enthalpic contribution that is slightly positive, and the entropic contribution more than compensating this penalty. In the case of the α phase, both contributions are negative leading to a greater stabilization of this phase upon mixing with Cs. From the structural point of view, cation mixing results in the distortion of the PbI$_3$ lattice. This distortion is distinctly higher in the α than in the β phase (Figure B.11), which in the case of pure FA perovskite is of a more regular structure. The fact that a distortion of the lattice leads to stabilization is consistent with the order of stability in $MAPbI_3$ perovskite, in which the structures become more ordered within the series orthorhombic → tetragonal → cubic as the temperature increases. To determine the stabilization induced by halide mixing we used an approach analogous to the one described above.

Concerning carrier mobility, the change of composition does not significantly affect the effective masses of hole and electrons, which remain close to the values of pure $FAPbI_3$ over the experimentally investigated range of Cs content. The effective hole mass passes from $m_{\alpha}^{h} = 0.087$ to 0.094 in going from the pure FA perovskite to a 25% content of Cs for the α phase, and from $m_{\beta}^{h} = 0.116$ to 0.123 for the β one. Also the effective mass of electrons is not significantly affected by the cationic composition. m_{α}^{e} goes from 0.23 α-$FAPbI_3$ to 0.2 in α-$Cs_{0.25}FA_{0.75}PbI_3$, and from 0.146 to 0.166 for the corresponding β phases. Similar to the case of cation mixing, we did not observe any significant change of m_h and m_e associated to halide mixing for the experimentally investigated composition range.

We also performed simulations of the trends in XRD patterns as a function of Cs content. At a Cs fraction of 20% or higher two additional peaks appear in the region $2\theta \sim 26°$ and 28°. The first peak is, indeed, already present in the pure β-$FAPbI_3$ (it is barely visible in the Figure 3.2a between the more intense peaks at $\sim 24°$ and $\sim 27°$, the second due to the FTO). At higher Cs content the feature at $\sim 26°$ becomes more intense and reveals to correspond to several peaks associated with different crystallographic planes (see Figure B.3a and B.3b). In pure FA and Cs-poor samples the interplane distance of these planes is the same, and the corresponding peaks are not distinguishable. At high Cs content the lattice distortions make the interplanar distances of the various planes in this angular region different, and the peaks only partly overlap, giving rise to the complex feature at $\sim 26°$. The peak at 28° is, indeed, better interpreted as a splitting of the single peak of the original β-$FAPbI_3$ system. At low Cs content, $x \leq 0.2$, the structure is cubic-like and the Pb-Pb distances along the three Pb-I-Pb directions are the same. At higher content this symmetry is broken, giving rise to the split peak (see Figure B.3a and B.3c). Consistent with experiments, this splitting increases with higher Cs content. Another tangible effect is that both peaks are shifted towards larger angles. This is due to an overall shrinking of the lattice with the replacement of the larger FA with the smaller Cs.

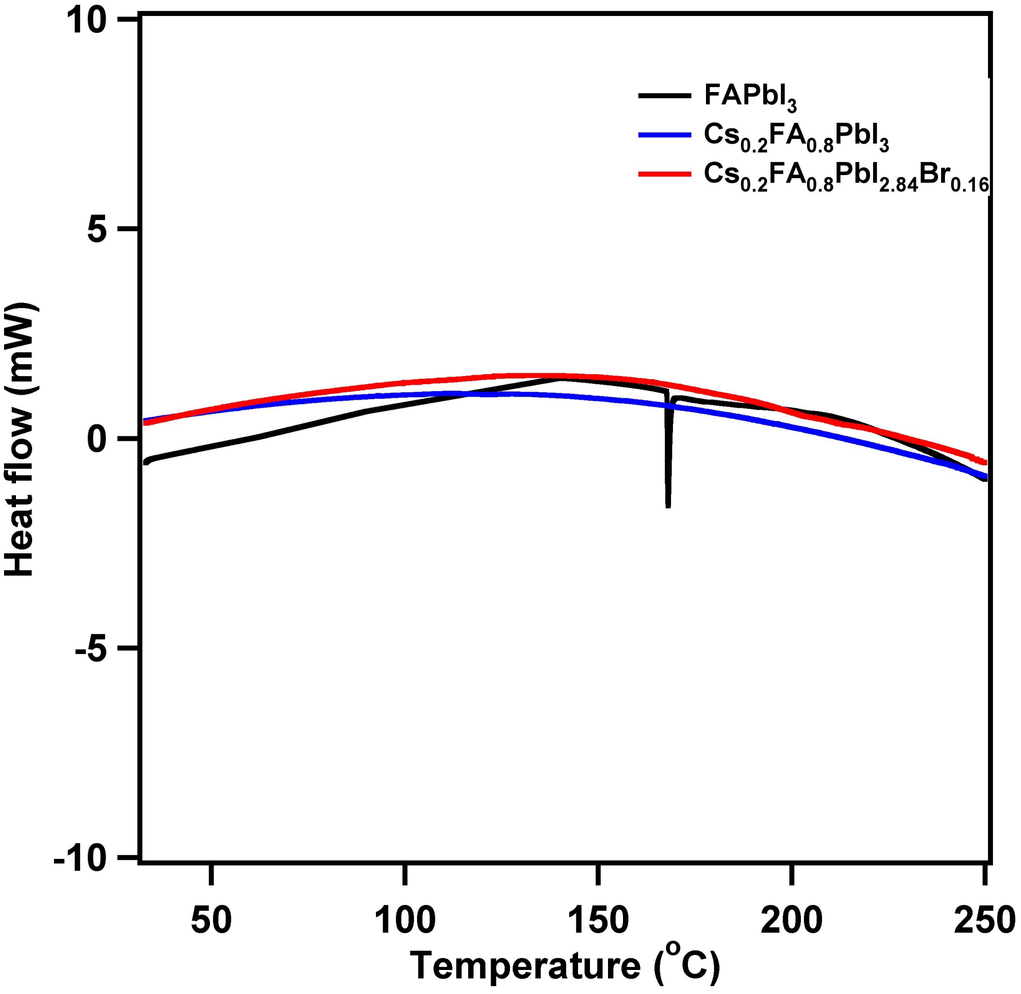

Figure B.1: DSC of $FAPbI_3$, $Cs_{0.2}FA_{0.8}PbI_3$ and $Cs_{0.2}FA_{0.8}PbI_{2.84}Br_{0.16}$. The DSC measurements were tested under N_2 atmosphere.

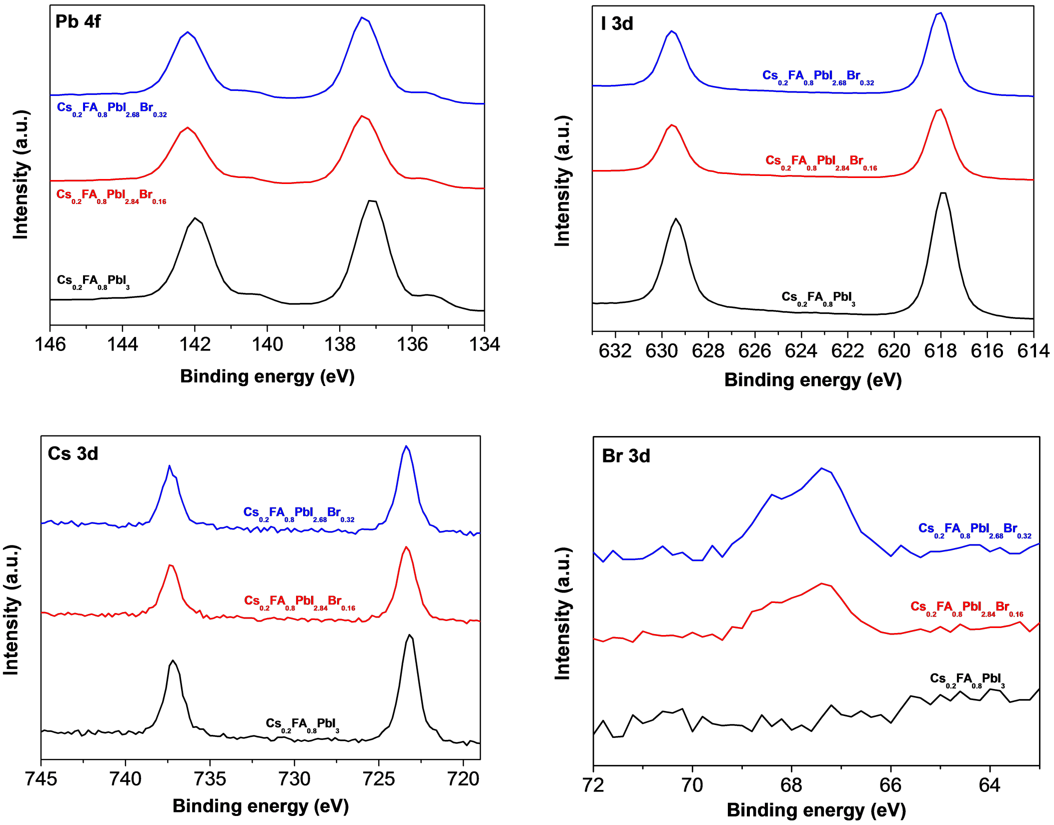

Figure B.2: XPS spectra of $Cs_{0.2}FA_{0.8}PbI_{(3-y)}Br_y$ perovskite films.

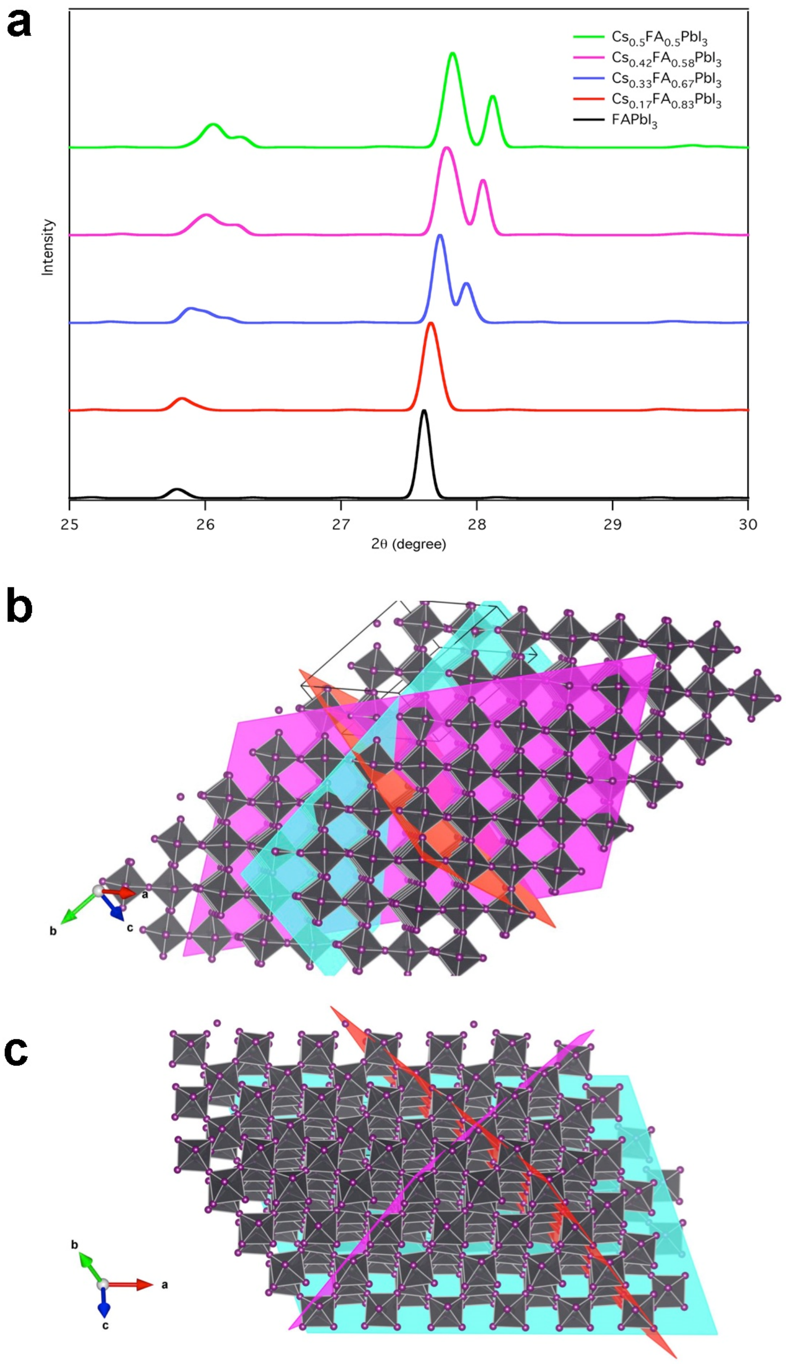

Figure B.3: (a) Simulated XRD patterns as a function of composition for Cs content $x = 0, 0.5$. (b) Main crystal planes corresponding to the peak at $\sim 26°$: $\bar{3}51$ (red), $13\bar{2}$ (purple) and $5\bar{1}0$ (cyan). (c) Main crystal planes corresponding to the peak at $\sim 28°$: $40\bar{2}$ (red), $4\bar{4}2$ (purple) and 042 (cyan).

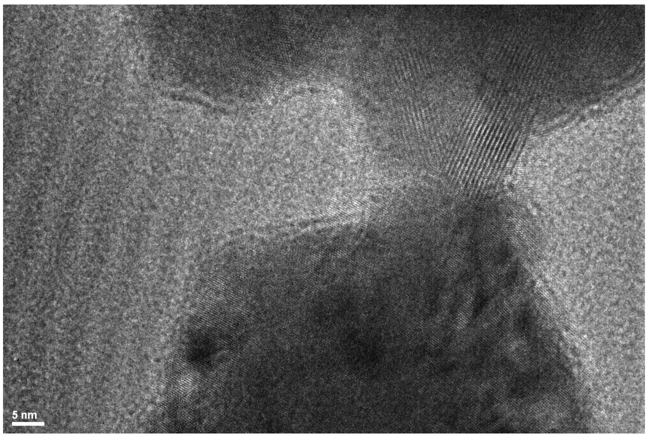

Figure B.4: High resolution TEM image of the $Cs_{0.2}FA_{0.8}PbI_{2.84}Br_{0.16}$ perovskite.

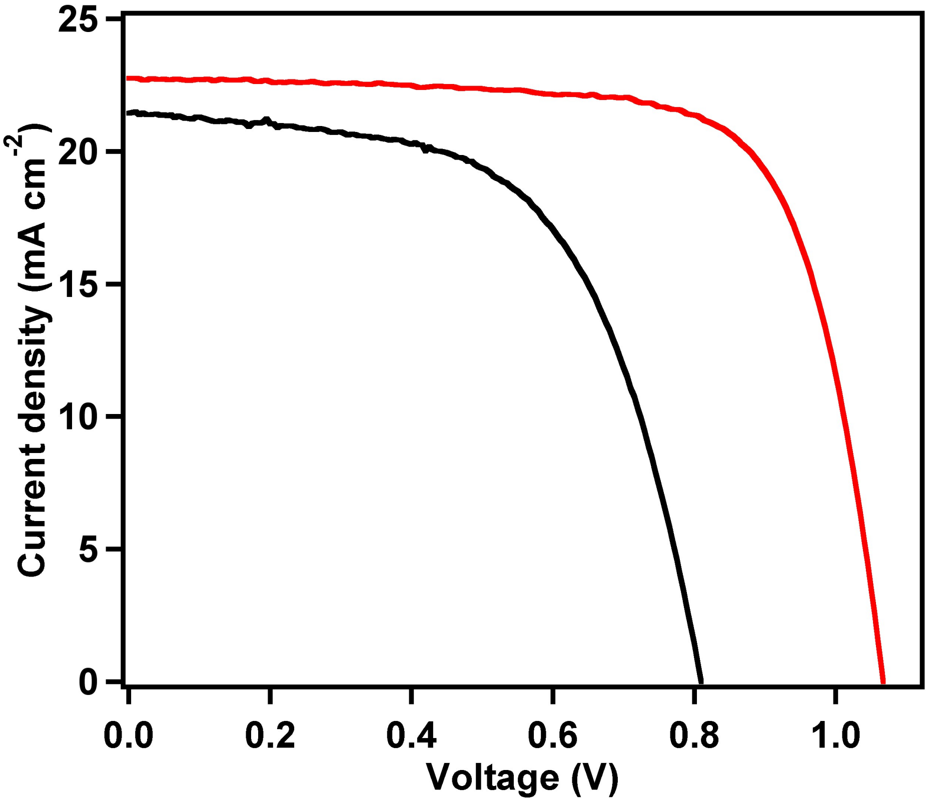

Figure B.5: J-V curve of the $FAPbI_3$ and champion $Cs_{0.2}FA_{0.8}PbI_{2.84}Br_{0.16}$ perovskite solar cells measured under simulated standard AM 1.5 solar illumination at room temperature.

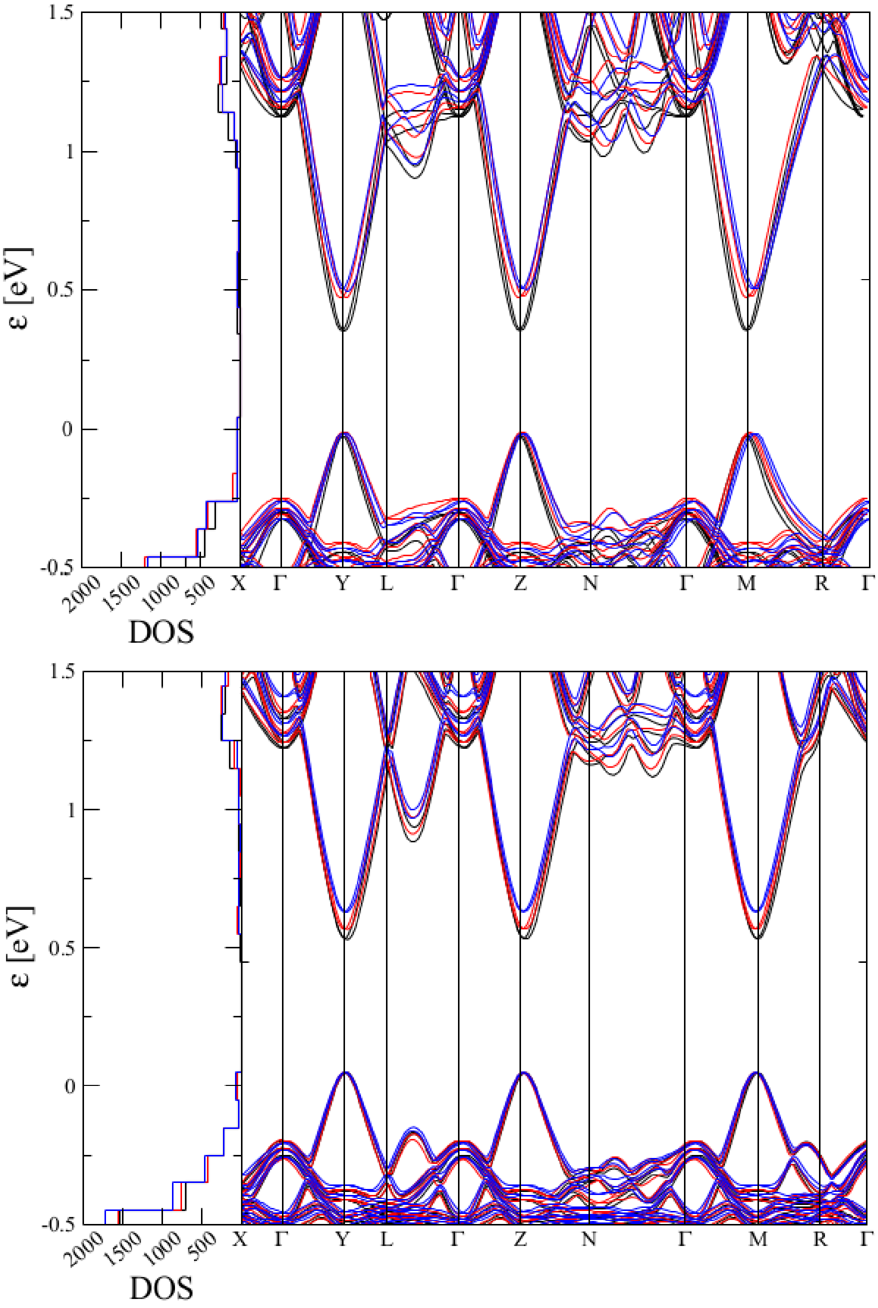

Figure B.6: Band structure of the α (top) and β (bottom) phase at $x = 0$ (black), $x = 0.08$ (red) and $x = 0.25$ (blue) Cs content. Bands are aligned such that the energy of the VBM is 0. On the left hand of the main panel the DOS is shown. This is obtained by binning the energy range, with bins of 0.1 eV, and building the corresponding histogram of the band structure.

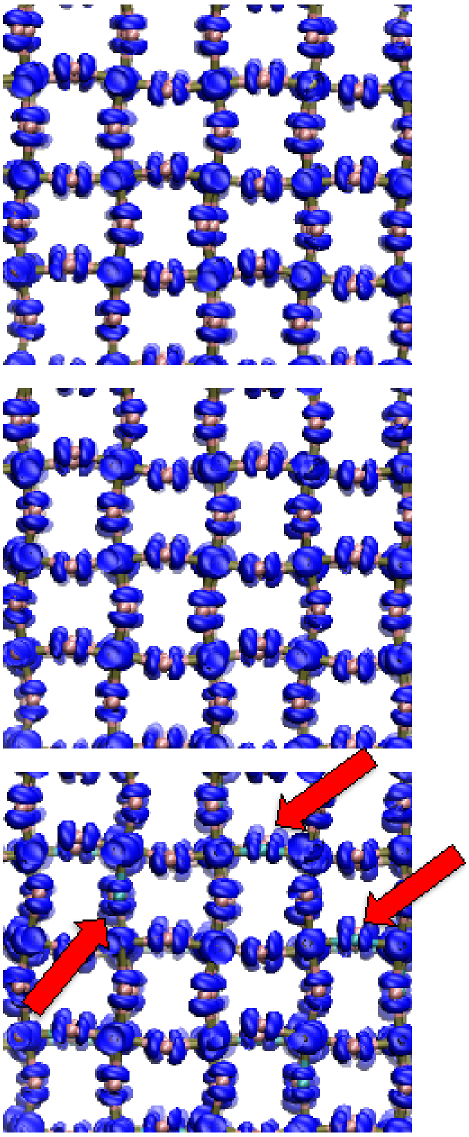

Figure B.7: VBM crystal orbital of (top) $FAPbI_3$ and (middle) $Cs_{0.25}FA_{0.75}PbI_3$ and (bottom) $Cs_{0.25}FA_{0.75}PbI_{2.5}Br_{0.5}$. For convenience, only Pb (green), I (pink) and Br (cyan) atoms are shown. It can be seen that the decrease of the Pb-I-Pb angle induced by the cation mixing results in a reduction of the antibonding interaction between I-5p and Pb-6s atomic orbitals. Halide mixing further increases the distortion of the structure, with a corresponding reduction of the Pb-6s and X-p antibonding overlap. In addition, the more compact Br-4p atomic orbitals (indicated by red arrows) further reduce the antibonding overlap in this crystal orbital.

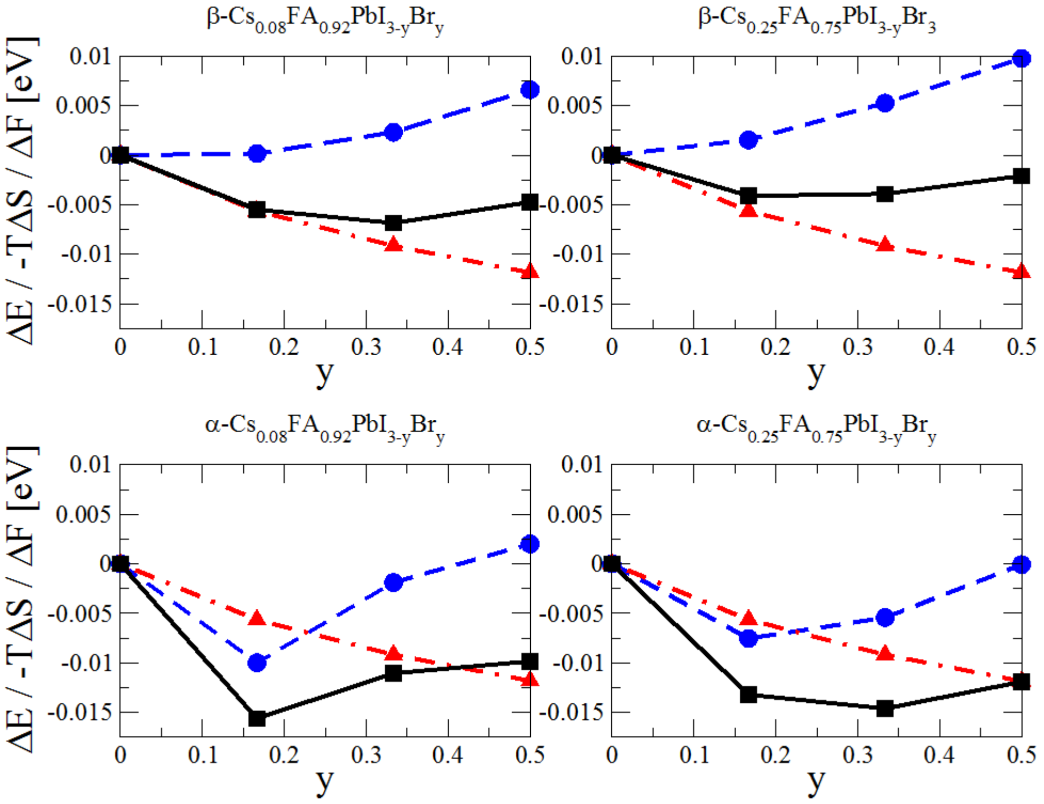

Figure B.8: Variation of internal energy ΔE (blue), mixing entropy contribution $-T\Delta S$ (red), and free energy $F = \Delta E - T\Delta S$ (black) as a function of Br content y for α and β phase of $\mathrm{Cs}_x\mathrm{FA}_{(1-x)}\mathrm{PbI}_{(3-y)}\mathrm{Br}_y$ with x=0.08 and 0.25.

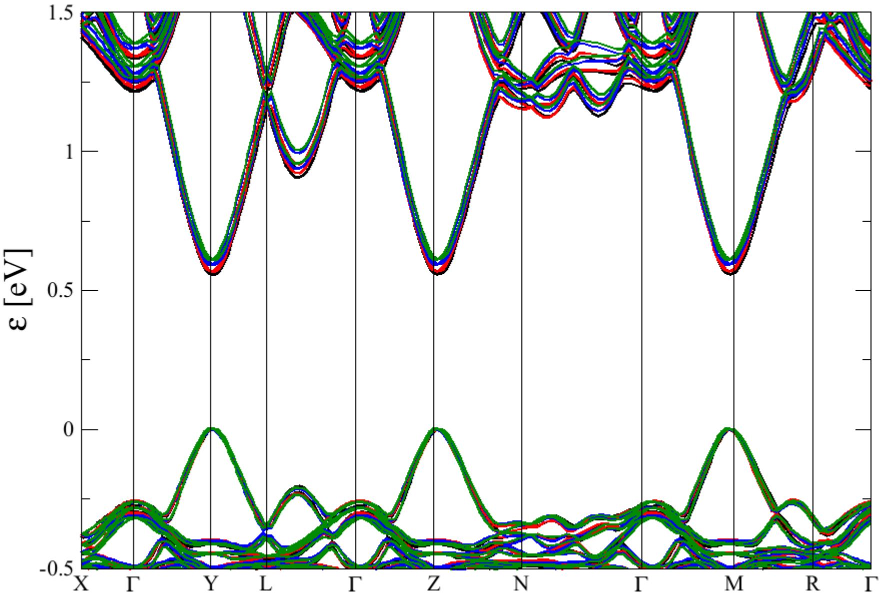

Figure B.9: Band structure of the $Cs_{0.25}FA_{0.75}PbI_{(3-y)}Br_y$, for y= 0 (black), 0.17 (red), 0.33 (blue), 0.5 (green).

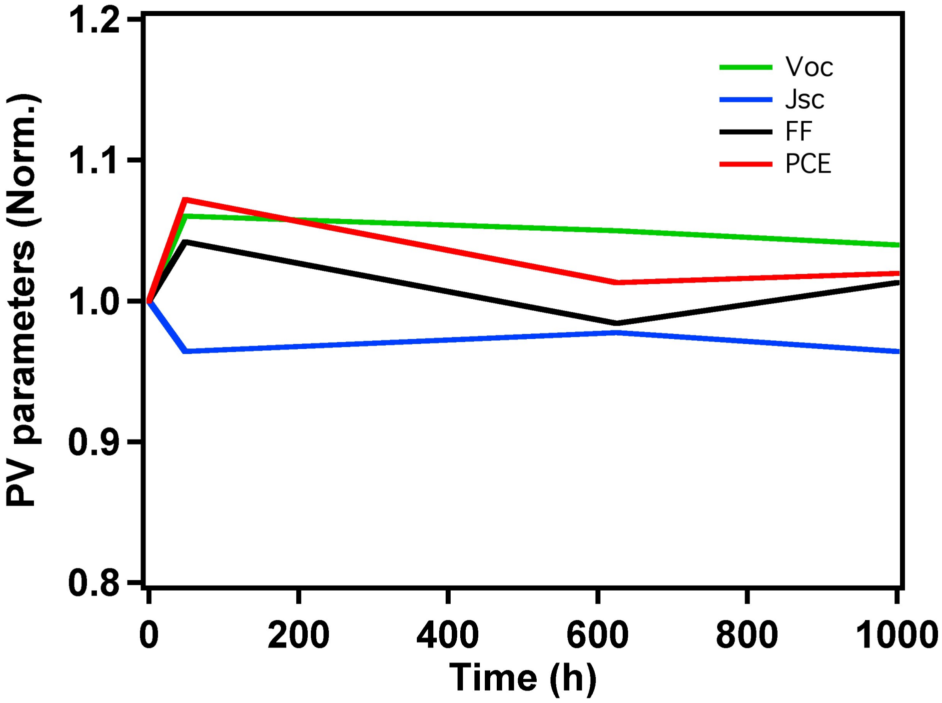

Figure B.10: Stability test results of $Cs_{0.2}FA_{0.8}PbI_3$. (Ambient conditions in dark).

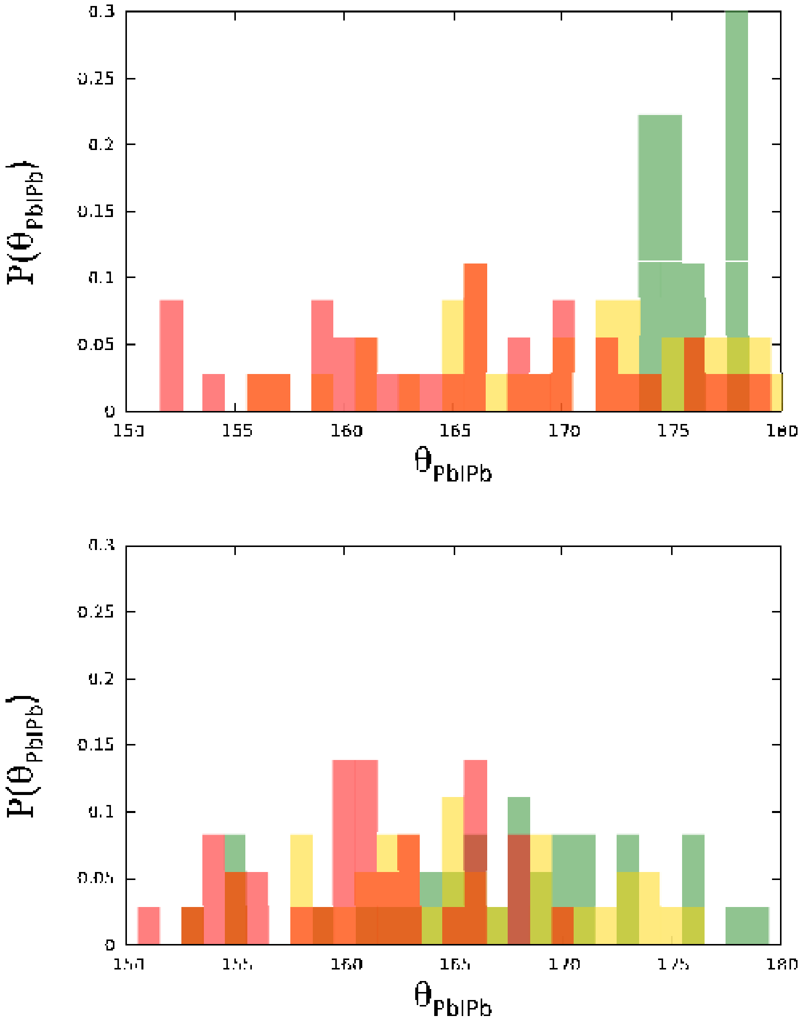

Figure B.11: Distribution of the Pb-I-Pb angle, $\Theta_{\mathrm{Pb-I-Pb}}$, in $\mathrm{Cs}_x\mathrm{FA}_{(1-x)}\mathrm{PbI}_3$, with $x = 0$ (green), $x = 0.17$ (yellow), and $x = 0.33$ (red). The data shown in the top panel are relative to the α phase, those in the bottom panel with respect to the β phase. $\Theta_{\mathrm{Pb-I-Pb}}$ in α-FAPbI_3 is not 180° because in the calculations the crystallographic sites of this perovskite with fractional occupation must be either occupied or empty, leading to a breaking of the crystal symmetry.

Appendix C

Band gap database

A database of 202 organic-inorganic halide perovskites that is currently used in machine-learning applications has been created. The structures vary from purely inorganic to purely organic, as well as mixed cation/mixed halide perovskites. For the development of the database, DFT[254, 255] calculations have been performed using the Quantum Espresso suite of codes.[351, 352] The GGA to DFT in combination with the PBE formulation has been employed,[327] and SOC effects were not included in the calculations. As mentioned, PBE calculations that they do not include SOC effects can correctly predict the band gap of lead halide perovskites, due to large error cancellations between SOC effects and the many-body effects from *e.g.*, the GW self-energy correction for the band gap.[349] Notably, this error cancellation screening does not take place in the case of tin halide perovskites. However, for the development of our database, we followed the same computational protocol for both lead and tin halide perovskites. Hence the estimated band gaps for tin compounds are not consistent with the experimental data.

C.1 Computational details

The Brillouin zone is sampled with a 3x3x3 Monkhorst-Pack **k**-points shifted grid,[354] for cell and structure optimizations. For the band gap calculations, a non-shifted 6x6x6 **k**-points grid is used. The interactions between valence electrons and core electrons and nuclei are described by ultrasoft pseudopotentials.[353] The Kohn-Sham orbitals are expanded in a plane wave basis set with a kinetic energy cutoff of 40 Ry and a density cutoff of 240 Ry, respectively. Below, we present the structures that have been employed for the development of the database.[150, 185, 420]

C.2 Structures

cubic-$CsSnBr_3$
orthorhombic-$CsSnBr_3$
*orthorhombic-$CsSnBr_3$
tetragonal-$CsSnBr_3$
cubic-$CsSnCl_3$
orthorhombic-$CsSnCl_3$
*orthorhombic-$CsSnCl_3$
tetragonal-$CsSnCl_3$
cubic-$CsSnI_3$
orthorhombic-$CsSnI_3$
*orthorhombic-$CsSnI_3$
tetragonal-$CsSnI_3$
cubic-$LiSnBr_3$
orthorhombic-$LiSnBr_3$
*orthorhombic-$LiSnBr_3$
tetragonal-$LiSnBr_3$
cubic-$LiSnCl_3$
orthorhombic-$LiSnCl_3$
*orthorhombic-$LiSnCl_3$
tetragonal-$LiSnCl_3$
cubic-$LiSnI_3$
orthorhombic-$LiSnI_3$
*orthorhombic-$LiSnI_3$
tetragonal-$LiSnI_3$
cubic-$NaSnBr_3$
orthorhombic-$NaSnBr_3$
*orthorhombic-$NaSnBr_3$
tetragonal-$NaSnBr_3$
cubic-$NaSnCl_3$
orthorhombic-$NaSnCl_3$
*orthorhombic-$NaSnCl_3$
tetragonal-$NaSnCl_3$
cubic-$NaSnI_3$
orthorhombic-$NaSnI_3$
*orthorhombic-$NaSnI_3$
tetra-$NaSnI_3$
cubic-$CsSnBr_{2.88}I_{0.12}$
cubic-$CsSnBr_{2.52}I_{0.48}$
cubic-$CsSnBr_3$

orthorhombic-$CsSnBr_3$
*orthorhombic-$CsSnBr_3$
tetragonal-$CsSnBr_3$
cubic-$CsSnCl_3$
orthorhombic-$CsSnCl_3$
*orthorhombic-$CsSnCl_3$
tetragonal-$CsSnCl_3$
cubic-$CsSnI_{2.88}Br_{0.12}$
cubic-$CsSnI_{2.52}Br_{0.48}$
cubic-$CsSnI_3$
orthorhombic-$CsSnI_3$
*orthorhombic-$CsSnI_3$
tetragonal-$CsSnI_3$
cubic-$LiSnBr_3$
orthorhombic-$LiSnBr_3$
*orthorhombic-$LiSnBr_3$
tetragonal-$LiSnBr_3$
cubic-$LiSnCl_3$
orthorhombic-$LiSnCl_3$
*orthorhombic-$LiSnCl_3$
tetragonal-$LiSnCl_3$
cubic-$NaSnBr_3$
orthorhombic-$NaSnBr_3$
*orthorhombic-$NaSnBr_3$
tetragonal-$NaSnBr_3$
cubic-$NaSnCl_3$
orthorhombic-$NaSnCl_3$
*orthorhombic-$NaSnBr_3$
tetragonal-$NaSnBr_3$
cubic-$NaSnCl_3$
orthorhombic-$NaSnCl_3$
*orthorhombic-$NaSnCl_3$
tetragonal-$NaSnCl_3$
cubic-$NaSnI_3$
orthorhombic-$NaSnI_3$
*orthorhombic-$NaSnI_3$
tetragonal-$NaSnI_3$
α-$Cs_{0.08}FA_{0.92}PbBr_3$
α-$Cs_{0.08}FA_{0.92}PbI_{2.16}Br_{0.84}$
α-$Cs_{0.08}FA_{0.92}PbI_{2.31}Br_{0.69}$

α-Cs$_{0.08}$FA$_{0.92}$PbI$_3$
α-Cs$_{0.08}$FA$_{0.92}$PbI$_{2.49}$Br$_{0.51}$
α-Cs$_{0.08}$FA$_{0.92}$PbI$_{2.64}$Br$_{0.36}$
α-Cs$_{0.08}$FA$_{0.92}$PbI$_{2.82}$Br$_{0.18}$
α-Cs$_{0.25}$FA$_{0.75}$PbBr$_3$
α-Cs$_{0.25}$FA$_{0.75}$PbI$_{2.16}$Br$_{0.84}$
α-Cs$_{0.25}$FA$_{0.75}$PbI$_{2.31}$Br$_{0.69}$
α-Cs$_{0.25}$FA$_{0.75}$PbI$_3$
α-Cs$_{0.25}$FA$_{0.75}$PbI$_{2.49}$Br$_{0.51}$
α-Cs$_{0.25}$FA$_{0.75}$PbI$_{2.64}$Br$_{0.36}$
α-Cs$_{0.25}$FA$_{0.75}$PbI$_{2.82}$Br$_{0.18}$
α-Cs$_{0.33}$FA$_{0.67}$PbI$_3$
α-Cs$_{0.41}$FA$_{0.59}$PbI$_3$
α-Cs$_{0.5}$FA$_{0.5}$PbI$_3$
α-CsPbI$_3$
α-FA$_{0.08}$Cs$_{0.92}$PbI$_3$
α-FA$_{0.16}$Cs$_{0.84}$PbI$_3$
α-FA$_{0.25}$Cs$_{0.75}$PbI$_3$
α-FA$_{0.33}$Cs$_{0.67}$PbI$_3$
α-FA$_{0.41}$Cs$_{0.59}$PbI$_3$
α-FA$_{0.5}$Cs$_{0.5}$PbI$_3$
α-FAPbBr$_3$
α-FAPbI$_3$
α-FAPbI$_{0.83}$Br$_{0.17}$
α-FAPbI$_{0.88}$Br$_{0.12}$
α-FAPbI$_{0.94}$Br$_{0.06}$
α-MA$_{0.08}$FA$_{0.92}$PbI$_3$
α-MA$_{0.16}$FA$_{0.84}$PbI$_3$
α-MA$_{0.25}$FA$_{0.75}$PbI$_3$
α-MA$_{0.33}$FA$_{0.67}$PbI$_3$
α-MA$_{0.41}$FA$_{0.59}$PbI$_3$
α-MA$_{0.5}$FA$_{0.5}$PbI$_3$
β-Cs$_{0.08}$FA$_{0.92}$PbBr$_3$
β-Cs$_{0.08}$FA$_{0.92}$PbI$_3$
β-Cs$_{0.08}$FA$_{0.92}$PbI$_{2.49}$Br$_{0.51}$
β-Cs$_{0.08}$FA$_{0.92}$PbI$_{2.64}$Br$_{0.36}$
β-Cs$_{0.02}$FA$_{0.92}$PbI$_{2.82}$Br$_{0.18}$
β-Cs$_{0.16}$FA$_{0.84}$PbI$_3$
β-Cs$_{0.25}$FA$_{0.75}$PbBr$_3$
β-Cs$_{0.25}$FA$_{0.75}$PbI$_3$

β-$Cs_{0.25}FA_{0.75}PbI_{2.49}Br_{0.51}$
β-$Cs_{0.25}FA_{0.75}PbI_{2.64}Br_{0.36}$
β-$Cs_{0.25}FA_{0.75}PbI_{2.82}Br_{0.18}$
β-$Cs_{0.33}FA_{0.67}PbI_3$
β-$Cs_{0.41}FA_{0.59}PbI_3$
β-$Cs_{0.5}FA_{0.5}PbI_3$
β-$CsPbI_3$
β-$FA_{0.08}Cs_{0.92}PbI_3$
β-$FA_{0.16}Cs_{0.84}PbI_3$
β-$FA_{0.25}Cs_{0.75}PbI_3$
β-$FA_{0.33}Cs_{0.67}PbI_3$
β-$FA_{0.41}Cs_{0.59}PbI_3$
β-$FAPbI_3$
$Cs_{0.16}MA_{0.16}FA_{0.68}PbI_3$
$Cs_{0.25}MA_{0.16}FA_{0.59}PbI_3$
δ-$Cs_{0.08}FA_{0.92}PbBr_3$
δ-$Cs_{0.08}FA_{0.92}PbI_3$
δ-$Cs_{0.08}FA_{0.92}PbI_{2.49}Br_{0.51}$
δ-$Cs_{0.08}FA_{0.92}PbI_{2.64}Br_{0.36}$
δ-$Cs_{0.08}FA_{0.92}PbI_{2.82}Br_{0.18}$
δ-$Cs_{0.16}FA_{0.84}PbI_3$
δ-$Cs_{0.25}FA_{0.75}PbBr_3$
δ-$Cs_{0.25}FA_{0.75}PbI_3$
δ-$Cs_{0.25}FA_{0.75}PbI_{2.49}Br_{0.51}$
δ-$Cs_{0.25}FA_{0.75}PbI_{2.82}Br_{0.18}$
δ-$Cs_{0.33}FA_{0.67}PbI_3$
δ-$Cs_{0.41}FA_{0.59}PbI_3$
δ-$Cs_{0.5}FA_{0.5}PbI_3$
δ-$CsPbI_3$
δ-$FA_{0.08}Cs_{0.92}PbI_3$
δ-$FA_{0.16}Cs_{0.84}PbI_3$
δ-$FA_{0.25}Cs_{0.75}PbI_3$
δ-$FA_{0.33}Cs_{0.67}PbI_3$
δ-$FA_{0.41}Cs_{0.59}PbI_3$
δ-$FA_{0.5}Cs_{0.5}PbI_3$
δ-$FAPbI_3$
δ-$MA_{0.83}FA_{0.17}PbI_3$
δ-$MA_{0.16}FA_{0.84}PbI_3$
δ-$MA_{0.25}FA_{0.75}PbI_3$
δ-$MA_{0.33}FA_{0.67}PbI_3$

δ-$MA_{0.41}FA_{0.59}PbI_3$
δ-$MA_{0.5}FA_{0.5}PbI_3$
orthorhombic-$FAPbBr_3$ (FA^+ with similar orientations)
orthorhombic-$FAPbBr_3$ (FA^+ with random orientations)
orthorhombic-$FAPbI_3$ (FA^+ with similar orientations)
orthorhombic-$FAPbI_3$ (FA^+ with random orientations)
orthorhombic-$MAPbI_3$ (MA^+ with similar orientations)
orthorhombic-$MAPbI_3$ (MA^+ with random orientations)
tetragonal-$MAPbI_3$
$Rb_{0.16}Cs_{0.08}FA_{0.76}PbI_3$
$Rb_{0.25}Cs_{0.08}FA_{0.67}PbI_3$
$Rb_{0.33}Cs_{0.08}FA_{0.59}PbI_3$
$Rb_{0.41}Cs_{0.08}FA_{0.51}PbI_3$
$Rb_{0.08}Cs_{0.16}FA_{0.76}PbI_3$
$Rb_{0.16}Cs_{0.16}FA_{0.68}PbI_3$
$Rb_{0.25}Cs_{0.16}FA_{0.59}PbI_3$
$Rb_{0.33}Cs_{0.16}FA_{0.51}PbI_3$
$Rb_{0.08}Cs_{0.25}FA_{0.67}PbI_3$
$Rb_{0.16}Cs_{0.25}FA_{0.59}PbI_3$
$Rb_{0.25}Cs_{0.25}FA_{0.5}PbI_3$
$Rb_{0.08}Cs_{0.33}FA_{0.59}PbI_3$
$Rb_{0.16}Cs_{0.33}FA_{0.51}PbI_3$
$Rb_{0.08}Cs_{0.41}FA_{0.51}PbI_3$
δ-$Rb_{0.16}Cs_{0.08}FA_{0.76}PbI_3$
δ-$Rb_{0.25}Cs_{0.08}FA_{0.67}PbI_3$
δ-$Rb_{0.33}Cs_{0.08}FA_{0.59}PbI_3$
δ-$Rb_{0.41}Cs_{0.08}FA_{0.51}PbI_3$
δ-$Rb_{0.08}Cs_{0.16}FA_{0.76}PbI_3$
δ-$Rb_{0.16}Cs_{0.16}FA_{0.68}PbI_3$
δ-$Rb_{0.25}Cs_{0.16}FA_{0.59}PbI_3$
δ-$Rb_{0.33}Cs_{0.16}FA_{0.51}PbI_3$
δ-$Rb_{0.08}Cs_{0.25}FA_{0.67}PbI_3$
δ-$Rb_{0.16}Cs_{0.25}FA_{0.59}PbI_3$
δ-$Rb_{0.25}Cs_{0.25}FA_{0.5}PbI_3$
δ-$Rb_{0.08}Cs_{0.33}FA_{0.59}PbI_3$
δ-$Rb_{0.16}Cs_{0.33}FA_{0.51}PbI_3$
δ-$Rb_{0.08}Cs_{0.41}FA_{0.51}PbI_3$
α-$Cs_{0.16}FA_{0.84}PbI_3$
δ-$Cs_{0.25}FA_{0.75}PbI_{2.64}Br_{0.36}$
$Rb_{0.08}Cs_{0.08}MA_{0.08}FA_{0.76}PbI_3$

$Rb_{0.16}MA_{0.08}FA_{0.76}PbI_3$
$Rb_{0.33}MA_{0.08}FA_{0.59}PbI_3$
$Rb_{0.16}Cs_{0.16}MA_{0.08}FA_{0.60}PbI_3$

*The structures have been created starting from a different initial orthorhombic structure.

Appendix D

Supporting Information - Atomistic origins of the limited phase stability of Cs^+-rich $FA_xCs_{(1-x)}PbI_3$ mixtures

D.1 Finite temperature effects

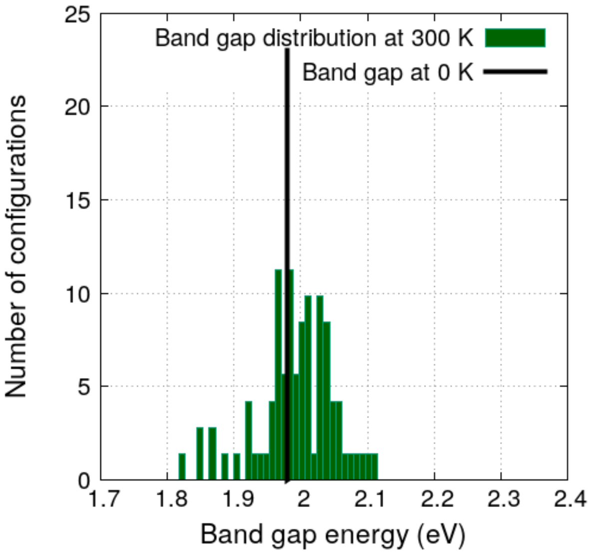

Figure D.1: Histogram of thermal distribution, for the orthorhombic phase with tilting angles different than 0° of $CsPbI_3$.

D.2 XRD characterization

XRD patterns were recorded on an X'Pert MPD PRO (Panalytical) diffractometer equipped with a ceramic tube (Cu anode, $\lambda = 1.54060$), a secondary graphite (002) monochromator and an RTMS X'Celerator detector (Panalytical) in an angle range of $2\theta = 5°$ to $40°$, by step scanning with a step of 0.02 degree.

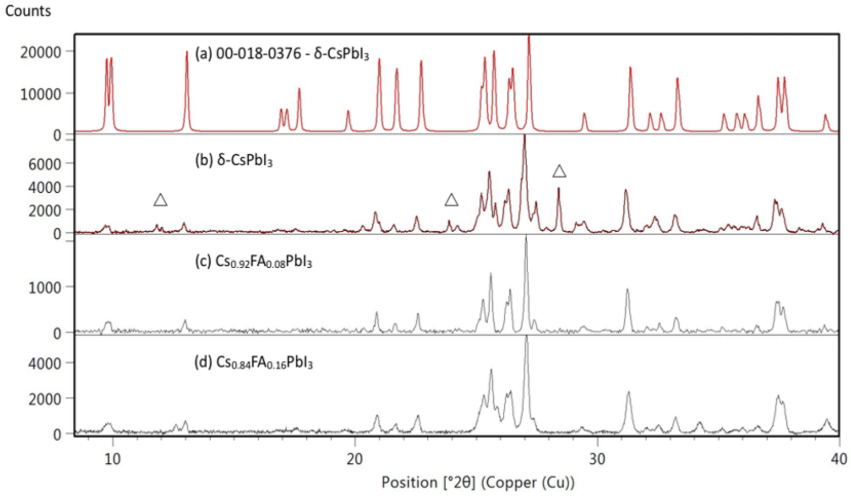

Figure D.2: Powder XRD characterization of the materials. (a) reference δ-$CsPbI_3$ pattern (ICDD number: 00-018-0376). Experimental patterns: (b) δ-$CsPbI_3$, (c) $FA_{0.08}Cs_{0.92}PbI_3$, (d) $FA_{0.16}Cs_{0.84}PbI_3$. '△' indicate an impurity phase (Cs_4PbI_6).

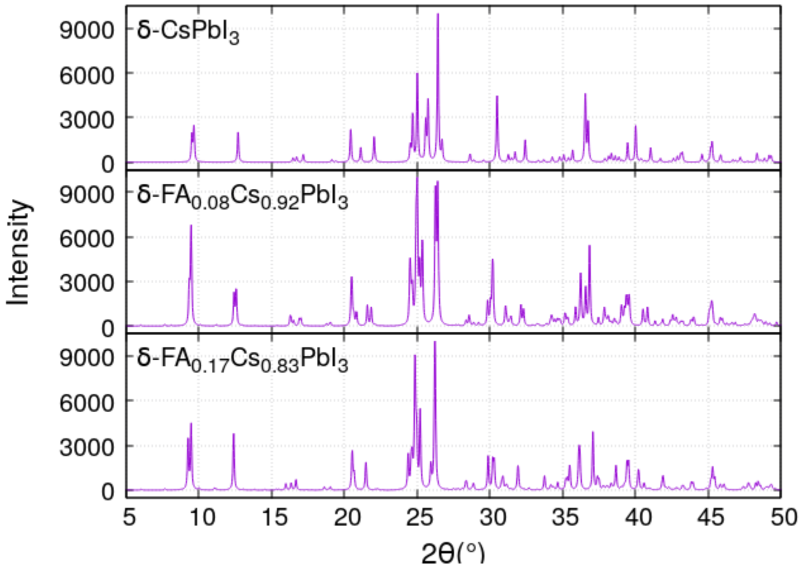

Figure D.3: Simulated powder XRD patterns with $\lambda = 1.54056$ and h,k,l=0,7,-5, in an angle range of $2\theta = 5°$ to $50°$, by step scanning with a step of 0.02 degree. (a) δ-$CsPbI_3$, (b) $FA_{0.08}Cs_{0.92}PbI_3$, (c) $FA_{0.17}Cs_{0.83}PbI_3$.

Bibliography

[1] National renewable energy laboratory (NREL), national center for photovoltaics (NCPV), 2019. URL `https://www.nrel.gov/pv/assets/pdfs/pv-efficiency-chart.20190103.pdf`.

[2] Global energy and CO_2 status report, (2017), 2018. URL `https://naturalsciences.ch/uuid/ea8ab164-24eb-51ec-8400-d060b1b40048?r=20181129105710_1543435629_cdaa0c0a-950b-5784-8225-7e658d0ecc38`.

[3] F. Barbir, T.N. Veziroğlu, and H.J. Plass. Environmental damage due to fossil fuels use. *International Journal of Hydrogen Energy*, 15(10):739 – 749, 1990.

[4] M. Kampa and E. Castanas. Human health effects of air pollution. *Environmental Pollution*, 151(2):362 – 367, 2008. Proceedings of the 4th International Workshop on Biomonitoring of Atmospheric Pollution (With Emphasis on Trace Elements).

[5] J. F. Mercure, H. Pollitt, J. E. Vinuales, N. R. Edwards, P. B. Holden, U. Chewpreecha, P. Salas, I. Sognnaes, A. Lam, and F. Knobloch. Macroeconomic impact of stranded fossil fuel assets. *Nature Climate Change*, 8: 588 – 593, 2018.

[6] N. L. Panwar, S. C. Kaushik, and S. Kothari. Role of renewable energy sources in environmental protection: A review. *Renewable and Sustainable Energy Reviews*, 15(3):1513 – 1524, 2011.

[7] G. Sliwoski, S. Kothiwale, J. Meiler, and E. W. Lowe. Computational methods in drug discovery. *Pharmacological Reviews*, 66(1):334–395, 2014.

[8] M. O. Steinhauser and S. Hiermaier. A review of computational methods in materials science: Examples from shock-wave and polymer physics. *International Journal of Molecular Sciences*, 10(12):5135–5216, 2009.

[9] E. Delyannis. Historic background of desalination and renewable energies. *Solar Energy*, 75(5):357 – 366, 2003.

[10] A. B. Mouchot. *(La) Chaleur solaire et ses applications industrielles.* Gauthier-Villars, 1869.

[11] René Sigrist, Horace-Bénédict de Saussure, Horace-Bénédict de Saussure, Glaciologiste Botaniste, Horace-Bénédict de Saussure, and Glaciologist Botanist. *Le capteur solaire de Horace-Bénédict de Saussure: genèse d'une science empirique.* Ed. Passé-Présent, 1993.

[12] L. Boufon. 1747-1748. Invention des mirroirs ardent pour brileur au grand distance (invention of hot mirrors burning at long distance). *Memoire Academie Royale Sciences*, page 82, 1747.

[13] A. E. Becquerel. Recherches sur les effets de la radiation chimique de la lumiere solaire au moyen des courants electriques. *CR Acad. Sci*, 9(145): 1, 1839.

[14] A. Mouchot. Resultat des experiences faites en divers points de l'Algerie, pour l'emploi industrielle de la chaleur solaire (results of some experiments in algeria, for industrial use of solar energy). *Comptes Rendu Acad Sci*, 86:1019–21, 1878.

[15] R. C. Jordan and W. E. Ibele. Richard C. Jordan. In *Proceedings of the World Symposium on Applied Solar Energy, Phoenix, Arizona, November 1-5, 1955*, page 81. Stanford Research Institute, 1956.

[16] N. W. Wheeler and W. W. Evans. Evaporating and distilling with solar heat. *US Patent*, (102.633), 1870.

[17] J. Harding. Apparatus for solar distillation. In *Minutes of the Proceedings of the Institution of Civil Engineers*, volume 73, pages 284–288. Thomas Telford-ICE Virtual Library, 1883.

[18] Z. A. Smith and K. D. Taylor. *Renewable and alternative energy resources: a reference handbook.* ABC-CLIO, 2008.

[19] A. Chodos. April 25, 1954: Bell labs demonstrates the first practical silicon solar cell. *APS News-This month in Physics history*, 2009.

[20] Space Age Began. Conditions in 1957. 2007.

[21] R. Lindsey. Physicist's solar airplane set to challenge the english channel. *The New York Times*, 1981.

[22] B. O'regan and M. Grätzel. A low-cost, high-efficiency solar cell based on dye-sensitized colloidal TiO_2 films. *Nature*, 353(6346):737, 1991.

[23] M. Grätzel. Photoelectrochemical cells. *Nature*, 414(6861):338, 2001.

[24] T. Novak. Solar powered vehicle, May 14 1985. US Patent 4,516,647.

[25] Solar impulse foundation. URL `https://solarimpulse.com/`.

[26] Y.-H. Lee, J.-S. Kim, J. Noh, I. Lee, H. J. Kim, S. Choi, J. Seo, S. Jeon, T.-S. Kim, J.-Y. Lee, and J. W. Choi. Wearable textile battery rechargeable by solar energy. *Nano Letters*, 13(11):5753–5761, 2013.

[27] A. Einstein. Concerning an heuristic point of view toward the emission and transformation of light. *Annalen der Physik*, 17:132 – 148, 1905.

[28] B. Van Zeghbroeck. Principles of semiconductor devices, 1997. URL `https://ecee.colorado.edu/~bart/book/ex025.htm`.

[29] Basic photovoltaic principles and methods. URL `https://www.nrel.gov/docs/legosti/old/1448.pdf`.

[30] N. W. Ashcroft and N. D. Mermin. *Solid state physics*. Harcourt College Publishers, 1976.

[31] K. Jäger, I. Olindo, A. H. M. Smets, R. A.C.M.M. van Swaaij, and M. Zeman. Solar energy, fundamentals, technology, and systems, 2014. URL `https://courses.edx.org/c4x/DelftX/ET.3034TU/asset/solar_energy_v1.1.pdf`.

[32] W. Shockley and H. J. Queisser. Detailed balance limit of efficiency of p-n junction solar cells. *Journal of applied physics*, 32(3):510–519, 1961.

[33] S. Rühle. Tabulated values of the Shockley-Queisser limit for single junction solar cells. *Solar Energy*, 130:139–147, 2016.

[34] A. Shah, P. Torres, R. Tscharner, N. Wyrsch, and H. Keppner. Photovoltaic technology: The case for thin-film solar cells. *Science*, 285(5428): 692–698, 1999.

[35] M. A. Green. Photovoltaics: technology overview. *Energy Policy*, 28(14): 989 – 998, 2000.

[36] Taesoo D. L. and Abasifreke U. E. A review of thin film solar cell technologies and challenges. *Renewable and Sustainable Energy Reviews*, 70: 1286 – 1297, 2017.

[37] D. E. Carlson and C. R. Wronski. Amorphous silicon solar cell. *Applied Physics Letters*, 28(11):671–673, 1976.

[38] D. Derkacs, S. H. Lim, P. Matheu, W. Mar, and E. T. Yu. Improved performance of amorphous silicon solar cells via scattering from surface plasmon polaritons in nearby metallic nanoparticles. *Applied Physics Letters*, 89 (9):093103, 2006.

[39] J. Britt and C. Ferekides. Thin-film CdS/CdTe solar cell with 15.8% efficiency. *Applied Physics Letters*, 62(22):2851–2852, 1993.

[40] X. Wu. High-efficiency polycrystalline CdTe thin-film solar cells. *Solar Energy*, 77(6):803 – 814, 2004.

[41] T. L. Chu and S. S. Chu. Recent progress in thin-film cadmium telluride solar cells. *Progress in Photovoltaics: Research and Applications*, 1(1): 31–42, 1993.

[42] N. Naghavi, S. Spiering, M. Powalla, B. Cavana, and D. Lincot. High-efficiency copper indium gallium diselenide (CIGS) solar cells with indium sulfide buffer layers deposited by atomic layer chemical vapor deposition (ALCVD). *Progress in Photovoltaics: Research and Applications*, 11(7): 437–443, 2003.

[43] K. Ramanathan, M. A. Contreras, C. L. Perkins, S. Asher, F. S. Hasoon, J. Keane, D. Young, M. Romero, W. Metzger, R. Noufi, J. Ward, and A. Duda. Properties of 19.2% efficiency ZnO/CdS/$CuInGaSe_2$ thin-film solar cells. *Progress in Photovoltaics: Research and Applications*, 11(4): 225–230, 2003.

[44] K. L. Chopra, P. D. Paulson, and V. Dutta. Thin-film solar cells: an overview. *Progress in Photovoltaics: Research and Applications*, 12(2-3): 69–92, 2004.

[45] J.-H. Yoon, J Song, and S.-J. Lee. Practical application of building integrated photovoltaic (BIPV) system using transparent amorphous silicon thin-film PV module. *Solar Energy*, 85(5):723 – 733, 2011.

[46] M. A. Green. Third generation photovoltaics: Ultra-high conversion efficiency at low cost. *Progress in Photovoltaics: Research and Applications*, 9(2):123–135, 2001.

[47] M. A. Green. *Third generation photovoltaics*. Springer, 2006.

[48] H. Katagiri, K. Jimbo, W. S. Maw, K. Oishi, M. Yamazaki, H. Araki, and A. Takeuchi. Development of CZTS-based thin film solar cells. *Thin Solid Films*, 517(7):2455 – 2460, 2009. Thin Film Chalogenide Photovoltaic Materials (EMRS, Symposium L).

[49] B. Shin, O. Gunawan, Y. Zhu, N. A. Bojarczuk, S. J. Chey, and S. Guha. Thin film solar cell with 8.4% power conversion efficiency using an earth-abundant Cu_2ZnSnS_4 absorber. *Progress in Photovoltaics: Research and Applications*, 21(1):72–76, 2013.

[50] Q. Guo, G. M. Ford, W.-C. Yang, B. C. Walker, E. A. Stach, H. W. Hillhouse, and R. Agrawal. Fabrication of 7.2% efficient CZTSSe solar cells using CZTS nanocrystals. *Journal of the American Chemical Society*, 132(49):17384–17386, 2010.

[51] K. Wang, O. Gunawan, T. Todorov, B. Shin, S. J. Chey, N. A. Bojarczuk, D. Mitzi, and S. Guha. Thermally evaporated Cu_2ZnSnS_4 solar cells. *Applied Physics Letters*, 97(14):143508, 2010.

[52] M. Grätzel. Dye-sensitized solar cells. *Journal of Photochemistry and Photobiology C: Photochemistry Reviews*, 4(2):145 – 153, 2003.

[53] M. Grätzel. Solar energy conversion by dye-sensitized photovoltaic cells. *Inorganic Chemistry*, 44(20):6841–6851, 2005.

[54] S. Günes, H. Neugebauer, and N. S. Sariciftci. Conjugated polymer-based organic solar cells. *Chemical Reviews*, 107(4):1324–1338, 2007.

[55] D. Wöhrle and D. Meissner. Organic solar cells. *Advanced Materials*, 3 (3):129–138, 1991.

[56] H. Hoppe and N. S. Sariciftci. Organic solar cells: An overview. *Journal of Materials Research*, 19(7):1924–1945, 2004.

[57] A.J Nozik. Quantum dot solar cells. *Physica E: Low-dimensional Systems and Nanostructures*, 14(1):115 – 120, 2002.

[58] P. V. Kamat. Quantum dot solar cells. semiconductor nanocrystals as light harvesters. *The Journal of Physical Chemistry C*, 112(48):18737–18753, 2008.

[59] C.-H. M. Chuang, P. R. Brown, V. Bulović, and M. G. Bawendi. Improved performance and stability in quantum dot solar cells through band alignment engineering. *Nature materials*, 13(8):796, 2014.

[60] A. Kojima, K. Teshima, Y. Shirai, and T. Miyasaka. Organometal halide perovskites as visible-light sensitizers for photovoltaic cells. *Journal of the American Chemical Society*, 131(17):6050–6051, 2009.

[61] J.-H. Im, C.-R. Lee, J.-W. Lee, S.-W. Park, and N.-G. Park. 6.5% efficient perovskite quantum-dot-sensitized solar cell. *Nanoscale*, 3:4088–4093, 2011.

[62] H.-S. Kim, C.-R. Lee, J.-H. Im, K.-B. Lee, T. Moehl, A. Marchioro, S.-J. Moon, R. Humphry-Baker, J.-H. Yum, J. E. Moser, M. Grätzel, and N.-G. Park. Lead iodide perovskite sensitized all-solid-state submicron thin film mesoscopic solar cell with efficiency exceeding 9%. *Scientific Reports*, 2: 591.

[63] M. M. Lee, J. Teuscher, T. Miyasaka, T. N. Murakami, and H. J. Snaith. Efficient hybrid solar cells based on meso-superstructured organometal halide perovskites. *Science*, 338(6107):643–647, 2012.

[64] L. Etgar, P. Gao, Z. Xue, Q. Peng, A. K. Chandiran, B. Liu, Md. K. Nazeeruddin, and M. Grätzel. Mesoscopic $CH_3NH_3PbI_3/TiO_2$ heterojunction solar cells. *Journal of the American Chemical Society*, 134:17396–17399, 2012.

[65] A. Mei, X. Li, L. Liu, Z. Ku, T. Liu, Y. Rong, M. Xu, M. Hu, J. Chen, Y. Yang, M. Grätzel, and H. Han. A hole-conductor–free, fully printable mesoscopic perovskite solar cell with high stability. *Science*, 345(6194): 295–298, 2014.

[66] M. Grätzel. The light and shade of perovskite solar cells. *Nature materials*, 13(9):838, 2014.

[67] J. Burschka, N. Pellet, S.-J. Moon, R. Humphry-Baker, P. Gao, M. K Nazeeruddin, and M. Grätzel. Sequential deposition as a route to high-performance perovskite-sensitized solar cells. *Nature*, 499(7458):316, 2013.

[68] S. Almosni, A. Delamarre, Z. Jehl, D. Suchet, L. Cojocaru, M. Giteau, B. Behaghel, A. Julian, C. Ibrahim, L. Tatry, H. Wang, T. Kubo, S. Uchida, H. Segawa, N. Miyashita, R. Tamaki, Y. Shoji, K. Yoshida, N. Ahsan, K. Watanabe, T. Inoue, M. Sugiyama, Y. Nakano, T. Hamamura, T. Toupance, C. Olivier, S. Chambon, L. Vignau, C. Geffroy, E. Cloutet, G. Hadziioannou, N. Cavassilas, P. Rale, A. Cattoni, S. Collin, F. Gibelli, M. Paire, L. Lombez, D. Aureau, M. Bouttemy, A. Etcheberry, Y. Okada, and J.-F. Guillemoles. Material challenges for solar cells in

the twenty-first century: directions in emerging technologies. *Science and Technology of Advanced Materials*, 19(1):336–369, 2018.

[69] A. Freundlich and A. Alemu. Multi quantum well multijunction solar cell for space applications. *physica status solidi (c)*, 2(8):2978–2981, 2005.

[70] T. Ameri, G. Dennler, C. Lungenschmied, and C. J. Brabec. Organic tandem solar cells: A review. *Energy & Environmental Science*, 2(4): 347–363, 2009.

[71] A. Luque, A. Marti, and C. Stanley. Understanding intermediate-band solar cells. *Nature Photonics*, 6(3):146, 2012.

[72] D. König, K. Casalenuovo, Y. Takeda, G. Conibeer, J.F. Guillemoles, R. Patterson, L.M. Huang, and M.A. Green. Hot carrier solar cells: Principles, materials and design. *Physica E: Low-dimensional Systems and Nanostructures*, 42(10):2862 – 2866, 2010.

[73] M. Kaltenbrunner, M. S. White, E. D. Głowacki, T. Sekitani, T. Someya, N. S. Sariciftci, and S. Bauer. Ultrathin and lightweight organic solar cells with high flexibility. *Nature communications*, 3:770, 2012.

[74] G. F. Brown and J. Wu. Third generation photovoltaics. *Laser & Photonics Reviews*, 3(4):394–405, 2009.

[75] S. Sharma, K. K. Jain, and A. Sharma. Solar cells: in research and applications-a review. *Materials Sciences and Applications*, 6(12):1145, 2015.

[76] A. De Vos. Detailed balance limit of the efficiency of tandem solar cells. *Journal of Physics D: Applied Physics*, 13(5):839, 1980.

[77] T. J. Coutts, K. A. Emery, and J. Scott Ward. Modeled performance of polycrystalline thin-film tandem solar cells. *Progress in Photovoltaics: Research and Applications*, 10(3):195–203, 2002.

[78] E. Kabir, P. Kumar, S. Kumar, A. A. Adelodun, and K.-H. Kim. Solar energy: Potential and future prospects. *Renewable and Sustainable Energy Reviews*, 82:894 – 900, 2018.

[79] S. Enkhardt. China may raise 2020 solar target to more than 200 GW. *pv magazine*, 2018. URL `https://www.pv-magazine.com/2018/11/05/china-may-raise-2020-solar-target-to-over-200-gw/`.

[80] Solar energy industries association. U.S. solar market insight, 2018. URL `https://www.seia.org/us-solar-market-insight`.

[81] SolarPower Europe. Global market outlook, for solar power / 2018 - 2022, 2018. URL `http://www.solarpowereurope.org/wp-content/uploads/2018/09/Global-Market-Outlook-2018-2022.pdf`.

[82] Swiss federal office of energy. Solar energy. URL `http://www.bfe.admin.ch/themen/00490/00497/index.html?lang=en`.

[83] A. S. Bhalla, R. Guo, and R. Roy. The perovskite structure-a review of its role in ceramic science and technology. *Materials Research Innovations*, 4 (1):3–26, 2000.

[84] H. Tanaka and M. Misono. Advances in designing perovskite catalysts. *Current Opinion in Solid State and Materials Science*, 5(5):381 – 387, 2001.

[85] C. Li, K. Chi Kwan Soh, and Ping Wu. Formability of ABO_3 perovskites. *Journal of Alloys and Compounds*, 372(1):40 – 48, 2004.

[86] V. M. Goldschmidt. Die gesetze der krystallochemie. *Naturwissenschaften*, 14(21):477–485, May 1926. ISSN 1432-1904. doi: 10.1007/BF01507527. URL `https://doi.org/10.1007/BF01507527`.

[87] Z. Li, M. Yang, J.-S. Park, S.-H. Wei, J. J. Berry, and K. Zhu. Stabilizing perovskite structures by tuning tolerance factor: Formation of formamidinium and cesium lead iodide solid-state alloys. *Chemistry of Materials*, 28(1):284–292, 2016.

[88] W. Travis, E. N. K. Glover, H. Bronstein, D. O. Scanlon, and R. G. Palgrave. On the application of the tolerance factor to inorganic and hybrid halide perovskites: a revised system. *Chem. Sci.*, 7:4548–4556, 2016.

[89] G. Kieslich, S. Sun, and A. K. Cheetham. Solid-state principles applied to organic-inorganic perovskites: new tricks for an old dog. *Chem. Sci.*, 5:4712–4715, 2014.

[90] W. Li, Z. Wang, F. Deschler, S. Gao, R. H. Friend, and A. K. Cheetham. Chemically diverse and multifunctional hybrid organic–inorganic perovskites. *Nature Reviews Materials*, 2(3):16099, 2017.

[91] C. C. Stoumpos, C. D. Malliakas, and M. G. Kanatzidis. Semiconducting tin and lead iodide perovskites with organic cations: Phase transitions, high mobilities, and near-infrared photoluminescent properties. *Inorganic Chemistry*, 52(15):9019–9038, 2013.

[92] G. Kieslich, S. Sun, and A. K. Cheetham. An extended tolerance factor approach for organic-inorganic perovskites. *Chemical science*, 6(6):3430–3433, 2015.

[93] D. B. Meadowcroft. Low-cost oxygen electrode material. *Nature*, 226 (5248):847, 1970.

[94] Y. Matsumoto, H. Yoneyama, and H. Tamura. Catalytic activity for electrochemical reduction of oxygen of lanthanum nickel oxide and related oxides. *Journal of Electroanalytical Chemistry and Interfacial Electrochemistry*, 79(2):319–326, 1977.

[95] T. Hyodo, M. Hayashi, N. Miura, and N. Yamazoe. Catalytic activities of rare-earth manganites for cathodic reduction of oxygen in alkaline solution. *Journal of The Electrochemical Society*, 143(11):L266–L267, 1996.

[96] W. G. Hardin, J. T. Mefford, D. A. Slanac, B. B. Patel, X. Wang, S. Dai, X. Zhao, R. S. Ruoff, K. P. Johnston, and K. J. Stevenson. Tuning the electrocatalytic activity of perovskites through active site variation and support interactions. *Chemistry of Materials*, 26(11):3368–3376, 2014.

[97] I. C. Man, H.-Y. Su, F. Calle-Vallejo, H. A. Hansen, J. I. Martínez, N. G. Inoglu, J. Kitchin, T. F. Jaramillo, J. K. Nørskov, and J. Rossmeisl. Universality in oxygen evolution electrocatalysis on oxide surfaces. *ChemCatChem*, 3(7):1159–1165, 2011.

[98] R. A. Rincón, E. Ventosa, F. Tietz, J. Masa, S. Seisel, V. Kuznetsov, and W. Schuhmann. Evaluation of perovskites as electrocatalysts for the oxygen evolution reaction. *ChemPhysChem*, 15(13):2810–2816, 2014.

[99] J. Sunarso, A. A. Torriero, W. Zhou, P. C. Howlett, and M. Forsyth. Oxygen reduction reaction activity of la-based perovskite oxides in alkaline medium: a thin-film rotating ring-disk electrode study. *The Journal of Physical Chemistry C*, 116(9):5827–5834, 2012.

[100] S. Shoji, G. Yin, M. Nishikawa, D. Atarashi, E. Sakai, and M. Miyauchi. Photocatalytic reduction of CO_2 by Cu_xO nanocluster loaded $SrTiO_3$ nanorod thin film. *Chemical Physics Letters*, 658:309–314, 2016.

[101] H. Kato, K. Asakura, and A. Kudo. Highly efficient water splitting into H_2 and O_2 over lanthanum-doped $NaTaO_3$ photocatalysts with high crystallinity and surface nanostructure. *Journal of the American Chemical Society*, 125(10):3082–3089, 2003.

[102] S. Li, J. Zhang, M. G. Kibria, Z. Mi, M. Chaker, D. Ma, R. Nechache, and F. Rosei. Remarkably enhanced photocatalytic activity of laser ablated au nanoparticle decorated $BiFeO_3$ nanowires under visible-light. *Chemical Communications*, 49(52):5856–5858, 2013.

[103] K. M. Parida, K. H. Reddy, S. Martha, D. P. Das, and N. Biswal. Fabrication of nanocrystalline $LaFeO_3$: an efficient sol-gel auto-combustion assisted visible light responsive photocatalyst for water decomposition. *International journal of hydrogen energy*, 35(22):12161–12168, 2010.

[104] W. T. H. Koch, R. Munser, W. Ruppel, and P. Würfel. Bulk photovoltaic effect in $BaTiO_3$. *Solid State Communications*, 17(7):847–850, 1975.

[105] M. Qin, K. Yao, and Y. C. Liang. High efficient photovoltaics in nanoscaled ferroelectric thin films. *Applied Physics Letters*, 93(12):122904, 2008.

[106] J. F. Annett. *Superconductivity, superfluids and condensates.* Oxford University Press, 2004.

[107] Y. Maeno, H. Hashimoto, K. Yoshida, S. Nishizaki, T. Fujita, J. G. Bednorz, and F. Lichtenberg. Superconductivity in a layered perovskite without copper. *Nature*, 372(6506):532, 1994.

[108] R. J. Cava, B. Batlogg, J. J. Krajewski, R. Farrow, L. W. Rupp Jr, A. E. White, K. Short, W. F. Peck, and T. Kometani. Superconductivity near 30 K without copper: the $Ba_{0.6}K_{0.4}BiO_3$ perovskite. *Nature*, 332(6167): 814, 1988.

[109] D. W. Murphy, S. Sunshine, R. B. Van Dover, R. J. Cava, B. Batlogg, S. M. Zahurak, and L. F. Schneemeyer. New superconducting cuprate perovskites. *Physical review letters*, 58(18):1888, 1987.

[110] T. He, Q. Huang, A. P. Ramirez, Y. Wang, K. A. Regan, N. Rogado, M. A. Hayward, M. K. Haas, J. S. Slusky, K. Inumara, et al. Superconductivity in the non-oxide perovskite $MgCNi_3$. *Nature*, 411(6833):54, 2001.

[111] J. G. Bednorz and K. A. Müller. Perovskite-type oxides-the new approach to high-T c superconductivity. *Reviews of Modern Physics*, 60(3):585, 1988.

[112] J.-M. Tarascon, W. R. McKinnon, L. H. Greene, G. W. Hull, Vogel, and E. M. Oxygen and rare-earth doping of the 90-K superconducting perovskite $YBa_2Cu_3O_{7-x}$. *Physical Review B*, 36(1):226, 1987.

[113] W. Känzig. Ferroelectrics and antiferroeletrics. In *Solid State Physics*, volume 4, pages 1–197. Elsevier, 1957.

[114] G. Burns and B. A. Scott. Lattice modes in ferroelectric perovskites: $PbTiO_3$. *Physical Review B*, 7(7):3088, 1973.

[115] R. E. Cohen. Origin of ferroelectricity in perovskite oxides. *Nature*, 358 (6382):136, 1992.

[116] P. V. Lambeck and G. H. Jonker. The nature of domain stabilization in ferroelectric perovskites. *Journal of Physics and Chemistry of Solids*, 47 (5):453–461, 1986.

[117] G. A. Samara. Pressure and temperature dependence of the dielectric properties and phase transitions of the ferroelectric perovskites: $PbTiO_3$ and $BaTiO_3$. *Ferroelectrics*, 2(1):277–289, 1971.

[118] D. D. Fong, G. B. Stephenson, S. K. Streiffer, J. A. Eastman, O. Auciello, P. H. Fuoss, and C. Thompson. Ferroelectricity in ultrathin perovskite films. *Science*, 304(5677):1650–1653, 2004.

[119] J. Curie and P. Curie. Développement par compression de l'électricité polaire dans les cristaux hémièdres à faces inclinées. *Bulletin de minéralogie*, 3(4):90–93, 1880.

[120] L. Bellaiche and D. Vanderbilt. Virtual crystal approximation revisited: Application to dielectric and piezoelectric properties of perovskites. *Physical Review B*, 61(12):7877, 2000.

[121] D. E. Cox, B. Noheda, G. Shirane, Y. Uesu, K. Fujishiro, and Y. Yamada. Universal phase diagram for high-piezoelectric perovskite systems. *Applied Physics Letters*, 79(3):400–402, 2001.

[122] S. Zhang, R. Xia, T. R. Shrout, G. Zang, and J. Wang. Piezoelectric properties in perovskite $0.948(K_{0.5}Na_{0.5})NbO_3$–$0.052LiSbO_3$ lead-free ceramics. *Journal of Applied Physics*, 100(10):104108, 2006.

[123] E. Strelcov, Q. Dong, T. Li, J. Chae, Y. Shao, Y. Deng, A. Gruverman, J. Huang, and A. Centrone. $CH_3NH_3PbI_3$ perovskites: Ferroelasticity revealed. *Science advances*, 3(4):e1602165, 2017.

[124] T. Atou, H. Chiba, K. Ohoyama, Y. Yamaguchi, and Y. Syono. Structure determination of ferromagnetic perovskite $BiMnO_3$. *Journal of Solid State Chemistry*, 145(2):639–642, 1999.

[125] H. Chiba, T. Atou, and Y. Syono. Magnetic and electrical properties of $Bi_{1-x}Sr_xMnO_3$: hole-doping effect on ferromagnetic perovskite $BiMnO_3$. *Journal of Solid State Chemistry*, 132(1):139–143, 1997.

[126] C. Zener. Interaction between the d-shells in the transition metals. ii. ferromagnetic compounds of manganese with perovskite structure. *Physical Review*, 82(3):403, 1951.

[127] G. H. Jonker and J. H. Van Santen. Ferromagnetic compounds of manganese with perovskite structure. *physica*, 16(3):337–349, 1950.

[128] F. Moussa, M. Hennion, J. Rodriguez-Carvajal, H. Moudden, L. Pinsard, and A. Revcolevschi. Spin waves in the antiferromagnet perovskite $LaMnO_3$: A neutron-scattering study. *Physical Review B*, 54(21):15149, 1996.

[129] Y. Zong, K. Fujita, H. Akamatsu, S. Murai, and K. Tanaka. Antiferromagnetism of perovskite $EuZrO_3$. *Journal of Solid State Chemistry*, 183 (1):168–172, 2010.

[130] Y. Moritomo, T. Akimoto, A. Nakamura, K. Ohoyama, and M. Ohashi. Antiferromagnetic metallic state in the heavily doped region of perovskite manganites. *Physical Review B*, 58(9):5544, 1998.

[131] Z.-K. Tan, R. S. Moghaddam, M. L. Lai, P. Docampo, R. Higler, F. Deschler, M. Price, A. Sadhanala, L. M. Pazos, D. Credgington, et al. Bright light-emitting diodes based on organometal halide perovskite. *Nature nanotechnology*, 9(9):687–692, 2014.

[132] N. Yantara, S. Bhaumik, F. Yan, D. Sabba, H. A. Dewi, N. Mathews, P. P. Boix, H. V. Demir, and S. Mhaisalkar. Inorganic halide perovskites for efficient light-emitting diodes. *The journal of physical chemistry letters*, 6 (21):4360–4364, 2015.

[133] H. Cho, S.-H. Jeong, M.-H. Park, Y.-H. Kim, C. Wolf, C.-L. Lee, J. H. Heo, A. Sadhanala, N. Myoung, S. Yoo, et al. Overcoming the electroluminescence efficiency limitations of perovskite light-emitting diodes. *Science*, 350(6265):1222–1225, 2015.

[134] J. Song, J. Li, X. Li, L. Xu, Y. Dong, and H. Zeng. Quantum dot light-emitting diodes based on inorganic perovskite cesium lead halides ($CsPbX_3$). *Advanced Materials*, 27(44):7162–7167, 2015.

[135] Y.-H. Kim, H. Cho, J. H. Heo, T.-S. Kim, N. Myoung, C.-L. Lee, S. H. Im, and T.-W. Lee. Multicolored organic/inorganic hybrid perovskite light-emitting diodes. *Advanced materials*, 27(7):1248–1254, 2015.

[136] M. Yuan, L. N. Quan, R. Comin, G. Walters, R. Sabatini, O. Voznyy, S. Hoogland, Y. Zhao, E. M. Beauregard, P. Kanjanaboos, et al. Perovskite energy funnels for efficient light-emitting diodes. *Nature nanotechnology*, 11(10):872, 2016.

[137] S. A. Veldhuis, P. P. Boix, N. Yantara, M. Li, T. C. Sum, N. Mathews, and S. G. Mhaisalkar. Perovskite materials for light-emitting diodes and lasers. *Advanced Materials*, 28(32):6804–6834, 2016.

[138] H. Zhu, Y. Fu, F. Meng, X. Wu, Z. Gong, Q. Ding, M. V. Gustafsson, M. T. Trinh, S. Jin, and X. Y. Zhu. Lead halide perovskite nanowire lasers with low lasing thresholds and high quality factors. *Nature materials*, 14(6): 636, 2015.

[139] Y. Xu, Q. Chen, C. Zhang, R. Wang, H. Wu, X. Zhang, G. Xing, W. W. Yu, X. Wang, Y. Zhang, et al. Two-photon-pumped perovskite semiconductor nanocrystal lasers. *Journal of the American Chemical Society*, 138 (11):3761–3768, 2016.

[140] G. Xing, N. Mathews, S. S. Lim, N. Yantara, X. Liu, D. Sabba, M. Grätzel, S. Mhaisalkar, and T. C. Sum. Low-temperature solution-processed wavelength-tunable perovskites for lasing. *Nature materials*, 13(5):476, 2014.

[141] H. Kim, J. S. Han, J. Choi, S. Y. Kim, and H. W. Jang. Halide perovskites for applications beyond photovoltaics. *Small Methods*, 2(3):1700310, 2018.

[142] A. Kojima, K. Teshima, T. Miyasaka, and Y. Shirai. Novel photoelectrochemical cell with mesoscopic electrodes sensitized by lead-halide compounds (2) in proc. 210th ECS meeting, 2006.

[143] Oxford PV^{TM} perovskite solar cell achieves 28% efficiency. URL `https://www.oxfordpv.com/news/oxford-pv-perovskite-solar-cell-achieves-28-efficiency`.

[144] G. E. Eperon, S. D. Stranks, C. Menelaou, M. B. Johnston, L. M. Herz, and H. J. Snaith. Formamidinium lead trihalide: a broadly tunable perovskite for efficient planar heterojunction solar cells. *Energy & Environmental Science*, 7(3):982–988, 2014.

[145] S. Pang, H. Hu, J. Zhang, S. Lv, Y. Yu, F. Wei, T. Qin, H. Xu, Z. Liu, and G. Cui. $NH_2CH{=}NH_2PbI_3$: An alternative organolead iodide perovskite sensitizer for mesoscopic solar cells. *Chemistry of Materials*, 26(3):1485–1491, 2014.

[146] T. M. Koh, K. Fu, Y. Fang, S. Chen, T. C. Sum, N. Mathews, S. G. Mhaisalkar, P. P. Boix, and T. Baikie. Formamidinium-containing metal-halide: an alternative material for near-IR absorption perovskite solar cells. *The Journal of Physical Chemistry C*, 118(30):16458–16462, 2013.

[147] F. Hao, C. C. Stoumpos, R. P. H. Chang, and M. G. Kanatzidis. Anomalous band gap behavior in mixed Sn and Pb perovskites enables broadening of absorption spectrum in solar cells. *Journal of the American Chemical Society*, 136(22):8094–8099, 2014.

[148] C. K. Møller. Crystal structure and photoconductivity of caesium plumbohalides. *Nature*, 182:1436.

[149] G. E. Eperon, G. M. Paterno, R. J. Sutton, A. Zampetti, A. A. Haghighirad, F. Cacialli, and H. J. Snaith. Inorganic caesium lead iodide perovskite solar cells. *Journal of Materials Chemistry A*, 3(39):19688–19695, 2015.

[150] S. Meloni, G. Palermo, N. Ashari-Astani, M. Grätzel, and U. Rothlisberger. Valence and conduction band tuning in halide perovskites for solar cell applications. *J. Mater. Chem. A*, 4:15997–16002, 2016.

[151] J. A. Flores-Livas, D. Tomerini, M. Amsler, A. Boziki, U. Rothlisberger, and S. Goedecker. Emergence of hidden phases of methylammonium lead iodide $CH_3NH_3PbI_3$ upon compression. *Phys. Rev. Materials*, 2:085201, 2018.

[152] S. Collavini, S. F. Völker, and J. L. Delgado. Understanding the outstanding power conversion efficiency of perovskite-based solar cells. *Angewandte Chemie International Edition*, 54(34):9757–9759, 2015.

[153] Q. Lin, A. Armin, R. Chandra R. Nagiri, P. L. Burn, and P. Meredith. Electro-optics of perovskite solar cells. *Nature Photonics*, 9(2):106, 2015.

[154] A. Miyata, A. Mitioglu, P. Plochocka, O. Portugall, J. T.-W. Wang, S. D. Stranks, H. J. Snaith, and R. J. Nicholas. Direct measurement of the exciton binding energy and effective masses for charge carriers in organic-inorganic tri-halide perovskites. *Nature Physics*, 11(7):582–587, 2015.

[155] M.-F. Lo, Z.-Q. Guan, T.-W. Ng, C.-Y. Chan, and C.-S. Lee. Electronic structures and photoconversion mechanism in perovskite/fullerene heterojunctions. *Advanced Functional Materials*, 25(8):1213–1218, 2015.

[156] G. Xing, N. Mathews, S. Sun, S. S. Lim, Y. M. Lam, M. Grätzel, S. Mhaisalkar, and T. C. Sum. Long-range balanced electron-and hole-transport lengths in organic-inorganic $CH_3NH_3PbI_3$. *Science*, 342(6156): 344–347, 2013.

[157] S. D. Stranks, G. E. Eperon, G. Grancini, C. Menelaou, M. J. P. Alcocer, T. Leijtens, L. M. Herz, A. Petrozza, and H. J. Snaith. Electron-hole diffusion lengths exceeding 1 micrometer in an organometal trihalide perovskite absorber. *Science*, 342(6156):341–344, 2013.

[158] C. Wehrenfennig, G. E. Eperon, M. B. Johnston, H. J. Snaith, and L. M. Herz. High charge carrier mobilities and lifetimes in organolead trihalide perovskites. *Advanced materials*, 26(10):1584–1589, 2014.

[159] M. Zhang, H. Yu, M. Lyu, Q. Wang, J.-H. Yun, and L. Wang. Composition-dependent photoluminescence intensity and prolonged recombination lifetime of perovskite $CH_3NH_3PbBr_{3-x}Cl_x$ films. *Chemical Communications*, 50(79):11727–11730, 2014.

[160] R. E. Brandt, V. Stevanović, D. S. Ginley, and T. Buonassisi. Identifying defect-tolerant semiconductors with high minority-carrier lifetimes: beyond hybrid lead halide perovskites. *MRS Communications*, 5(2):265–275, 2015.

[161] J. M. Ball and A. Petrozza. Defects in perovskite-halides and their effects in solar cells. *Nature Energy*, 1(11):16149, 2016.

[162] M. L. Agiorgousis, Y.-Y. Sun, H. Zeng, and S. Zhang. Strong covalency-induced recombination centers in perovskite solar cell material $CH_3NH_3PbI_3$. *Journal of the American Chemical Society*, 136(41):14570–14575, 2014.

[163] F. Wang, S. Bai, W. Tress, A. Hagfeldt, and F. Gao. Defects engineering for high-performance perovskite solar cells. *npj Flexible Electronics*, 2(1): 22, 2018.

[164] T. M. Brenner, D. A. Egger, A. M. Rappe, L. Kronik, G. Hodes, and D. Cahen. Are mobilities in hybrid organic-inorganic halide perovskites actually 'high'? *The Journal of Physical Chemistry Letters*, 6(23):4754–4757, 2015.

[165] C. Motta, F. El-Mellouhi, and S. Sanvito. Charge carrier mobility in hybrid halide perovskites. *Scientific reports*, 5:12746, 2015.

[166] L. M. Herz. Charge-carrier mobilities in metal halide perovskites: fundamental mechanisms and limits. *ACS Energy Letters*, 2(7):1539–1548, 2017.

[167] C. Wehrenfennig, M. Liu, H. J. Snaith, M. B. Johnston, and L. M. Herz. Charge-carrier dynamics in vapour-deposited films of the organolead halide perovskite $CH_3NH_3PbI_{3-x}Cl_x$. *Energy & Environmental Science*, 7 (7):2269–2275, 2014.

[168] J. Lim, M. T. Horantner, N. Sakai, J. M. Ball, S. Mahesh, N. K. Noel, Y.-H. Lin, J. B. Patel, D. P. McMeekin, M. B. Johnston, B. Wenger, and H. J. Snaith. Elucidating the long-range charge carrier mobility in metal halide perovskite thin films. *Energy Environ. Sci.*, 12:169–176, 2019.

[169] K. G. Stamplecoskie, J. S. Manser, and P. V. Kamat. Dual nature of the excited state in organic-inorganic lead halide perovskites. *Energy Environ. Sci.*, 8:208–215, 2015.

[170] M. Park, A. J. Neukirch, S. E. Reyes-Lillo, M. Lai, S. R. Ellis, D. Dietze, J. B. Neaton, P. Yang, S. Tretiak, and R. A. Mathies. Excited-state vibrational dynamics toward the polaron in methylammonium lead iodide perovskite. *Nature communications*, 9(1):2525, 2018.

[171] S. Nah, B. Spokoyny, X. Jiang, C. Stoumpos, C. M. M. Soe, M. G. Kanatzidis, and E. Harel. Transient sub-bandgap states in halide perovskite thin films. *Nano letters*, 18(2):827–831, 2018.

[172] J. P. H. Rivett, L. Z. Tan, M. B. Price, S. A. Bourelle, N. J. L. K. Davis, J. Xiao, Y. Zou, R. Middleton, B. Sun, A. M. Rappe, et al. Long-lived polarization memory in the electronic states of lead-halide perovskites from local structural dynamics. *Nature communications*, 9(1):3531, 2018.

[173] T. Xu, L. Chen, Z. Guo, and T. Ma. Strategic improvement of the long-term stability of perovskite materials and perovskite solar cells. *Physical Chemistry Chemical Physics*, 18(39):27026–27050, 2016.

[174] A. H. Slavney, R. W. Smaha, I. C. Smith, A. Jaffe, D. Umeyama, and H. I. Karunadasa. Chemical approaches to addressing the instability and toxicity of lead-halide perovskite absorbers. *Inorganic chemistry*, 56(1): 46–55, 2016.

[175] A. M. A. Leguy, Y. Hu, M. Campoy-Quiles, M. I. Alonso, O. J. Weber, P. Azarhoosh, M. Van Schilfgaarde, M. T. Weller, T. Bein, J. Nelson, et al. Reversible hydration of $CH_3NH_3PbI_3$ in films, single crystals, and solar cells. *Chemistry of Materials*, 27(9):3397–3407, 2015.

[176] J. A. Christians, P. A. Miranda Herrera, and P. V. Kamat. Transformation of the excited state and photovoltaic efficiency of $CH_3NH_3PbI_3$ perovskite upon controlled exposure to humidified air. *Journal of the American Chemical Society*, 137(4):1530–1538, 2015.

[177] J. Yang, B. D. Siempelkamp, D. Liu, and T. L. Kelly. Investigation of $CH_3NH_3PbI_3$ degradation rates and mechanisms in controlled humidity environments using in situ techniques. *ACS nano*, 9(2):1955–1963, 2015.

[178] I. C. Smith, E. T. Hoke, D. Solis-Ibarra, M. D. McGehee, and H. I. Karunadasa. A layered hybrid perovskite solar-cell absorber with enhanced moisture stability. *Angewandte Chemie*, 126(42):11414–11417, 2014.

[179] Z.-Q. Ma, Y. Shao, P. K. Wong, X. Shi, and H. Pan. Structural and electronic properties of two-dimensional organic–inorganic halide perovskites and their stability against moisture. *The Journal of Physical Chemistry C*, 122(11):5844–5853, 2018.

[180] Y.-B. Lu, C. Guan, H. Sun, W.-Y. Cong, H. Yang, and P. Zhang. Investigations on enhanced moisture resistance of two-dimensional layered hybrid organic-inorganic perovskites $(C_4H_9NH_3)_2PbI_4$. *The Journal of Physical Chemistry C*, 2018.

[181] R. K. Misra, S. Aharon, B. Li, D. Mogilyansky, I. Visoly-Fisher, L. Etgar, and E. A. Katz. Temperature-and component-dependent degradation of perovskite photovoltaic materials under concentrated sunlight. *The journal of physical chemistry letters*, 6(3):326–330, 2015.

[182] D. J. Slotcavage, H. I. Karunadasa, and M. D. McGehee. Light-induced phase segregation in halide-perovskite absorbers. *ACS Energy Letters*, 1 (6):1199–1205, 2016.

[183] A. Dualeh, P. Gao, S. I. Seok, M. K. Nazeeruddin, and M. Grätzel. Thermal behavior of methylammonium lead-trihalide perovskite photovoltaic light harvesters. *Chemistry of Materials*, 26(21):6160–6164, 2014.

[184] N. Pellet, P. Gao, G. Gregori, T.-Y. Yang, M. K. Nazeeruddin, J. Maier, and M. Grätzel. Mixed-organic-cation perovskite photovoltaics for enhanced solar-light harvesting. *Angewandte Chemie*, 126(12):3215–3221, 2014.

[185] C. Yi, J. Luo, S. Meloni, A. Boziki, N. Ashari-Astani, C. Grätzel, S. M. Zakeeruddin, U. Röthlisberger, and M. Grätzel. Entropic stabilization of mixed A-cation ABX_3 metal halide perovskites for high performance perovskite solar cells. *Energy & Environmental Science*, 9(2):656–662, 2016.

[186] M. Saliba, T. Matsui, J.-Y. Seo, K. Domanski, J.-P. Correa-Baena, M. K. Nazeeruddin, S. M. Zakeeruddin, W. Tress, A. Abate, A. Hagfeldt, et al. Cesium-containing triple cation perovskite solar cells: improved stability, reproducibility and high efficiency. *Energy & environmental science*, 9(6): 1989–1997, 2016.

[187] M. Saliba, T. Matsui, K. Domanski, J.-Y. Seo, A. Ummadisingu, S. M. Zakeeruddin, J.-P. Correa-Baena, W. R. Tress, A. Abate, A. Hagfeldt, et al. Incorporation of rubidium cations into perovskite solar cells improves photovoltaic performance. *Science*, 354(6309):206–209, 2016.

[188] N. K. Noel, S. D. Stranks, A. Abate, C. Wehrenfennig, S. Guarnera, A.-A. Haghighirad, A. Sadhanala, G. E. Eperon, S. K. Pathak, M. B. Johnston, et al. Lead-free organic-inorganic tin halide perovskites for photovoltaic applications. *Energy & Environmental Science*, 7(9):3061–3068, 2014.

[189] F. Hao, C. C. Stoumpos, D. H. Cao, R. P. H. Chang, and M. G. Kanatzidis. Lead-free solid-state organic-inorganic halide perovskite solar cells. *Nature Photonics*, 8(6):489, 2014.

[190] M. H. Kumar, S. Dharani, W. L. Leong, P. P. Boix, R. R. Prabhakar, T. Baikie, C. Shi, H. Ding, R. Ramesh, M. Asta, et al. Lead-free halide perovskite solar cells with high photocurrents realized through vacancy modulation. *Advanced Materials*, 26(41):7122–7127, 2014.

[191] T. Krishnamoorthy, H. Ding, C. Yan, W. L. Leong, T. Baikie, Z. Zhang, M. Sherburne, S. Li, M. Asta, N. Mathews, et al. Lead-free germanium iodide perovskite materials for photovoltaic applications. *Journal of Materials Chemistry A*, 3(47):23829–23832, 2015.

[192] A. H. Slavney, T. Hu, A. M. Lindenberg, and H. I. Karunadasa. A bismuth-halide double perovskite with long carrier recombination lifetime for photovoltaic applications. *Journal of the American Chemical Society*, 138(7): 2138–2141, 2016.

[193] G. Volonakis, M. R. Filip, A. A. Haghighirad, N. Sakai, B. Wenger, H. J. Snaith, and F. Giustino. Lead-free halide double perovskites via heterovalent substitution of noble metals. *The journal of physical chemistry letters*, 7(7):1254–1259, 2016.

[194] E. T. McClure, M. R. Ball, W. Windl, and P. M. Woodward. Cs_2AgBiX_6 (X= Br, Cl): new visible light absorbing, lead-free halide perovskite semiconductors. *Chemistry of Materials*, 28(5):1348–1354, 2016.

[195] M. I. H. Ansari, A. Qurashi, and M. K. Nazeeruddin. Frontiers, opportunities, and challenges in perovskite solar cells: A critical review. *Journal of Photochemistry and Photobiology C: Photochemistry Reviews*, 35:1–24, 2018.

[196] M. Khalaji Assadi, S. Bakhoda, R. Saidur, and H. Hanaei. Recent progress in perovskite solar cells. *Renewable and Sustainable Energy Reviews*, 81: 2812 – 2822, 2018.

[197] M. J. Carnie, C. Charbonneau, M. L. Davies, J. Troughton, T. M. Watson, K. Wojciechowski, H. Snaith, and D. A. Worsley. A one-step low temperature processing route for organolead halide perovskite solar cells. *Chemical communications*, 49(72):7893–7895, 2013.

[198] M. Liu, M. B. Johnston, and H. J. Snaith. Efficient planar heterojunction perovskite solar cells by vapour deposition. *Nature*, 501(7467):395, 2013.

[199] J. Cui, H. Yuan, J. Li, X. Xu, Y. Shen, H. Lin, and M. Wang. Recent progress in efficient hybrid lead halide perovskite solar cells. *Science and Technology of Advanced Materials*, 16(3):036004, jun 2015.

[200] Q. Chen, H. Zhou, Z. Hong, S. Luo, H.-S. Duan, H.-H. Wang, Y. Liu, G. Li, and Y. Yang. Planar heterojunction perovskite solar cells via vapor-assisted solution process. *Journal of the American Chemical Society*, 136 (2):622–625.

[201] D. Prochowicz, M. Franckevičius, A. M. Cieślak, S. M. Zakeeruddin, M. Grätzel, and J. Lewiński. Mechanosynthesis of the hybrid perovskite $CH_3NH_3PbI_3$: characterization and the corresponding solar cell efficiency. *Journal of Materials Chemistry A*, 3(41):20772–20777, 2015.

[202] Z.-Y. Zhu, Q.-Q. Yang, L.-F. Gao, L. Zhang, A.-Y. Shi, C.-L. Sun, Q. Wang, and H.-L. Zhang. Solvent-free mechanosynthesis of composition-tunable cesium lead halide perovskite quantum dots. *The Journal of Physical Chemistry Letters*, 8(7):1610–1614, 2017.

[203] J.-L. Do and T. Friščić. Mechanochemistry: a force of synthesis. *ACS central science*, 3(1):13–19, 2016.

[204] I. Hussain, H. P. Tran, J. Jaksik, J. Moore, N. Islam, and M. J. Uddin. Functional materials, device architecture, and flexibility of perovskite solar cell. *Emergent Materials*, 1(3-4):133–154, 2018.

[205] J.-Y. Jeng, Y.-F. Chiang, M.-H. Lee, S.-R. Peng, T.-F. Guo, P. Chen, and T.-C. Wen. $CH_3NH_3PbI_3$ perovskite/fullerene planar-heterojunction hybrid solar cells. *Advanced Materials*, 25(27):3727–3732, 2013.

[206] W. Ke, G. Fang, J. Wan, H. Tao, Q. Liu, L. Xiong, P. Qin, J. Wang, H. Lei, G. Yang, et al. Efficient hole-blocking layer-free planar halide perovskite thin-film solar cells. *Nature communications*, 6:6700, 2015.

[207] D. Zhou, T. Zhou, Y. Tian, X. Zhu, and Y. Tu. Perovskite-based solar cells: materials, methods, and future perspectives. *Journal of Nanomaterials*, 2018, 2018.

[208] First building-integrated deployment shows perovskite solar's growing maturity, 2019.

[209] S. W. Eaton, M. Lai, N. A. Gibson, A. B. Wong, L. Dou, J. Ma, L.-W. Wang, S. R. Leone, and P. Yang. Lasing in robust cesium lead halide perovskite nanowires. *Proceedings of the National Academy of Sciences*, 113(8):1993–1998, 2016.

[210] C. Gu and J.-S. Lee. Flexible hybrid organic-inorganic perovskite memory. *ACS nano*, 10(5):5413–5418, 2016.

[211] B. Hwang, C. Gu, D. Lee, and J.-S. Lee. Effect of halide-mixing on the switching behaviors of organic-inorganic hybrid perovskite memory. *Scientific Reports*, 7:43794, 2017.

[212] C. Muthu, S. Agarwal, A. Vijayan, P. Hazra, K. B. Jinesh, and V. C. Nair. Hybrid perovskite nanoparticles for high-performance resistive random access memory devices: Control of operational parameters through chloride doping. *Advanced Materials Interfaces*, 3(18):1600092, 2016.

[213] S. Yakunin, M. Sytnyk, D. Kriegner, S. Shrestha, M. Richter, G. J. Matt, H. Azimi, C. J. Brabec, J. Stangl, M. V. Kovalenko, et al. Detection of X-ray photons by solution-processed lead halide perovskites. *Nature photonics*, 9(7):444, 2015.

[214] H. Wei, Y. Fang, P. Mulligan, W. Chuirazzi, H.-H. Fang, C. Wang, B. R. Ecker, Y. Gao, M. A. Loi, L. Cao, et al. Sensitive X-ray detectors made of methylammonium lead tribromide perovskite single crystals. *Nature Photonics*, 10(5):333, 2016.

[215] X. Liu, T. Xu, Y. Li, Z. Zang, X. Peng, H. Wei, W. Zha, and F. Wang. Enhanced X-ray photon response in solution-synthesized $CsPbBr_3$ nanoparticles wrapped by reduced graphene oxide. *Solar Energy Materials and Solar Cells*, 187:249–254, 2018.

[216] N. Vicente and G. Garcia-Belmonte. Methylammonium lead bromide perovskite battery anodes reversibly host high Li-ion concentrations.

[217] Y.-J. Kim, T.-V. Dang, H.-J. Choi, B.-J. Park, J.-H. Eom, H.-A. Song, D. Seol, Y. Kim, S.-H. Shin, J. Nah, et al. Piezoelectric properties of $CH_3NH_3PbI_3$ perovskite thin films and their applications in piezoelectric generators. *Journal of Materials Chemistry A*, 4(3):756–763, 2016.

[218] R. Ding, H. Liu, X. Zhang, J. Xiao, R. Kishor, H. Sun, B. Zhu, G. Chen, F. Gao, X. Feng, et al. Flexible piezoelectric nanocomposite generators based on formamidinium lead halide perovskite nanoparticles. *Advanced Functional Materials*, 26(42):7708–7716, 2016.

[219] M. P. Allen and D. J. Tildesley. *Computer simulation of liquids*. Oxford university press, 2017.

[220] R. P. Feynman. Simulating physics with computers. *International journal of theoretical physics*, 21(6-7):467–488, 1982.

[221] F. Jensen. *Introduction to computational chemistry*. John wiley & sons, 2017.

[222] R. W. Hockney and J. W. Eastwood. *Computer simulation using particles*. crc Press, 1988.

[223] W. F. van Gunsteren, P. K. Weiner, and A. J. Wilkinson. *Computer simulation of biomolecular systems: theoretical and experimental applications*, volume 3. Springer Science & Business Media, 2013.

[224] W. A. Curtin and R. E. Miller. Atomistic/continuum coupling in computational materials science. *Modelling and simulation in materials science and engineering*, 11(3):R33, 2003.

[225] K. Binder. *Monte Carlo and molecular dynamics simulations in polymer science*. Oxford University Press, 1995.

[226] T. J. R. Hughes. *The finite element method: linear static and dynamic finite element analysis*. Courier Corporation, 2012.

[227] C. A. Taylor, M. T. Draney, J. P. Ku, D. Parker, B. N. Steele, K. Wang, and C. K. Zarins. Predictive medicine: Computational techniques in therapeutic decision-making. *Computer Aided Surgery: Official Journal of the International Society for Computer Aided Surgery (ISCAS)*, 4(5):231–247, 1999.

[228] W. L. Luyben. *Process modeling, simulation and control for chemical engineers*. McGraw-Hill Higher Education, 1989.

[229] J. Ingham, I. J. Dunn, E. Heinzle, J. E. Prenosil, and J. B. Snape. *Chemical engineering dynamics: an introduction to modelling and computer simulation*, volume 3. John Wiley & Sons, 2008.

[230] M. Fontana. Computer simulations, mathematics and economics. *International Review of Economics*, 53(1):96–123, 2006.

[231] N. Kaplan, I. K. Moore, Y. Fondufe-Mittendorf, A. J. Gossett, D. Tillo, Y. Field, E. M. LeProust, T. R. Hughes, J. D. Lieb, J. Widom, et al. The DNA-encoded nucleosome organization of a eukaryotic genome. *Nature*, 458(7236):362, 2009.

[232] W. L. Jorgensen. The many roles of computation in drug discovery. *Science*, 303(5665):1813–1818, 2004.

[233] G. Pizzi, A. Cepellotti, R. Sabatini, N. Marzari, and B. Kozinsky. AiiDA: automated interactive infrastructure and database for computational science. *Computational Materials Science*, 111:218–230, 2016.

[234] G. Hautier, A. Jain, H. Chen, C. Moore, S. P. Ong, and G. Ceder. Novel mixed polyanions lithium-ion battery cathode materials predicted by high-throughput ab initio computations. *Journal of Materials Chemistry*, 21 (43):17147–17153, 2011.

[235] G. Hautier, C. Fischer, V. Ehrlacher, A. Jain, and G. Ceder. Data mined ionic substitutions for the discovery of new compounds. *Inorganic chemistry*, 50(2):656–663, 2010.

[236] H. Chen, G. Hautier, A. Jain, C. Moore, B. Kang, R. Doe, L. Wu, Y. Zhu, Y. Tang, and G. Ceder. Carbonophosphates: a new family of cathode materials for Li-ion batteries identified computationally. *Chemistry of Materials*, 24(11):2009–2016, 2012.

[237] M. J. Klein. Max Planck and the beginnings of the quantum theory. *Archive for History of Exact Sciences*, 1(5):459–479, 1961.

[238] P. W. Atkins. *Physical chemistry 6th edn.* Oxford University Press, 180pp, 1998.

[239] C. J. Calbick. The discovery of electron diffraction by davisson and germer. *The Physics Teacher*, 1(2):63–91, 1963.

[240] S. Diner, D. Fargue, G. Lochak, and F. Selleri. *The Wave-particle dualism: a tribute to Louis de Broglie on his 90th birthday*, volume 3. Springer Science & Business Media, 2012.

[241] L. D. Landau and E. M. Lifshitz. *Quantum mechanics: non-relativistic theory*, volume 3. Elsevier, 2013.

[242] F. Gross. *Relativistic quantum mechanics and field theory.* John Wiley & Sons, 2008.

[243] M. Born. Statistical interpretation of quantum mechanics. *Science*, 122 (3172):675–679, 1955.

[244] P. W. Atkins and R. S. Friedman. *Molecular quantum mechanics.* Oxford university press, 2011.

[245] L. N. Hand and J. D. Finch. *Analytical mechanics.* Cambridge University Press, 1998.

[246] E. Schrödinger. Quantisierung als eigenwertproblem. *Annalen der physik*, 385(13):437–490, 1926.

[247] D. Marx and J. Hutter. *Ab initio molecular dynamics: basic theory and advanced methods.* Cambridge University Press, 2009.

[248] M. Born and R. Oppenheimer. Zur quantentheorie der molekeln. *Annalen der physik*, 389(20):457–484, 1927.

[249] J. C. Tully. Perspective on “zur quantentheorie der molekeln”. *Theoretical Chemistry Accounts*, 103(3-4):173–176, 2000.

[250] Ursula R. Introduction to electronic structure methods, 2014. URL `https://lcbc.epfl.ch/wp-content/uploads/2018/10/lecture_2014.pdf`.

[251] B. Curchod. A classical and quantum trajectory description of nonadiabatic dynamics within time-dependent density functional theory. Technical report, EPFL, 2013.

[252] J. C. Slater. The theory of complex spectra. *Physical Review*, 34(10):1293, 1929.

[253] A Szabo and N. S. Ostlund. Modern quantum chemistry: Introduction to advanced electronic structure theory (Macmillan, New York, 1982). *Science*, 231:555, 1986.

[254] P. Hohenberg and W. Kohn. Inhomogeneous electron gas. *Phys. Rev.*, 136:B864–B871, 1964.

[255] W. Kohn and L. J. Sham. Self-consistent equations including exchange and correlation effects. *Phys. Rev.*, 140:A1133–A1138, 1965.

[256] J. C. Slater. Atomic shielding constants. *Physical Review*, 36(1):57, 1930.

[257] H. Taketa, S. Huzinaga, and K. O-ohata. Gaussian-expansion methods for molecular integrals. *Journal of the physical society of Japan*, 21(11): 2313–2324, 1966.

[258] L. Kantorovich. *Quantum theory of the solid state: an introduction*, volume 136. Springer Science & Business Media, 2004.

[259] M. C. Payne, M. P. Teter, D. C. Allan, T. A. Arias, and J. D. Joannopoulos. Iterative minimization techniques for ab initio total-energy calculations: molecular dynamics and conjugate gradients. *Rev. Mod. Phys.*, 64: 1045–1097, 1992.

[260] D. R. Hamann, M. Schlüter, and C. Chiang. Norm-conserving pseudopotentials. *Physical Review Letters*, 43(20):1494, 1979.

[261] G. B. Bachelet, D. R. Hamann, and M. Schlüter. Pseudopotentials that work: From H to Pu. *Physical Review B*, 26(8):4199, 1982.

[262] CASTEP. Theory in castep. URL `https://www.tcm.phy.cam.ac.uk/castep/documentation/WebHelp/content/modules/castep/thcasteppseudo.htm`.

[263] D. Vanderbilt. Soft self-consistent pseudopotentials in a generalized eigenvalue formalism. *Physical review B*, 41(11):7892, 1990.

[264] V. Fock. Näherungsmethode zur lösung des quantenmechanischen mehrkörperproblems. *Zeitschrift für Physik*, 61(1-2):126–148, 1930.

[265] D. R. Hartree and W. Hartree. Self-consistent field, with exchange, for beryllium. *Proceedings of the Royal Society of London. Series A-Mathematical and Physical Sciences*, 150(869):9–33, 1935.

[266] C. D. Sherrill. An introduction to Hartree-Fock molecular orbital theory. *School of Chemistry and Biochemistry Georgia Institute of Technology*, 2000.

[267] M. Levy. Universal variational functionals of electron densities, first-order density matrices, and natural spin-orbitals and solution of the v-representability problem. *Proceedings of the National Academy of Sciences*, 76(12):6062–6065, 1979.

[268] E. H. Lieb. Density functionals for coulomb systems. *International Journal of Quantum Chemistry*, 24(3):243–277, 1983.

[269] J. P. Perdew, K. Burke, and M. Ernzerhof. Generalized gradient approximation made simple. *Physical review letters*, 77(18):3865, 1996.

[270] J. Tao, J. P. Perdew, V. N. Staroverov, and G. E. Scuseria. Climbing the density functional ladder: Nonempirical meta-generalized gradient approximation designed for molecules and solids. *Physical Review Letters*, 91(14):146401, 2003.

[271] C. Adamo and V. Barone. Toward reliable density functional methods without adjustable parameters: The PBE0 model. *The Journal of chemical physics*, 110(13):6158–6170, 1999.

[272] S. Grimme. Semiempirical hybrid density functional with perturbative second-order correlation. *The Journal of chemical physics*, 124(3):034108, 2006.

[273] L. Brillouin. Les électrons libres dans les métaux et le rôle des reflexions de Bragg. *J. phys. radium*, 1(11):377–400, 1930.

[274] E. Wigner and F. Seitz. On the constitution of metallic sodium. *Physical Review*, 43(10):804, 1933.

[275] D. W. Ball. The basics of spectroscopy. SPIE-The International Society for Optical Engineering, 2001.

[276] J. Franck and E. G. Dymond. Elementary processes of photochemical reactions. *Transactions of the Faraday Society*, 21(February):536–542, 1926.

[277] E. Condon. A theory of intensity distribution in band systems. *Physical Review*, 28(6):1182, 1926.

[278] E. Runge and E. K. U. Gross. Density-functional theory for time-dependent systems. *Physical Review Letters*, 52(12):997, 1984.

[279] F. D. Murnaghan et al. J. frenkel, wave mechanics; advanced general theory. *Bulletin of the American Mathematical Society*, 41(11):776–776, 1935.

[280] R. van Leeuwen. Causality and symmetry in time-dependent density-functional theory. *Physical review letters*, 80(6):1280, 1998.

[281] R. van Leeuwen. Mapping from densities to potentials in time-dependent density-functional theory. *Physical review letters*, 82(19):3863, 1999.

[282] M. A. L. Marques, C. A. Ullrich, F. Nogueira, A. Rubio, K. Burke, and E. K. U. Gross. *Time-dependent density functional theory*, volume 706. Springer Science & Business Media, 2006.

[283] M. E. Casida. *Time-Dependent Density Functional Response Theory for Molecules.*

[284] I. Tamm. Relativistic interaction of elementary particles. *J. Phys.(USSR)*, 9:449, 1945.

[285] M. Barbatti, A. J. A. Aquino, and H. Lischka. The UV absorption of nucleobases: semi-classical ab initio spectra simulations. *Phys. Chem. Chem. Phys.*, 12:4959–4967, 2010.

[286] D. Frenkel and B. Smit. *Understanding molecular simulation: from algorithms to applications*, volume 1. Elsevier, 2001.

[287] D. Chandler. Introduction to modern statistical mechanics. *Introduction to Modern Statistical Mechanics, by David Chandler, pp. 288. Foreword by David Chandler. Oxford University Press, Sep 1987. ISBN-10: 0195042778. ISBN-13: 9780195042771*, page 288, 1987.

[288] N. Shuichi. Constant temperature molecular dynamics methods. *Progress of Theoretical Physics Supplement*, 103:1–46, 1991.

[289] T. D. Kühne. Second generation Car-Parrinello molecular dynamics. *Wiley Interdisciplinary Reviews: Computational Molecular Science*, 4(4):391–406, 2014.

[290] R. Car and M. Parrinello. Unified approach for molecular dynamics and density-functional theory. *Phys. Rev. Lett.*, 55:2471–2474, 1985.

[291] I. Frank, J. Hutter, D. Marx, and M. Parrinello. Molecular dynamics in low-spin excited states. *The Journal of Chemical Physics*, 108:4060–4069, 1998.

[292] B. Lee, J. He, R. P. H. Chang, and M. G. Kanatzidis. All-solid-state dye-sensitized solar cells with high efficiency. *Nature*, 485(7399):486, 2012.

[293] H. Zhou, Q. Chen, G. Li, S. Luo, T. Song, H.-S. Duan, Z. Hong, J. You, Y. Liu, and Y. Yang. Interface engineering of highly efficient perovskite solar cells. *Science*, 345(6196):542–546, 2014.

[294] Q. Dong, Y. Fang, Y. Shao, P. Mulligan, J. Qiu, L. Cao, and J. Huang. Electron-hole diffusion lengths > 175 μm in solution-grown $CH_3NH_3PbI_3$ single crystals. *Science*, 347(6225):967–970.

[295] D. Shi, V. Adinolfi, R. Comin, M. Yuan, E. Alarousu, A. Buin, Y. Chen, S. Hoogland, A. Rothenberger, K. Katsiev, Y. Losovyj, X. Zhang, P. A. Dowben, O. F. Mohammed, E. H. Sargent, and O. M. Bakr. Low trap-state density and long carrier diffusion in organolead trihalide perovskite single crystals. *Science*, 347(6221):519–522, 2015.

[296] W. S. Yang, J. H. Noh, N. J. Jeon, Y. C. Kim, S. Ryu, J. Seo, and S. I. Seok. High-performance photovoltaic perovskite layers fabricated through intramolecular exchange. *Science*, 348(6240):1234–1237, 2015.

[297] N. J. Jeon, J. H. Noh, W. S. Yang, Y. C. Kim, S. Ryu, J. Seo, and S. I. Seok. Compositional engineering of perovskite materials for high-performance solar cells. *Nature*, 517(7535):476, 2015.

[298] N. J. Jeon, J. H. Noh, Y. C. Kim, W. S. Yang, S. Ryu, and S. I. Seok. Solvent engineering for high-performance inorganic-organic hybrid perovskite solar cells. *Nature materials*, 13(9):897, 2014.

[299] Z. Xiao, Q. Dong, C. Bi, Y. Shao, Y. Yuan, and J. Huang. Solvent annealing of perovskite-induced crystal growth for photovoltaic-device efficiency enhancement. *Advanced Materials*, 26(37):6503–6509, 2014.

[300] T. Zhang, M. Yang, Y. Zhao, and K. Zhu. Controllable sequential deposition of planar $CH_3NH_3PbI_3$ perovskite films via adjustable volume expansion. *Nano Letters*, 15(6):3959–3963, 2015.

[301] J.-W. Lee, D.-J. Seol, A.-N. Cho, and N.-G. Park. High-efficiency perovskite solar cells based on the black polymorph of $HC(NH_2)_2PbI_3$. *Advanced Materials*, 26(29):4991–4998, 2014.

[302] H. Ito, H. Onuki, and R. Onaka. Optical and photoelectronic studies of $CsPbCl_3$ and $CsPbBr_3$. *Journal of the Physical Society of Japan*, 45(6): 2043–2044, 1978.

[303] C. C. Stoumpos, C. D. Malliakas, J. A. Peters, Z. Liu, M. Sebastian, J. Im, T. C. Chasapis, A. C. Wibowo, D. Y. Chung, A. J. Freeman, B. W. Wessels, and M. G. Kanatzidis. Crystal growth of the perovskite semiconductor $CsPbBr_3$: A new material for high-energy radiation detection. *Crystal Growth & Design*, 13(7):2722–2727, 2013.

[304] L. Protesescu, S. Yakunin, M. I. Bodnarchuk, F. Krieg, R. Caputo, C. H. Hendon, R. X. Yang, A. Walsh, and M. V. Kovalenko. Nanocrystals of cesium lead halide perovskites ($CsPbX_3$, X = Cl, Br, and I): Novel optoelectronic materials showing bright emission with wide color gamut. *Nano Letters*, 15(6):3692–3696, 2015.

[305] D. Zhang, S. W. Eaton, Y. Yu, L. Dou, and P. Yang. Solution-phase synthesis of cesium lead halide perovskite nanowires. *Journal of the American Chemical Society*, 137(29):9230–9233, 2015.

[306] Q. A. Akkerman, V. D'Innocenzo, S. Accornero, A. Scarpellini, A. Petrozza, M. Prato, and L. Manna. Tuning the optical properties of cesium lead halide perovskite nanocrystals by anion exchange reactions. *Journal of the American Chemical Society*, 137(32):10276–10281, 2015.

[307] M. Kulbak, D. Cahen, and G. Hodes. How important is the organic part of lead halide perovskite photovoltaic cells? efficient $CsPbBr_3$ cells. *The Journal of Physical Chemistry Letters*, 6(13):2452–2456, 2015.

[308] D. M. Trots and S. V. Myagkota. High-temperature structural evolution of caesium and rubidium triiodoplumbates. *Journal of Physics and Chemistry of Solids*, 69(10):2520 – 2526, 2008.

[309] H. Choi, J. Jeong, H.-B. Kim, S. Kim, B. Walker, G.-H. Kim, and J. Y. Kim. Cesium-doped methylammonium lead iodide perovskite light absorber for hybrid solar cells. *Nano Energy*, 7:80 – 85, 2014.

[310] J.-W. Lee, D.-H. Kim, H.-S. Kim, S.-W. Seo, S. M. Cho, and N.-G. Park. Formamidinium and cesium hybridization for photo- and moisture-stable perovskite solar cell. *Advanced Energy Materials*, 5(20):1501310, 2015.

[311] R. Lindblad, D. Bi, B. Park, J. Oscarsson, M. Gorgoi, H. Siegbahn, M. Odelius, E. M. J. Johansson, and H. Rensmo. Electronic structure of $TiO_2/CH_3NH_3PbI_3$ perovskite solar cell interfaces. *The Journal of Physical Chemistry Letters*, 5(4):648–653, 2014.

[312] G. E. Eperon, S. D. Stranks, C. Menelaou, M. B. Johnston, L. M. Herz, and H. J. Snaith. Formamidinium lead trihalide: a broadly tunable perovskite for efficient planar heterojunction solar cells. *Energy Environ. Sci.*, 7:982–988, 2014.

[313] H.-S. Kim, C.-R. Lee, J.-H. Im, K.-B. Lee, T. Moehl, A. Marchioro, S.-J. Moon, R. Humphry-Baker, J.-H. Yum, J. E. Moser, et al. Lead iodide perovskite sensitized all-solid-state submicron thin film mesoscopic solar cell with efficiency exceeding 9%. *Scientific reports*, 2:591, 2012.

[314] W. Shockley and H. J. Queisser. Detailed balance limit of efficiency of p-n junction solar cells. *Journal of Applied Physics*, 32(3):510–519, 1961.

[315] Z. Huang, D. Wang, S. Wang, and T. Zhang. Highly efficient and stable $MAPbI_3$ perovskite solar cell induced by regulated nucleation and Ostwald recrystallization. *Materials*, 11(5):778, 2018.

[316] T. M. Koh, K. Fu, Y. Fang, S. Chen, T. C. Sum, N. Mathews, S. G. Mhaisalkar, P. P. Boix, and T. Baikie. Formamidinium-containing metal-halide: An alternative material for near-IR absorption perovskite solar cells. *The Journal of Physical Chemistry C*, 118(30):16458–16462, 2014.

[317] C. D. Bailie, M. G. Christoforo, J. P. Mailoa, A. R. Bowring, E. L. Unger, W. H. Nguyen, J. Burschka, N. Pellet, J. Z. Lee, M. Grätzel, R. Noufi, T. Buonassisi, A. Salleo, and M. D. McGehee. Semi-transparent perovskite solar cells for tandems with silicon and CIGS. *Energy Environ. Sci.*, 8: 956–963, 2015.

[318] T. Todorov, T. Gershon, O. Gunawan, C. Sturdevant, and S. Guha. Perovskite-kesterite monolithic tandem solar cells with high open-circuit voltage. *Applied Physics Letters*, 105(17):173902, 2014.

[319] C. D. Bailie and M. D. McGehee. High-efficiency tandem perovskite solar cells. *MRS Bulletin*, 40(8):681–686, 2015.

[320] T. Leijtens, K. A. Bush, R. Prasanna, and M. D. McGehee. Opportunities and challenges for tandem solar cells using metal halide perovskite semiconductors. *Nature Energy*, pages 2058–7546, 2018.

[321] C. C. Stoumpos and M. G. Kanatzidis. The renaissance of halide perovskites and their evolution as emerging semiconductors. *Accounts of Chemical Research*, 48(10):2791–2802, 2015.

[322] M. Lai, Q. Kong, C. G. Bischak, Y. Yu, L. Dou, S. W. Eaton, N. S. Ginsberg, and P. Yang. Structural, optical, and electrical properties of phase-controlled cesium lead iodide nanowires. *Nano Research*, 10(4):1107–1114, Apr 2017.

[323] G. E. Eperon, G. M. Paternò, R. J. Sutton, A. Zampetti, A. A. Haghighirad, F. Cacialli, and H. J. Snaith. Inorganic caesium lead iodide perovskite solar cells. *J. Mater. Chem. A*, 3:19688–19695, 2015.

[324] Weijun Ke, I. Spanopoulos, C. C. Stoumpos, and M. G. Kanatzidis. Myths and reality of $\mathrm{HPbI_3}$ in halide perovskite solar cells. *Nature communications*, 9(1):4785, 2018.

[325] R. J. Sutton, M. R. Filip, A. A. Haghighirad, N. Sakai, B. Wenger, F. Giustino, and H. J. Snaith. Cubic or orthorhombic? Revealing the crystal structure of metastable black-phase $\mathrm{CsPbI_3}$ by theory and experiment. *ACS Energy Letters*, 2018.

[326] D. B. Mitzi. Templating and structural engineering in organic–inorganic perovskites. *J. Chem. Soc., Dalton Trans.*, pages 1–12, 2001.

[327] J. P. Perdew, K. Burke, and Y. Wang. Generalized gradient approximation for the exchange-correlation hole of a many-electron system. *Phys. Rev. B*, 54:16533–16539, 1996.

[328] J. Wiktor, U. Rothlisberger, and A. Pasquarello. Predictive determination of band gaps of inorganic halide perovskites. *The Journal of Physical Chemistry Letters*, 8(22):5507–5512, 2017.

[329] M. I. Dar, G. Jacopin, S. Meloni, A. Mattoni, N. Arora, A. Boziki, S. M. Zakeeruddin, U. Rothlisberger, and M. Grätzel. Origin of unusual bandgap shift and dual emission in organic-inorganic lead halide perovskites. *Science Advances*, 2(10), 2016.

[330] O. A. Vydrov and T. Van Voorhis. Nonlocal van der Waals density functional: The simpler the better. *The Journal of Chemical Physics*, 133(24): 244103, 2010.

[331] R. Sabatini, T. Gorni, and S. de Gironcoli. Nonlocal van der Waals density functional made simple and efficient. *Phys. Rev. B*, 87:041108, 2013.

[332] F. Brivio, J. M. Frost, J. M. Skelton, A. J. Jackson, O. J. Weber, M. T. Weller, A. R. Goñi, A. M. A. Leguy, P. R. F. Barnes, and A. Walsh. Lattice dynamics and vibrational spectra of the orthorhombic, tetragonal, and cubic phases of methylammonium lead iodide. *Phys. Rev. B*, 92: 144308, 2015.

[333] D. Prochowicz, P. Yadav, M. Saliba, M. Saski, S. M. Zakeeruddin, J. Lewiński, and M. Grätzel. Mechanosynthesis of pure phase mixed-cation $MA_xFA_{1-x}PbI_3$ hybrid perovskites: photovoltaic performance and electrochemical properties. *Sustainable Energy & Fuels*, 1(4):689–693, 2017.

[334] B. A. Rosales, L. Wei, and J. Vela. Synthesis and mixing of complex halide perovskites by solvent-free solid-state methods. *Journal of Solid State Chemistry*, 271:206–215, 2019.

[335] D. J. Kubicki, D. Prochowicz, A. Hofstetter, P. Pechy, S. M. Zakeeruddin, M. Grätzel, and L. Emsley. Cation dynamics in mixed-cation $(MA)_x(FA)_{1-x}PbI_3$ hybrid perovskites from solid-state NMR. *Journal of the American Chemical Society*, 139(29):10055–10061, 2017.

[336] D. J. Kubicki, D. Prochowicz, A. Hofstetter, M. Saski, P. Yadav, D. Bi, N. Pellet, J. Lewinski, S. M. Zakeeruddin, M. Grätzel, et al. Formation of stable mixed guanidinium-methylammonium phases with exceptionally long carrier lifetimes for high-efficiency lead iodide-based perovskite photovoltaics. *Journal of the American Chemical Society*, 140(9):3345–3351, 2018.

[337] D. J. Kubicki, D. Prochowicz, A. Hofstetter, S. M. Zakeeruddin, M. Grätzel, and L. Emsley. Phase segregation in potassium-doped lead halide perovskites from 39K solid-state NMR at 21.1 T. *Journal of the American Chemical Society*, 2018.

[338] D. Bi, X. Li, J. V. Milić, D. J. Kubicki, N. Pellet, J. Luo, T. LaGrange, P. Mettraux, L. Emsley, S. M. Zakeeruddin, et al. Multifunctional molecular modulators for perovskite solar cells with over 20% efficiency and high operational stability. *Nature communications*, 9(1):4482, 2018.

[339] M. M. Tavakoli, W. Tress, J. V. Milić, D. Kubicki, L. Emsley, and M. Grätzel. Addition of adamantylammonium iodide to hole transport layers enables highly efficient and electroluminescent perovskite solar cells. *Energy & Environmental Science*, 11(11):3310–3320, 2018.

[340] D. J. Kubicki, D. Prochowicz, A. Pinon, G. Stevanato, A. Hofstetter, S. M. Zakeeruddin, M. Grätzel, and L. Emsley. Doping and phase segregation in Mn^{2+}-and Co^{2+}-doped lead halide perovskites from 133 Cs and 1 H NMR relaxation enhancement. *Journal of Materials Chemistry A*, 2019.

[341] B. A. Rosales, L. Men, S. D. Cady, M. P. Hanrahan, A. J. Rossini, and J. Vela. Persistent dopants and phase segregation in organolead mixed-halide perovskites. *Chemistry of Materials*, 28(19):6848–6859, 2016.

[342] B. A. Rosales, M. P. Hanrahan, B. W. Boote, A. J. Rossini, E. A. Smith, and J. Vela. Lead halide perovskites: Challenges and opportunities in advanced synthesis and spectroscopy. *ACS Energy Letters*, 2(4):906–914, 2017.

[343] A. Karmakar, A. M. Askar, G. M. Bernard, V. V. Terskikh, M. Ha, S. Patel, K. Shankar, and V. K. Michaelis. Mechanochemical synthesis of methylammonium lead mixed-halide perovskites: Unraveling the solid-solution behavior using solid-state NMR. *Chemistry of Materials*, 30(7):2309–2321, 2018.

[344] D. J. Kubicki, D. Prochowicz, A. Hofstetter, S. M Zakeeruddin, M. Grätzel, and L. Emsley. Phase segregation in Cs-, Rb-and K-doped mixed-cation $(MA)_x(FA)_{1-x}PbI_3$ hybrid perovskites from solid-state NMR. *Journal of the American Chemical Society*, 139(40):14173–14180, 2017.

[345] W. Xiang, Z. Wang, D. J. Kubicki, W. Tress, J. Luo, D. Prochowicz, S. Akin, L. Emsley, J. Zhou, G. Dietler, et al. Europium-doped $CsPbI_2Br$ for stable and highly efficient inorganic perovskite solar cells. *Joule*, 3(1): 205–214, 2019.

[346] D. Prochowicz, P. Yadav, M. Saliba, D. J. Kubicki, M. M. Tavakoli, S. M. Zakeeruddin, J. Lewiński, L. Emsley, and M. Grätzel. One-step mechanochemical incorporation of an insoluble cesium additive for high performance planar heterojunction solar cells. *Nano Energy*, 49:523–528, 2018.

[347] A. Karmakar, M. S. Dodd, S. Agnihotri, E. Ravera, and V. K. Michaelis. Cu (II)-doped $Cs_2SbAgCl_6$ double perovskite: A lead-free, low-bandgap material. *Chemistry of Materials*, 30(22):8280–8290, 2018.

[348] A. Abragam and A. Abragam. *The principles of nuclear magnetism.* Number 32. Oxford university press, 1961.

[349] J. Even, L. Pedesseau, J.-M. Jancu, and C. Katan. Importance of spin–orbit coupling in hybrid organic/inorganic perovskites for photovoltaic applications. *The Journal of Physical Chemistry Letters*, 4(17): 2999–3005, 2013.

[350] P. Umari, E. Mosconi, and F. De Angelis. Relativistic GW calculations on $CH_3NH_3PbI_3$ and $CH_3NH_3SnI_3$ perovskites for solar cell applications. *Scientific reports*, 4:4467, 2014.

[351] P. Giannozzi, S. Baroni, N. Bonini, M. Calandra, R. Car, C. Cavazzoni, D. Ceresoli, G. L. Chiarotti, M. Cococcioni, I. Dabo, A. Dal Corso, S. de Gironcoli, S. Fabris, G. Fratesi, R. Gebauer, U. Gerstmann, C. Gougoussis, A. Kokalj, M. Lazzeri, L. Martin-Samos, N. Marzari, F. Mauri, R. Mazzarello, S. Paolini, A. Pasquarello, L. Paulatto, C. Sbraccia, S. Scandolo, G. Sclauzero, A. P. Seitsonen, A. Smogunov, P. Umari, and R. M. Wentzcovitch. Quantum espresso: a modular and open-source software project for quantum simulations of materials. *Journal of Physics: Condensed Matter*, 21(39):395502, 2009.

[352] P. Giannozzi, O. Andreussi, T. Brumme, O. Bunau, M. Buongiorno Nardelli, M. Calandra, R. Car, C. Cavazzoni, D. Ceresoli, M. Cococcioni, N. Colonna, I. Carnimeo, A. Dal Corso, S. de Gironcoli, P. Delugas, R. A. DiStasio Jr, A. Ferretti, A. Floris, G. Fratesi, G. Fugallo, R. Gebauer, U. Gerstmann, F. Giustino, T. Gorni, J. Jia, M. Kawamura, H.-Y. Ko, A. Kokalj, E. Küçükbenli, M. Lazzeri, M. Marsili, N. Marzari, F. Mauri, N. L. Nguyen, H.-V. Nguyen, A. Otero-de-la Roza, L. Paulatto, S. Poncé, D. Rocca, R. Sabatini, B. Santra, M. Schlipf, A. P. Seitsonen, A. Smogunov, I. Timrov, T. Thonhauser, P. Umari, N. Vast, X. Wu, and S. Baroni. Advanced capabilities for materials modelling with quantum espresso. *Journal of Physics: Condensed Matter*, 29(46):465901, 2017.

[353] A. Dal Corso. Pseudopotentials periodic table: From H to Pu. *Computational Materials Science*, 95:337 – 350, 2014.

[354] H. J. Monkhorst and J. D. Pack. Special points for brillouin-zone integrations. *Phys. Rev. B*, 13:5188–5192, 1976.

[355] A. Alkauskas, P. Broqvist, and A. Pasquarello. Defect energy levels in density functional calculations: Alignment and band gap problem. *Phys. Rev. Lett.*, 101:046405, 2008.

[356] CPMD, http://www.cpmd.org/, copyright IBM corp 1990-2015, copyright MPI für festkörperforschung Stuttgart 1997-2001.

[357] S. Goedecker, M. Teter, and J. Hutter. Separable dual-space gaussian pseudopotentials. *Phys. Rev. B*, 54:1703–1710, 1996.

[358] C. Hartwigsen, S. Goedecker, and J. Hutter. Relativistic separable dual-space gaussian pseudopotentials from H to Rn. *Phys. Rev. B*, 58:3641–3662, 1998.

[359] M. Krack. Pseudopotentials for H to Kr optimized for gradient-corrected exchange-correlation functionals. *Theoretical Chemistry Accounts*, 114(1): 145–152, 2005.

[360] S. Nosé. A molecular dynamics method for simulations in the canonical ensemble. *Molecular Physics*, 52(2):255–268, 1984.

[361] S. Nosé. A unified formulation of the constant temperature molecular dynamics methods. *The Journal of Chemical Physics*, 81(1):511–519, 1984.

[362] W. G. Hoover. Canonical dynamics: Equilibrium phase-space distributions. *Phys. Rev. A*, 31:1695–1697, Mar 1985.

[363] S. De Wolf, J. Holovsky, S.-J. Moon, P. Löper, B. Niesen, M. Ledinsky, F.-J. Haug, J.-H. Yum, and C. Ballif. Organometallic halide perovskites: Sharp optical absorption edge and its relation to photovoltaic performance. *The Journal of Physical Chemistry Letters*, 5(6):1035–1039, 2014.

[364] G. Giorgi, J.-I. Fujisawa, H. Segawa, and K. Yamashita. Organic-inorganic hybrid lead iodide perovskite featuring zero dipole moment guanidinium cations: A theoretical analysis. *The Journal of Physical Chemistry C*, 119 (9):4694–4701, 2015.

[365] M. Szafrański. Investigation of phase instabilities in guanidinium halogenoplumbates(II). *Thermochimica Acta*, 307(2):177 – 183, 1997.

[366] A. D. Jodlowski, A. Yépez, R. Luque, L. Camacho, and G. de Miguel. Benign-by-design solventless mechanochemical synthesis of three-, two-, and one-dimensional hybrid perovskites. *Angewandte Chemie International Edition*, 55(48):14972–14977.

[367] N. De Marco, H. Zhou, Q. Chen, P. Sun, Z. Liu, L. Meng, E.-P. Yao, Y. Liu, A. Schiffer, and Y. Yang. Guanidinium: A route to enhanced carrier lifetime and open-circuit voltage in hybrid perovskite solar cells. *Nano Letters*, 16(2):1009–1016, 2016.

[368] A. D. Jodlowski, C. Roldán-Carmona, G. Grancini, M. Salado, M. Ralaiarisoa, S. Ahmad, N. Koch, L. Camacho, G. De Miguel, and M. K. Nazeeruddin. Large guanidinium cation mixed with methylammonium in lead iodide perovskites for 19% efficient solar cells. *Nature Energy*, 2 (12):972, 2017.

[369] O. Nazarenko, M. R. Kotyrba, M. Wörle, E. Cuervo-Reyes, S. Yakunin, and M. V. Kovalenko. Luminescent and photoconductive layered lead halide perovskite compounds comprising mixtures of cesium and guanidinium cations. *Inorganic Chemistry*, 56(19):11552–11564, 2017.

[370] O. Nazarenko, M. R. Kotyrba, S. Yakunin, M. Aebli, G. Rainò, B. M. Benin, M. Wörle, and M. V. Kovalenko. Guanidinium-formamidinium lead iodide: A layered perovskite-related compound with red luminescence at room temperature. *Journal of the American Chemical Society*, 140(11): 3850–3853, 2018.

[371] R. J. Stoddard, A. Rajagopal, R. L. Palmer, I. L. Braly, A. K.-Y. Jen, and H. W. Hillhouse. Enhancing defect tolerance and phase stability of high-bandgap perovskites via guanidinium alloying. *ACS Energy Letters*, 3(6):1261–1268, 2018.

[372] N. D. Pham, C. Zhang, V. T. Tiong, S. Zhang, G. Will, A. Bou, J. Bisquert, P. E. Shaw, A. Du, G. J. Wilson, and H. Wang. Tailoring crystal structure of $FA_{0.83}Cs_{0.17}PbI_3$ perovskite through guanidinium doping for enhanced performance and tunable hysteresis of planar perovskite solar cells. *Advanced Functional Materials*, 0(0):1806479.

[373] J. P. Perdew, A. Ruzsinszky, G. I. Csonka, O. A. Vydrov, G. E. Scuseria, L. A. Constantin, X. Zhou, and K. Burke. Restoring the density-gradient expansion for exchange in solids and surfaces. *Phys. Rev. Lett.*, 100:136406, 2008.

[374] L. Dimesso, A. Quintilla, Y.-M. Kim, U. Lemmer, and W. Jaegermann. Investigation of formamidinium and guanidinium lead tri-iodide powders as precursors for solar cells. *Materials Science and Engineering: B*, 204: 27 – 33, 2016.

[375] B. Fultz. Vibrational thermodynamics of materials. *Progress in Materials Science*, 55(4):247 – 352, 2010.

[376] L. Hedin. New method for calculating the one-particle Green's function with application to the electron-gas problem. *Physical Review*, 139(3A): A796–A823, 1965.

[377] J. P. Perdew, M. Ernzerhof, and K. Burke. Rationale for mixing exact exchange with density functional approximations. *The Journal of Chemical Physics*, 105(22):9982–9985, 1996.

[378] Y. Fu, H. Zhu, C. C. Stoumpos, Q. Ding, J. Wang, M. G. Kanatzidis, X. Zhu, and S. Jin. Broad wavelength tunable robust lasing from single-crystal nanowires of cesium lead halide perovskites (CsPbX3, X = Cl, Br, I). *ACS Nano*, 10(8):7963–7972, 2016.

[379] K. Park, J. W. Lee, J. D. Kim, N. S. Han, D. M. Jang, S. Jeong, J. Park, and J. K. Song. Light-matter interactions in cesium lead halide perovskite nanowire lasers. *The Journal of Physical Chemistry Letters*, 7(18):3703–3710, 2016.

[380] Z. Liu, Q. Shang, C. Li, L. Zhao, Y. Gao, Q. Li, J. Chen, S. Zhang, X. Liu, Y. Fu, and Q. Zhang. Temperature-dependent photoluminescence and lasing properties of $CsPbBr_3$ nanowires. *Applied Physics Letters*, 114 (10):101902, 2019.

[381] Y. Wang, X. Li, X. Zhao, L. Xiao, H. Zeng, and H. Sun. Nonlinear absorption and low-threshold multiphoton pumped stimulated emission from all-inorganic perovskite nanocrystals. *Nano Letters*, 16(1):448–453, 2016.

[382] Y. Xu, Q. Chen, C. Zhang, R. Wang, H. Wu, X. Zhang, G. Xing, W. W. Yu, X. Wang, Y. Zhang, and M. Xiao. Two-photon-pumped perovskite semiconductor nanocrystal lasers. *Journal of the American Chemical Society*, 138(11):3761–3768, 2016.

[383] X. Du, G. Wu, J. Cheng, H. Dang, K. Ma, Y.-W. Zhang, P.-F. Tan, and S. Chen. High-quality $CsPbBr_3$ perovskite nanocrystals for quantum dot light-emitting diodes. *RSC Adv.*, 7:10391–10396, 2017.

[384] D. Yang, P. Li, Y. Zou, M. Cao, H. Hu, Q. Zhong, J. Hu, B. Sun, S. Duhm, Y. Xu, and Q. Zhang. Interfacial synthesis of monodisperse $CsPbBr_3$

nanorods with tunable aspect ratio and clean surface for efficient light-emitting diode applications. *Chemistry of Materials*, 31(5):1575–1583, 2019.

[385] K. Wu, G. Liang, Q. Shang, Y. Ren, D. Kong, and T. Lian. Ultrafast interfacial electron and hole transfer from $CsPbBr_3$ perovskite quantum dots. *Journal of the American Chemical Society*, 137(40):12792–12795, 2015.

[386] A. Swarnkar, R. Chulliyil, V. K. Ravi, M. Irfanullah, A. Chowdhury, and A. Nag. Colloidal $CsPbBr_3$ perovskite nanocrystals: Luminescence beyond traditional quantum dots. *Angewandte Chemie*, 127(51):15644–15648, 2015.

[387] J. Maes, L. Balcaen, E. Drijvers, Q. Zhao, J. De Roo, A. Vantomme, F. Vanhaecke, P. Geiregat, and Z. Hens. Light absorption coefficient of $CsPbBr_3$ perovskite nanocrystals. *The Journal of Physical Chemistry Letters*, 9(11):3093–3097, 2018.

[388] J. Xue, D. Yang, B. Cai, X. Xu, J. Wang, H. Ma, X. Yu, G. Yuan, Y. Zou, J. Song, and H. Zeng. Photon-induced reversible phase transition in $CsPbBr_3$ perovskite. *Advanced Functional Materials*, 29(13):1807922, 2019.

[389] S. Hirotsu, J. Harada, M. Iizumi, and K. Gesi. Structural phase transitions in $CsPbBr_3$. *Journal of the Physical Society of Japan*, 37(5):1393–1398, 1974.

[390] A. D. Wright, C. Verdi, R. L. Milot, G. E. Eperon, M. A. Pérez-Osorio, H. J. Snaith, F. Giustino, M. B. Johnston, and L. M. Herz. Electron-phonon coupling in hybrid lead halide perovskites. *Nature communications*, 7:11755, 2016.

[391] H.-H. Fang, R. Raissa, M. Abdu-Aguye, S. Adjokatse, G. R. Blake, J. Even, and M. A. Loi. Photophysics of organic–inorganic hybrid lead iodide perovskite single crystals. *Advanced Functional Materials*, 25(16): 2378–2385, 2015.

[392] K. Wu, A. Bera, C. Ma, Y. Du, Y. Yang, L. Li, and T. Wu. Temperature-dependent excitonic photoluminescence of hybrid organometal halide perovskite films. *Phys. Chem. Chem. Phys.*, 16:22476–22481, 2014.

[393] A. Shinde, R. Gahlaut, and S. Mahamuni. Low-temperature photoluminescence studies of $CsPbBr_3$ quantum dots. *The Journal of Physical Chemistry C*, 121(27):14872–14878, 2017.

[394] Q. Han, W. Wu, W. Liu, Q. Yang, and Y. Yang. Temperature-dependent photoluminescence of $CsPbX_3$ nanocrystal films. *Journal of Luminescence*, 198:350 – 356, 2018.

[395] A. Dey, P. Rathod, and D. Kabra. Role of localized states in photoluminescence dynamics of high optical gain $CsPbBr_3$ nanocrystals. *Advanced Optical Materials*, 6(11):1800109, 2018.

[396] S. M. Lee, C. J. Moon, H. Lim, Y. Lee, M. Y. Choi, and J. Bang. Temperature-dependent photoluminescence of cesium lead halide perovskite quantum dots: Splitting of the photoluminescence peaks of $CsPbBr_3$ and $CsPb(Br/I)_3$ quantum dots at low temperature. *The Journal of Physical Chemistry C*, 121(46):26054–26062, 2017.

[397] H. Chen, A. Guo, J. Zhu, L. Cheng, and Q. Wang. Tunable photoluminescence of $CsPbBr_3$ perovskite quantum dots for their physical research. *Applied Surface Science*, 465:656 – 664, 2019.

[398] K. Wei, X. Zheng, X. Cheng, C. Shen, and T. Jiang. Observation of ultrafast exciton–exciton annihilation in $CsPbBr_3$ quantum dots. *Advanced Optical Materials*, 4(12):1993–1997, 2016.

[399] J. Chen, K. Žídek, P. Chábera, D. Liu, P. Cheng, L. Nuuttila, M. J. Al-Marri, H. Lehtivuori, M. E. Messing, K. Han, K. Zheng, and T. Pullerits. Size- and wavelength-dependent two-photon absorption cross-section of $CsPbBr_3$ perovskite quantum dots. *The Journal of Physical Chemistry Letters*, 8(10):2316–2321, 2017.

[400] J. Aneesh, A. Swarnkar, V. Kumar Ravi, R. Sharma, A. Nag, and K. V. Adarsh. Ultrafast exciton dynamics in colloidal $CsPbBr_3$ perovskite nanocrystals: Biexciton effect and auger recombination. *The Journal of Physical Chemistry C*, 121(8):4734–4739, 2017.

[401] K. Miyata, D. Meggiolaro, M. T. Trinh, P. P. Joshi, E. Mosconi, S. C. Jones, F. De Angelis, and X.-Y. Zhu. Large polarons in lead halide perovskites. *Science Advances*, 3(8), 2017.

[402] F. Ambrosio, J. Wiktor, F. De Angelis, and A. Pasquarello. Origin of low electron–hole recombination rate in metal halide perovskites. *Energy Environ. Sci.*, 11:101–105, 2018.

[403] M. A. Idowu, S. H. Yau, O. Varnavski, and T. Goodson. Evolution of the dynamics of as-deposited and annealed lead halide perovskites. *ACS Photonics*, 4(5):1195–1206, 2017.

[404] M. Bokdam, T. Sander, A. Stroppa, S. Picozzi, D. D. Sarma, C. Franchini, and G. Kresse. Role of polar phonons in the photo excited state of metal halide perovskites. *Scientific reports*, 6:28618, 2016.

[405] J. S. Manser and P. V. Kamat. Band filling with free charge carriers in organometal halide perovskites. *Nature Photonics*, 8(9):737, 2014.

[406] K. G. Stamplecoskie, J. S. Manser, and P. V. Kamat. Dual nature of the excited state in organic-inorganic lead halide perovskites. *Energy & Environmental Science*, 8(1):208–215, 2015.

[407] S. Nah, B. Spokoyny, X. Jiang, C. Stoumpos, C. M. M. Soe, M. G. Kanatzidis, and E. Harel. Transient sub-bandgap states in halide perovskite thin films. *Nano Letters*, 18(2):827–831, 2018.

[408] N. Yarita, H. Tahara, T. Ihara, T. Kawawaki, R. Sato, M. Saruyama, T. Teranishi, and Y. Kanemitsu. Dynamics of charged excitons and biexcitons in $CsPbBr_3$ perovskite nanocrystals revealed by femtosecond transient-absorption and single-dot luminescence spectroscopy. *The journal of physical chemistry letters*, 8(7):1413–1418, 2017.

[409] J. Butkus, P. Vashishtha, K. Chen, J. K. Gallaher, S. K. K. Prasad, D. Z. Metin, G. Laufersky, N. Gaston, J. E. Halpert, and J. M. Hodgkiss. The evolution of quantum confinement in $CsPbBr_3$ perovskite nanocrystals. *Chemistry of Materials*, 29(8):3644–3652, 2017.

[410] M. C. Brennan, J. Zinna, and M. Kuno. Existence of a size-dependent stokes shift in $CsPbBr_3$ perovskite nanocrystals. *ACS Energy Letters*, 2 (7):1487–1488, 2017.

[411] M. C. Brennan, J. E. Herr, T. S. Nguyen-Beck, J. Zinna, S. Draguta, S. Rouvimov, J. Parkhill, and M. Kuno. Origin of the size-dependent stokes shift in $CsPbBr_3$ perovskite nanocrystals. *Journal of the American Chemical Society*, 139(35):12201–12208, 2017.

[412] L. Wang, C. McCleese, A. Kovalsky, Y. Zhao, and C. Burda. Femtosecond time-resolved transient absorption spectroscopy of $CH_3NH_3PbI_3$ perovskite films: Evidence for passivation effect of PbI_2. *Journal of the American Chemical Society*, 136(35):12205–12208, 2014.

[413] P. T. C. So, C. Y. Dong, K. M. Berland, T. French, and E. Gratton. *Time-Resolved Stimulated-Emission and Transient-Absorption Microscopy and Spectroscopy*, pages 427–469. Springer US, 2002.

[414] S. Sharma, J. K. Dewhurst, A. Sanna, and E. K. U. Gross. Bootstrap approximation for the exchange-correlation kernel of time-dependent density-functional theory. *Phys. Rev. Lett.*, 107:186401, Oct 2011.

[415] P. Baudin. comp_chem_py, a python library for computational chemistry, 2019. URL `http://doi.org/10.5281/zenodo.2580170`.

[416] P. S. Whitfield, N. Herron, W. E. Guise, K. Page, Y. Q. Cheng, I. Milas, and M. K. Crawford. Structures, phase transitions and tricritical behavior of the hybrid perovskite methyl ammonium lead iodide. *Scientific reports*, 6:35685, 2016.

[417] M. Mladenović and U. Rothlisberger. Origins of the unusual band gap inversion in formamidinium lead-tin bromide mixtures. *in preparation.*

[418] A. M. Rappe, K. M. Rabe, E. Kaxiras, and J. D. Joannopoulos. Optimized pseudopotentials. *Phys. Rev. B*, 41:1227–1230, 1990.

[419] W. Setyawan and S. Curtarolo. High-throughput electronic band structure calculations: Challenges and tools. *Computational Materials Science*, 49 (2):299 – 312, 2010.

[420] O. A. Syzgantseva, M. Saliba, M. Grätzel, and U. Rothlisberger. Stabilization of the perovskite phase of formamidinium lead triiodide by methylammonium, Cs, and/or Rb doping. *The Journal of Physical Chemistry Letters*, 8(6):1191–1196, 2017.

Ariadni Boziki

PERSONAL DETAILS

Professional address	Av. F.-A. Forel 2, CH-1015 Lausanne, Switzerland
Professional phone	+41 21 69 30323
Email	`ariadni.boziki@epfl.ch`
Birth	May 17, 1991
Nationality	Greek

EDUCATION

PhD - École Polytechnique Fédérale de Lausanne, Switzerland - Institute of Chemical Sciences and Engineering

01/12/2014 - Present

Laboratory of Computational Chemistry and Biochemistry

Thesis title: "Computational studies of the structural and optical properties of organic-inorganic lead halide perovskites"

Thesis advisor: Prof. Dr Ursula Röthlisberger

Diploma of Chemical Engineering - National Technical University of Athens, Greece

16/09/2009 - 17/09/2014

School of Chemical Engineering (5-year studies equivalent to Master's degree)

Average score: 8.65/10

Diploma thesis title: "Molecular simulations of polymeric melts confined by solid surfaces"

Thesis advisor: Prof. Dr. Doros N. Theodorou

Grade of Diploma thesis: 10/10

WORK EXPERIENCE

AIR LIQUIDE HELLAS S.A.

Industry, (Aspropyrgos, Athens, Greece) **29/09/2013 - 08/11/2013**

Internship

Production technology and quality control of gases.

SMALTOLIN S.A. Industrial Paints
Industry, (Koropi, Athens, Greece) 06/07/2012 - 02/10/2012
Internship
Production department and quality control of paints and varnishes.

QUALIFE Medicinal Herbs
Trading Company, (Koropi, Athens, Greece) 10/08/2011 - 10/10/2011
Internship
Development of sales and marketing plans. Control and storage of raw materials.

Laboratory of Pharmaceuticals and Cosmetics of Nikos Augerinos and Christina Augerinou
Laboratory of pharmaceuticals and cosmetics, (Koropi, Athens, Greece) 11/07/2011 - 29/07/2011
Internship
Production of natural cosmetics, glycolic and alcoholic extracts, vegetal oils extracts, herbal distillates, medicinal tinctures, and herbal tonics.

Institute of Molecular Oncology, Biomedical Sciences Research Center "Alexander Fleming"
Laboratory, (Vari, Athens, Greece) 02/07/2010 - 30/07/2010
Internship
Protein identification through trypsinization, using nano-HPLC, and mass spectrometry.

LANGUAGES

Greek (mother tongue)
English (C2, Certificate of Proficiency in English)
French (B2, Diplome d'etudes en langue française)

COMPUTER SKILLS

Languages	FORTRAN, BASH SCRIPTING
Operating Systems	LINUX, Mac OS, Windows

Softwares QUANTUM ESPRESSO, CPMD, TINKER, DL POLY, LAMMPS, MATLAB, GNUPLOT, XMGRACE, ORIGIN, VMD, VESTA, MATHCAD, AUTOCAD, ASPEN, COMSOL, AIIDA, MICROSOFT OFFICE, LaTeX

MEMBERSHIPS

1. Swiss Chemical Society (2015 - Present)
2. Technical chamber of Greece (23/10/2014 - Present)
3. NRP 70 Energy Turnaround (01/12/2014 - 30/11/2018)
4. NCCR MARVEL (01/12/2014 - 30/04/2018)

TEACHING EXPERIENCE

Supervision of three bachelor projects.

Co-supervision of one master project.

Teaching assistant in the course: "Introduction to Electronic structure methods"
Instructor: Prof. Dr. Ursula Röthlisberger
Fall semesters: 2015 - 2017

Teaching assistant in the course: "Molecular dynamics and Monte-Carlo simulations"
Instructor: Prof. Dr. Ursula Röthlisberger
Spring semesters: 2015 - 2018

OTHER EXPERIENCES

1. Member of the NCCR MARVEL Junior Seminars organizing committee (01/12/2016 - 30/04/2018)
2. Volunteer at the nonprofit organization, SOS EAU GITERANYI (Responsible for researching funds) (10/2017 - Present)

LIST OF PUBLICATIONS

1. J. A. Flores-Livas, D. Tomerini, M. Amsler, **A. Boziki**, U. Röthlisberger, and S. Goedecker. Emergence of hidden phases of methylammonium lead iodide ($CH_3NH_3PbI_3$) upon compression, *Phys Rev Mater*, **2**, 085201 (2018).

2. J. Teuscher, J. C. Brauer, A. Stepanov, A. Solano, **A. Boziki**, M. Chergui, J.-P. Wolf, U. Röthlisberger, N. Banerji, and J.-E. Moser. Charge separation and carrier dynamics in donor-acceptor heterojunction photovoltaic systems, *Struct Dyn*, **4**, 061503 (2017).
3. A. P. Sgouros, G. G. Vogiatzis, G. Kritikos, **A. Boziki**, A. Nikolakopoulou, D. Liveris, and D. N. Theodorou. Molecular simulations of free and graphite capped polyethylene films: estimation of the interfacial free energies, *Macromolecules*, **50**, 8827-8844 (2017).
4. M. I. Dar, G. Jacopin, S. Meloni, A. Mattoni, N. Arora, **A. Boziki**, S. M. Zakeeruddin, U. Röthlisberger, and M. Grätzel. Origin of unusual bandgap shift and dual emission in organic-inorganic lead halide perovskites, *Sci Adv*, **2**, e1601156 (2016).
5. C. Yi, J. Luo, S. Meloni, **A. Boziki**, N. Ashari-Astani, C. Grätzel, S. M. Zakeeruddin, U. Röthlisberger, and M. Grätzel. Entropic stabilization of mixed A-cation ABX_3 metal halide perovskites for high performance perovskite solar cells, *Energy Environ Sci*, **9**, 656-662 (2016).

LIST OF PAPERS IN PREPARATION

1. **A. Boziki**, D. J. Kubicki, A. Mishra, S. Meloni, L. Emsley, M. Grätzel, and U. Rothlisberger. Atomistic origins of the limited phase stability of Cs^+-rich $FA_xCs_{(1-x)}PbI_3$ mixtures.
2. **A. Boziki**, M. Mladenović, M. Grätzel, and U. Rothlisberger. Why choosing the right partner is important: stabilization of ternary $Cs_yGUA_xFA_{(1-y-x)}PbI_3$ mixtures via incorporation of Cs^+.
3. **A. Boziki**, M. I. Dar, M. Grätzel, and U. Rothlisberger. Molecular origin of the asymmetric photoluminescence spectra of $CsPbBr_3$ at low temperature.
4. **A. Boziki**, P. J. Baudin, E. Liberatore, N. Ashari-Astani, M. Mladenović and U. Rothlisberger. Simulations of the ultrafast transient absorption dynamics and of the possible formation of polarons in $CsPbBr_3$.
5. **A. Boziki**, U. Rothlisberger. Estimation of the entropic contribution to the free energy of halide perovskites.

CONFERENCES AND WORKSHOPS

1. "10^{th} Triennial Congress of the International Society for Theoretical Chemical Physics (ISTCP 2019)", Tromsø, Norway (11/07/2019 - 17/07/2019)

   Poster presentation: "Atomistic origins of the preferential stabilization of perovskite over non-perovskite phases of mixed cation lead halide perovskites"

2. "10^{th} International Conference on Hybrid and Organic Photovoltaics", Benidorm, Spain (28/05/2018 - 31/05/2018)

   Poster presentation: "Structure discovery of organic-inorganic halide perovskites"

3. "MARVEL junior seminar", Lausanne, Switzerland (11/05/2017)

   Oral talk: "Crystal discovery of organic-inorganic halide perovskites"

4. "MUST Annual Meeting 2017", Grindelwald, Switzerland (10/01/2017 - 11/01/2017

   Poster presentation: "Absorption and emission characteristics of organic-inorganic lead halide perovskites"

5. "MARVEL Review and Retreat 2016", Lausanne, Switzerland (08/09/2016)

   Highlight oral talk: "Phase stabilization through cation mixing of lead halide perovskites"

6. "8^{th} International Conference of Hybrid and Organic Photovoltaics", Swansea, United Kingdom (29/06/2016 - 01/07/2016)

   Oral talk: "Molecular origin of phase stabilization through cation mixing of lead halide perovskites"

   Poster presentation: "A polarizable model potential for $MAPbI_3$"

7. "CECAM Workshop: Perovskite solar cells - The quest for a theoretical description", Lausanne, Switzerland (25/08/2015 - 28/08/2015)

8. "Nothing is perfect - The quantum mechanics of defects", Ascona, Switzerland (26/04/2015 - 29/04/2015)

9. "9^{th} National Chemical Engineering Conference: the contribution of chemical engineering in sustainable development", Athens, Greece (23/05/2013 - 25/05/2013)

10. "Bioenergy Conference: Scientific approach and analysis of biomass, biofuels and biogas. Raw materials. Technology and applications", Athens, Greece (07/10/2012)

TUTORIALS AND SCHOOLS

1. "Advanced Workshop on High-Performance and High-Throughput Materials Simulations using Quantum ESPRESSO", Trieste, Italy (16/01/2017 - 27/01/2017)
2. "MARVEL/MaX/Psi-k Tutorial on high-throughput computations: general methods and applications using AiiDA", Lausanne, Switzerland (22/06/2016 - 24/06/2016)

AWARDS AND HONORS

1. Prize for the best poster during the 10^{th} Triennial Congress of the International Society for Theoretical Chemical Physics (ISTCP 2019), sponsored by American Chemical Society (ACS).
2. English language scholarship from the non-profit Michael Lascaris Scholarship Trust in Chicago, USA.
3. Honor in the mathematical contest of the Greek Mathematical Society (2007)

INTERESTS - ACTIVITIES

Music: 24 years of piano playing with regular lessons, practice and participation to concerts and 10 years of opera singing with regular lessons and recent participation at the choir of EPFL. Associate of music theory teacher certification.
Dance: Dancing ballet since the age of 4 years old, following regular lessons and participating to ballet performances.
Literature: Interested in poetry, prose and philosophy. Recitations of poems for three years in the Greek society of writers.

REFERENCES

Available upon request

Ce document a été imprimé au Centre d’impression EPFL,
imprimerie climatiquement neutre, certifiée myClimate.